

NASA/CR—1999-209310



# Large Eddy Simulations and Turbulence Modeling for Film Cooling

Sumanta Acharya  
Louisiana State University, Baton Rouge, Louisiana

---

September 1999

## The NASA STI Program Office . . . in Profile

Since its founding, NASA has been dedicated to the advancement of aeronautics and space science. The NASA Scientific and Technical Information (STI) Program Office plays a key part in helping NASA maintain this important role.

The NASA STI Program Office is operated by Langley Research Center, the Lead Center for NASA's scientific and technical information. The NASA STI Program Office provides access to the NASA STI Database, the largest collection of aeronautical and space science STI in the world. The Program Office is also NASA's institutional mechanism for disseminating the results of its research and development activities. These results are published by NASA in the NASA STI Report Series, which includes the following report types:

- **TECHNICAL PUBLICATION.** Reports of completed research or a major significant phase of research that present the results of NASA programs and include extensive data or theoretical analysis. Includes compilations of significant scientific and technical data and information deemed to be of continuing reference value. NASA's counterpart of peer-reviewed formal professional papers but has less stringent limitations on manuscript length and extent of graphic presentations.
- **TECHNICAL MEMORANDUM.** Scientific and technical findings that are preliminary or of specialized interest, e.g., quick release reports, working papers, and bibliographies that contain minimal annotation. Does not contain extensive analysis.
- **CONTRACTOR REPORT.** Scientific and technical findings by NASA-sponsored contractors and grantees.
- **CONFERENCE PUBLICATION.** Collected papers from scientific and technical conferences, symposia, seminars, or other meetings sponsored or cosponsored by NASA.
- **SPECIAL PUBLICATION.** Scientific, technical, or historical information from NASA programs, projects, and missions, often concerned with subjects having substantial public interest.
- **TECHNICAL TRANSLATION.** English-language translations of foreign scientific and technical material pertinent to NASA's mission.

Specialized services that complement the STI Program Office's diverse offerings include creating custom thesauri, building customized data bases, organizing and publishing research results . . . even providing videos.

For more information about the NASA STI Program Office, see the following:

- Access the NASA STI Program Home Page at <http://www.sti.nasa.gov>
- E-mail your question via the Internet to [help@sti.nasa.gov](mailto:help@sti.nasa.gov)
- Fax your question to the NASA Access Help Desk at (301) 621-0134
- Telephone the NASA Access Help Desk at (301) 621-0390
- Write to:  
NASA Access Help Desk  
NASA Center for AeroSpace Information  
7121 Standard Drive  
Hanover, MD 21076

NASA/CR—1999-209310



# Large Eddy Simulations and Turbulence Modeling for Film Cooling

Sumanta Acharya  
Louisiana State University, Baton Rouge, Louisiana

Prepared under Grant NAG3-1641

National Aeronautics and  
Space Administration

Glenn Research Center

---

September 1999

## Acknowledgments

The work included in this report was funded by NAG3-1641 grant from NASA-Glenn under the Advanced Subsonic Technology program. The period of funding was from 1994-1997, and a no-cost extension was granted till September 30, 1998. The support from NASA-Glenn is gratefully acknowledged. The grant was monitored by the Turbine Branch headed by Dr. Raymond Gaugler. The initial contract monitor for the grant was Dr. John Schwab, and was followed by Dr. Chi-Rong Wang. Both contract monitors and Dr. Gaugler have been very helpful and supportive of our work, and we truly appreciate their understanding, patience and time. Dr. Louis Chiappetta of United Technology Research Center (UTRC) and Dr. Seyf Tanrikut of Pratt & Whitney provided the initial encouragement to explore Large Eddy Simulation for film cooling applications. Their help and guidance in the development of the proposal is appreciated. The computational work was performed on a variety of platforms.

These include the following: (1) CRAY C-90 at NAS Facility, NASA-Ames; (2) CRAY YMP, NASA-Glenn Research Center; (3) NAVO T3E parallel computers; (4) NAVO T-90 computer; (5) LSU's MASPAR-1 system; (6) University of Iowa, MasPar-2 system; (7) LSU-ME-CFD Lab, ALFA workstations. The computational support from all these facilities is gratefully acknowledged. We particularly appreciate the help of Ms. Susan Johnson of NASA-Glenn, and Ms. Annette May of ONR for helping us with computer time. The computer codes and results presented in this report were done by a number of graduate students and research associates under the supervision of Professor Sumanta Acharya. The primary contributors to this effort include the following: (1) Mr. Frank Muldoon, Ph. D student; (2) Mr. Mayank Tyagi, Ph. D student; (3) Mr. Asif Hoda, Ph. D student; (4) Mr. Chirdeep Sharma, M. S student; (5) Dr. M. Taeibi-Rahni, Research Associate. In addition, Mr. Raymond Jones, Ph. D student, has also provided assistance to this effort. The report is organized into several independent chapters, and each chapter can be read without reference to the earlier chapters. For this reason, each chapter has its own references section, and there is some repetition in the literature survey and problem description in successive chapters. Readers of this report are encouraged to contact Professor Acharya for any questions or clarifications.

Available from

NASA Center for Aerospace Information  
7121 Standard Drive  
Hanover, MD 21076  
Price Code: A07

National Technical Information Service  
5285 Port Royal Road  
Springfield, VA 22100  
Price Code: A07

**Final Grant Report**

**Large Eddy Simulations and Turbulence Modeling for Film Cooling**

**NASA-Glenn Grant  
NAG3-1641**

Contract Monitors  
**Dr. Chi R. Wang**  
**Dr. Raymond E. Gaugler**  
**Turbine Branch**

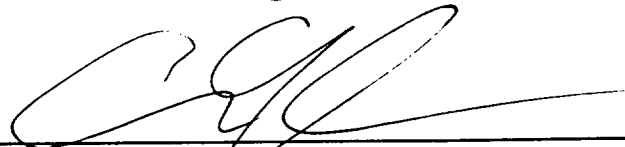
National Aeronautics and Space Administration  
Glenn Research Center  
21000 Brookpark Road  
Cleveland, Ohio 44135

Submitted By



---

**Sumanta Acharya**  
Mechanical Engineering Department  
Louisiana State University  
Baton Rouge, LA 70803



---

**Dr. Charles E. Graham**  
Director  
Office of Sponsored Research  
Louisiana State University

## TABLE OF CONTENTS

	<u>PAGE</u>
I. ACKNOWLEDGEMENTS	3
II. INTRODUCTION	4
III. DIRECT NUMERICAL SIMULATION (DNS) OF A ROW OF NORMAL FILM COOLING JETS IN A CROSSFLOW	9
IV. DIRECT NUMERICAL SIMULATION (DNS) OF NORMAL FILM COOLING JETS IN A PERIODIC CROSSFLOW	38
V. LARGE EDDY SIMULATION (LES) OF NORMAL FILM COOLING JETS IN CROSSFLOW: FREESTREAM TURBULENCE EFFECTS	73
VI. LARGE EDDY SIMULATIONS OF JETS IN CROSSFLOW: LARGE SCALE TURBULENCE EFFECTS	83
VII. LARGE EDDY SIMULATION (LES) OF INCLINED FILM COOLING JETS IN CROSSFLOW	97
VIII. REYNOLDS-AVERAGED-NAVIER STOKES (RANS) SIMULATIONS OF NORMAL FILM COOLING JETS IN CROSSFLOW	110
IX. CONCLUDING REMARKS AND FUTURE WORK	132

# CHAPTER I

## ACKNOWLEDGEMENTS

The work included in this report was funded by NAG3-1641 grant from NASA-Glenn under the Advanced Subsonic Technology program. The period of funding was from 1994-1997, and a no-cost extension was granted till Sep. 30, 1998. The support from NASA-Glenn is gratefully acknowledged.

The grant was monitored by the Turbine Branch headed by Dr. Raymond Gaugler. The initial contract monitor for the grant was Dr. John Schwab, and was followed by Dr. Chi-Rong Wang. Both contract monitors and Dr. Gaugler have been very helpful and supportive of our work, and we truly appreciate their understanding, patience and time.

Dr. Louis Chiappetta of United Technology Research Center (UTRC) and Dr. Seyf Tanrikut of Pratt & Whitney provided the initial encouragement to explore Large Eddy Simulation for film cooling applications. Their help and guidance in the development of the proposal is appreciated.

The computational work was performed on a variety of platforms. These include the following:

1. CRAY C-90 at NAS Facility, NASA-Ames
2. CRAY YMP, NASA-Glenn Research Center
3. NAVO T3E parallel computers
4. NAVO T-90 computer
5. LSU's MASP-1 system
6. Univ. of Iowa, MasPar-2 system
7. LSU-ME-CFD Lab, ALFA workstations

The computational support from all these facilities is gratefully acknowledged. We particularly appreciate the help of Ms. Susan Johnson of NASA-Glenn, and Ms. Annette May of ONR for helping us with computer time.

The computer codes and results presented in this report were done by a number of graduate students and research associates under the supervision of Professor Sumanta Acharya. The primary contributors to this effort include the following:

1. Mr. Frank Muldoon, Ph.D student
2. Mr. Mayank Tyagi, Ph. D student
3. Mr. Asif Hoda, Ph. D student
4. Mr. Chirdeep Sharma, M. S student
5. Dr. M.Taeibi-Rahni, Research Associate

In addition, Mr. Raymond Jones, Ph. D student, has also provided assistance to this effort.

The report is organized into several independent chapters, and each chapter can be read without reference to the earlier chapters. For this reason, each chapter has its own references section, and there is some repetition in the literature survey and problem description in successive chapters. Readers of this report are encouraged to contact Professor Acharya for any questions or clarifications.

## CHAPTER II

### INTRODUCTION

#### MOTIVATION AND OBJECTIVES

Film cooling of gas turbine blades, in which a cool gas is injected at select locations over the blade surface, is extensively used in military and commercial gas turbines. Even for one row of holes, the flow field is quite complex with a wide variety of influence parameters such as blowing angles, lateral spacing, blowing ratio, density ratio, injection hole diameter and shape, and the state of the approaching mainstream flow and coolant gas flow. The cooling gas is generally air, trapped from the compressor, and is therefore a source of flow loss. Further, injection of coolant gas has two opposing effects on the heat transfer. The thermal dilution effect reduces heat transfer to the blade, but crossflow injection increases turbulence levels in the flow, and this can lead to an increase in the heat transfer. The gains achieved by film cooling must overcome the deleterious effects of flow losses and turbulence enhancement, and since these gains and losses depend on the influence parameters, a careful optimization of the film cooling process for each gas turbine design is necessary. Due to the large number of influence parameters, design optimization through experiments can be quite expensive and time-consuming, and from a practical perspective, a reliable computationally efficient predictive procedure would be extremely beneficial to the gas turbine industry. The proposed research represents an effort in this direction.

The present state of the art in numerical predictions is generally not satisfactory, due primarily to the incorrect closure expressions used for modeling turbulence. Generally, the Reynolds averaged equations have been solved, and an eddy viscosity concept based on a gradient approximation for the turbulent stresses has been used. The eddy viscosity has been calculated either from an algebraic model (see for example, Kulisa et al., 1992; Yavuzkurt et al., 1980; Herring, 1975) or a two-equation turbulence model (Demuren et al., 1986; Haas et al., 1992; Chiappette, 1994) originally proposed by Launder and Spalding (1974) and Jones and Launder (1972). This approach generally leads to an overprediction of the coolant jet penetration in the normal (to the surface) direction (Kulisa et al., 1992; Chiappetta, 1994) and grossly inaccurate predictions of the cooling effectiveness near the injection holes (Chiappetta, 1994; Haas et al., 1992). Since the film cooling effectiveness is of primary interest to the industrial designer, any predictive model that is unable to predict the effectiveness correctly is not wholly satisfactory.

The deficiencies of a Reynolds-Averaged Navier Stokes (RANS) formulation for turbulent flow are well known: the space-time computational grid are too coarse to resolve the dynamic scales in the turbulent flow, and the statistical effects of turbulence fluctuations on the mean flow are modeled using either algebraic eddy viscosity models, two-equation models or Reynolds stress models. The accuracy of the predictions are therefore strongly dependent on the accuracy of the closure approximations, and to date, the RANS formulation has not yielded accurate predictions in complex flowfields. In Direct Numerical Simulations (DNS), the computational mesh is chosen so as to resolve all essential scales in the turbulent flow, and no modeling is required. However, due to the fine mesh needed, the DNS is limited to lower Reynolds number flows. As the Reynolds number is increased, the scales in the flow diminish, and the mesh resolution becomes prohibitively expensive. To permit optimization of film cooling design over a wide parameter range, a computationally efficient procedure is needed by the gas

turbine industry, and therefore DNS is not a viable alternative at this time. A suitable compromise between the RANS and DNS is the Large Eddy Simulation (LES) approach, in which, the larger scales of the flow are resolved directly, and the small scale fluctuations are modeled. The basic premise of the LES approach is that the scales that are dynamically resolved are the important ones, and that the errors introduced in modeling the small scale fluctuations are considerably smaller than the errors in the RANS formulation where the entire turbulence stresses are modeled.

The objective of the proposed research is to perform Direct numerical Simulations (DNS) and Large Eddy Simulations (LES) for the film cooling process, and to evaluate and improve advanced forms of the two equation turbulence models. It is important to note that in the near field of the film cooling jet, the large scale structures are likely to control the mixing process, as has been shown in free jet studies (see, for example, the review by Ho and Huerre, 1984) and it is this mixing that dictates the normal and transverse penetration of the jet. Thus the RANS computations, that are incapable of supporting flow instabilities that lead to the evolution and growth of large scale structures, are not expected to give realistic predictions in the near field of the coolant jets. Perhaps, ad-hoc modifications to closure models used in the RANS formulation can be made, so that predictions, in an average sense, will improve. DNS/LES, on the other hand, will be able to resolve the large eddies in the near field of the coolant jets, and should therefore yield more realistic predictions. The use of DNS/LES for selected film cooling configurations is therefore the first objective of the proposed work. Evaluation of advanced turbulence models in the RANS formulation is the second objective of the work.

## **SPECIFIC TASKS COMPLETED**

The work done under this project involved code development as well as application of the codes developed to the film cooling problem. Since DNS/LES codes are not routinely available, a considerable level of effort was spent in developing and testing codes and algorithms. Several students were involved in this effort, and this led to the independent development of several codes. No detailed discussions on the code or algorithms are presented here; instead, a brief description of the numerical methodology is presented in the successive chapters. In reading these chapters, the reader will realize that different computing codes were developed and utilized at different stages of the research, and the code and algorithm development have been evolutionary processes. The same can be said about the use of turbulence models, and the use of subgrid stress models in the LES simulations. Professor Acharya and his group continue to work on these problems at the time of writing this report.

Essentially five different codes were developed and utilized in performing this research. These can be summarized as follows:

1. A dual-time stepping pseudo-compressibility based approach for solving the incompressible Navier Stokes equations was developed for DNS studies. Several versions of this code were tested and include: (a) a collocated multi-block finite-difference code (b) a staggered multi-block, multi-grid finite difference code (c) a collocated multi-block spectral code. Currently efforts are being pursued to include multi-grid procedure into the collocated multi-block finite difference code. Higher order finite differences are used and range from sixth-order central differences for the diffusion term to fifth order upwind biased approximation for the convection terms. Second and third order-accurate local time stepping schemes have been employed. For the spectral method, Chebyshev basis functions are used. More description of

some aspects of this method are described in Chapter III. The code has been optimized with HPF to run on the Cray T-90 parallel platform. A paper is being prepared outlining the details of this pseudo-compressibility DNS method.

2. A collocated higher order finite difference code using a fractional step approach and a pressure-Poisson solver has also been developed. This code has been used primarily for DNS simulations. Higher order finite differences are again employed for the convection and diffusion terms while the pressure Poisson equation is solved using a mixed spectral-finite difference procedure. This mixed procedure entails a Fourier decomposition in the spanwise direction reducing the 3-dimensional pressure-Poisson equation to a 2-dimensional equation for each wave number in the spanwise direction. The resulting 2-dimensional equation is then solved by a direct matrix-diagonalization based procedure. The resulting method is computationally very efficient. The code has been optimized to execute on a massively parallel platform, the MasPar1 and MasPar2. Additional details of this method are presented in Chapter IV.
3. A staggered higher-order finite difference code using a fractional step approach and a pressure-Poisson solver has been developed for LES simulations. The formulation is similar to that described in 2. above, except that a staggered grid is employed. The code is currently a single block code, but is computationally very efficient. LES calculations are being performed on a Digital-Alfa 500 workstation with typical single-day run times for a complete LES simulations for the film cooling application. Additional details of this code and subgrid models used can be found in Chapters V and VI. Results in Chapters V and VI are presented with the dynamic mixed model for the subgrid stresses. Additional work (not reported in this report) can be found in papers written for the 2<sup>nd</sup> AFOSR DNS/LES conference in Rutgers, NJ, June 1999 (paper presents hole aspect ratio effects on film cooling flow behavior), and the 1999 ASME-IMECE Conference, November, 1999, Nashville (paper presents length scale effects on dispersion of the film cooling jet). Further, we are currently producing results with improved subgrid stress models such as the inverse model for subgrid stress estimation, and with LES simulations for surface heat transfer and film cooling effectiveness. Papers on these issues will be written during the summer of 1999, and will be available by the end of summer.
4. A staggered finite volume code for RANS simulations. The code uses a SIMPLER type formulation, and at most, second order accurate schemes. A line relaxation procedure is used to obtain the solutions. Several turbulence models have been employed ranging from high Re and low-Re versions of linear two-equation models, and non-linear two-equation models. Currently solutions are being obtained with the Reynolds-stress transport models and a recently formulated  $v_2$ -f model by Durbin at Stanford's Center for Turbulence Research. Results from these activities are currently being written up for publication.
5. In order to extend RANS calculations into more complex geometries, a pseudo-compressibility based RANS solver, first developed at NASA-Ames (called INS3D), is being employed. The code is a multi-block curvilinear code and uses an implicit approximate factorization scheme, 3<sup>rd</sup> or 5<sup>th</sup> order vector-flux splitting for the convective terms, and a second order accurate central difference approximation for the viscous terms. A GMRES relaxation procedure is used to obtain the solutions to

the equations. We have extended this codes capability and integrated several advanced turbulence models into this RANS solver. Work is currently underway to extend this code into a curvilinear LES code so that LES calculations on complex airfoil geometries and hole shapes can be achieved.

## **PUBLICATIONS RESULTING FROM THE WORK**

*(Papers listed below have already been written, and copies of these papers are now available on request. Several other papers are currently being written, and these will be available at a later time)*

1. Muldoon, F., and Acharya, S., "Dynamics of Large Scale Structures for Jets in CrossFlow", *ASME J. of Turbomachinery*, Vol. 121, No. 3, July 1999
2. Muldoon, F., and Acharya, S., "Dynamics of Large Scale Structures for Jets in CrossFlow", *ASME-International Gas Turbine Conference*, 1998, Stockholm, Paper ASME 98-GT-019
3. Sharma, C., and Acharya, S., "Direct Numerical Simulation of Flow and Heat Transfer in a Periodic Channel Flow with Slot Injection and Suction: I- Injection Results" *ASME-International Mechanical Engineering Congress and Exposition (IMECE)*, Anaheim, November 1998, HTD Vol 361-1, pp. 363-388; also submitted *J. Fluid Mechanics*
4. Hoda, A., and Acharya, S., "Predictions of a Film Coolant Jet in Crossflow with Different Turbulence Models", *ASME Journal of Turbomachinery*, Accepted for Publication April 1999
5. Hoda, A., and Acharya, S., "Predictions of a Film Coolant Jet in Crossflow with Different Turbulence Models", *ASME-IGTI Intl. Gas Turbine Conference*, Indianapolis, June 1999.
6. Muldoon, F., and Acharya, S., "Numerical Investigation of the Dynamical Behavior of a Row of Square Jets in Crossflow over a Surface", *ASME-IGTI Intl. Gas Turbine Conference*, Indianapolis, June 1999.
7. Tyagi, M., and Acharya, S., "Large Eddy Simulation of a Jet in Crossflow: Freestream Turbulence Effects", *ASME/JSME Fluids Engineering Meeting*, San Francisco, July 1999.
8. Tyagi, M., and Acharya, S., "Large Eddy Simulations of an Inclined Jet in Crossflow", *ASME-ISHMT Heat Transfer Conference*, Pune, January 2000, submitted
9. Tyagi, M., and Acharya, S., "Large Eddy Simulation of a Jet in Crossflow: Effect of Freestream Turbulence Length Scales", *ASME-IMECE Conference*, Nov. 1999, *Nashville*

10. Tyagi, M., and Acharya, S., "Hole-Aspect Ratio Effects for a Jet in Crossflow", 2<sup>nd</sup> AFOSR DNS/LES conference in Rutgers, NJ, June 1999

## REFERENCES

- Chiappetta, L., 1994, Private Communication
- Demuren, A. O., 1986a, Modeling Turbulent Jets in a Crossflow, in Encyclopedia of Fluid Mechanics, N. P. Chereisinoff, ed., Vol. 2-1, Gulf Pub. Co., pp. 431-465
- Haas, W., Rodi, W., and Schonung, B., 1992, The Influence of Density Difference Between Hot and Coolant Gas on Film Cooling by a Row of Holes: Predictions and Experiments, ASME J. Turbomachinery, Vol. 114, pp. 747-755
- Herring, M. J., 1975, A Method of Predicting the Behavior of a Turbulent Boundary Layer with Discrete Transpiration Jets, ASME J. Engg. for Power, Vol. 97, pp.214-225
- Ho, C. J. and Huerre, P., 1984, Perturbed Shear Layers, Ann. Re. Fluid Mech., Vol. 16, pp.365-424
- Jones, W., and Launder, B. E., 1972, The Prediction of Laminarization with a Two Equation Model of Turbulence, Int. J. Heat Mass Transfer, Vol. 15, pp. 301-314
- Kulisa, P., Leboeuf, F., and Perrin, G., 1992, Computation of a Wall Boundary Layer with Discrete Jet Injections, ASME J. Turbomachinery, Vol. 114, pp.756-764
- Launder, B. and Spalding, D.B., 1974, The Numerical Computation of Turbulent Flows, Comp. Meth. Appl. Mech. Engg., Vol. 3, pp. 269-289
- Yavuzkurt, S., Moffat, R. J., and Kays, W. M., 1980, Full Coverage Film Cooling. Part 2. Prediction of Recovery Region Hydrdynamics, J. Fluid Mech., Vol. 101, pp159-178

## CHAPTER III

### DIRECT NUMERICAL SIMULATION (DNS) OF A ROW OF NORMAL FILM COOLING JETS IN A CROSSFLOW

#### ABSTRACT

Results of a three dimensional unsteady computational study of a row of jets injected normal to a cross-flow are presented with the aim of understanding the dynamics of the large scale structures in the region near the jet. The jet hole is square in cross-section, and the jet to cross-flow velocity ratio is 0.5. The calculations are based on higher-order finite differences, and are performed on extremely refined spatial and temporal meshes so that all the important energy-carrying scales are resolved. Results obtained indicate that the near field large scale structures include the shear layer vortices, the counter rotating vortex pair (CVP), the horseshoe vortex system, and wake and wall vortices. The dynamics of these structures appear to be significantly influenced by a time-periodic interaction between the jet hole boundary layer and the approaching crossflow. This periodic behavior involves the approaching crossflow periodically ingressing into the jet hole region and pushing the injected jet back toward the trailing edge at a Strouhal number of 0.44 based on the jet velocity and diameter. A new mechanism for the formation of shear layer vortices is identified and consists of alternate shedding of positive vorticity from the hole leading edge boundary layer and negative vorticity from the leading horseshoe vortex. Comparison of the predicted turbulent statistics with experimental measurements are made and reasonable agreement is observed.

#### NOMENCLATURE

D	Width of the square jet hole exit
Re	Reynolds number based on the jet velocity and diameter
T	dimensional time
t	dimensionless time ( $T/D/V_{jet}$ )
U	dimensional velocity in the crossflow direction
V	dimensional velocity normal to the surface
W	dimensional velocity in the spanwise direction
u	non-dimensional ( $=U/V_{jet}$ ) velocity in the crossflow direction
v	non-dimensional ( $=V/V_{jet}$ ) velocity normal to the surface
w	non-dimensional ( $=W/V_{jet}$ ) velocity in the spanwise direction
X	dimensional coordinate in the crossflow direction
Y	dimensional coordinate normal to the surface
Z	dimensional coordinate in the spanwise direction
x	non-dimensional coordinate ( $=X/D$ ) in the crossflow direction
y	non-dimensional coordinate ( $=Y/D$ ) normal to the surface
z	non-dimensional coordinate ( $=Z/D$ ) in the spanwise direction
$\beta$	pseudo-compressibility parameter
$\tau$	pseudo-time

## INTRODUCTION

Jets in crossflow are encountered in a number of engineering applications including film cooling of turbine blades and combustor walls, V/STOL aircrafts, flow-control of missiles, chimney discharges into the environment and effluent or chemical by-product discharges into flowing water bodies. The flow field for the jet-in-a-crossflow is quite complex as demonstrated by a number of flow visualization studies (for example, Fric and Roshko, 1994; Kelso et al., 1996; Andreopoulos, 1985), and measurements (Andreopoulos and Rodi, 1984; Kamotani and Gerber, 1972). These studies clearly reveal that in the near field of the jet, the large-scale structures play a dominant role, and that these structures are quite unsteady in nature. The majority of the reported computational studies have primarily solved the Reynolds-Averaged-Navier-Stokes (RANS) equations, and due to the intrinsic time-averaging that is associated with these equations, the dynamical nature of the vortical structures can not be predicted. Further, turbulence models have to be introduced, and the accuracy of even the time averaged calculations are themselves compromised by the validity of the model. Examples of RANS calculations are those of Patankar et al., (1977), Sykes et al. (1986), Kim and Benson (1992), Demuren (1993), and Garg and Gaugler, (1994, 1995). More recently, Jones (1996) and Yuan and Street (1996) presented Large Eddy Simulations (LES) that resolve the dynamics of the large scales and model the small scales, and observed some of the reported phenomena in the experiments. However, to correctly reproduce the flow physics, a time-accurate and space-accurate calculation has to be performed on meshes that temporally and spatially resolve all the energy carrying structures in the flow. With such a procedure, no models for turbulence have to be introduced, and the flow physics is expected to be correctly predicted.

The application of interest in the present chapter is the film cooling of gas turbine blades. In this configuration, a row of coolant jets is injected into a hot crossflow. The goal of the jets is to provide a wide coverage of the blade surface. This problem differs from the single-jet-in-crossflow studies, in that, the spanwise boundaries are no longer freestream boundaries. They are periodic or symmetry (for time averaged calculations) boundary conditions. Further the blowing ratios of interest in turbine blade cooling are usually low (ranging from 0.5 to 2), and for low blowing ratios the flow development in the injection hole is affected by the crossflow leading to a highly non-uniform jet-exit profile. This is in contrast to the more commonly studied single-jet studies at high blowing ratios where the hole exit profile is more or less symmetrical and is not strongly influenced by the crossflow. Since the vorticity exiting the hole has a very strong influence on the downstream development of the dynamical structures, appropriate specification of the jet-exit conditions is necessary. This requirement dictates that the calculation should include the flow development in the coolant hole which the majority of the computational studies have ignored.

The goal of this chapter is to present time-and space accurate calculations for a typical film cooling configuration, with the specific intent of understanding the dynamics of the various vortical structures in the near-field. Jet-Reynolds number of interest in film cooling applications range from 5,000 to 50,000, while blowing ratios of interest range from 0.5-2. The lower parametric ranges have been selected to keep the computational problem feasible. Increasing the Reynolds numbers would require greater spatial and temporal mesh resolution, while increasing the blowing ratio increases jet penetration that would increase the vertical extent of the computational domain, and would again increase the number of grid points in the calculation

domain. However, since the flow development in the coolant jet-hole is critical to the near field evolution of the flow structures, the calculation domain is extended  $6.5 D$  into the jet hole to include the effects of the crossflow on the flow development in the jet hole.

Square jet-holes injected vertically upwards into the crossflow are considered in this study. There are two reasons for this choice of geometrical configuration. First, time averaged measurements for this configuration have been reported by Ajersch et al. (1995), and therefore the present predictions can be validated with the reported measurements. Second, square holes on a flat surface permits the use of a Cartesian mesh that considerably simplifies the computational problem over that required by a curvilinear mesh for a round hole.

## NUMERICAL METHOD

The governing equations are the three-dimensional, unsteady incompressible Navier-Stokes equations. As there are no shocks, the non-conservative form of the equations is chosen. The non-conservative form requires less floating point operations for a finite difference representation of the convective terms than the conservative form.

The three-dimensional, incompressible Navier-Stokes equations in their unsteady form are solved using the method of artificial compressibility. The method of artificial compressibility was first proposed by Chorin (1968) for steady state solutions to the Navier-Stokes equations. In this method the incompressible continuity equation is modified by the addition of a first derivative of pressure, divided by a constant  $\beta$ , with respect to a pseudo-time ( $\tau$ ). First derivatives of  $u$ ,  $v$  and  $w$  with respect to a pseudo-time are also added to their respective momentum equations. This creates a situation similar to that of the compressible Navier-Stokes equations in which the effect of pressure appears in the continuity equation due to the presence of a derivative of density with respect to time. When steady state is reached in pseudotime the added terms become zero and the system of equations is satisfied. This method has been used by many researchers to solve the steady state Navier-Stokes equations. More recently solutions to the unsteady Navier-Stokes equations have been obtained by adding the appropriate real time derivative terms to the momentum equations and obtaining a converged solution in pseudotime for each real time step. This approach has much in common with recent methods for solving the compressible Navier-Stokes equations at low Mach numbers.

The governing equations were reduced to non dimensional units by the use of  $D$  and the average velocity of the jet. The physical parameter of interest is the jet Reynolds number. The pseudo-compressibility parameter  $\beta$  and the pseudo-time step ( $\Delta\tau$ ) are chosen so as to maximize the rate of convergence. In general the larger  $\beta$  is the smaller  $\Delta\tau$  must be in order to maintain stability. Also the larger  $\beta$  is relative to  $\Delta\tau$  the smaller the residual of the continuity equation will be relative to that of the momentum equations. The value of  $\beta$  used in this chapter was 30.

The numerical method was verified by using the code to compute the common benchmark problem of vortex shedding behind a square cylinder. The value of the computed Strouhal number was well within the range of that reported by others.

### Spatial and Temporal Differencing

The non-conservative form of the equations are differenced on a staggered Cartesian grid. A staggered grid is used to prevent the problem of pressure-velocity decoupling. A third order accurate convective scheme has been developed. This scheme uses a four point upwind biased stencil derived from a Taylor series expansion for the convective terms. The diffusive terms are represented by fourth order accurate central differences.

Points that lie near boundaries are represented by lower (second) order finite differences. Since a staggered grid is used, i.e.  $u$ ,  $v$ ,  $w$  and  $p$  are defined at different locations it is necessary to interpolate the velocity components onto each other. This is done by fitting a Lagrange surface, defined by four points, over the desired location. The pressure gradient terms and continuity equation are represented by sixth order accurate finite differences derived from a Taylor series expansion. Lower order central differences are used near boundaries. A third order accurate backward finite difference is used to represent the temporal terms involving real time. Since the time accuracy of the transient behavior in pseudo time is of no concern, first order forward differencing in pseudo-time is used. The resulting algorithm is explicit in pseudo-time. This explicit formulation is well suited to processing on vector and parallel computers.

### **Grid**

The grid is a staggered Cartesian grid with unequal spacing in the  $X$  and  $Y$  directions. Two zones are used. The first grid contains everything on and above the surface from which the jet exits. The second grid contains the plenum and 7 points in the  $Y$  direction of the first grid. The coordinates of grid points that lie in both of the grids are the same. Thus no interpolation between the two zones are needed, and the calculation from one zone to another is handled seamlessly. The locations where the velocity components are defined are halfway between the locations where pressure is defined.

### **Boundary Conditions**

The first block above the flat plate uses periodic boundary conditions in the  $z$ -direction. For the outflow boundary, the common convective boundary condition is used. Due to the staggered grid arrangement, only one velocity component can be specified on each boundary. The  $u$  component can be specified on a  $YZ$  plane boundary, the  $v$  component on a  $XZ$  and the  $w$  component on a  $XY$  plane. The other two velocity components require special treatment. This is done by defining a velocity component outside the boundary in such a way that linear interpolation between it and the velocity component immediately inside the boundary yields the correct value on the boundary. No pressure boundary conditions are necessary as a result of the staggered grid arrangement. At the inlet to the first zone, a  $1/7$ -th power law turbulent velocity profile with a boundary layer thickness equal to  $2D$  is specified. This profile approximates the measured conditions of Ajersch et al. (1995) where the crossflow boundary layer approaching the jet was tripped by a thin rod to ensure a turbulent boundary layer. For the second zone (the hole development tube), a uniform velocity profile ( $v$ =average velocity of the jet,  $u=w=0$ ) was used at the entrance to the hole development tube.

### **PROBLEM DESCRIPTION**

As noted earlier, the physical configuration (Fig. 1) chosen corresponds to an experimental study reported by Ajersch et al. (1995). The coolant jets are injected at 90 degrees (vertically upwards) from a square-cross-section inlet duct with an average velocity of 5.5m/s. The width ( $D$ ) of the square jet exit hole is 12.7mm. The freestream value of the crossflow velocity is 11m/s. Both the jet and crossflow are at the same (room) temperature. The Reynolds number based on  $D$  and the average jet velocity is 4700.

There are two major differences between the problem in this study and that of Ajersch et al. (1995). The first difference is related to the fact that no artificial time-varying perturbations were used at the inlet to either zone to mimic white noise or freestream turbulence. In the actual

experiments, freestream turbulence is slightly less than 5%. The second difference relates to the choice of the freestream location. In order to minimize the computational domain, the freestream boundary condition was imposed at  $y = 3.5$  in this study. This decision was made based on observations that for the blowing ratio of 0.5 considered in this study, the jet penetration did not exceed  $2.5D$  in the computational domain. However, because of this arbitrary choice of the freestream boundary location, some differences with respect to the measurements may be expected. The differences are expected to be largest for the vertical component of velocity and near the freestream boundary. While the differences could be reduced by increasing the vertical extent of the freestream boundary, this would be associated with the added penalty of increasing the number of grid points and requiring more computational resources. Therefore the choice of  $3.5D$  was considered to be a suitable compromise, where reasonable agreement with measurements can be shown in order to validate the calculations, and sufficient resolution can be obtained at the Reynolds number of interest to resolve all the essential scales in the flow. Since the focus of the work is in understanding the flow dynamics of the large scale structures, the latter requirement for resolving the flow scales is extremely important.

The grid used had dimensions of  $300 \times 100 \times 100$  for the first zone (over the flat plate) and dimensions of  $54 \times 240 \times 34$  for the second zone (in the coolant hole region). This translates to 3.53 million grid points. The grid points were clustered towards the solid surfaces and towards the hole exit boundaries. An estimate of the Kolmogorov length scale ( $\eta = \{v^3/\epsilon\}^{0.25}$ ) was made (approximately equal to 0.1mm), and the mesh dimensions used (of the order of 0.3 mm over the jet hole) are estimated to resolve the scales of the flow in the inertial sub-range. A coarser grid was also used. This grid had dimensions of  $186 \times 62 \times 70$  for the first zone and dimensions of  $27 \times 180 \times 24$  for the second zone. This resulted in 0.924 million grid points. Validation of the computed results is provided through comparisons with measurements shown in the next section.

## RESULTS

### Time averaged Results

The time averaged results presented are obtained through ensemble averaging the instantaneous quantities after the initial transients have disappeared and the results reach a quasi-periodic state. The ensemble-averaging of the instantaneous velocities ( $u$ ,  $v$ ,  $w$ ), and normal stresses ( $u'^2$ ,  $v'^2$ ,  $w'^2$ ) are performed over 8250 time steps (which corresponds to 25 flow through times based on the freestream velocity).

Fig. 2 shows the time-averaged velocity vector plots at various  $x$ -locations. These plots show the two distinct features that the many investigators using turbulence models have reported. As will be shown, the instantaneous velocity field is very different. At  $x=1$  (roughly half-diameter away from the downstream edge of the jet-hole) distinct kidney shaped vortices representing the CVP can be seen on either side of the jet-centerline. Near the periodic boundaries, a pair of horseshoe vortices both rotating in the same direction and opposite to the adjacent CVP can be observed. At this  $x$ -location, the symmetry on either side of the jet hole center-plane is very good. At  $x=3$  the kidney shaped vortex has become much larger and lifted off of the surface. The eye of the CVP is roughly at a  $y$ -location of 1. The horseshoe vortex has become more pronounced and extends from the periodic boundary to  $0.8D$  towards the center of the jet. Thus, the horseshoe is seen to be partly entrained below the CVP. At  $x=8$ , the kidney shaped vortex has grown significantly and is centered roughly at  $y=1.5$ . The horseshoe vortices have also grown considerably and are situated directly below the CVP. Surprisingly, at this  $x$ -

location and beyond, a significant degree of asymmetry is noted in the horseshoe vortex structures, with two distinct vortices seen for negative  $z$ -values and one horseshoe vortex seen for positive  $z$ -values. It is observed that in the far-field of the jet-hole, where the structures have grown in size but weakened in strength, there is a low-frequency unsteadiness (or meandering) of the structures in the spanwise direction. Due to the low frequencies associated with this unsteady motion, time-averaging over 8,250 time-steps is unable to eliminate the asymmetry. To confirm the source of asymmetry, calculations were done with roughly 1 million grid points (this required less computational resources, and allowed the calculations to be performed for a longer number of time steps). The time averaged results based on ensemble averaging over 9,000 time steps showed the same asymmetry as seen in Fig. 2c. However, the time averaged results based on 27,000 time-steps eliminated the asymmetry. Therefore, the asymmetry seen in Fig. 2c is clearly linked to a low frequency spanwise motion of streamwise oriented vortices. Such an observation does not appear to have been previously reported.

In Fig. 2, the velocity vectors are overlaid on contours of the turbulence kinetic energy. The highest turbulence kinetic energy is associated with the deflected jet region. As will be seen later, the bending of the jet by the crossflow produces large values of the turbulent stresses that lead to significant turbulence production. The horseshoe vortices and the wake are associated with lower levels of turbulence kinetic energy.

Attention is next turned toward presenting the time averaged statistics (mean velocities and turbulence stresses) at different  $x$ - and  $z$ - values. These time averaged quantities for the fine and coarse grid are compared with the data of Ajersch et al. (1995). The coarse grid results are included to give a perspective for the grid independence of the solutions. It is simply not feasible to adopt the traditional approach, that is, half the grid spacing or use 28 million grid points, as is expected in Reynolds-Averaged simulations (where considerably fewer points are used). This less expensive coarse grid can also be used to get an estimate of the time period needed for gathering statistics. Although the predicted quantities are expected to be similar to those measured, exact agreement is not expected. This is due to the differences between the computational and experimental conditions described earlier, and include primarily the absence of any freestream turbulence in the computations and the imposition of a freestream at  $3.5D$  above the surface. Furthermore, in the absence of any other information, uniform flow conditions were specified at the inlet to the coolant hole, and this uniform flow condition is unlikely to be true in the experiments where the flow entering the coolant hole is expected to be a function of the plenum and hole design. Also due to the distribution of grid points computational results were not obtained at exactly the same locations as measured by Ajersch et al. (1995). For all these reasons, exact agreement between the computations and the experiments should not be expected.

The difference between the coarse grid statistics averaged over 9000 and 39000 time steps (Fig. 3-6) can be seen to be reasonably small except for the mean  $v$  velocity at  $x=3$  and  $x=5$ . This suggests that the fine grid statistics have been taken over a sufficient number (8250) of time steps. However as mentioned above this is not sufficient at certain locations far downstream.

The time averaged components of velocity and the turbulence kinetic energy are shown for various  $x$ -values ( $x=1, 3, 5$  and  $8$ ) and at two spanwise locations:  $z=0$  corresponding to the centerplane of the jet (Fig. 3), and  $z=-0.5$  corresponding to the spanwise edge of the jet hole (Fig.4). The  $u$  component of velocity has the same profile shape as that of Ajersch et al (1995). The velocities are somewhat overpredicted and particularly so in the wake region compared to

the data of Ajersch et al. (1995). This is, in part, due to the freestream boundary condition imposed at  $3.5D$  from the surface. At  $x=1$ , negative velocities are predicted behind the jet ( $z=0$  and  $-0.5$ ). However the flow recovery in both the streamwise and spanwise direction is more rapid in the computations than in the experiments. Thus the predicted recirculation behind the jet is smaller than that measured. This discrepancy may be linked to the differences in the flow development in the coolant hole due to different inflow conditions at the entrance to the coolant flow delivery tube in the computations and the experiments. The predicted velocity profiles beyond the recirculation region clearly show three distinct flow zones: an accelerating wall jet region near the wall induced by the entrained crossflow, a wake region with an almost constant flat profile, and a shear layer region representing the deflected jet where large velocity gradients are observed. These distinct three-flow-zones appear to be sustained as far downstream as  $x=8$ . In the crossflow region between the hole and the periodic boundary,  $z=-1$  (not shown), a boundary layer type profile is observed, and the predicted profiles appear to agree well with the measurements.

The differences between the current predictions and the data of Ajersch et al. (1995) is expectedly more pronounced for the  $v$ -component of velocity. These discrepancies are again attributed to the differences in the flow development in the coolant tube and to the imposition of freestream conditions at  $3.5D$  in the computations. The effect of the latter can be clearly seen in the differences in the predictions and the experiments in the upper half ( $y>1.5$ ) of the computational domain in Figs 3-5. Since the  $v$ -velocity changes sign across the CVP, the differences between the predicted and measured values may be exacerbated if the predicted CVP is slightly displaced in the spanwise direction relative to that in the experiments. The predicted  $v$ -velocities, however, are consistent with expectations, while the measurements at  $z=0$  show significant scatter. At  $z=0$  (Fig. 3), the  $v$ -velocities are mostly positive till  $x=5$  as expected from the sense of rotation of the CVP. At  $x=8$ , negative  $v$  is noted close to the wall associated with the encroachment of the horseshoe vortex directly below the CVP. No such observation can be made from the measurements, which, on the contrary, show negative  $v$ -velocities above the CVP. At  $z=-0.5$  (Fig. 4), the predicted trends are remarkably similar to those measured even if the actual magnitudes of the measured values are significantly greater. Both the predicted and measured  $v$  show a dual peak with positive values at  $x=1$ . From Fig. 2, it can be seen that at this  $x$ -location,  $z=-0.5$  corresponds to the inner upward-directed leg of the CVP, and the dual peaks are associated with the lower edge of the CVP (at a  $y$  approximately equal to 0.2) and the upward deflection of the jet (at a  $y$  approximately equal to 0.6). At the other  $x$ -locations shown, the CVP has grown in size, and the eye of the CVP has moved closer to the centerline. The  $z=-0.5$  line cuts almost through the middle of the CVP, and associated with this, both predictions and measurements show negative velocities close to the wall (outer edge of the CVP moving downwards) and positive velocities further away from the wall (inner edge of the CVP moving upwards). At  $z=-1$  (not shown), the predicted and measured  $v$ -velocities near the wall are negative in the near field ( $x<5$ ) reflecting the downwash of the CVP. The agreement between the predictions and the experiments is remarkably good in this region. In the far field, as the horseshoe encroaches below the CVP, positive velocities associated with the horseshoe can be observed close to the surface. This behavior does not appear to be reproduced by the experiments, but has been reported by several other investigators at higher blowing ratios including Andreopoulos and Rodi (1984).

The time averaged  $w$ -component of velocity at the center plane ( $z=0$ ) should be zero if no asymmetry at the hole exit exists. However, as seen in Fig. 3, the measurements show non-zero

values close to the wall, and a lot of scatter in the data. The predictions also show some non-zero values near the wall, although they are considerably smaller than the experimental values. These are related to the low-frequency oscillations in the spanwise directions. Time-averaging over a significantly longer number of steps is expected to eliminate these small deviations from zero. At  $z=-0.5$  (Figs. 4) and  $z=-1$  (not shown), the spanwise velocity profiles show the expected behavior associated with the CVP, positive velocities near the wall representing the inward motion of the CVP along its lower edge, and negative velocities away from the wall representing the outward motion of the CVP along its upper edge. The agreement with the measured data appears to be quite good except at a few points where the experiments show anomalous behavior. At  $x=5$  and  $8$ , negative  $w$ -velocities can be seen very close to the surface, and are again associated with the encroachment of the horseshoe into the wake region below the CVP.

The turbulence kinetic energy profiles in Figs. 3-4 show the same general trends as those measured, with the peak kinetic energy at  $z=0$  and  $-0.5$  associated with the deflection of the crossflow over the jet and the bending of the jet. Thus, in the near-field ( $x=1$ ), the kinetic energy peaks less than 0.5-hole-diameter from the surface, while further downstream as the CVP representing the deflected jet grows larger and lifts off the surface, the peak kinetic energy location shifts upwards, to roughly 1-hole-diameter off the surface at  $x=3$  and  $5$ , and 1.5-hole-diameter at  $x=8$ . The predictions appear to overestimate the magnitude of the peak and its location. However these discrepancies are possibly related to differences in the freestream turbulence levels and jet hole entry conditions in the experiments and computations. Away from the jet-region, at  $z=-1$  (not shown), the measured turbulence kinetic energy profile is more akin to that of a boundary layer. However, the predictions show two peaks. Very close to the surface, the presence of the horseshoe leads to a local peak in the kinetic energy, while further away, the second peak is associated with the crossflow boundary layer.

Attention is next turned to the profiles of the normal stresses that are shown in Fig. 5 ( $z=0$ ), and Fig. 6 ( $z=-0.5$ ). Along the jet center-plane (Fig. 5), significant anisotropy is observed at  $x=1$ , where the  $u$ -rms predicted is nearly twice the  $v$ -rms and  $w$ -rms values. As will be seen later in the vorticity contours (Figs. 8 and 9), the peak  $u$ -rms in the near field at  $z=0$  is associated with shear layer vortices on the leeward side of the jet that show a significant amount of periodic unsteadiness (Fig. 8). The measurements also show anisotropy with  $u$ -rms  $>$   $w$ -rms  $>$   $v$ -rms, but the anisotropy is significantly smaller. As the flow progresses downstream, the peak-rms values are closer to each other in magnitude; however the profile shapes and the location of the peaks are somewhat different even as far downstream as  $x=8$ . For  $x=3$ ,  $5$ , and  $8$ , the predicted and measured  $u$ -rms profiles show dual peaks. The primary peak is associated with the deflected-jet shear layer where the velocity gradient  $\partial u/\partial y$  is large. The  $y$ -location of the measured and predicted primary peaks are the same although the predicted values are greater than those measured. The smaller peak is much closer to the wall in the predictions, and is due to the wall-jet behavior noted in Fig. 3. The  $v$ -rms predictions are again greater than those measured, and show a fairly flat plateau that correlates well with  $\partial u/\partial y$  in the jet-shear-layer region. The  $w$ -rms predictions appear to agree better with the measurements than the other two components, and show a peak that is considerably closer to the wall. This peak is presumably associated with the entrainment of the crossflow and the horseshoe into the wake region, and correlates with  $\partial w/\partial z$ .

At  $z=-0.5$  (Fig. 6), the predicted and measured profiles are in satisfactory agreement with each other. The trends observed are similar to that at  $z=0$  with two notable differences. The first is that the secondary peak in  $u$ -rms observed in Fig. 5 becomes as dominant as the primary peak

in the deflected jet region. This is because  $z=-0.5$  represents a location directly through the eye of CVP at  $x=3, 5,$  and  $8,$  and the near wall region experiences high values of  $\partial w/\partial y$  leading to the production of  $u$ -rms. Furthermore, at the spanwise edge of the jet there is strong crossflow entrainment along the wall leading to destabilizing streamline curvature of the crossflow that enhances turbulence. The second difference relative to Fig. 5 is that in the far field, the  $w$ -rms components shows a second peak for  $y$  between 1 and 1.5, and is presumably associated with  $\partial u/\partial z$  that can be significant along the spanwise edge of the deflected jet.

At  $z=-1$  (not shown), the normal stresses predicted are generally in good agreement with those measured. The differences noted in the freestream are due to the specification of zero freestream turbulence in the computations. There are also differences in the near field ( $x=1$ ), where the rms values are overpredicted near the walls. These differences however may be linked to the differences in the computed hole exit profile relative to those measured. The  $u$ -rms profile predicts a peak that is larger and closer to the wall compared to the measured values. This appears to be linked to the larger predicted values of the spanwise velocity gradient  $\partial w/\partial y$  relative to that measured. The  $v$ -rms profiles near the surface appear to compare well with those measured at  $x=3, 5,$  and  $8.$  These profiles appear to be characteristic of a developing boundary layer. The  $w$ -rms profiles again show good agreement and appear to reproduce the two peaks near the wall observed in the measurements. The lower peak is clearly linked to the horseshoe, while the upper peak is presumably related to the edges of the CVP where  $\partial u/\partial z$  can be significant.

It is clear from the above that the normal stresses  $u_i'^2$  do not correlate with  $\partial u_i/\partial x_i$  (no summation implied) as expected from the Boussinesq-gradient approximation. Therefore turbulence models embodying this approximation (such as the two-equation turbulence models) are unlikely to do well.

## Dynamics

In this section, instantaneous snapshots of the vorticity, pressure and velocity vectors are presented to understand the spatial and temporal evolution of the larger scales in the flowfield. As will be seen, the instantaneous structures are considerably more complex, and there are strong dynamical interactions that eventually control the flow behavior. The strong flow dynamics indicate that a time averaged calculation procedure is inherently unsuited to predict such a dynamical flowfield.

Fig. 7 shows all three components of vorticity at one arbitrary instance in time and at four cross-stream planes corresponding to  $x=-0.6, -0.0037, 0.527, 1.09,$  and  $1.64.$  The  $x$ -vorticity contours show the spatial development of the CVP and the horseshoe. Just upstream of the hole ( $x=-0.6$ ), the re-orientation of the horseshoe vortex from  $z$ -vorticity to  $x$ -vorticity can be observed. The CVP can be seen to be a distinct coherent structure at  $x=-0.0037$  (close to the hole mid-plane), and is flanked on either side by a horseshoe vortex system that appears to consist of three vortices, two that are counter-rotating to the CVP and one in-between these two that has the same sense of rotation as the CVP. Directly above the deflected jet are a set of vortices, with both positive and negative vorticity, that are presumably associated with the shear layer vortices along the leading edge of the jet, stretched and reoriented by the secondary flows driving the CVP. Such secondary vortices riding atop the CVP have been observed by others (see Haven and Kurosaka, 1998; Sharma and Acharya, 1998 for example). At  $x=0.527$  (just downstream of the hole exit), the CVP structures are still quite coherent, and have grown in size. However evidence of interaction with structures in the wake region between the CVP can be seen. At  $x=1.09,$  there

is strong dynamical interaction between the CVP and the wake-structures that have grown significantly in size and strength. While the CVP is still clearly discernible, it is a fairly convoluted structure interspersed with structures having vorticity of the opposite sign. At  $x=1.64$ , the CVP structure can not be clearly identified. However, evidence of the horseshoe vortex can still be clearly seen at this  $x$ -location.

In examining the  $y$ -vorticity, it can be seen that as the crossflow is deflected around the jet, the streamline curvature in the  $z$ - $x$  plane leads to the generation of the  $y$ -component of vorticity. This can be seen both upstream of the hole and in the mid-hole region. Downstream of the hole, wake vortices can be clearly identified by the array of elongated (in the vertical direction) vortical structures. As noted by Kelso et al. (1996) and Fric and Roshko (1994), these unsteady structures are clearly present in the wake, and have their origins in the crossflow boundary layer that is entrained into the wake region. The horseshoe vortex structures also appear to be associated with  $y$ -vorticity implying rotation of these structures in the  $x$ - $z$  plane. This rotation may be induced by the strong pressure gradients in the  $x$ - $z$  plane and the associated movement of the crossflow into the wake regions.

The  $z$ -vorticity contours before the jet hole ( $x=-0.6$ ) clearly show the horseshoe vortex system in front of the jet (negative vorticity), and the boundary layer vorticity (positive) emerging from the leading edge of the hole. These structures with positive and negative vorticity are stripped by the jet and ride on top of the jet as seen by the  $z$ -vorticity contours near the jet hole midplane ( $x=-0.0037$ ). These structures on the windward side of the jet represent the shear layer vortices. This behavior can be clearly seen in Fig. 8. The negative vorticity emerging from the trailing edge of the jet hole can be clearly seen in the contours at  $x=0.527$ , and the important role it plays in the shedding of leeward side shear layer vortices is also evident in the contours at this  $x$ -location and at the  $x$ -locations fur downstream. At  $x=1.09$ , the vorticity along the wall is positive, and is induced by the instantaneously reversed flow. The positive vorticity is then entrained by the under-side of the deflected jet characterized, as noted above, by negative vorticity from the trailing edge of the jet-hole. Thus the leeward side of the deflected jet is defined by both positive and negative vorticity patches as seen at  $x=1.09$  and  $1.64$ . At both these  $x$ -locations interaction between the vortices on the windward and leeward side can be noted.

The rest of the figures presented in this chapter focus on the dynamical or temporal behavior of the structures presented so far. The most interesting phenomena noted, and one not reported earlier, is a dynamical interaction of the horseshoe vortices in the front of the jet hole with the hole-leading-edge boundary layer structures. This is illustrated in Fig. 8 which shows the spanwise vorticity contours at the jet center plane, and Fig. 9 which shows the corresponding pressure contours. Four time instances are shown in these figures. It is observed that the crossflow shifts the jet toward the downstream edge of the jet hole, and there is significant ingestion of the crossflow into the exit hole. However, this process shows a distinct time-periodic variation that does not appear to have been reported before. At a time instance shown in Fig. 8a and 9a, the stagnation pressure upstream of the jet has built up significantly due to the flow blockage induced by the injected jet into the crossflow. At this time instance, the structure of the horseshoe vortices can be clearly seen to consist of two clockwise eddies with a counter-clockwise eddy straddled in-between. This structure is consistent with the flow visualization pictures of Kelso et al (1996). The boundary layer vortex along the leading edge of the hole is expectedly in the counter-clockwise direction. The increase in pressure upstream of the jet shifts the jet downstream, and pushes the leading horseshoe vortex into the jet hole region. This also causes the boundary-layer vorticity along the jet hole leading edge to be displaced downstream

and away from the leading edge of the jet hole. At a subsequent time shown in Fig. 8b, the crossflow has penetrated significantly into the exit hole, with the leading horseshoe vortex completely inside the exit hole. The exiting jet has been pushed well into the hole, and the deflected jet exits outwards from only a portion (approximately 50%) of the jet hole exit area in this plane. The jet hole leading edge vortex is seen to be stretched by the crossflow resulting in the formation of shear layer vortices along the windward side of the jet. At this instance in time, the pressure inside the hole has built up due to the crossflow having pushed the jet back leading to low velocity regions and flow ingestion along the upstream half of the hole exit. The high pressures inside the exit hole starts pushing the deflected jet vertically upwards and back towards the leading edge of the hole. This leads to the upward displacement of the ingested horseshoe which is then entrained and stretched by the crossflow along the windward edge of the exiting jet (Fig. 8c and 9c). Thus along the windward side both positive counter-clockwise vortices (originating from the leading edge boundary layer) and negative clockwise vortices (originating from the horseshoe system) are observed. These positive and negative vortices appear to arrange themselves in an alternate pattern (Fig. 8a, 8d). It should be pointed out that while several investigators (Fric and Roshko (1994) , Kelso et al. (1996), Andreopoulos (1985)) have noted the formation of the shear layer vortices, and have pointed to Kelvin-Helmholtz instabilities or the hole leading edge vorticity as the source, the entrainment and stretching of the leading horseshoe vortex along the upper edge of the deflected jet leading to alternate positive and negative vortex pairs, and the association of these vortices with the periodic pressure variations and jet deflections, does not appear to have been reported. Along the leeward side, the negative boundary layer vorticity from the trailing edge of the jet hole, rolls up into distinct spanwise vortical structures. These are convected downstream, and into the highly unsteady near-wake region. The recirculation immediately downstream of the jet leads to positive vorticity along the wall, and in the wake region patches of positive and negative vorticity can be seen. The near wall negative vorticity can be seen to be entrained into the underside of the deflected jet (Fig. 8) and interacts with the vortex pairs on the windward side.

The non-dimensional frequency associated with the above-described time-periodic behavior of the jet and the crossflow is around 0.44. It should be noted that this periodic jet pulsation leads to a large time-periodic variation in the vertical component of velocity and therefore the blowing ratio. This variation is shown in Fig. 9(e-h) at four spatial locations.  $x = 0.245$  and  $y=3.22 \times 10^{-3}$  (Fig. 9h) corresponds to a vertical location near the hole exit plane and a streamwise location nearly midway between the hole center and the trailing edge of the hole. At this location, a strong inverse correlation between velocity and pressure can be observed. The vertical component of the jet-velocity can be seen to have an almost sinusoidal variation (between 1.1 and 1.6) associated directly with the periodic excursion of the crossflow over the hole with an accompanying reduction of the crossflow area through which the jet exits. This variation in the jet exit velocity and blowing ratio causes the vertical jet penetration to also have a significant time-periodic variation. This time periodic variation of the jet penetration can persist for several diameters downstream of the jet exit as shown later in the streamwise vorticity contour and cross-stream velocity vectors in  $y-z$  planes. Fig. 9e is a location roughly half-diameter downstream of the hole trailing edge and one-diameter above the surface. This location corresponds to the windward edge of the shear layer, where one can see higher frequency components due to the shear layer vortices during those times where the periodic jet pulsation moves the shear layer onto the point being monitored. These higher frequencies are roughly 10 times greater than the 0.44 non-dimensional frequency associated with the periodic insurgence of

the crossflow, and indicates that the crossflow stretching of the horseshoe or hole leading edge vorticity leads to the formation of several vortex pairs. These pairs intensify and become stronger as they convect downstream. Near the downstream edge of the hole, they appear to interact with the vortical structures forming along the leeward edge of the hole, and at certain time instances self induction of vorticity across adjacent vortex pairs can be noted. Fig. 9f shows a location on the leeward side of the deflected jet, and evidence of shear layer vortices can be seen periodically. The frequency of the shear layer vortices on the leeward side is comparable to that on the windward side. Fig. 9g is a location near the jet-exit plane and in the front half of the jet hole exit. Flow at this location is in the direct path of the crossflow ingestion, and strong negative  $v$ -velocities can be seen at certain time instances.

The periodic insurgence of the horseshoe vortex over the jet exit hole can be clearly seen in the  $x$ - $z$  plane contour plots of the vertical velocity vector shown in Fig. 10 at four time instances. The signature of the horseshoe vortex can be seen by the U-shaped necklace pattern upstream of the hole. All three vortices can be identified. As the horseshoe vortex system moves over the jet exit hole it begins to break up (Fig. 10b) and part of it rides up on top of the jet. The periodic ingression of the horseshoe and the crossflow over the jet hole and the associated partial blockage of the hole can be seen clearly in Fig. 10. The entrainment of the crossflow into the wake region, and the footprint of the wake vortices can also be clearly seen in this figure.

Fig 11 shows the velocity vectors in the streamwise plane  $x=0$  (middle of the hole) and pressure contours. In Fig. 11a, the CVP can be clearly seen along the outer edges of the jet. The centers of the CVP are associated with low pressures. As the pressure in the plenum builds up, and the ingressing crossflow and horseshoe pinches the hole from all sides, the right CVP is lifted upwards and inwards (Fig. 11b). A new CVP then begins to form (Fig. 11c), and grows to its full size (Fig. 11d). This feature is consistent with Fig. 7, and the flow visualizations of Ajersch et al (1995) and Haven and Kurosaka (1998) who report satellite vortices above the CVP.

Fig. 12 shows the velocity vectors and the  $x$  component of vorticity in the  $yz$  plane at  $x=1$ . The CVP is seen to consist of many vortices arranged in a rather chaotic fashion. The structure of a CVP can be seen in that the left side of the CVP is associated mainly with negative vorticity while the right side is associated mainly with positive vorticity. In Fig. 12a the horseshoe vortices can be clearly seen. Comparing Fig. 12c with 12d, one can note that the jet penetration changes significantly with time. As noted earlier, this is associated with the periodic interaction of the crossflow with the jet coming out of the hole. This periodic variation in the jet penetration persists well downstream of the hole.

## CONCLUDING REMARKS

A time-accurate calculation of a row of jets injected into a crossflow has been performed on a fine grid with 3.44 million grid points along with a coarser grid of 0.924 million grid points. The goal of the work is to identify and understand the dynamics of the important energy carrying structures in the flow. The following are the major conclusions of this work.

1. The important structures identified include: a horseshoe vortex system that consists of an anti-clockwise eddy sandwiched between two clockwise eddies, shear-layer vortices on the windward and leeward sides of the deflected jet, and unsteady wake vortices.
2. A dynamical interaction is observed between the flow in the coolant-tube and the approaching crossflow which leads to a periodic ingression of the crossflow over the

coolant hole. The non-dimensional frequency corresponding to this periodic behavior is around 0.44. This periodic behavior leads to the leading horseshoe vortex and the hole-leading edge vorticity to be alternately stripped and carried along the top or windward side of the jet. This mechanism is primarily responsible for the shear layer vortices along the windward side of the jet.

3. The periodic ingress of the crossflow leads to variations in the hole-exit area through which the jet is discharged. This variation leads to periodic fluctuations in the jet velocity leaving the hole, and periodic variations in the jet penetration. These periodic variations in the jet penetration manifest themselves several diameters (greater than 8) downstream of the injection hole leading to an up and down flapping of the CVP and the associated structures.
4. In the instantaneous images, the CVP loses its coherence beyond 1-hole diameter downstream. Satellite eddies above the CVP can be seen in the near field of the jet. Time averaged plots show that the CVP retains its structure well downstream of the hole (greater than 8D).
5. The horseshoe vortices show a low frequency unsteadiness or meandering in the spanwise directions.
6. The time-averaged stresses clearly show significant anisotropy in the near field and indicate that the Boussinesq gradient approximation for the stresses is inappropriate.

## REFERENCES

- Ajersch, P., Zhou, J.M., Ketler, S., Salcudean, M. & Gartshore, I., S. 1995 "Multiple Jets in a Crossflow : Detailed measurements and Numerical Simulations" , *ASME Paper 95-GT-9*
- Andreopoulos J. 1985 "On the structure of jets in a crossflow" *J.Fluid Mech.* vol. 157, pp.163-197
- Andreopoulos J. & Rodi W. 1984 "Experimental investigation of jets in a crossflow" *J.Fluid Mech.* vol. 138, pp.93-127
- Chorin, A. J. 1968 "Numerical Solution of the Navier-Stokes Equations", *Math. Comput.*, Vol. 22, pp.745-762
- Crabb D., Durao D.F.G., & Whitelaw 1981 "A round jet normal to a crossflow" *J. of Fluids Engineering*, Vol. 103, pp.142-153
- Demuren A.O. 1993 "Characteristics of three-dimensional jets in crossflow" *Int. J. Engng Sci.* Vol 31 No. 6, pp.899-913
- Fornberg B. G. 1988 "Generation of finite difference formulas on arbitrarily spaced grids" *Mathematics of Computations* vol. 31 Number 184, pp. 699-706
- Fric T. F., & Roshko A. 1994 "Vortical structure in the wake of a transverse jet" *J. Fluid Mech.* vol. 279, pp. 1-47
- Garg, V. K., & Gaugler R. E., 1995 "Effect of velocity and temperature distribution at the hole exit on film cooling of turbine blades", *ASME paper 95-GT-2*
- Garg, V. K., & Gaugler R. E., 1994 "Prediction of film cooling on gas turbine airfoils", *ASME paper 94-GT-2*
- Jones, W. P. & Wille, M. 1996 "Large eddy simulation of a round jet in crossflow" *Engineering Turbulence Modeling and Experiments* 3. Ed. Rodi, W. and Bergeles, G. pp.199-209
- Kelso R. M., & Lim T.T., & Perry A. E. 1996 "An Experimental Study of Round Jets in Cross-Flow", *J. Fluid Mech.* Vol. 306 pp. 111-144

- Kim, S.W., & Benson, T.J. 1992 "Calculation of a circular jet in crossflow with a multiple-time-scale turbulence model" *Int. J. Comp. Phys.* vol 59. pp. 308-315
- Kamotani, Y., & Gerber, I., 1972 "Experiments on a turbulent jet in a crossflow, *J. Fluid Mech.*, Vol. 306, pp. 111-144
- Patankar, S.V. Basu, D.K. & Alpay, S.A., 1977 "Prediction of the three-dimensional velocity field of a deflected turbulent jet" *Trans. SME I: J. Fluids Engng* 99, pp. 758-762
- Sharma, C., & Acharya, S., 1998 "Direct numerical simulation of a coolant jet in a periodic crossflow" NASA/CR-1998-208674
- Sykes, R.I., Lewellen, W.S. & Parker, S.F. 1986 "On the vorticity dynamics of a turbulent jet in a crossflow" *J. Fluid Mech.* Vol. 80, pp. 49-80
- Yuan, L.L., & Street, R.L. 1996 "Large Eddy Simulation of a Jet in Crossflow" *ASME Fluids Engineering Division* Vol. 242, pp. 253-265

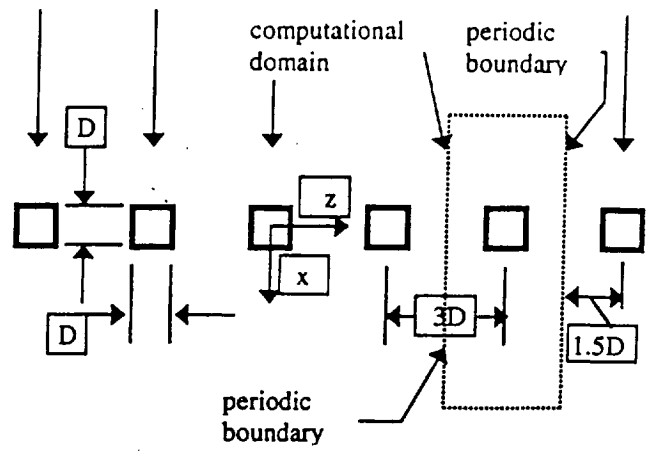
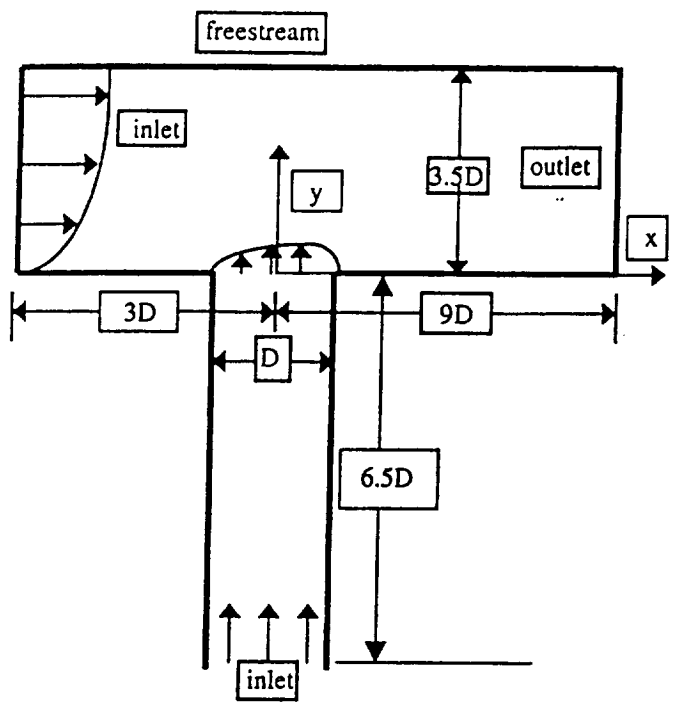


Figure 1 Computational Domain

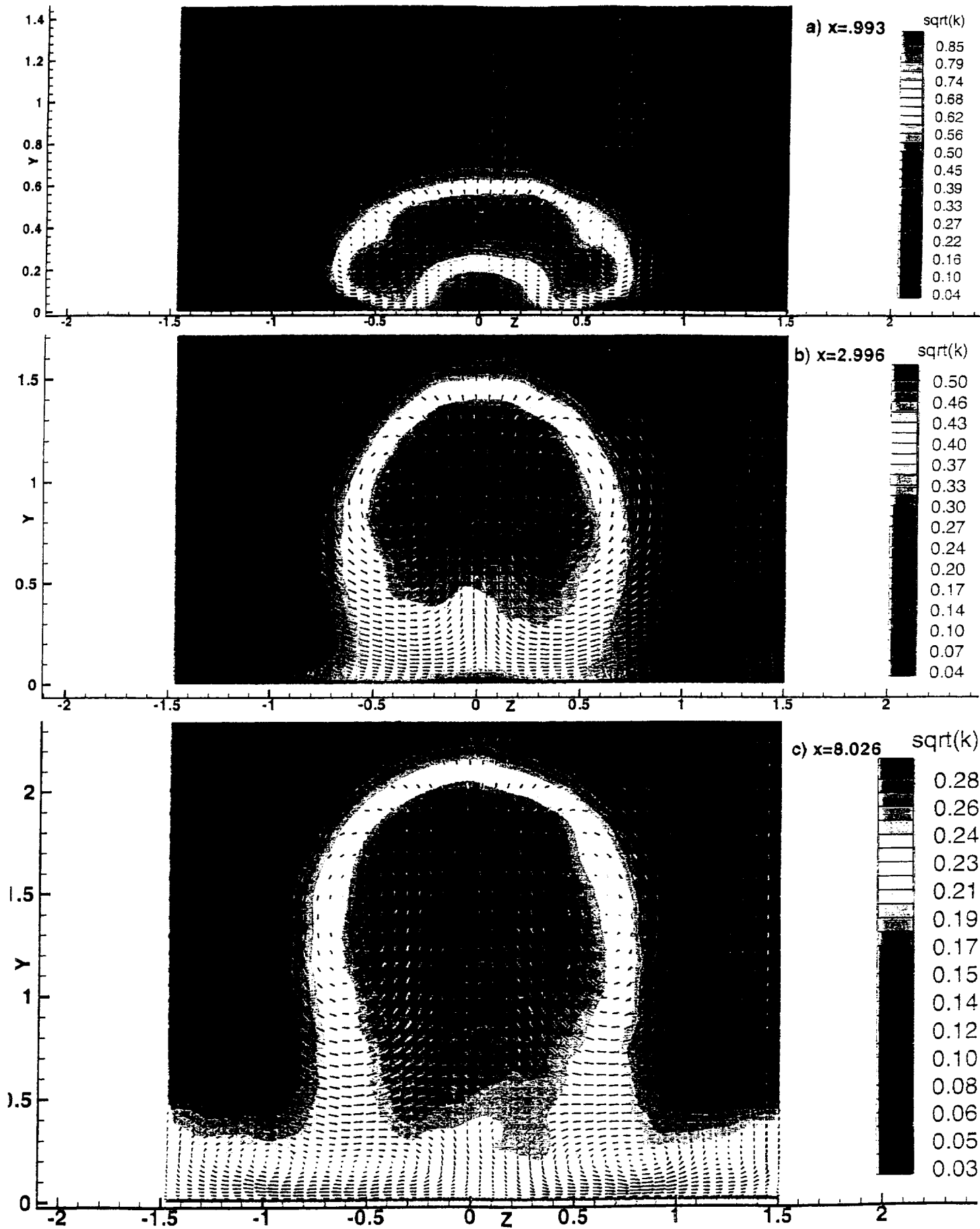


Figure 2 Time averaged velocity vectors and square root of turbulent kinetic energy

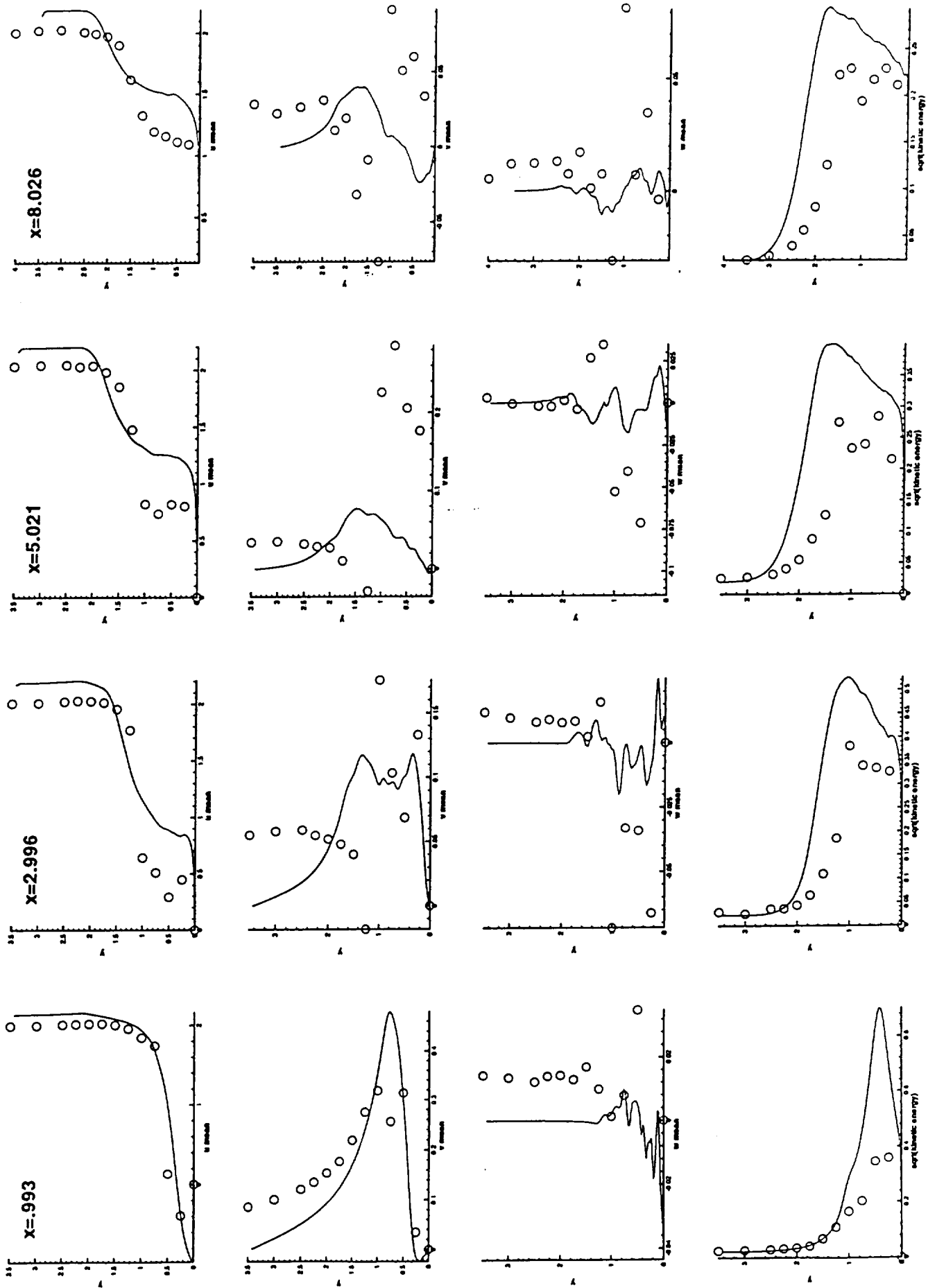


Figure 3 Time averaged components of velocity and turbulent kinetic energy at  $z=1.51 \times 10^2$ , Ajersch et al at  $z=0$

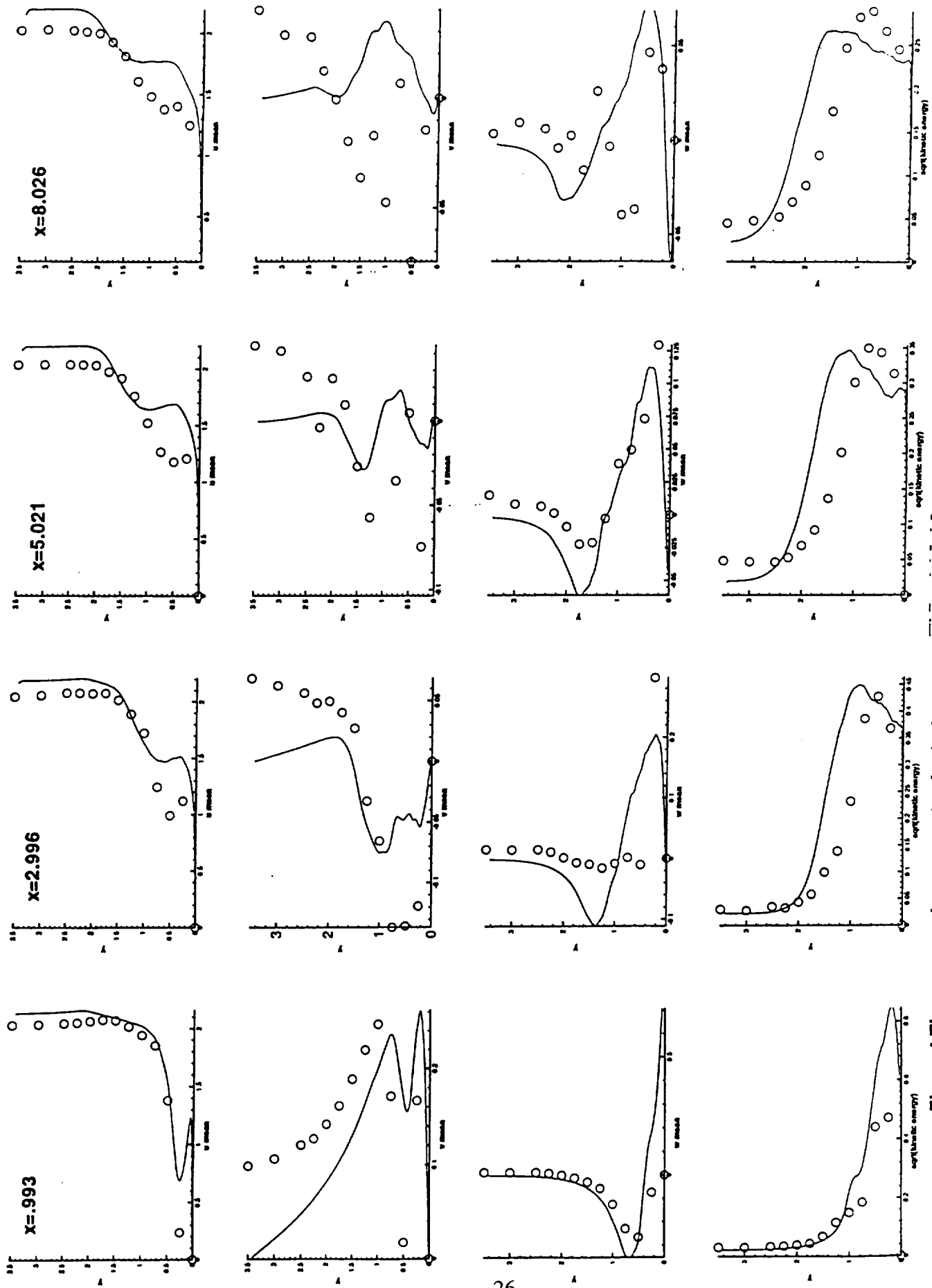


Figure 4 Time averaged components of velocity and turbulent kinetic energy at  $z = -0.5$ , Ajersch et al at  $z = -0.5$

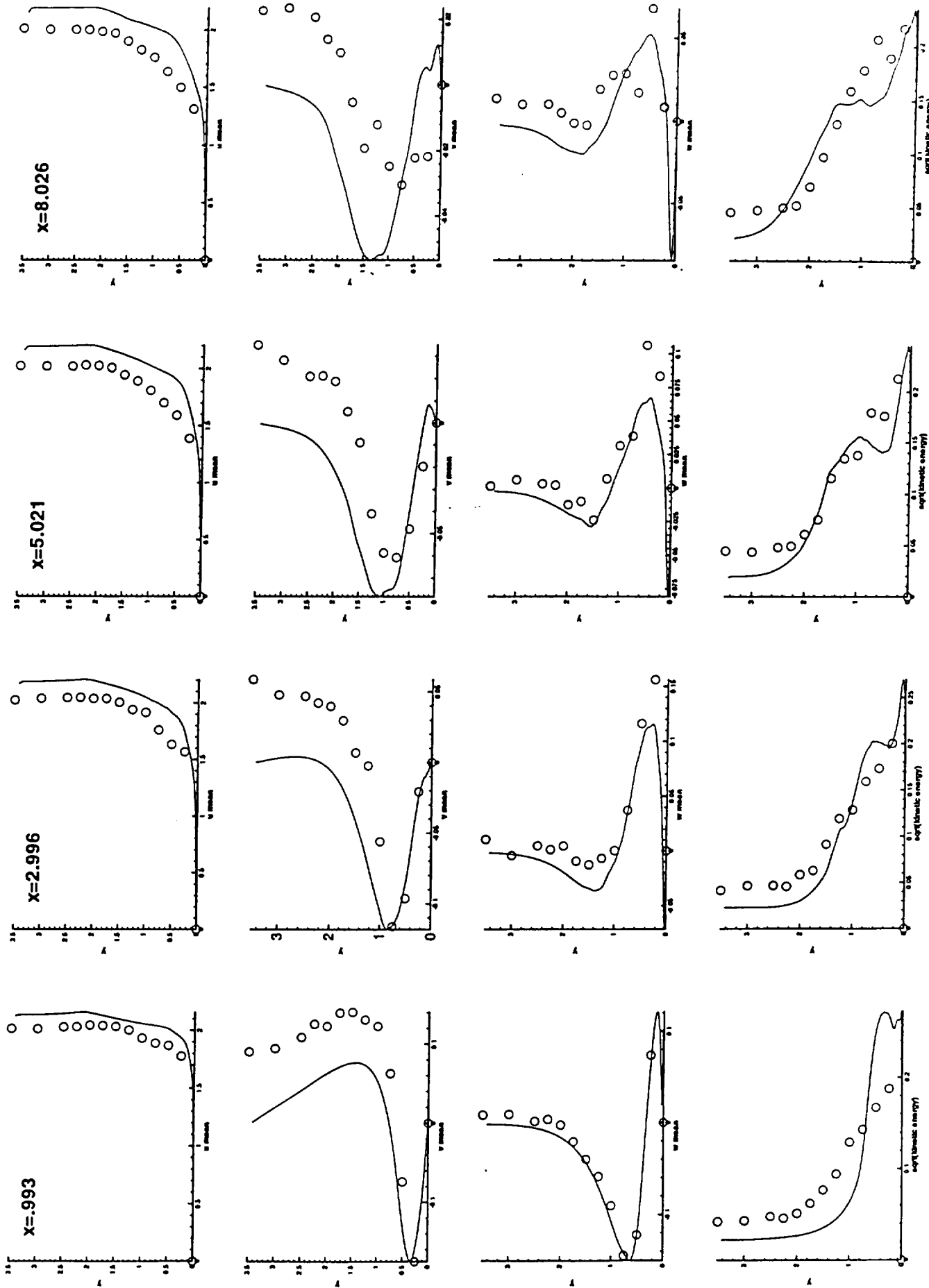


Figure 5 Time averaged components of velocity and turbulent kinetic energy at  $z = -.984$ , Ajersch et al at  $z = -1$

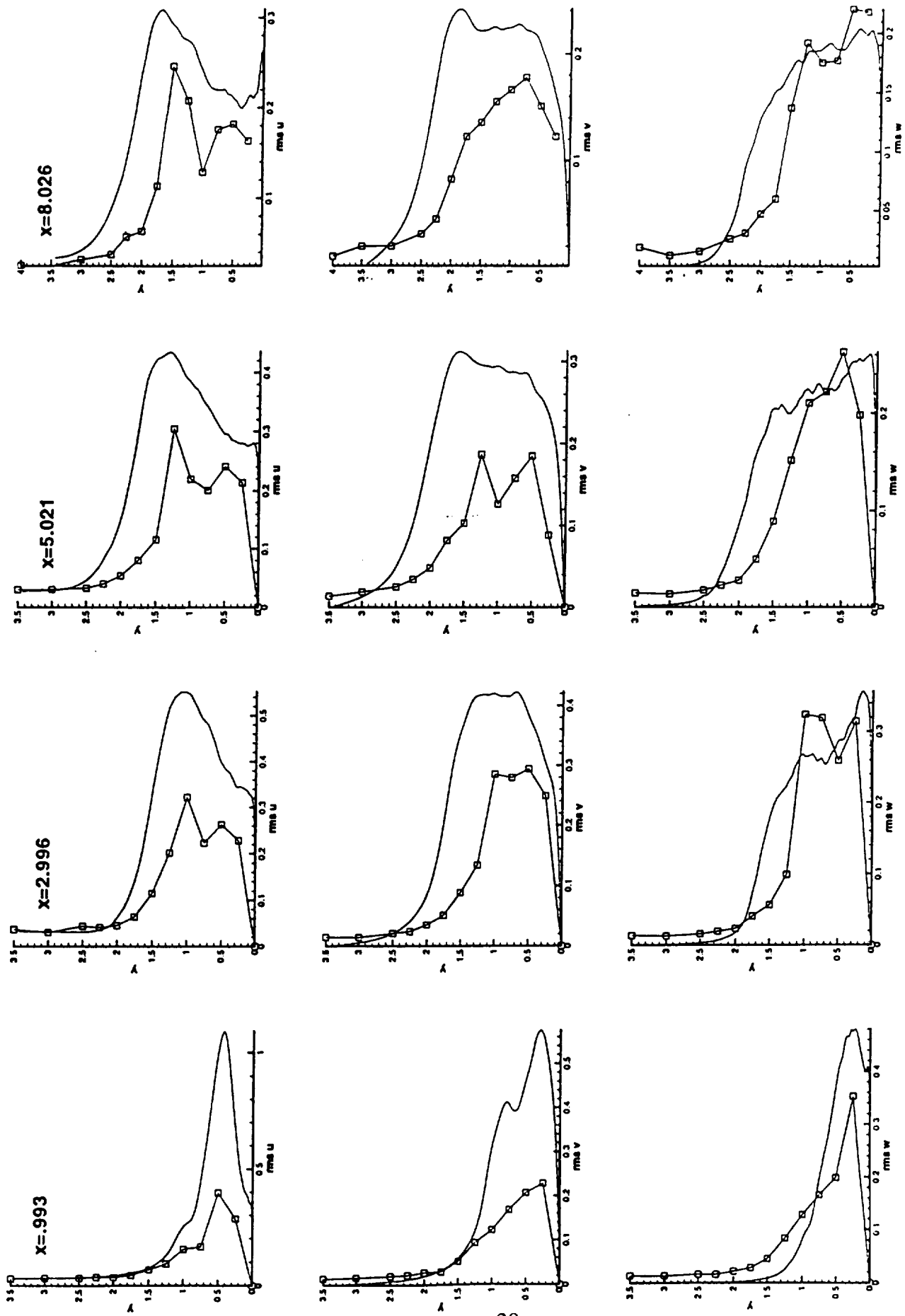


Figure 6 Root mean square of the components of velocity at  $z=1.51 \times 10^2$ , Ajersch et al at  $z=0$



Figure 7 x,y and z components of vorticity at a single time instant, x axis has been increased by a factor of 2

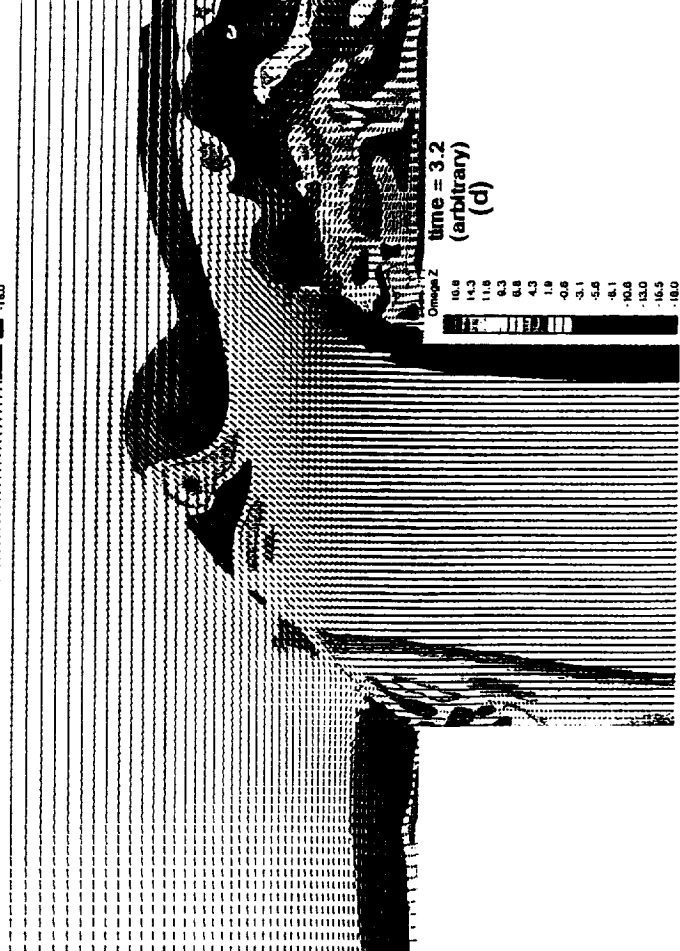
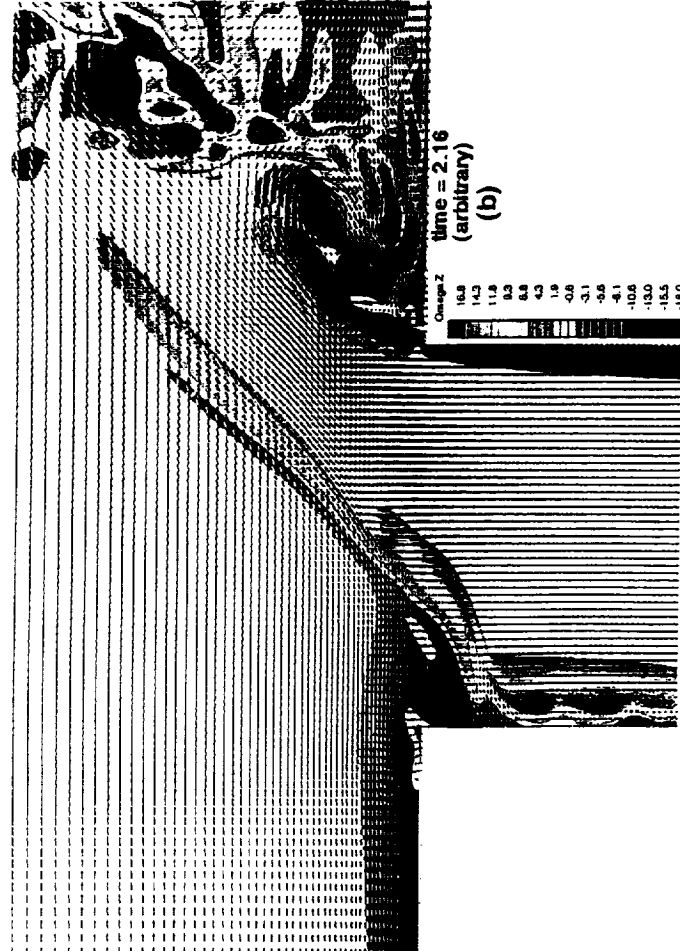


Figure 8 z component of vorticity in the xy plane at  $z=1.51 \times 10^2$



Figure 9 pressure in the xy plane at  $z=1.51 \times 10^2$

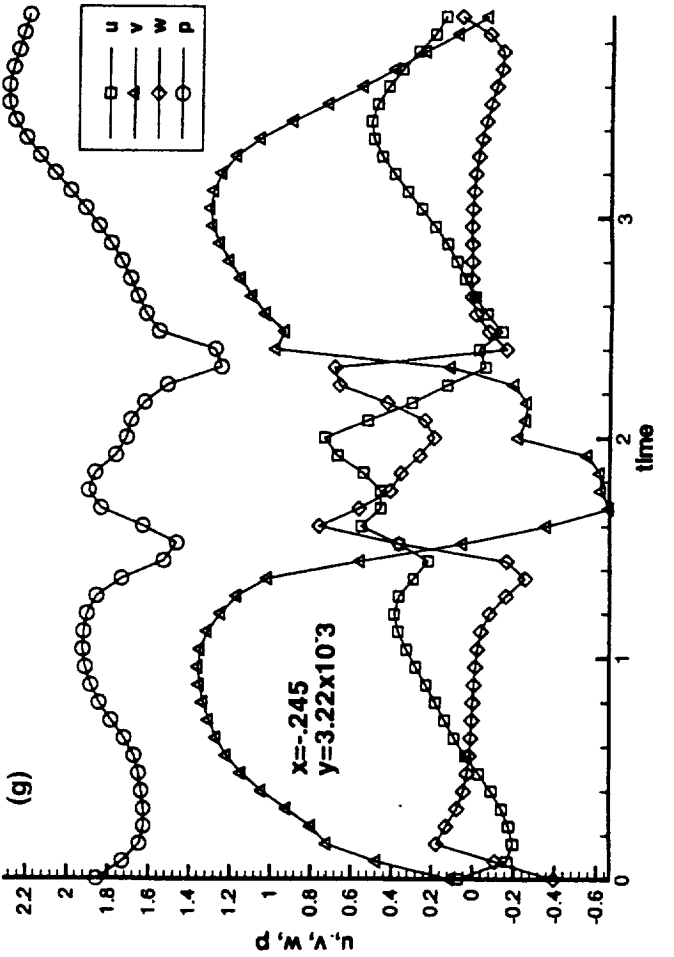
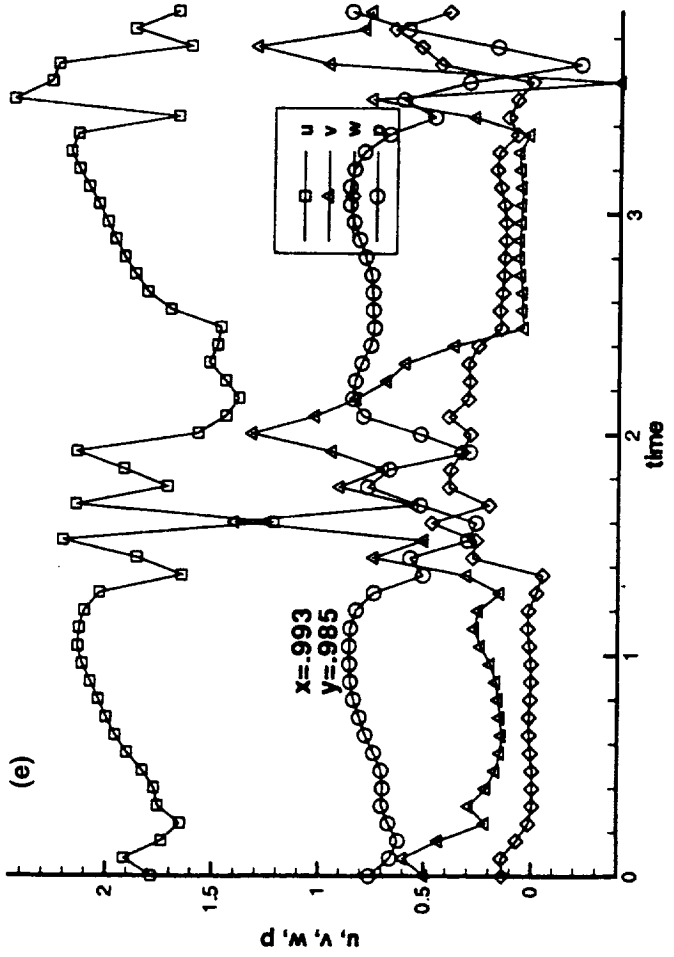
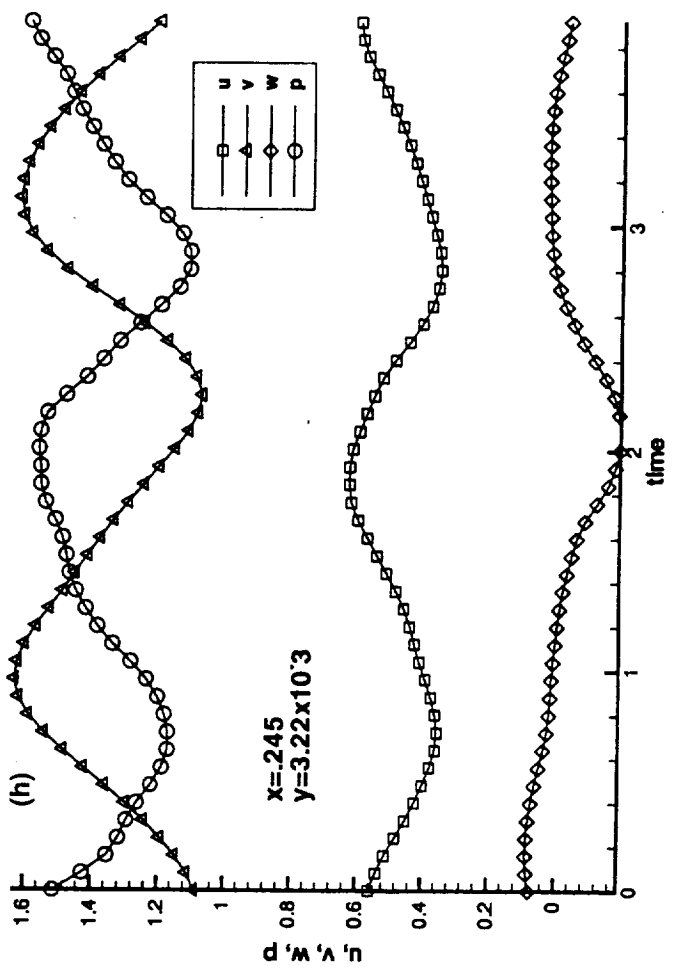
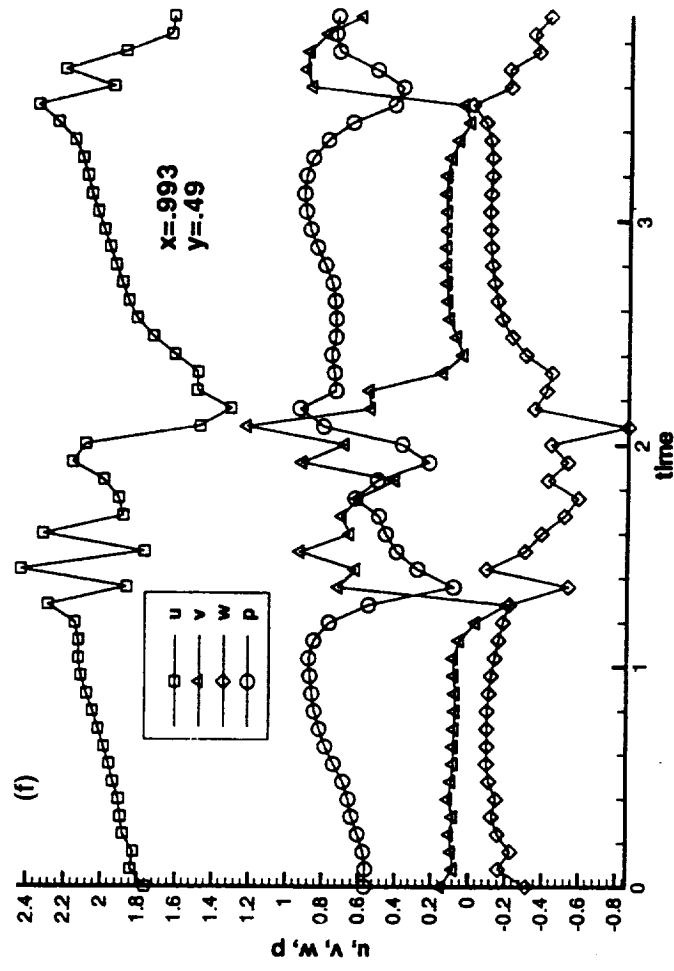


Figure 9 Time history at  $z=0$

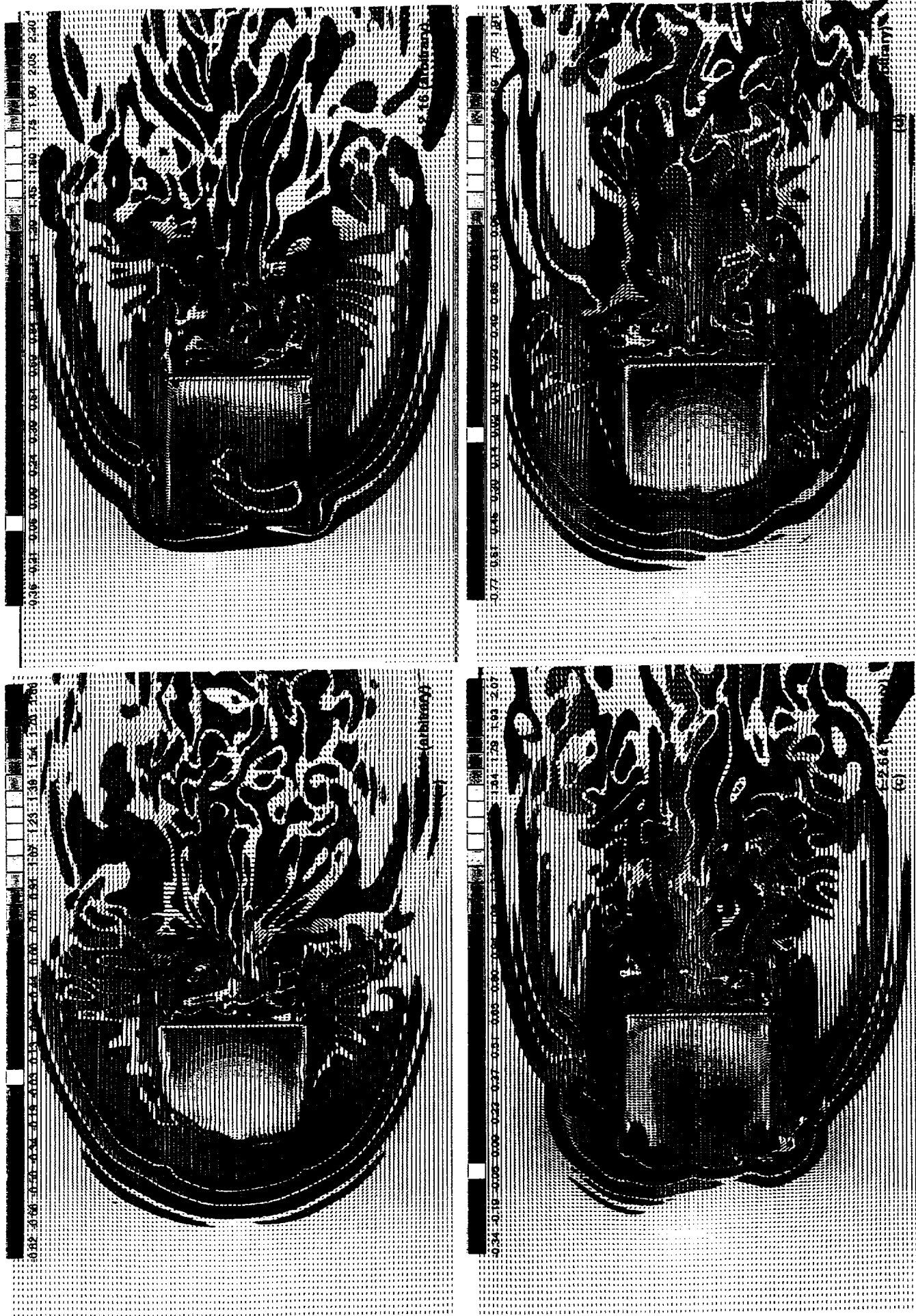


Figure 10 Velocity vectors and contours of  $v$  in the  $xz$  plane at  $y=3.14e2$

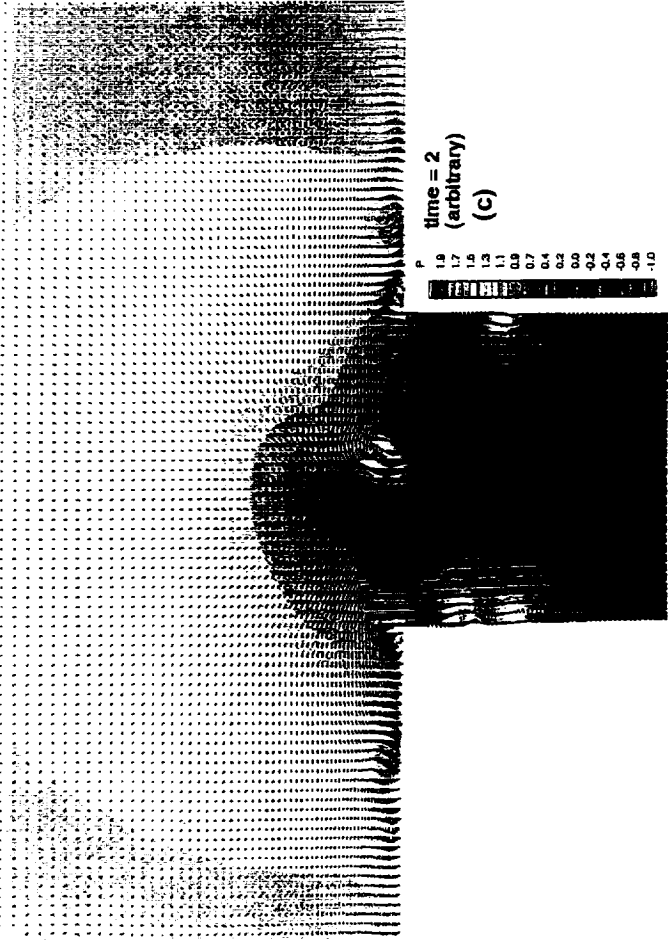
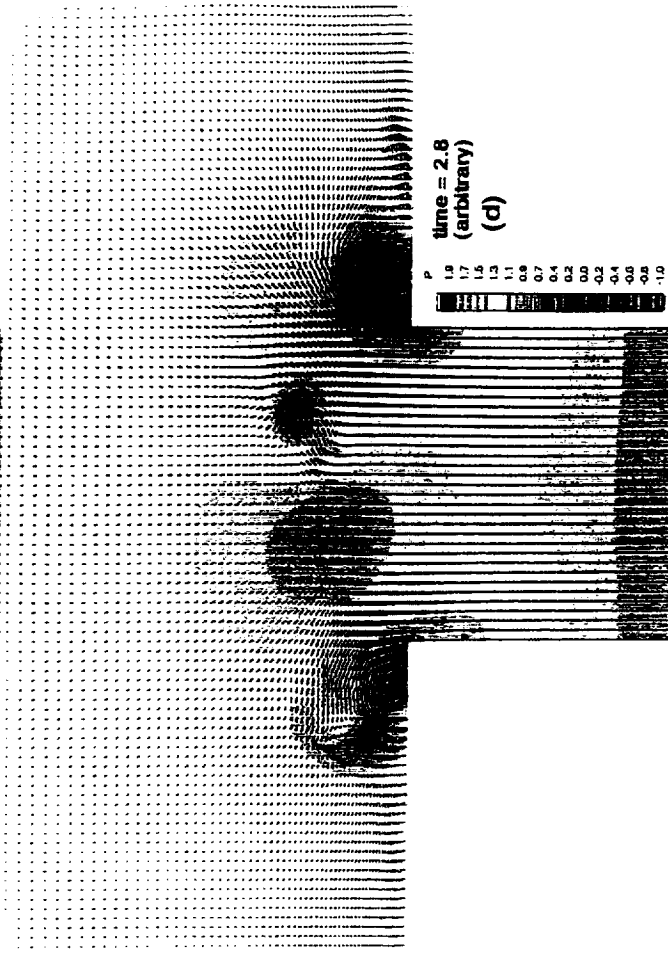
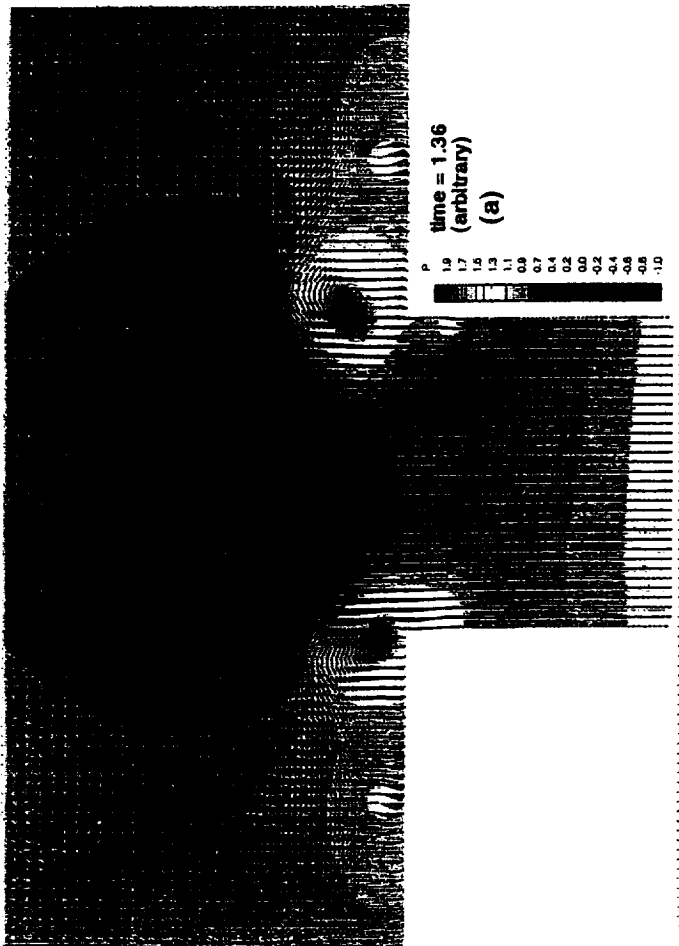
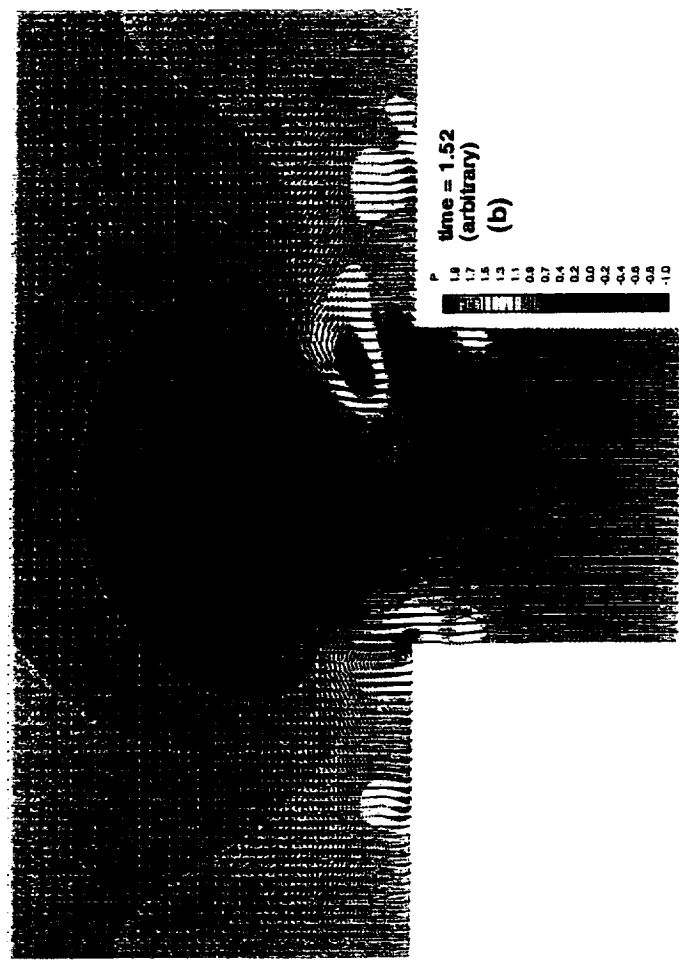


Figure 11 pressure and velocity vectors in the yz plane at x=0

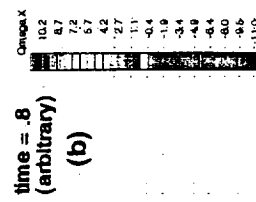
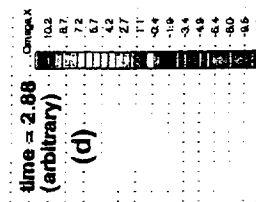
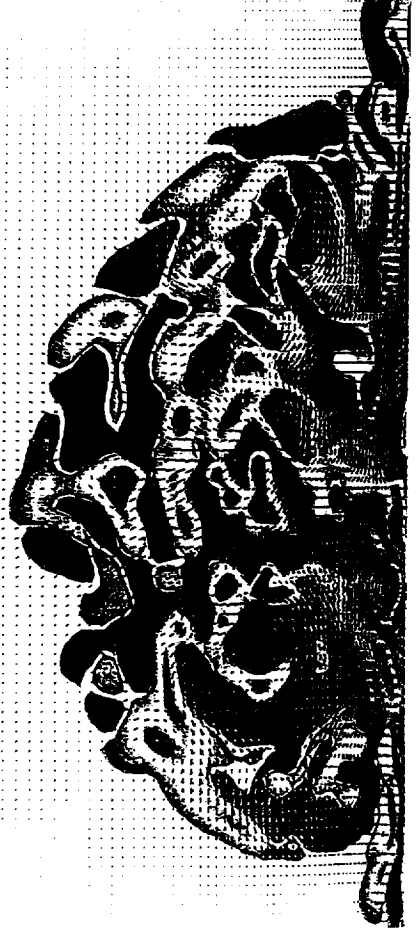
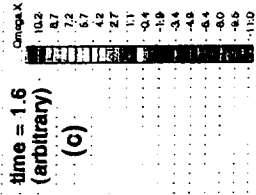
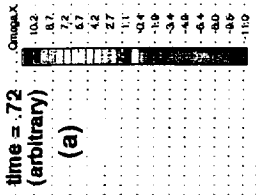


Figure 12 x component of vorticity and velocity vectors in the yz plane at x=.993

## CHAPTER IV

### DIRECT NUMERICAL SIMULATION (DNS) OF NORMAL FILM COOLING JETS IN A PERIODIC CROSSFLOW

#### ABSTRACT

A Direct Numerical Simulation of a coolant jet injected normally into a periodic crossflow is presented. The physical situation simulated represents a periodic module in a coolant hole array with a heated crossflow. A collocated finite difference scheme is used which is fifth-order accurate spatially and second-order accurate temporally. The scheme is based on a fractional step approach and requires the solution of a pressure-Poisson equation. The simulations are obtained for a blowing ratio of 0.25 and a channel Reynolds number of 5600. The simulations reveal the dynamics of several large scale structures including the Counter-rotating Vortex Pair (CVP), the horse-shoe vortex, the shear layer vortex, the wall vortex and the wake vortex. The origins and the interactions of these vortical structures are identified and explored. Also presented are the turbulence statistics and how they relate to the flow structures.

#### INTRODUCTION

In recent years, Direct Numerical Simulation (DNS) has become a powerful tool in understanding flow physics and the interaction between various dynamical scales in the flow. Numerical Simulation of channel flows, due to its geometrical simplicity, has been studied most commonly in the DNS literature. Orszag et al. (1980) studied transition from laminar to turbulent flow using a 3-step time splitting method, Fourier series expansions in the spanwise and streamwise directions and Chebyshev polynomial expansion in the direction normal to the walls. Orszag et al. (1983) later used the same algorithm, but with an explicit Adams-Bashforth integration scheme, to perform a DNS of turbulent channel flow. A DNS for a curved channel flow was carried out by Moser et al. (1984) at  $Re_\tau = 180$  again using a spectral method. Kim et al. (1987) used a Fourier Chebyshev pseudospectral method to study fully turbulent channel flow at the same Reynolds number and presented a large number of turbulence statistics. A finite difference DNS for a turbulent channel flow was presented by Rai et al. (1989) who showed the need for higher order accurate upwind schemes to yield accurate simulations.

These initial successes with the DNS method spurred the investigation of slightly more complex situations. Gavrillakis (1992) and Huser and Biringen (1993) both reported DNS for flow in a square duct geometry. Lyons et al. (1991) studied fully developed passive heat transfer in a direct simulation based on spectral method. Kasagi et al. (1992) and Kim and Moin (1989) obtained the solution to the energy equation for channel flows using a DNS procedure. Sumitani and Kasagi (1995) have reported a DNS in a channel flow with uniform suction and injection. More recently, Pointel et al (1996) have presented a DNS of channel flow with heat transfer using a collocated fifth-order accurate finite difference procedure. The calculations were done for a  $Re_\tau = 180$  on a  $128 \times 64 \times 64$  grid and were found to be in good agreement with the DNS data of Kim et al. (1987) and the measurements of Kreplin and Eckelmann (1979).

The present work aims to extend the work of Pointel et al. (1996) for a more complex flow situation, and intends to perform a DNS of a periodic cross-flow in a channel with a vertical slot-injection of coolant through the bottom surface. Examples of slot injection into a crossflow include the film cooling of gas turbine blades and combustor walls, flow control of aircraft and

missiles through blowing, and effluent discharges into air or water bodies. The application of primary interest here is the film cooling of gas turbine blades.

Jets in crossflow, as encountered in film cooling configurations, represent a rather complex flow situation. Several investigators have studied the features of the flow field associated with a single jet in a crossflow. The counter rotating vortex pair (CVP) is the most dominant structure observed, and persists far downstream of the jet injection. The CVP is a consequence of the reorientation of the jet-hole vorticity by the crossflow (Foss (1980), Andreopoulos (1985), Kelso et al. (1996)). Shear layer or ring vortices have also been observed in the near field of the jet. These vortices are driven by the Kelvin-Helmoltz instability. Horseshoe vortices are produced as a consequence of the jet obstructing the crossflow producing an adverse pressure gradient just upstream of the jet. These vortices have spanwise vorticity when they form, and as they travel downstream they are deflected by the crossflow and acquire streamwise vorticity rotating in a direction opposite to the CVP. Wake vortices which exist between the wall and the jet have also been observed (Fric and Roshko, 1994).

The majority of the studies aimed at numerically examining the details of the flow structures have approached the problem by solving the Reynolds Averaged Navier Stokes (RANS) equations. This time-averaged approach requires the use of turbulence models and makes predictions of the dynamic nature of vortices unfeasible. RANS calculations have been reported by Patankar et al. (1977), Sykes et al. (1986), Kim and Benson (1992) and Demuren (1993). Recently Large Eddy Simulations (LES) that resolve the dynamics of the large scales only and model the small scales have been presented by Jones (1996) and Yuan and Street (1996).

The geometrical configuration of interest considered in this work is shown in Figure 1. The primary flow (called the crossflow) in the channel is in the x-direction. The coolant jet is injected vertically upwards from a rectangular slot on the bottom surface. Periodic boundary conditions are imposed on the crossflow in the x-direction. The periodic flow in the x-direction makes the computational problem not only simpler to handle but it also allows us to mimic the effects of upstream film coolant holes. In a film cooling configuration with a series of parallel holes in the streamwise direction, the downstream coolant hole will see the downwash from the upstream coolant hole, and this effect is incorporated in the present configuration with the streamwise periodic boundary condition. Single coolant hole studies with Dirichlet inflow and outflow conditions can not simulate the upstream hole effects. The correct alternative is to include all rows of holes in the calculation domain, but performing a DNS calculation for such a configuration is considerably more difficult than the simpler single-hole situation considered in this work. However, for a single hole domain, the imposition of periodic boundaries in the crossflow direction is inappropriate, unless a suction boundary condition is incorporated, since with injection alone there is a net addition of mass across the lower surface. Therefore, in order to impose periodic conditions in the primary flow direction, a slot-suction boundary condition is imposed on the top wall. The normal suction velocity and temperature at the top wall is made exactly equal to the normal injection velocity and temperature at the bottom wall so that the mass, momentum and energy injected in exactly balances that sucked out. The blowing (or suction) ratio (injection velocity/crossflow velocity) is taken to be sufficiently small (0.25) so that the injection and suction effects are primarily confined to a small distance normal to the surface.

In the spanwise direction, a row of film coolant holes are assumed to be present. Therefore, in the computational domain of this study, consisting of a single hole, periodic spanwise boundary conditions are imposed.

## NUMERICAL PROCEDURE

Assuming constant density, and using the channel half-width  $\delta$  as the length scale, and the friction velocity  $u_\tau$  for the fully-developed channel flow (with no injection or suction) as the velocity scale, the non-dimensional continuity equation and the Navier Stokes equation for each velocity component  $u_i$  ( $i=1, 2$  and  $3$  represent the  $u, v, w$  velocity components) can be written as:

$$\vec{\nabla} \cdot \vec{u} = 0 \quad (1)$$

$$\frac{\partial u_i}{\partial t} + (\vec{u} \cdot \vec{\nabla}) u_i = -\vec{\nabla} p + \frac{1}{Re_\tau} \nabla^2 u_i \quad (2)$$

In the above equation,  $p$  represents the pressure and  $Re_\tau$  represents the Reynolds number based on the fully-developed channel flow friction velocity. For the temperature, iso-flux, iso-thermal conditions proposed by Kasagi et al. (1992) have been adopted. According to their investigations, for iso-flux conditions, the variations in the wall temperature for air flow can be considered to be negligible. Hence we can assume the wall to be locally isothermal. The isoflux condition implies that the ensemble averaged wall temperature (over  $z$  and  $t$ ), increases linearly with  $x$ -direction. Hence the bulk mean temperature averaged over  $z$  and  $t$  also increases linearly in  $x$ -direction and can be obtained from an energy balance. We also assume that the injection and suction jets are at the same temperature but lower than that of the wall. Hence the overall energy balance is preserved. The non-dimensional energy equation can then be expressed as:

$$\frac{\partial \theta}{\partial t} + (\vec{u} \cdot \vec{\nabla}) \theta = \frac{1}{Re_\tau Pr} \nabla^2 \theta + \frac{2}{\int_{-1}^1 \bar{u} dy} \quad (3a)$$

where

$$\theta(x, y, z, t) = \frac{\langle T_w \rangle T(x, y, z, t)}{T_\tau} \quad (3b)$$

and  $T_\tau$  is the friction temperature given by  $q_w / (\rho c_p u_\tau)$ , and  $q_w$  and  $\langle T_w \rangle$  are the ensemble averaged heat flux and wall temperature (over  $z$  and  $t$ ) respectively.

Results are obtained for a  $Re_\tau = 180$ . This corresponds to a channel Reynolds number  $Re_m$  based on the mean velocity and the channel height of 5600. As noted earlier, DNS results for fully developed channel flow at this  $Re_\tau$  value were reported by Kim et al. (1987) and Pointel et al. (1996). Since in the configuration considered in this study, the net mass addition is zero,  $Re_\tau = 180$  represents an average value for the channel. The injection and suction jet-holes were placed in the center of the lower and upper walls and were rectangular in shape with the long dimension of the hole ( $d$ ) along the crossflow direction ( $x$ ) and the short dimension of the hole ( $w$ ) in the spanwise direction ( $z$ ). The corresponding non-dimensional hole sizes  $d/\delta$  and  $w/\delta$  were 0.5 and 0.2 respectively. The actual non-dimensional lengths of the computational domain were chosen to be  $4\pi \times 2 \times 0.4\pi$ . These correspond with the  $4\pi \times 2 \times 2\pi$  computational domain dimensions of Pointel et al. (1996), except in the spanwise direction where coolant hole spacings of  $2.5d$  ( $=1.25 \times 0.4\pi$  in non-dimensional units) has been assumed.

As noted earlier, the flow and temperature variables are assumed to be periodic in the x and z directions. Dirichlet, zero velocity and temperature, boundary conditions were imposed at the channel walls while a zero-value Neumann condition was imposed on the normal pressure gradient at the wall. At the injection and suction slots, the normal velocity is set equal to 0.25 of the mean crossflow velocity corresponding to the fully developed channel flow at  $Re_\tau=180$ , and the temperature is set to a value lower than the wall temperature, and is assigned a non-dimensional value of 0.5.

The Fractional Step approach originally developed by Chorin (1967) was used for integrating the equations. In the first step, the momentum equation without the pressure gradient contribution is solved using a second order explicit Adams-Bashforth time-integration for the convection and streamwise and spanwise diffusion terms. For the normal-diffusion term, an implicit Crank-Nicholson scheme is used. This approach uses an intermediate velocity (denoted by  $\tilde{u}$ ), and for a typical velocity component, say u, has the following form:

$$\frac{\tilde{u} - u^n}{\Delta t} = \frac{3}{2}(C^n + D_e^n) - \frac{1}{2}(C^{n-1} + D_e^{n-1}) + \frac{1}{2}(D_i^n + \tilde{D}_i). \quad (4)$$

Here C represent the convection terms,  $D_e$  represents the streamwise and spanwise diffusion terms and  $D_i$  represents the normal diffusive term.

The velocity field is computed in the second step:

$$\frac{u^{n+1} - \tilde{u}}{\Delta t} = -\nabla \phi^{n+1} \quad (5)$$

where the pseudo pressure  $\phi$  is related to the pressure by:

$$\phi - \frac{\Delta t}{2Re} \frac{\partial^2 \phi}{\partial y^2} = p \quad (6)$$

We can apply the divergence operator on equation (5) and use continuity of velocity field to obtain the pressure Poisson equation:

$$\frac{1}{\Delta t} \nabla \cdot \tilde{u} = \nabla \cdot (\nabla \phi^{n+1}). \quad (7)$$

Once the pseudo pressure is known the velocity field  $u^{n+1}$  can be calculated from equation (5). The scalar field for temperature is then obtained by integration of the energy equation. We use a similar approach to the momentum equation to get the fractional step equations from which we can directly obtain the temperature field.

The spatial discretization was done using the non-conservative formulation of the convective and diffusive terms on a collocated grid with velocity and pressures at the center of the control volume. The convective terms were treated by a fifth order upwind biased approximation as used by Rai et al. (1989). The diffusive terms are treated by a sixth order accurate seven point central difference stencil. For the boundary terms we used one sided differences to maintain the accuracy of the scheme. The pressure Poisson equation is discretized

using the 4-2 consistent formulation as recommended by Najjar et al. (1994). This involves second order discretization of the divergence operator and fourth order discretization of the pressure gradient operator. In the continuity equation, which is used for updating the velocity field at the cell faces, the gradient operator is represented by a fourth order finite difference formulation.

The implementation of the numerical procedure, described below, is done on a MasPar MP-2. This is a massively parallel computer and provides a suitable platform for computer intensive DNS calculations. The MasPar is a SIMD machine, which has a  $128 \times 64$  parallel processors (PE) array. We have used a grid of  $128 \times 64 \times 64$  for the calculation, which is uniform in the x and z direction, and non-uniform in the y direction. Each (I, J) node is mapped on to a PE. Each PE has a local memory of 64K and provides the storage in the third (K) dimension.

The time integration was first done for the velocity field till the flow reached a fully developed state. Then the thermal field was allowed to reach the fully developed state before the calculation of mean quantities was started. Typically 60,000 time steps were required to get to this stage. The calculation of the mean quantities was done over 20,000 non-dimensional time steps. This was followed by the calculation for the turbulent statistics and this was done over 8000 steps. During the statistics calculation we also calculated the instantaneous vorticity profiles for various streamwise, crossstream and spanwise planes at various time steps in order to present the time evolving characteristics for the flow field.

## RESULTS AND DISCUSSION

In making an assessment of the adequacy of the grid size used in the present study where the mean  $Re_\tau$  is 180, we make comparisons with the grid resolution of reported channel flow studies at a  $Re_\tau$  of 180. Pointel et al. (1996) used a  $128 \times 64 \times 64$  grid for simulating fully developed channel flow in a  $4\pi \times 2 \times 2\pi$  domain at a  $Re_\tau$  of 180. Results obtained are shown in Figure 2 and compared with the DNS predictions of Kim et al. (1987) and the experimental data of Kreplin and Eckelmann (1979). As can be seen, the comparison is quite good. The same  $128 \times 64 \times 64$  grid was employed in the present problem which has a smaller computational domain of  $4\pi \times 2 \times 0.4\pi$ , and therefore has an improved resolution. The resolution in wall-coordinates are noted to be:  $\Delta x^+ = 17.67$ ,  $\Delta y^+ = 0.018 - 23.76$ ,  $\Delta z^+ = 3.59$ . In comparison, Kasagi et al. (1992) reported corresponding grid spacings of 18.4, 0.08-4.9 and 7.4 in a  $5\pi \times 2 \times 2\pi$  computational domain. Similar grid spacings of 17.7, 0.05-4.4, and 5.9 were also used by Kim and Moin (1989) and Kim et al. (1987) in a  $4\pi \times 2 \times 2\pi$  computational domain at the same Reynolds number. Moser and Moin (1984) used  $128 \times 65 \times 128$  points in a similar computational domain and comparable Reynolds number, and reported that this resolution was adequate to resolve all the essential turbulent scales. Lu and Hetsroni (1995), in their direct simulation of channel flow with heat transfer at a comparable Reynolds number, have used  $\Delta x^+$ ,  $\Delta y^+$ , and  $\Delta z^+$  values of 32, 0.4-20, and 8. Based on these comparisons, the grid size used in this study should be deemed to be adequate.

In presenting the results below, the origin of the coordinate system is fixed at the jet-hole center. The x and y dimensions are scaled with the long dimension of the jet hole (d) oriented in the direction of the crossflow, while the z dimension is scaled with the spanwise dimension of the jet hole (w).

### ***Characteristics of the Flowfield***

Figures 3(a) and (b) present the  $u$  and  $v$  velocity contours in the spanwise midplane ( $z/w = 0$ ), and correspond to the vector plots shown in figures 5(a) and 5(b). For clarity, several of the plots are stretched in the vertical or spanwise directions. Figure 3(a) and 5(a) clearly show the almost immediate bending of the jet due to the strong crossflow. The jet penetration is confined to a  $y/\delta$  of about 0.5 or a  $y/d$  of about 1 which corresponds to the long-dimension of the jet-hole (hereinafter referred to as the jet diameter). Figure 5a clearly shows that at the channel mid-plane ( $y/d=2$ ), the crossflow velocity is relatively unaffected by the injection or suction slots. This observation supports the earlier premise that the behavior of the film-coolant injection jet can be studied independent of the suction jet, and that the observations made should hold for a film cooling configuration with a series of coolant holes in the crossflow (or primary flow) direction.

A weak horseshoe vortex system is observed in Fig. 3(a) and in the near-wall detail of the velocity vectors shown in Fig. 5(b). The vortex system extends over one hole diameter upstream of the jet and appears to consist of two clockwise eddies rotating side by side. However, the horse-shoe vortex system does not appear to be deflected around the jet as it does at higher blowing ratios (see Fric and Roshko, 1994; Kelso et al., 1996; Muldoon and Acharya, 1998). No footprint of the vortex is seen in the  $x$ -vorticity contour along a horizontal plane just above the lower surface (Fig. 3c).

In examining the instantaneous  $v$ -velocity contours (Fig. 3b), it can be seen that roughly 5 hole diameters downstream of the injection location ( $x/d=5$ ), alternate pockets of positive and negative  $v$ -contours are present (note the high level of stretching in the  $y$ -direction). These are analogous to those observed by Kim et al. (1987), and represents ejection and sweep events associated with a developing boundary layer. In the near vicinity of the injection hole,  $1 < x/d < 5$ , the behavior is different with primarily positive near wall velocities.

The  $x$ -vorticity contours shown in Figure 3c indicate the existence of a dominant wall-vortex structure close to the lower surface with vorticity opposite to the CVP. Thus downstream of the injection hole, positive vorticity is seen close to the wall in the right half (viewing the flow from a downstream point) and negative vorticity is noted in the left half. Further away from the wall, at a higher  $y/d$  value, the CVP is encountered and the sign of the vorticity reverses. This can be seen in the cross-sectional ( $y$ - $z$ ) plots of  $x$ -vorticity presented later. Figure 3c also shows the generation of negative and positive  $x$ -vorticity on the right and left edges of the jet hole; these represent the source of vorticity for the CVP. It is however important to note, that the vorticity for the CVP does not originate from any in-hole boundary layer vorticity (as has often been reported in the literature), since at the jet exit plane a uniform  $v$ -velocity was specified. Rather, the  $x$ -vorticity along the jet-hole edges is generated by the interaction of the injected velocity and the crossflow.

Figure 4 shows the velocity vectors in different cross-stream planes at  $x/d=0.5, 2, 5$  and 10. At  $x/d = 0.5$  we can see the jet penetration to be more than  $y/d = 1.8$ . However beyond a  $y/d$  of 1, the velocity magnitudes in the  $y$ - $z$  plane are considerably smaller than the velocities in the  $x$ - $y$  plane, and therefore as seen in Fig. 5a, the flowfield is relatively unaffected by the jet beyond a  $y/d$  of 1. We can see the evolution of the CVP around  $z/w = \pm 0.8$  for  $y/d < 0.2$ . There is considerable flow across the spanwise periodic boundaries indicating a significant level of lateral transport, and interaction between spanwise adjacent coolant jets. Both inflow and outflow are noted across the periodic boundaries. We also note the absence of any symmetry across the  $z/w=0$  boundary. In fact by  $x/d=10$ , the CVP has lost its bound-vortex structure and no

semblance of symmetry exists across  $z/w=0$ . In the near field ( $x/d < 5$ ), each half of the CVP is clearly associated with a weak counter-rotating eddy system above it.

Figure 5c shows that there is a significant amount of entrainment of the crossflow into the wake of the jet. This clearly appears to persist up to about  $x/\delta$  of 9 at which point the wake appears to meander away from the jet-hole centerline. A close inspection also reveals flow reversals of the entrained crossflow near the jet-hole centerline. These reversals are most clearly seen between  $x/d$  of 3 and 5 in Fig. 5c, and represent the onset of the wall-vortex system which will be clearly evident in the  $x$ -vorticity contours in a  $y$ - $z$  plane presented later.

Figure 6 shows the profiles of the mean velocity and temperature, non-dimensionalized by the corresponding average friction-velocity  $u_\tau$  (which is the same as the friction velocity for fully developed turbulent channel flow at the same average Reynolds number  $Re_\tau=180$  of this study) and the average friction-temperature  $T_\tau$ . The profiles are presented for several  $x/d$  locations and two  $z/w$  planes,  $z/w=0$  corresponding to the jet-center plane, and  $z/w=-1.9$  representing a location between the jet-hole and the spanwise periodic boundary. The near-wall behavior ( $y^+=y.Re_\tau/\delta < 12$ ), appears to conform somewhat to the law-of-the-wall behavior with a maximum deviation of less than 30%. However, in the turbulent region ( $y^+ > 12$ ), log-law behavior is not observed even off the jet-center plane and upstream of the jet ( $z/w=-1.9$ ,  $x/d=-2$ ) due to the effect of vortical flow structures. At  $z/w=-1.9$ , the near-wall behavior appears to be only mildly altered by the spanwise cross-stream flow downstream of the jet. In fact, Fig. 5c indicates that the spanwise cross-stream flow close to the wall at  $z/w=-1.9$  is relatively weak. The maximum deviation from the  $x/d=-2$  profile appears to occur in the vicinity of  $x/d=2$ , beyond which flow recovery is initiated. The profiles in the jet-center plane (Fig. 6b and 6d) indicate significant distortion of the near-wall behavior by the jet. This distortion begins at the upstream end of the jet ( $x/d=-0.5$ ) with a significant reduction in the wall-gradients. Flow recovery begins downstream of the jet, but the recovery in the inner-region ( $y^+ < 12$ ) is substantially faster than in the outer-region ( $y^+ > 12$ ), leading to a change in the sign of the slope in the velocity profile in the buffer region and immediately above it ( $7 < y^+ < 35$  or  $0.08 < y/d < 0.39$ ). Such changes in the slope of the velocity profile can lead to the development of flow instabilities and large-scale vortical structures. This  $y/d$  region can be seen to correlate with the region associated with the growth of large scale structures in the vorticity contours presented later.

Figure 7 shows the time history of spanwise vorticity at  $z/w = 0$ . The time-series is presented at time instances  $t_1, t_2, \dots, t_8$ , separated by  $\Delta t=0.02$  where  $\Delta t$  is the non-dimensional time interval. The figures indicate the predominant negative  $\omega_z$  on the windward side which is indicative of the crossflow bending due to the jet. Patches of positive vorticity can be seen on the leeward side of the jet. The vortices on the windward and leeward side of the jet are driven by Kelvin-Helmholtz instabilities, and are generally referred to as shear layer or spanwise-jet-vortices. These vortices, particularly those from the windward side, appear to be peeled by the crossflow and convected downstream. In fact the near-wall boundary-layer region downstream of the jet is dominated by the negative vorticity partly originating from the windward side of the jet, and partly associated with a developing boundary layer. The dynamical nature of the vortices should be noted in the time-series presented. Note the vortices on the windward side at time  $t_3$  between  $y/d$  of 0.5 and 1. At the next time-instance, a necking process is initiated, and subsequently two vortices form and convect downstream. A third vortex is transported to the near wall region downstream of the jet. Upstream of the jet the horseshoe vortex system consisting of two eddies can be observed, but it can be seen to be rather small and localized.

Figure 8 shows the instantaneous  $x$ -vorticity at  $x/d=-0.5$  (upstream edge of the injection hole) and at  $x/d=0.5$  (downstream edge of the injection hole). At  $x/d=-0.5$ , the beginnings of the CVP can clearly be seen. This was also observed in Fig. 3c, and implies that the  $x$ -vorticity of the same sign as the CVP is originated on the windward side through the interaction between the jet and the crossflow. Both at  $x/d=-0.5$  and  $0.5$ , the CVP appears to be straddled by an eddy rotating in the opposite direction. This is possibly the horse-shoe vortex that lifts up above the CVP at this low blowing ratio. Reported studies in the literature at higher blowing ratios indicate that the horse-shoe vortex is deflected in the spanwise direction by the jet and travels downstream along the wall parallel to the CVP. In the present case, the signature of the horse-shoe vortex in the spanwise direction is not observed, and we believe that at the low blowing ratio considered here, since the jet is immediately bent by the crossflow, the horse-shoe vortex instead of being pushed in the spanwise direction is pushed up in the vertical direction to ride above the CVP.

Figure 9(a) shows the time-series (presented  $2\Delta t$  apart) of the  $x$ -vorticity at  $x/d=2$ . Three distinct structures can be observed: the CVP, the horse-shoe vortex system, and a wall vortex below the CVP. The orientation of the wall vortex and the horse-shoe vortex are in the same direction and opposite to the CVP. The wall vortex is due to the entrainment of the crossflow into the wake of the jet. The entrained crossflow encounters high pressures along the jet-hole centerplane which drives the flow along the wall away from the centerplane, thus establishing a wall-vortex. The horse-shoe vortex is now shifted outwards toward the periodic boundaries, but still remains lifted off the surface. In examining the time-series, one notes that the CVP undergoes significant distortion with time. There is also significant spanwise transport of vorticity across the periodic boundaries leading to fairly effective spanwise mixing.

At  $x/d=5$  (Fig. 9(b)), a noticeable interaction between the wall-vortex and the CVP is seen. The wall-vortex can be seen to be entrained upwards towards the CVP, and in this process is reoriented into  $y$ -vorticity representing wake vortices (seen in Fig. 10 and 11). This reorientation of the wall-vortex system into a wake vortex system has also been reported by Fric and Roshko (1994) and Kelso et al. (1996).

Further downstream at  $x/d = 10$  (not shown), we cannot clearly identify the CVP as being an organized structure spanning both sides of the jet-hole vertical midplane. There is significant vortical activity though, but of a much more complex nature, and indicates the persistence of the wake.

Figure 10 shows the instantaneous  $\omega_y$  contours close to the lower surface at  $y/d = 0.002$ , while Fig. 11 shows the time history of  $\omega_y$  contours at  $y/d = 0.0239$  respectively. In Figure 10, we note that the wake vortices strongly manifest themselves primarily beyond  $x/d=5$  which is the approximate location where we noted upward entrainment and reorientation of the wall vortex system (Figure 9(b)). This observation provides further evidence of the correlation between the wall-vortex and the wake-vortex system. The wake vortices are in the form of a series of co-rotating or counter-rotating adjacent eddies that have features quite distinct from those behind a rigid cylinder. At earlier  $x/d$  locations, upstream of  $x/d=5$ , the wall vortex had remained fairly stable and bound to the near wall-region, and no significant presence of a series of adjacent co- and counter- rotating wake vortices was noted. Instead,  $y$ -vorticity in the near wake ( $x/d < 5$ ) was observed in the form of a near-contiguous elongated chain (see Figure 10 and 11) and stems from the interaction of the jet and the deflected crossflow which leads to significant values of the  $\partial u / \partial z$  term (and therefore  $\omega_y$ ) along the spanwise edges of the jet. This vorticity is entrained into the near wake ( $x/d < 5$ ), and eventually breaks down further downstream, contributing also to the

strong wake vortex system observed beyond  $x/d$  of 5. The time series behavior shown in Fig. 11 also indicates that the wake structure oscillates around the jet-hole center-plane in the near field, but exhibits significant asymmetry in the far field. At time instances  $t_1$ ,  $t_3$  and  $t_5$ , for example, the wake vortex system beyond  $x/d$  of 6 is skewed considerably towards positive  $z/w$  values. This departure from symmetry was also noted earlier in velocity vector plots of Fig. 5c.

Figure 12 presents the instantaneous pressure contours at  $y/d=0.0239$  at four time-instances. The adverse pressure gradient upstream of the jet can clearly be seen, and is responsible for the horse-shoe vortex system. In the jet-hole region, and downstream of it, the pressure distribution shows a necklace pattern. Note that in the region  $-0.5 < x/d < 0.5$  there is a strong pressure gradient in the crossflow directed inwards in the spanwise direction toward the jet. This inward pressure gradient combined with the adverse pressure gradient the flow encounters at the jet interface leads to the generation of  $x$ -vorticity of the same-sign as the CVP along the spanwise boundaries of the jet-hole ( $z/w = \pm 0.5$ ). This mechanism therefore appears to be responsible for the initial development of the CVP.

Downstream of the jet-hole, the spanwise pressure gradient is directed inwards towards the jet centerline. This pressure gradient is responsible for the inward entrainment of the crossflow that is the source of the wall vortex system. Note that downstream of about  $x/d=5$ , the coherence of the pressure contours is somewhat lost leading to the asymmetric wake pattern reported earlier.

### Time-averaged Statistics

Figure 13 and 14 show the rms contours at  $x/d=0.5, 2, 5$  and  $10$ . At  $x/d=0.5$ ,  $v_{rms}$  and  $w_{rms}$  are comparable in magnitude with the latter attaining slightly larger values, but  $u_{rms}$  is nearly twice the  $v_{rms}$  and  $w_{rms}$  values. The  $u_{rms}$  and  $w_{rms}$  plots correlate well with each other exhibiting maximas in regions of high unsteady  $\omega_x$  vorticity, that is in the outer regions of the CVP and the CVP-horseshoe vortex interface (see Fig. 8) that exhibit a significant level of unsteadiness, and near the spanwise periodic boundaries across which significant vorticity transport occurs (Fig. 8 shows only one instance in time, and shows high vorticity near the  $z/w=-3$  boundary. At other instances in time high vorticity is seen at the  $z/w=3$  boundary as shown in Fig. 9). The  $v_{rms}$  and  $t_{rms}$  profiles correlate well with each other, but do not show a strong correlation with the  $u_{rms}$  and  $w_{rms}$  plots. In fact the peak values are obtained near  $y/d \approx 1$ , and appears to correspond to the extent of the vertical jet penetration. The interface between the jet and the crossflow, is characterized by Kelvin-Helmholtz instabilities and high spanwise vorticity  $\omega_z$  (see Fig. 7), and is therefore associated with high  $v_{rms}$ . Since the jet and the crossflow are at different temperatures, their interface is also associated with high  $t_{rms}$ . The aforementioned correlation between the rms values and the coherent structures imply that the large scales are largely responsible for the production of turbulent stresses. At  $x/d=2$ , the behavior of the rms profiles is quite similar to that at  $x/d=0.5$ , except that the  $t_{rms}$  profiles shows high values both in regions of high  $v_{rms}$  (interface between the upper edge of the jet and the crossflow) and high  $u_{rms}$  (interface between the CVP and the crossflow). Further downstream ( $x/d=5$  and  $10$ ) the jet deflection is complete, and the CVP dominates growing in size and strength. All the rms-profiles now correlate with the high vorticity regions of the CVP, and as a consequence correlate well with each other. At  $x/d=10$ , we still observe  $u_{rms} > v_{rms} > w_{rms}$ , although the relative magnitudes are closer to each other than they were at  $x/d=0.5$ . Note that the time-averaged rms-profiles at  $x/d=10$  show reasonable symmetry around  $z/w=0$ , while the instantaneous profiles shown earlier (Fig. 5c and 8-11) displayed significant asymmetry in the spanwise direction.

The rms profiles in the  $z/w=0$  plane are shown in Figure 15. All the peak values occur downstream of the jet injection ( $x/d=0$ ), but the upwash effect is clearly evident. High rms values enter the computational domain from the upstream boundary, and the flow development downstream of the injection point is constrained by these high rms values. The  $u_{rms}$  value peaks first in the  $x$ -direction (near  $x/d=5$ ) and occurs closest to the wall ( $y/d=0.25$ ), while the  $v_{rms}$  peaks around  $x/d=6.5$ . These peak locations correspond with the location where the shear layer vortices saturate in strength (see Fig.7). The other rms values  $w_{rms}$  and  $t_{rms}$  peak at an  $x/d$  in the vicinity of 7. Note that in the vicinity of this  $x/d$  (in the range of 5-7), significant reorientation of the wall vortex system into a wake vortex system occurs, and therefore the wake- and wall-vortex structures apparently play an important role in the  $w_{rms}$  and  $t_{rms}$  values.

Figure 16 and 17 present the Reynolds stress components at  $x/d=0.5, 2, 5$  and 10. As expected,  $u'v'$  is observed to be symmetric about  $z/w = 0$ , and  $u'w'$  and  $v'w'$  are observed to be antisymmetric about  $z/w = 0$ . The high  $u'v'$  values are associated with the jet-crossflow interface shown in Fig. 7, where shear layer vortices primarily form. At  $x/d=10$ , distinct regions of upper and lower interfaces are no longer clearly evident and a large patch of high  $u'v'$  is noted in the jet-flow region. High values of  $u'v'$  are also associated with the vortical structures transported across the periodic boundaries. These structures lead to large values of  $\partial u/\partial y$  and therefore  $u'v'$ . The  $u'w'$  and  $v'w'$  values are high in regions of large  $\partial u/\partial z$  and  $\partial v/\partial z$  respectively. These regions are again associated with the jet-crossflow interfaces and the vortical structures crossing the periodic boundaries. Note that the clover-leaf shape and the sign of the  $v'w'$  contours near the wall for  $x/d > 5$  indicate the existence of counter-rotating eddies near the wall, i.e., the CVP and the wall vortex, in the  $y$ - $z$  plane. In comparing the magnitudes of the shear stresses, in the near field ( $x/d < 2$ ),  $u'w' > u'v' > v'w'$  with  $u'w'$  being substantially higher presumably due to large  $\partial u/\partial z$  values near the edges of the jet. Further downstream,  $u'w'$  and  $u'v'$  become more comparable in magnitude.

Figure 18 presents the Reynolds stresses in the  $z/w = 0$  plane. The peak shear stresses, in all cases occur downstream of  $x/d=5$ . The  $u'v'$  contours correlate best with the  $v_{rms}$  contours (Fig.15) and therefore correlate with the shear layer vortices, and peak at the locations where these vortices saturate in strength. At  $x/d=5$ , for example, the peak  $u'v'$  value shown in Fig. 17 is 2.85 and its  $y/d$  location correlates with the shear layer vortices, while secondary bimodal peaks (of the order of 1) occur at  $y/d=0.25$  which correlates with the CVP and the horseshoe vortices. The  $v'w'$  contours appear to be consistent with the nature of the near-wall flow structure in the  $y$ - $z$  plane. Close to the wall, the wall vortex produces negative  $v'w'$  values. The wall vortex system gains prominence, as seen earlier, around  $x/d=5$  and therefore large negative  $v'w'$  values are obtained in the vicinity of this  $x/d$  value. Further downstream, the wall vortex is entrained as an upflow into the CVP, and as seen in Fig. 11, wake vortices are noted. The  $v'w'$  contours in this region show a more complex behavior and are positive. The  $u'w'$  contours also correlate well with the crossflow entrainment. They peak where the crossflow is a maximum (around  $x/d=5$ ), and decay further downstream.

Figure 19 and 20 present the turbulent heat flux correlations at  $x/d=0.5, 2, 5$  and 10. The turbulent heat flux correlations appear to correlate reasonably well with the rms values and the behavior of the large scale vortical structures, thus indicating the important role these structures play in the turbulent heat transport. In comparing the magnitudes  $u't' > w't' > v't'$  in the near field ( $x/d < 5$ ) indicating that the streamwise velocity fluctuations are most responsible for the heat transfer from the surface. Further downstream, at  $x/d=10$ , the  $v't'$  values become comparable in

magnitude to the  $u't'$  values, while the  $w't'$  decrease in magnitude and become less important. The heat flux distributions at  $z/d=0$  in the  $x$ - $y$  plane are shown in Fig. 21, and support the above observations. The maximum  $w't'$  occurs near  $x/d=5$  where there is significant spanwise entrainment of the crossflow. The peak in the  $u't'$  and  $v't'$  occur downstream of  $x/d=5$  and at a  $y/d$  location of approximately 0.5. These peak values are therefore associated with the spanwise shear layer vortical structures (Fig.7).

Figure 22 presents the turbulent viscosity factor  $\nu_{t,ij}$  calculated as:

$$\nu_{t,ij} = \frac{-u_i u_j}{\left[ \frac{\partial u_i}{\partial x_j} + \frac{\partial u_j}{\partial x_i} \right]} \quad (8)$$

where all terms on the right hand side of the above equation are computed from the DNS results. The viscosity factors are presented in a  $x$ - $z$  plane corresponding to a  $y/d=0.1085$ . While all three viscosity factors  $\nu_{t,12}$ ,  $\nu_{t,13}$ ,  $\nu_{t,23}$  were computed, only  $\nu_{t,12}$  is presented. Note that the magnitudes of the individual viscosity factors  $\nu_{t,12}$ ,  $\nu_{t,13}$ ,  $\nu_{t,23}$  at the same point are substantially different in magnitude indicating the anisotropy in the flowfield. The  $\nu_{t,12}$  clearly corresponds to the wake structure shown in Fig. 11, and indicates that the large-scales clearly have a role in the values of the turbulent viscosity. The footprint of the horseshoe can also be seen upstream of the jet hole. The  $\nu_{t,13}$ ,  $\nu_{t,23}$  values show less coherence with respect to the large scale structures, and are characterized more by patches of high positive and negative viscosity factors. The positive and negative values of the viscosity factors are associated with the fact that both the turbulent shear stress and the mean strain rate can have both positive and negative values. Clearly, any use of an isotropic turbulent viscosity is going to be unsuccessful in capturing the true behavior.

## CONCLUDING REMARKS

A Direct Numerical Simulation of a film coolant jet injected normally into a crossflow has been presented. The crossflow Reynolds number is 5600 and the blowing ratio is 0.25. Both flow and heat transfer predictions are presented. The following major observations are made:

1. Jet penetration is limited to 1.8 hole diameters, with the primary crossflow velocity relatively unaffected beyond 1 hole diameter.
2. A weak horse-shoe vortex system consisting of two clockwise eddies is noted within one hole diameter upstream of the jet. This horseshoe vortex is deflected upwards and rides over the CVP in the near field of the jet.
3. The near-field past jet reattachment is characterized by developing boundary layer behavior with ejection and sweep events commonly termed as turbulent bursts. However, these events are largely controlled by the large scale vortical structures.
4. The origins of the CVP is associated with the  $x$ -vorticity generated by the interaction of the injected jet with the crossflow. Therefore hole-boundary-layer vorticity is not essential for the generation of the CVP.
5. There is a significant amount of crossflow in the near field ( $x/d < 5$ ) of the jet. This crossflow encounters an adverse gradient along the jet-hole centerline and is responsible for the

formation of the wall vortex system. The wall vortex is fairly stable for  $x/d$  up to 5, but beyond that is entrained into the CVP and is reoriented as a wake vortex system.

6. Along the upper edges of the jet, Kelvin-Helmholtz instability leads to the formation of the shear layer vortices. These vortices are peeled and convected downstream.
7. The  $v_{rms}$  and  $t_{rms}$  contours appear to be most strongly correlated with each other and with the shear layer vortices in the near field. The  $u_{rms}$  and  $w_{rms}$  contours appear to be the largest at the interface between the CVP and the horse-shoe vortex and along the periodic boundaries at the locations associated with significant spanwise crossflow. In general,  $u_{rms} > w_{rms} > v_{rms}$ . The strong correlation of these statistics with the large scale structures point to the importance of the latter in controlling the surface heat transfer and the near field mixing between the crossflow and the coolant stream.
8. The viscosity factors show considerably anisotropy and in the horizontal ( $x$ - $z$ ) plan show correlation with the large scale structures. Existing statistical models based on isotropy are clearly going to be inadequate in modeling this complex flow. Current efforts are focussed in examining the budgets of the turbulence kinetic energy and the dissipation rates, in order to provide some guidance toward turbulence modeling.

## REFERENCES

- Andreopoulos, J., 1985, On the structure of jets in a crossflow, *Journal of Fluid Mechanics*, Vol. 157
- Chorin, A. J., 1967, A numerical method for solving incompressible viscous flow problems. *Journal of Computational Physics*, 2:12-26
- Demuren, A. O., 1993, Characteristics of three dimensional jets in crossflow, *International Journal of Engineering Science*, No. 6, pp. 899-913
- Fric, T. F., and Roshko, A., 1994, Vortical structure in the wake of a transverse jet, *Journal of Fluid Mechanics*, Vol. 279, pp. 1-47
- Foss, J., 1980, Interaction region phenomenon for the jets in a cross-flow problem, *Rep. SFB 80/E/161, Univ. Karlsruhe*
- Gavrilakis, S., 1992, Numerical simulation of low reynolds number turbulent flow through a straight square duct, *Journal of Fluid Mechanics*, Vol. 244, pp. 101-129
- Huser, A., and Biringen, S., 1993, Direct numerical simulation of turbulent flow in a square duct, *Journal of Fluid Mechanics*, Vol. 257, pp. 65-95
- Jones, W. P., and Willie, M., 1996, Large eddy simulation of a round jet in crossflow, *Engineering Turbulence Modeling and Experiments 3*, Ed. Rodi, W. and Bergeles, G., pp. 199-209
- Kasagi, N., Tomita, Y., and Kuroda, A., 1992, Direct Numerical Simulation of Passive Scalar Field in a Turbulent Channel Flow, *Transactions of the ASME*, Vol. 114, pp. 598-606.
- Kelso, R. M., Lim, T. T., and Perry A. E., 1996 An experimental study of jets in crossflow, *Journal of Fluid Mechanics*, Vol. 306, pp. 111-144
- Kim, S. W., and Benson, T. J., 1992, Calculation of a circular jet in crossflow with a multiple time scale turbulence model, *International Journal of Computational Physics*, Vol. 59, pp. 308
- Kim, J., Moin P., and Moser, P., 1987, Turbulence statistics in fully developed channel flow at low reynolds number, *Journal of Fluid Mechanics*, Vol. 177, pp. 133-166

- Kim, J., and Moin, P., 1989, Transport of passive scalars in a turbulent channel flow, in *Turbulent Shear Flows VI*, J. C. Andre et al eds., Springer Verlag, Berlin, pp. 85-96
- Kreplin, H., and Eckelman, H., 1979, Behavior of the three fluctuating velocity components in the wall region of a turbulent channel flow, *Phys. of Fluids*, Vol. 22, pp. 1233-1239
- Lu, D. M., and Hetsroni, G., 1995, Direct numerical simulation of a turbulent open channel flow with passive heat transfer, *Int. J. Heat and Mass Transfer*, Vol. 38, pp. 3241-3251
- Lyons, S. L., Hanratty, T. J., and McLaughlin, J. B., 1991, Direct numerical simulation of a passive heat transfer in a turbulent channel flow, *Int. J. Heat Mass Transfer*, Vol. 34, pp. 1149-1161
- Moser, R. D., and Moin, P., 1984, Direct numerical simulation of curved turbulent channel flow, *NASA TM 85974*
- Muldoon, F., and Acharya, S., 1998, Dynamics of large-scale structures for jets in crossflow, *43rd Intl. Gas Turbine Institute Conference*, Stockholm, Sweden; also NASA/CR-1998-206606
- Najjar, F. M., and Vanka, S. P., 1994, Simulations of unsteady fluid flows on the CM-5. *Symposium on Advances in Computational Methods in Fluid Dynamics, ASME/Fluid Division Summer Meeting.*
- Orszag, S. A., and Kells, S. C., 1980, Transition to turbulence in plain Poiseuille and plane Couette flow, *Journal of Fluid Mechanics*, Vol. 96, pp. 159-205
- Orszag, S. A., and Patera, A. T., 1983, Transition to turbulence in plane Poiseuille and plane Couette flow, *Journal of Fluid Mechanics*, Vol. 128, pp. 347-385
- Pointel, G., Acharya, S., and Sharma, C., "Direct Numerical Simulations of Convective Heat Transfer", *1996 Energy Technology Conference and Exposition*, Houston, January 1996.
- Patankar, S. V., Basu, D. K., and Alpay, S. A., 1977, Prediction of the three dimensional velocity field of a deflected turbulent jet, *Transactions of the ASME*
- Rai, M., and Moin, P., 1989, Direct simulations of turbulent flow using finite-difference schemes. *AIAA Paper 89-6039.*
- Simutani, Y., and Kasagi, N., 1995, Direct numerical simulation of turbulent transport with uniform wall injection and suction, *AIAA Journal*, Vol. 33, pp. 1220-1228
- Sykes, R. I., Lewellen, W. S., and Parker, S. F., 1986, On the vorticity dynamics of a turbulent jet in a crossflow, *Journal of Fluid Mechanics*, Vol. 80, pp. 49-80
- Yuan, L. L., and Street, R. L., 1996, Large eddy simulation of a jet in crossflow, *ASME Fluids Engineering Division*, Vol. 242

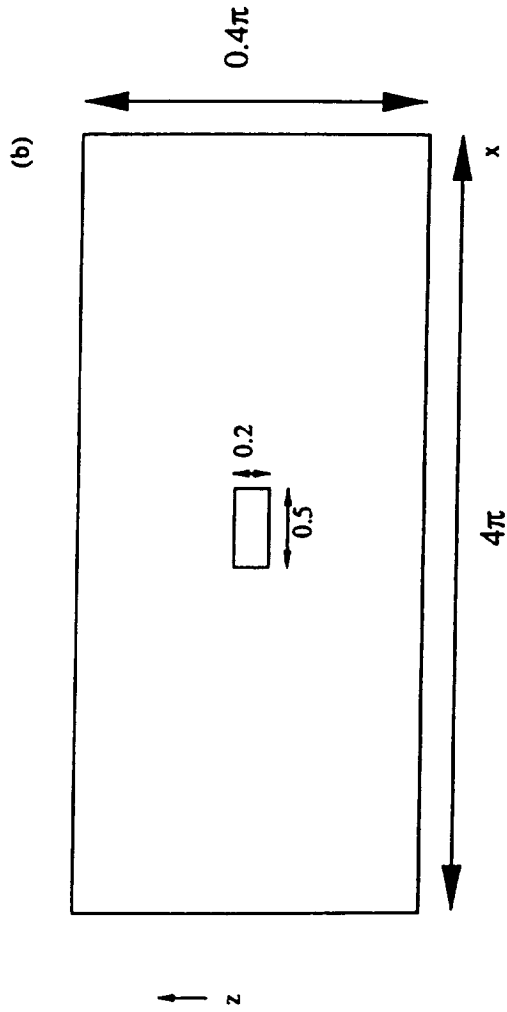
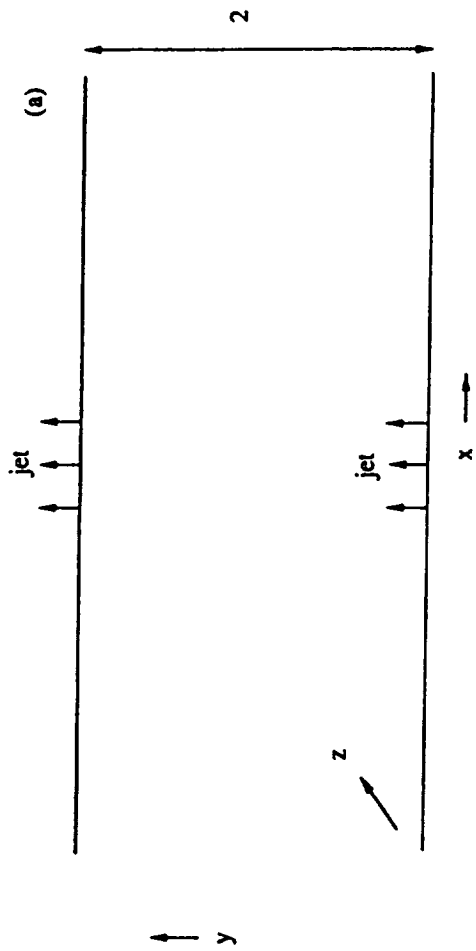


Figure 1 Flow schematic (a) side view (b) top view (dimensions nondimensionalized by channel half width)

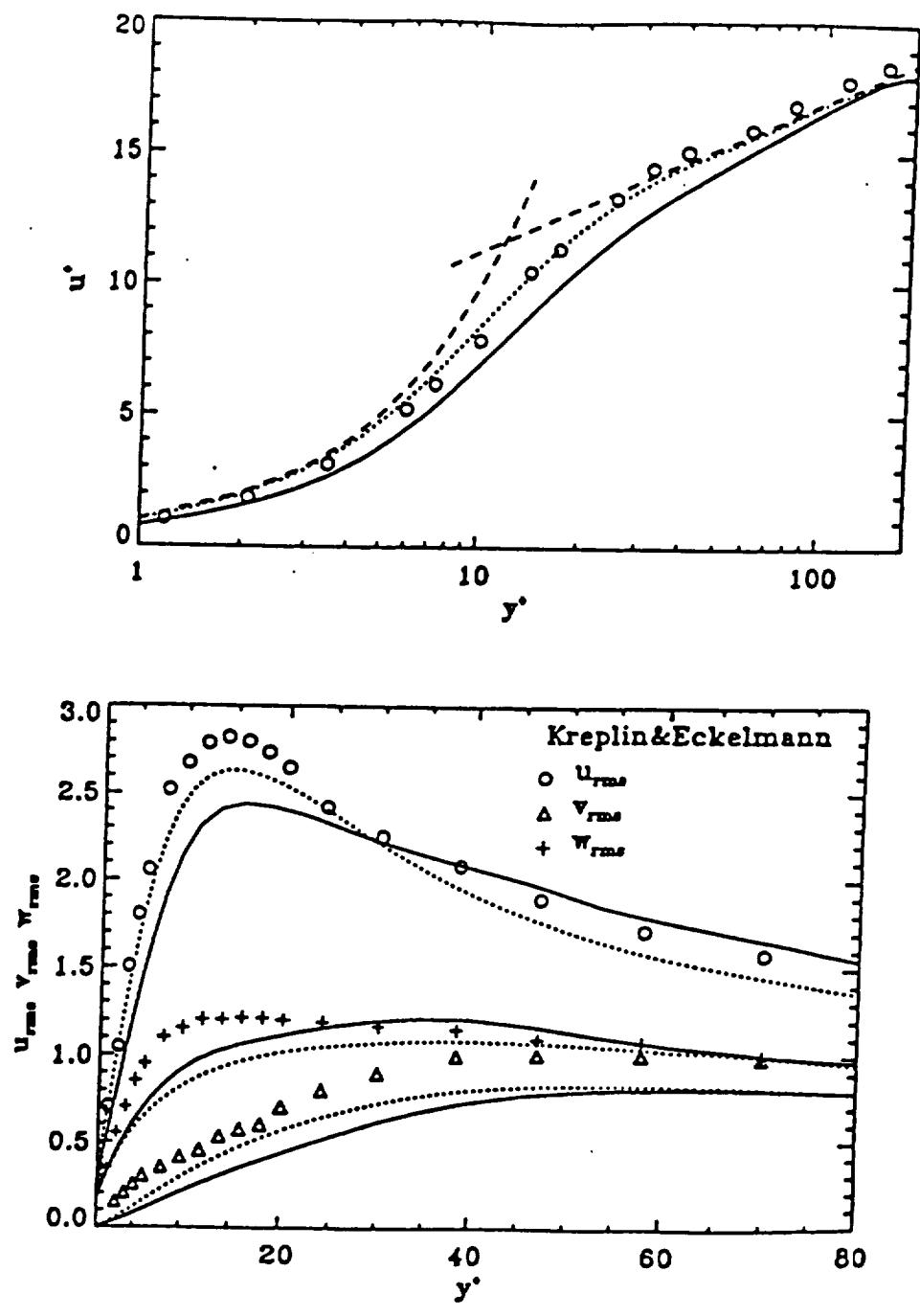
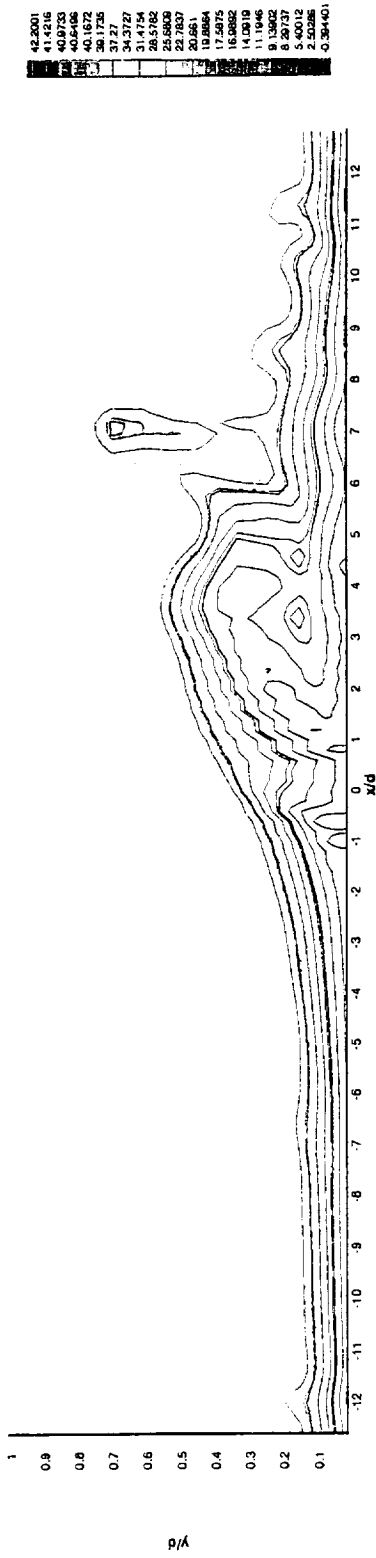
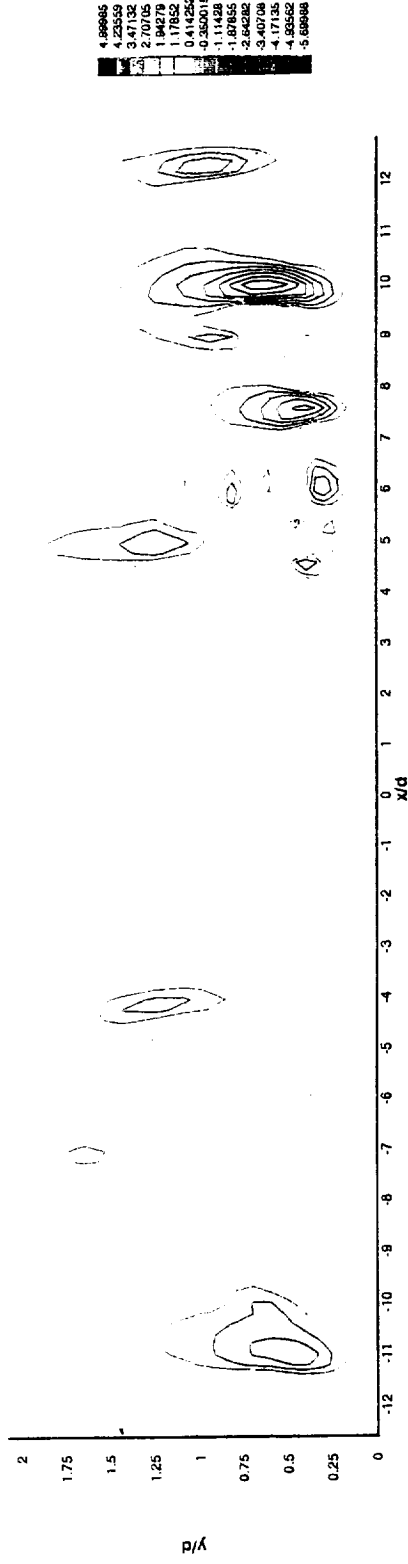


Figure 2: Comparison of DNS predictions of Pointel et al., 1996 (—) with the DNS predictions of Kim et al., 1987 (·····) and experimental data of Kreplin and Eckelmann (o, +, Δ). Law of the wall shown by (- - - -) lines

(a)



(b)



(c)

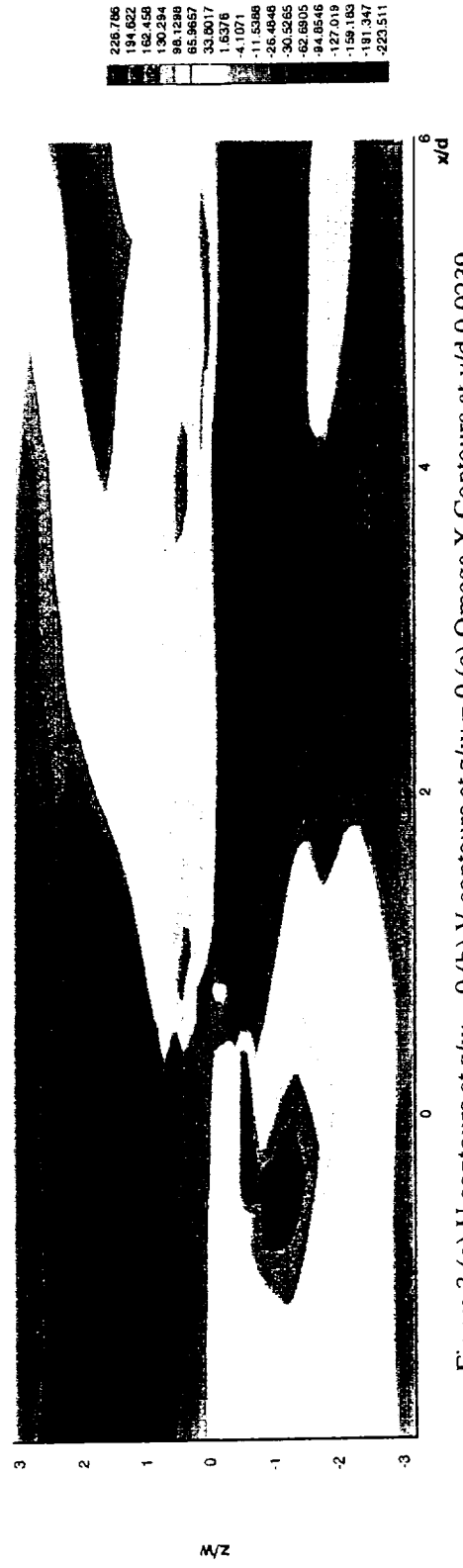


Figure 3 (a) U contours at  $z/w = 0$  (b) V contours at  $z/w = 0$  (c) Omega X contours at  $y/d = 0.0239$

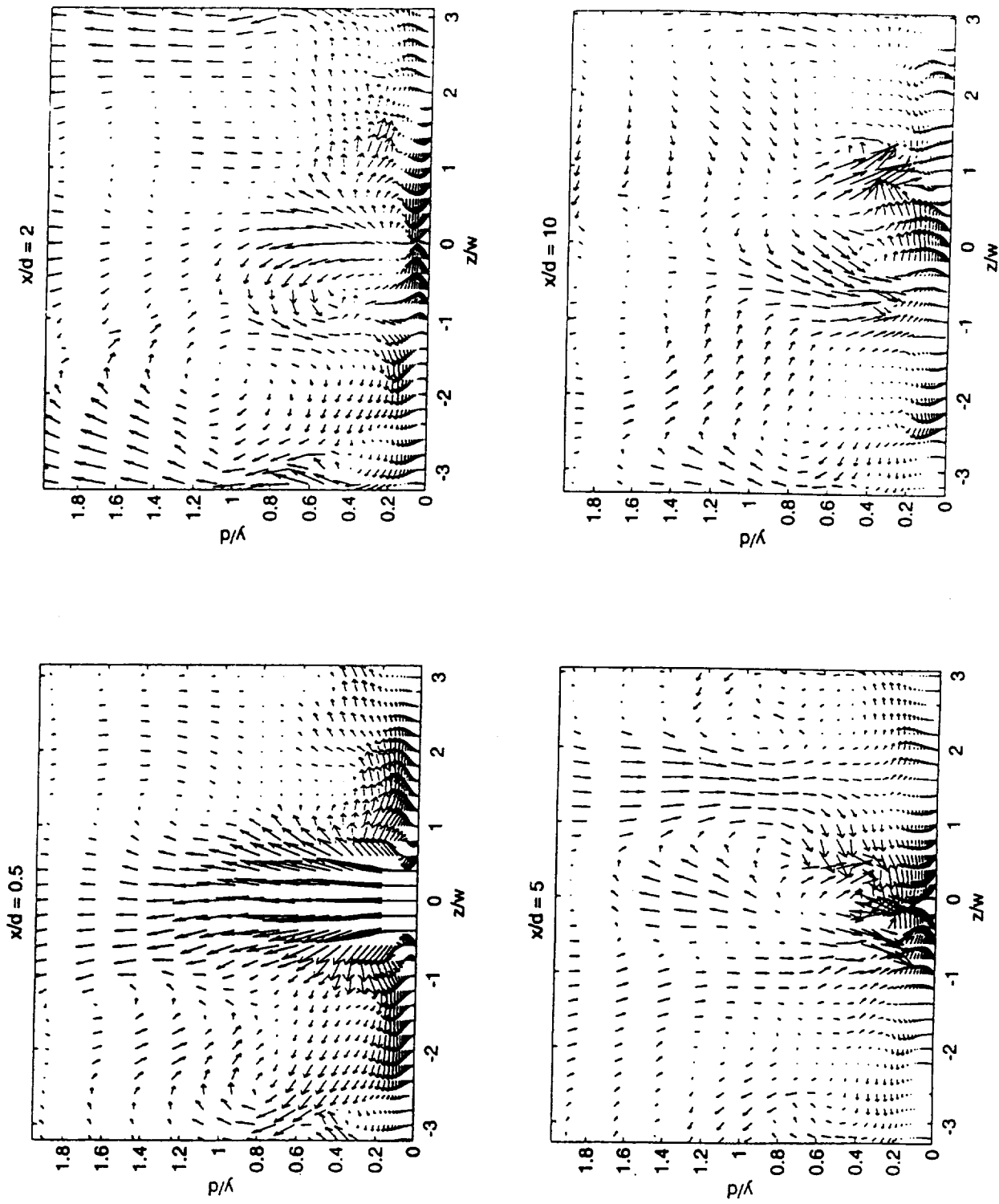


Figure 4 Instantaneous velocity vectors in the cross stream planes

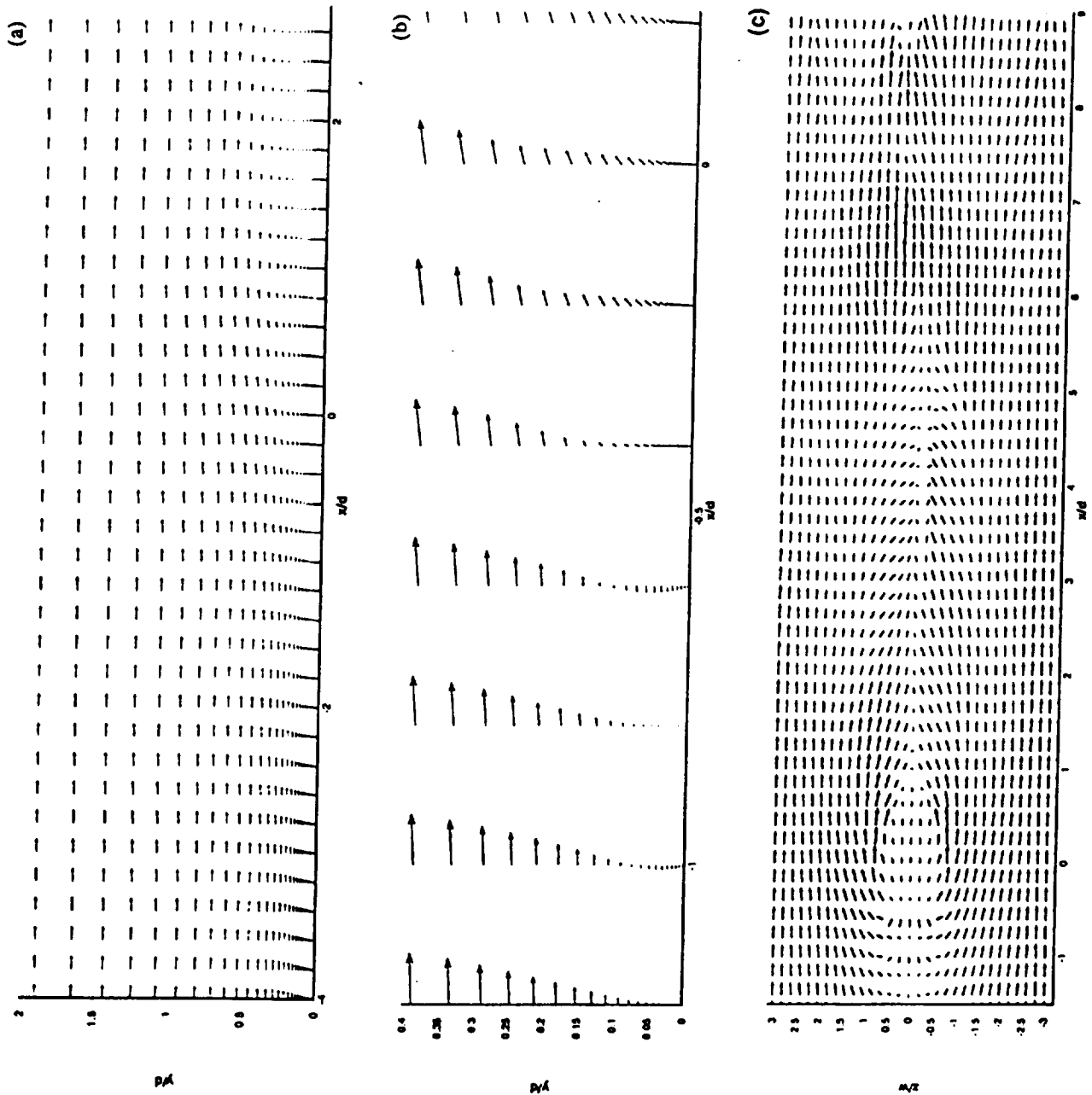


Figure 5 Instantaneous velocity vectors at (a)  $z/w = 0$  (b) Near wall details (c)  $y/d = 0.0239$

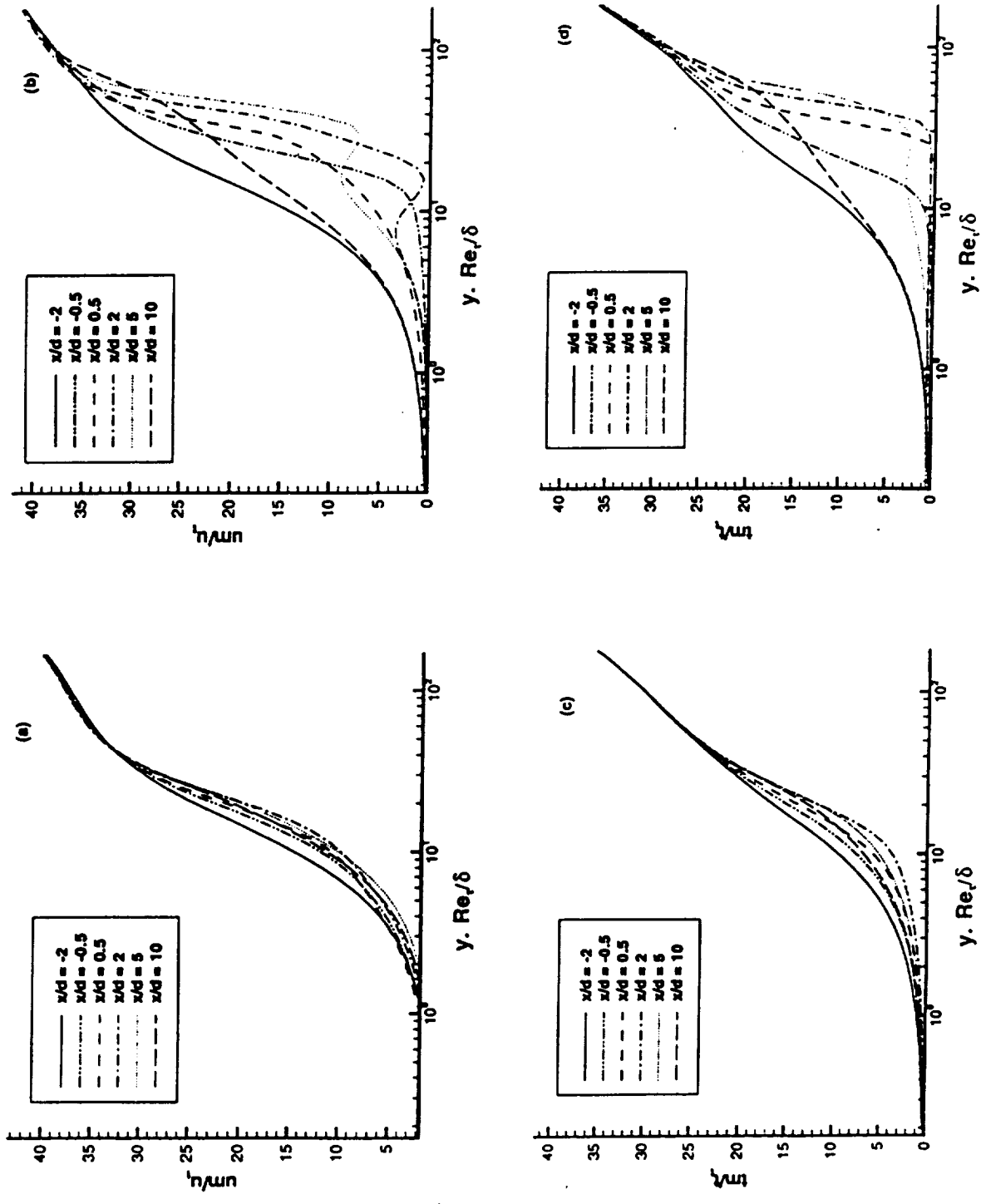


Figure 6 U mean profiles at (a)  $z/w = -1.9$  (b)  $z/w = 0$  (c)  $z/w = -1.9$  (d)  $z/w = 0$

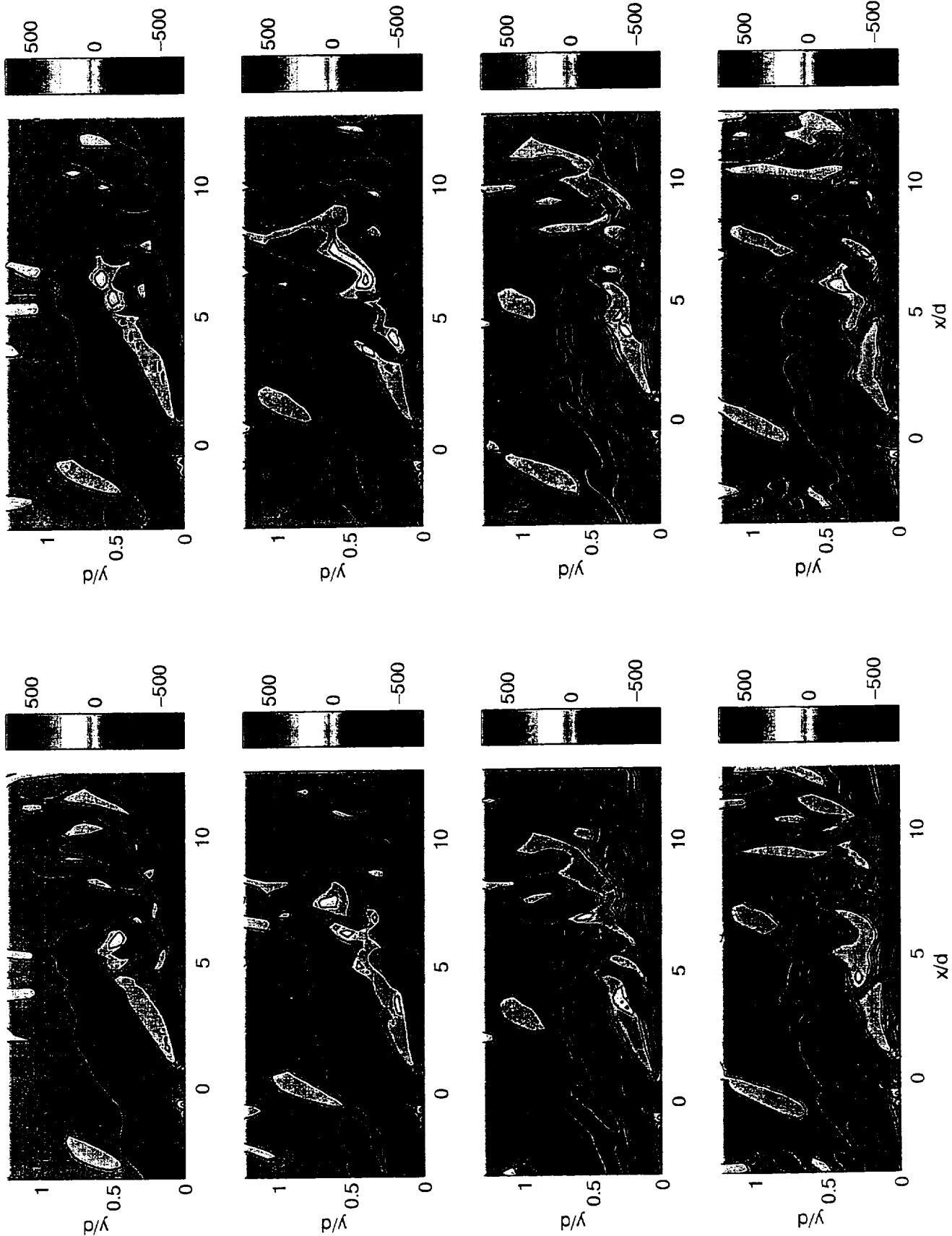


Figure 7  $\omega_7$  contours at  $z/w = 0$ ;  $\Delta t = 0.02$  units

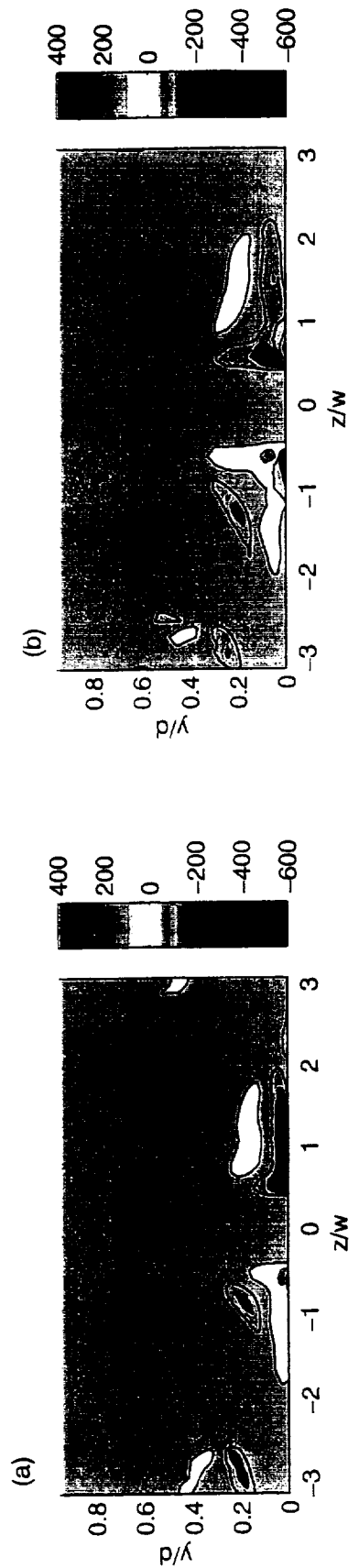


Figure 8  $\omega_x$  contours at (a)  $x/d = -0.5$  (b)  $x/d = 0.5$

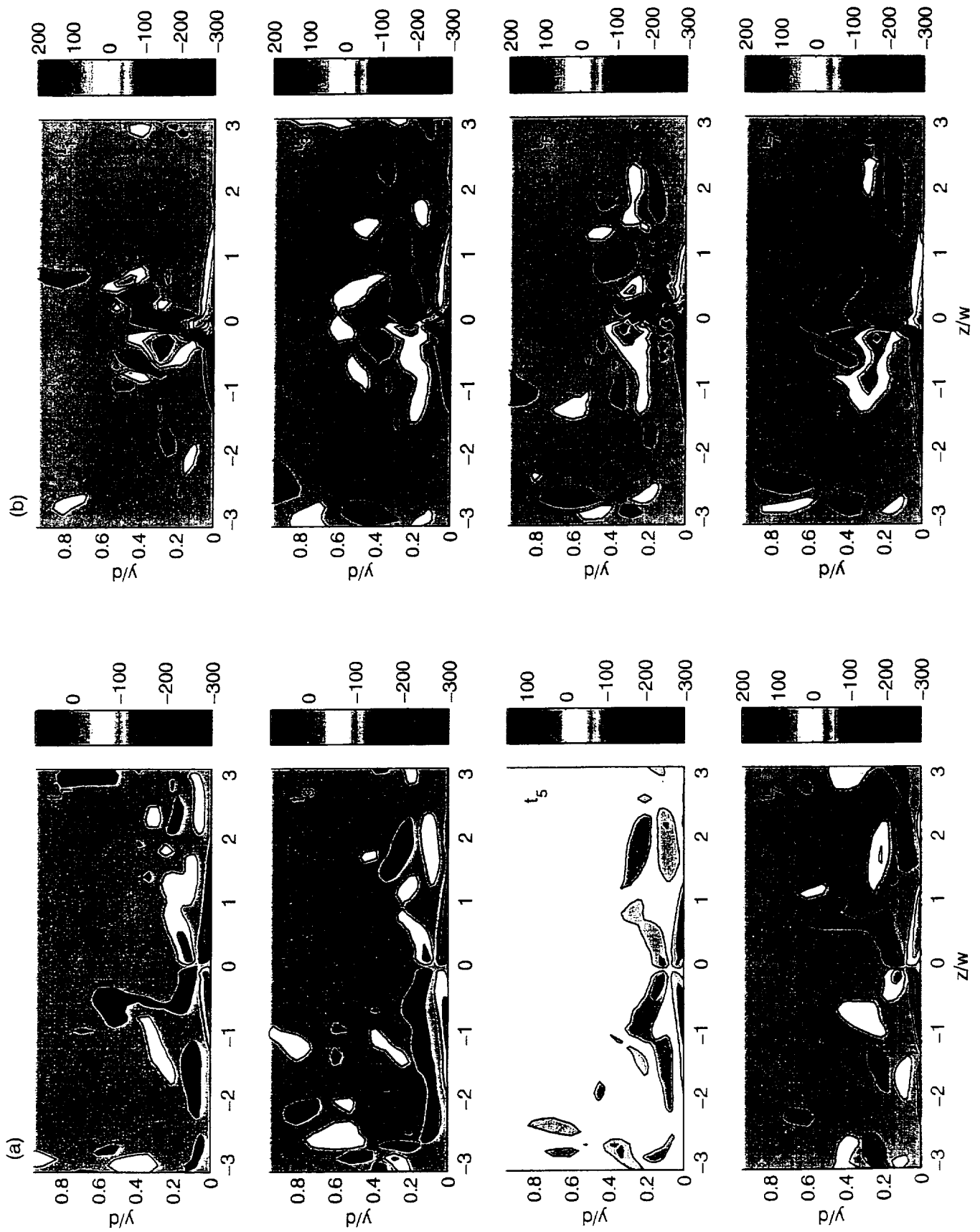


Figure 9  $\omega_x$  contours at (a)  $x/d = 2$  (b)  $x/d = 5$ ;  $\Delta t = 0.02$  units

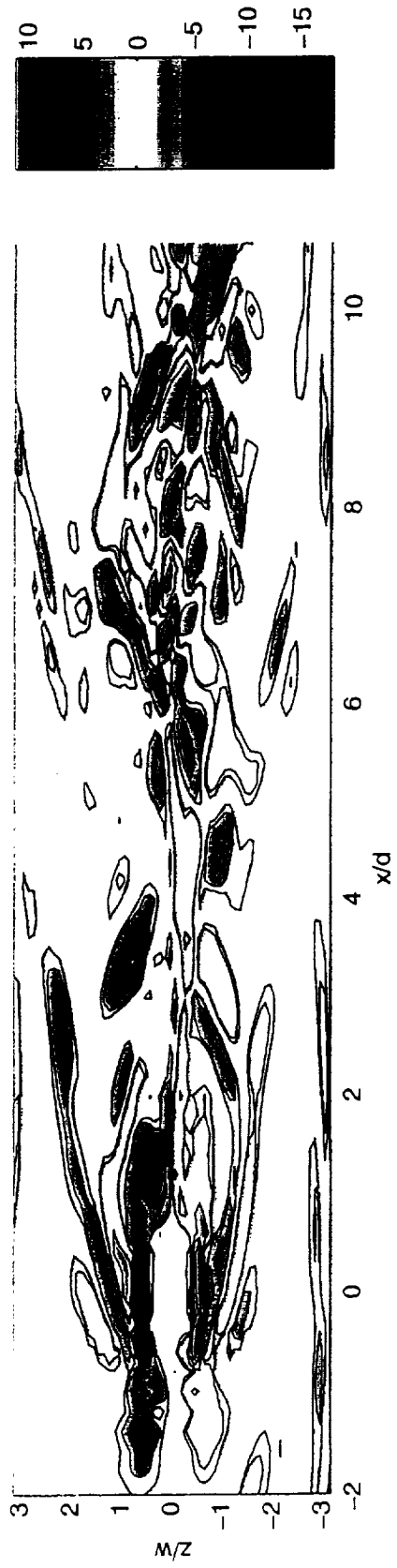


Figure 10  $\omega_y$  contours at (a)  $y/d = 0.002$

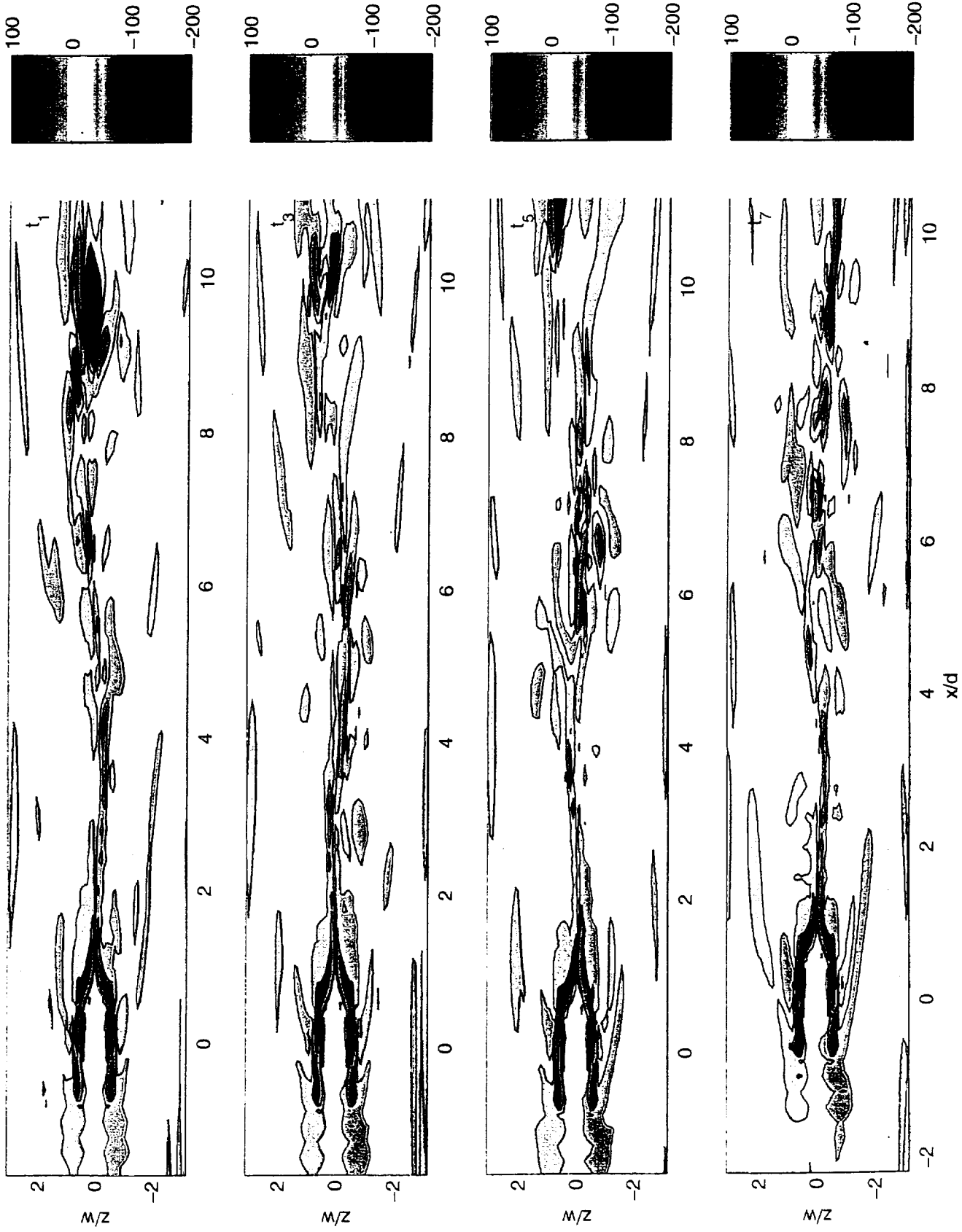


Figure 11  $\omega_z$  contours at  $y/d = 0.239$ ;  $\Delta t = 0.02$  units

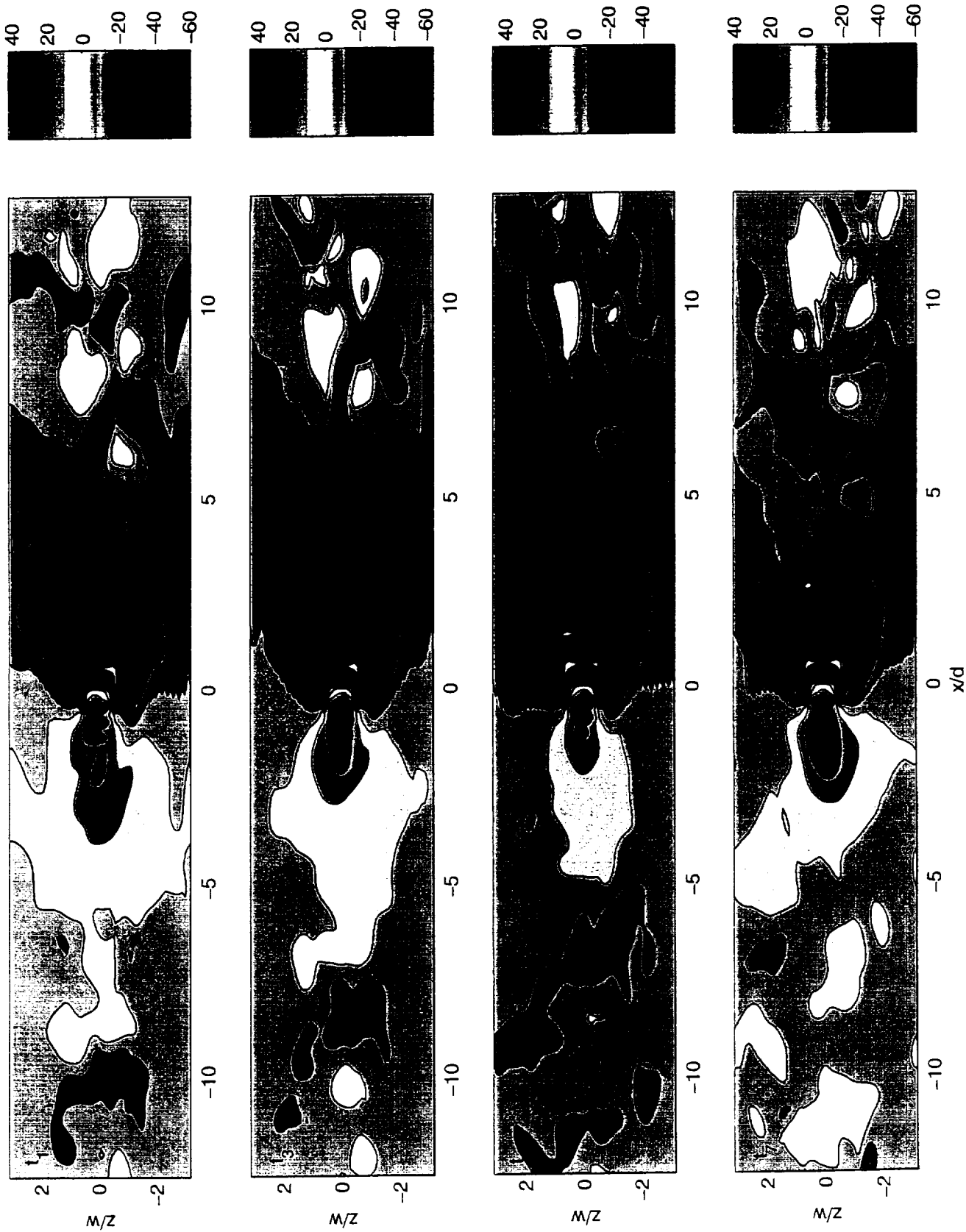


Figure 12 Pressure contours at  $v/d = 0.0239$ ;  $\Delta t = 0.02$  units

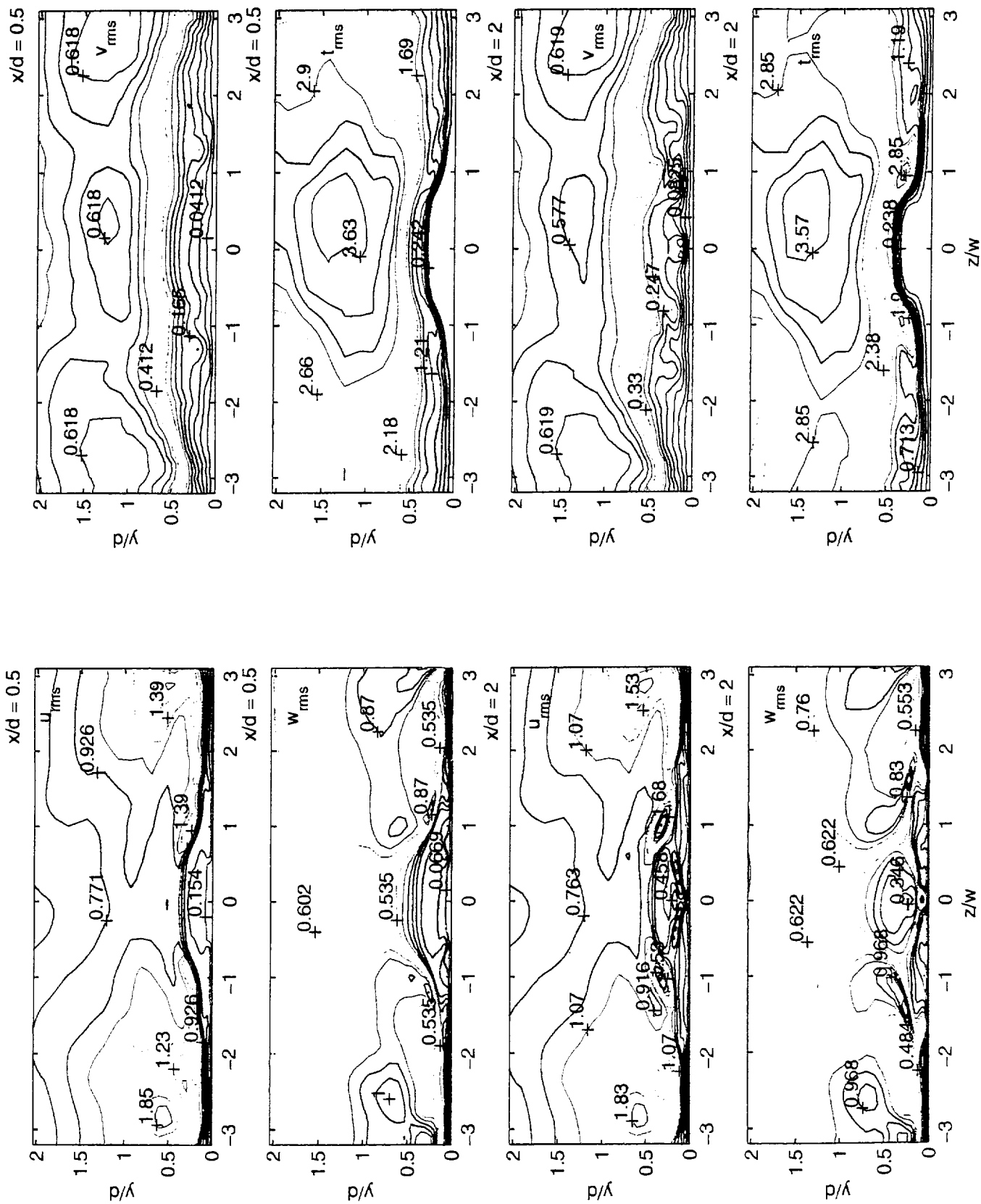


Figure 13 rms contours at  $x/d = 0.5$  and 2

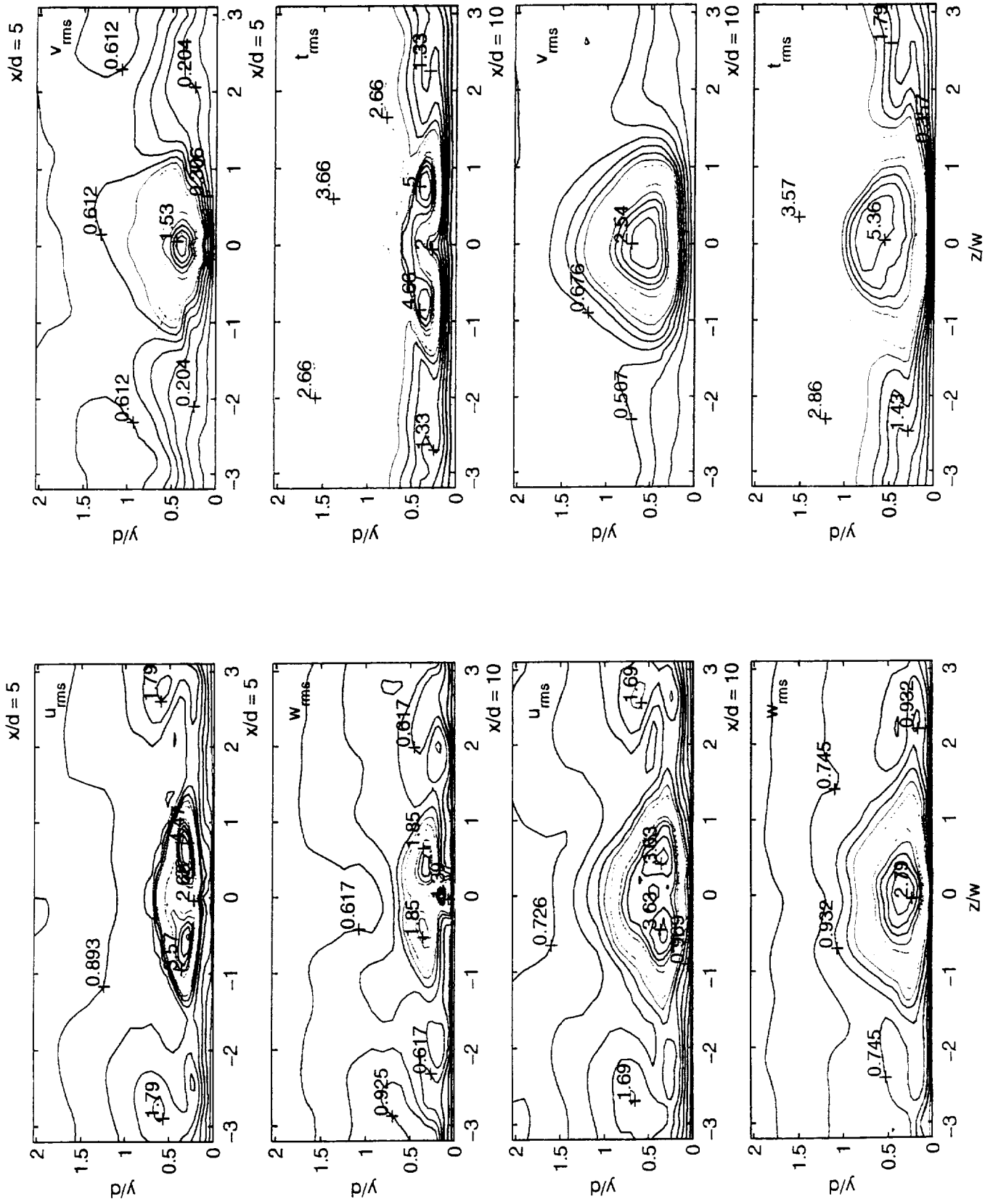


Figure 14 rms contours at  $x/d = 5$  and 10

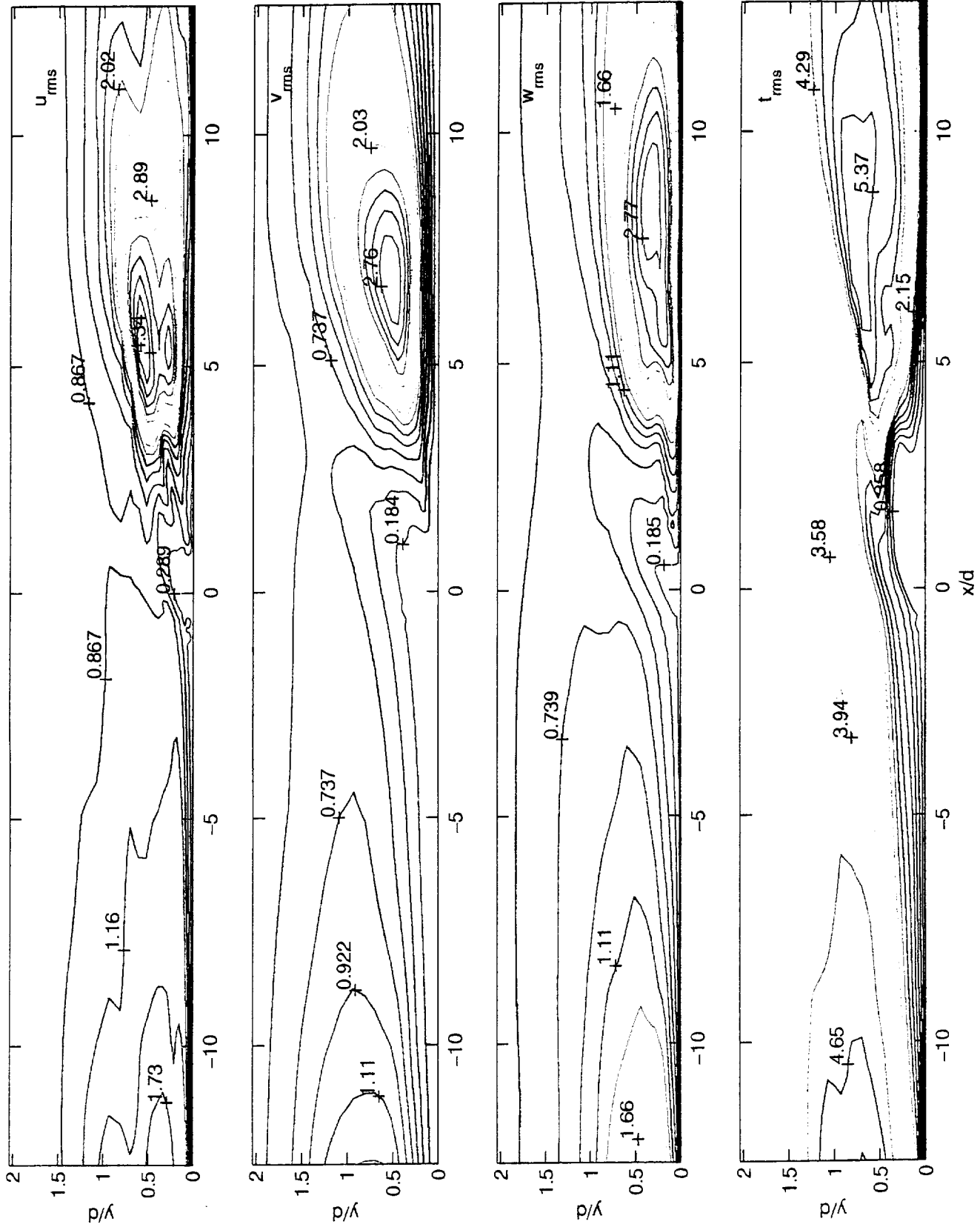


Figure 15 rms contours at  $z/w = 0$

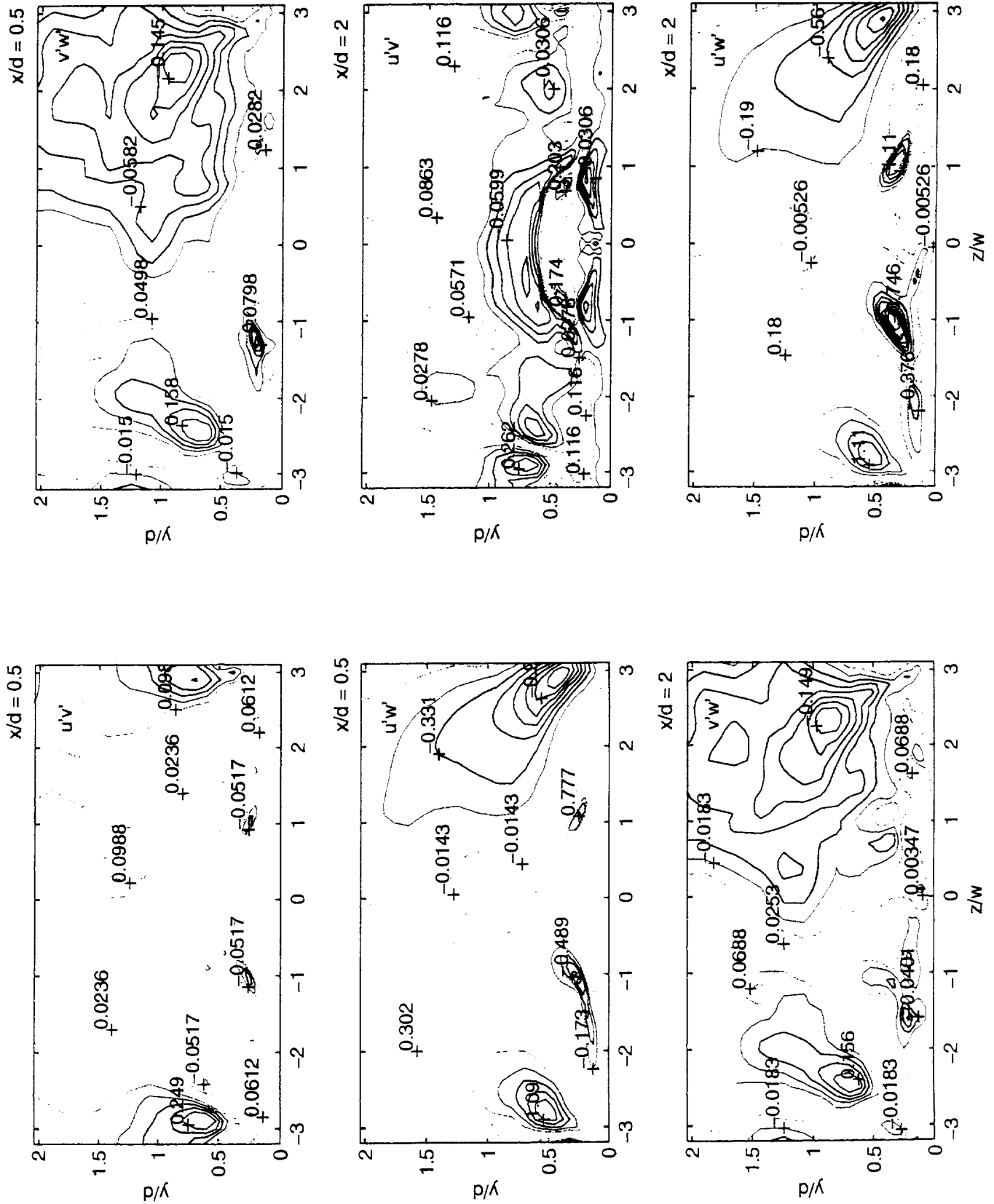


Figure 16 shear stress contours at  $x/d = 0.5$  and 2



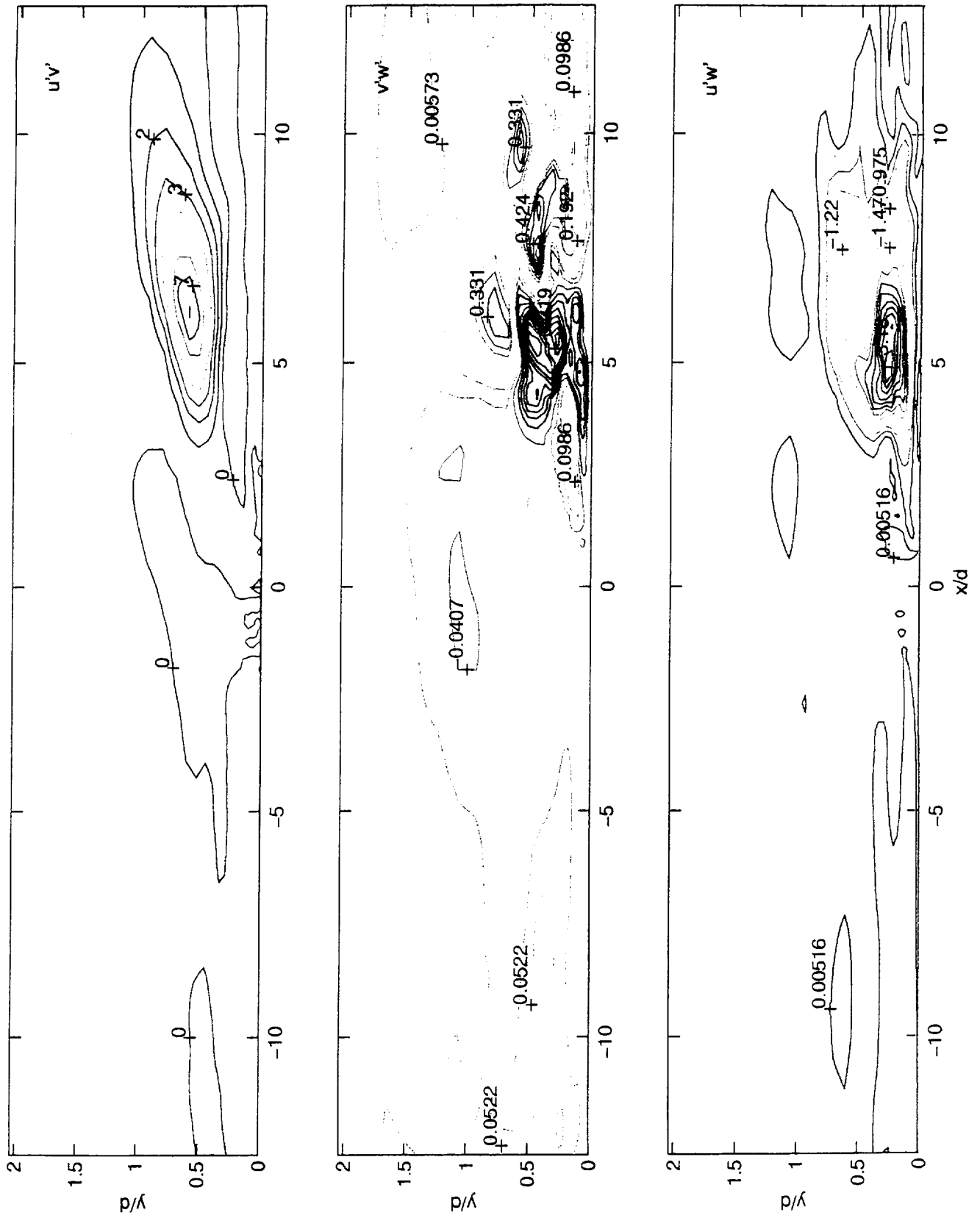


Figure 18 shear stress contours at  $z/w = 0$

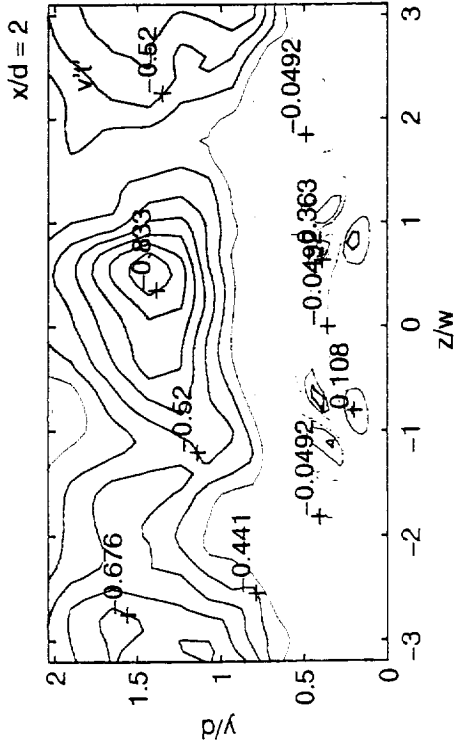
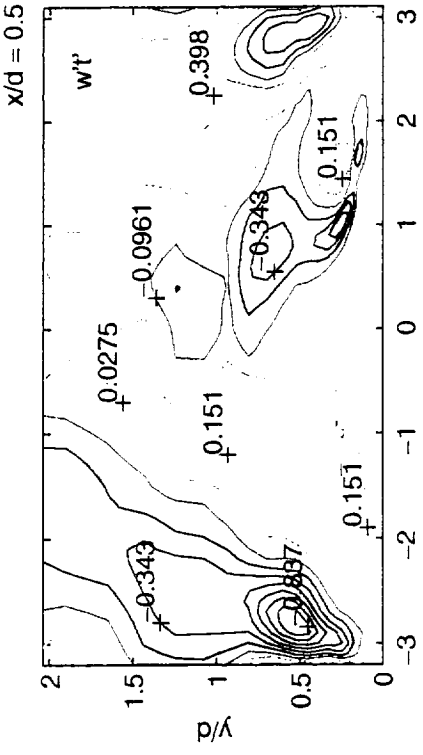
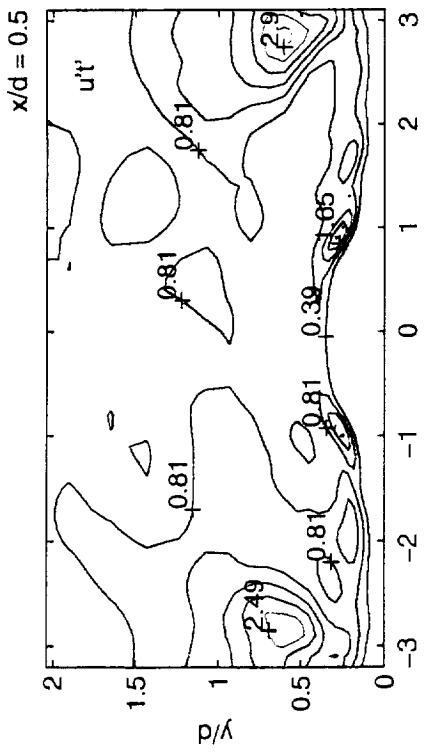
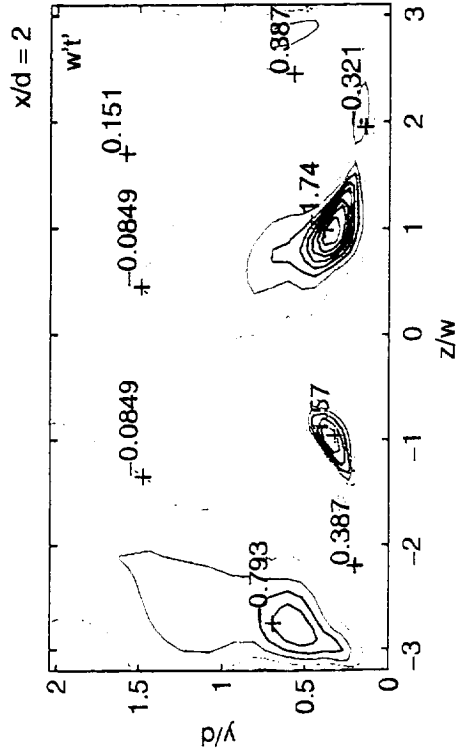
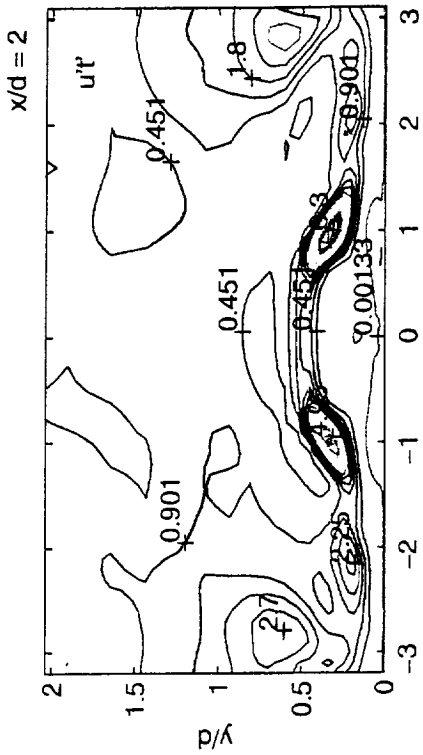
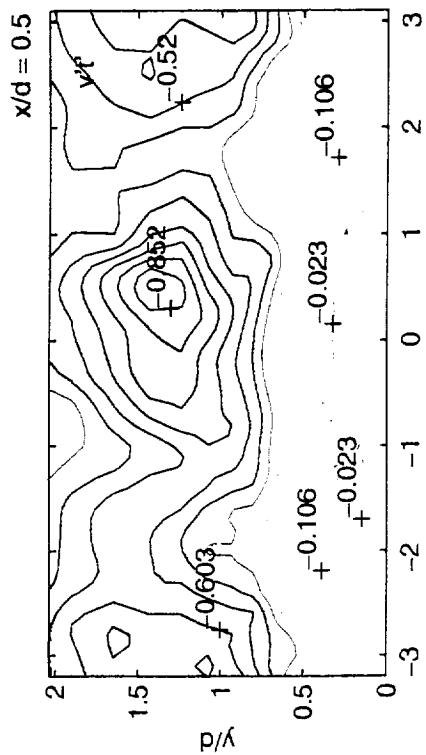


Figure 19 turbulent heat flux contours at  $x/d = 0.5$  and 2

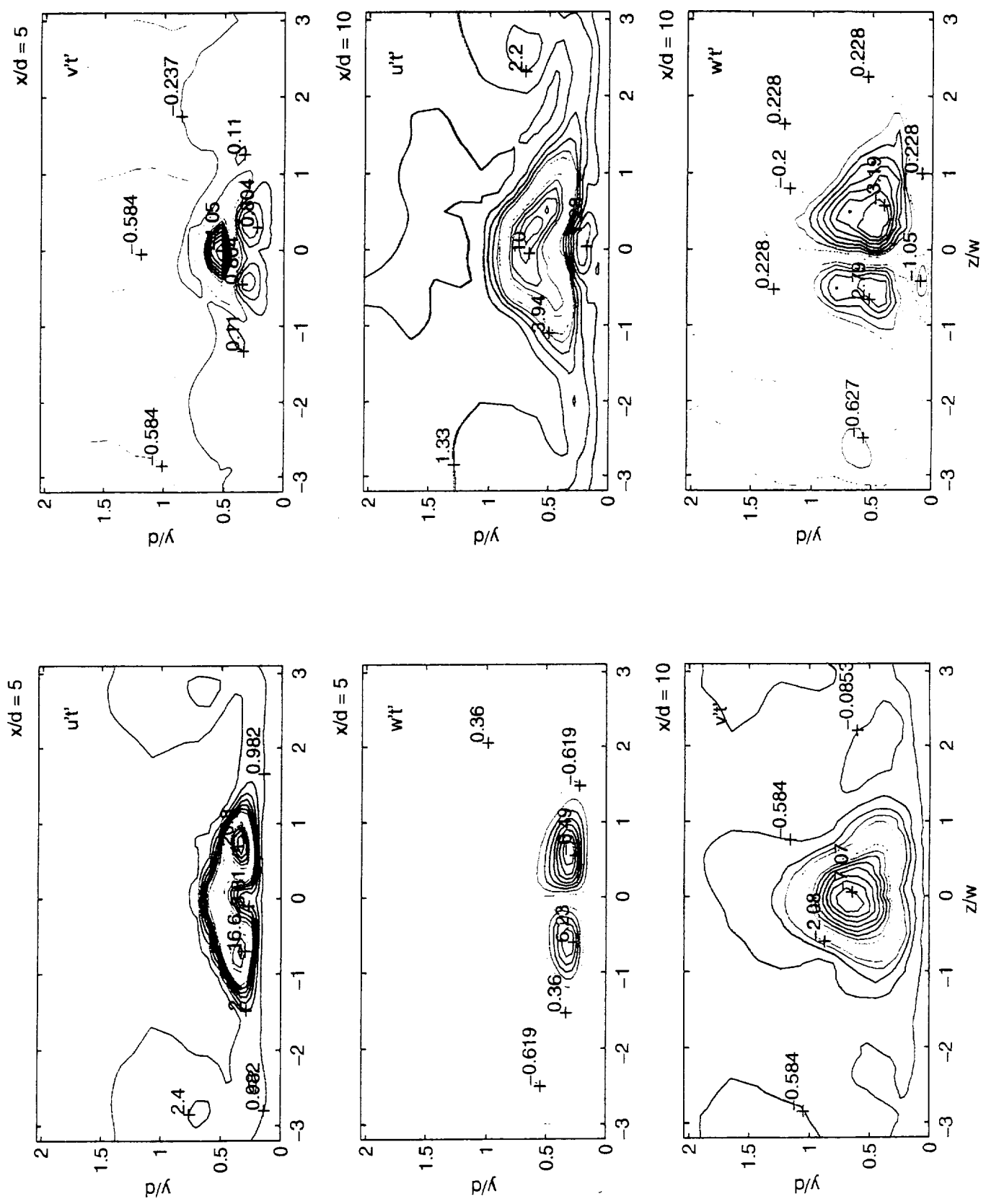


Figure 20 turbulent heat flux contours at  $x/d = 5$  and 10

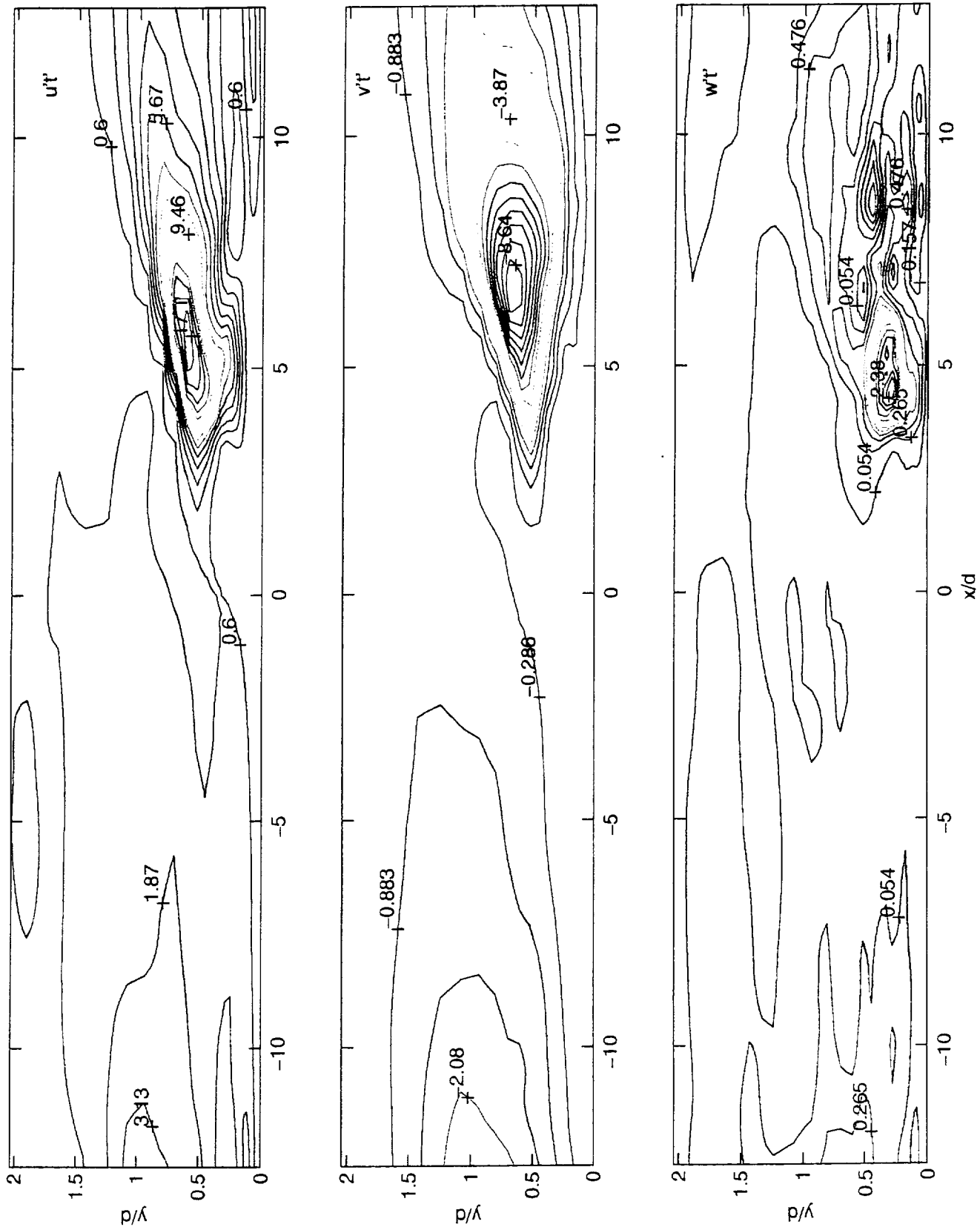


Figure 21 turbulent heat flux contours at  $z/w = 0$

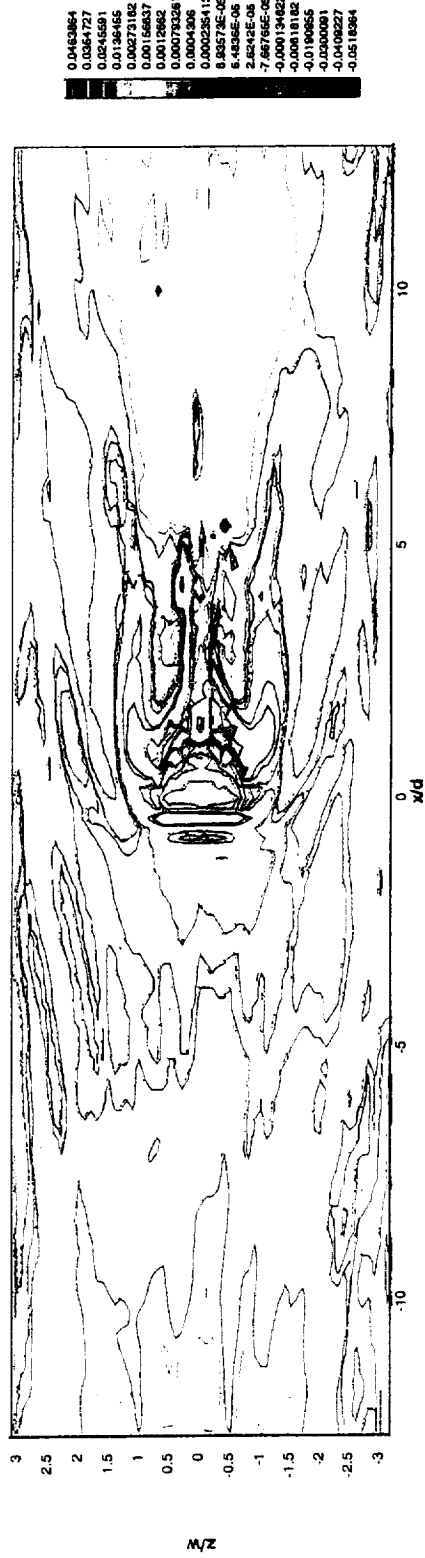


Figure 22 Turbulent viscosity factor (12) at  $y/d = 0.1085$

## CHAPTER V

### LARGE EDDY SIMULATION (LES) OF NORMAL FILM COOLING JETS IN CROSSFLOW: FREESTREAM TURBULENCE EFFECTS

#### ABSTRACT

The dispersion of film coolant jets in crossflow depends on a complex interaction between the jets and the mainstream. Large eddy simulations of square jets in crossflow are performed in this chapter to study the effects of free-stream turbulence levels on the dispersion of the coolant jets. Free-stream turbulence is characterized here by small scale grid generated turbulence. The effects of free-stream turbulence intensity levels of 5% and 15% are studied for jet to crossflow blowing ratio of 0.5 at a jet Reynolds number of 4700.

With high levels of small scale free-stream turbulence, strong intermittent flow structures generated at the jet-mainstream interface disperse the jet by moving surrounding fluid into the jet core, and ejecting the jet fluid into the mainstream. Greater jet penetration and jet-mainstream mixing is observed for higher turbulence levels. The lateral spread of the jet is also increased by the higher free-stream turbulence intensity.

#### NOMENCLATURE

Tu	Turbulence Intensity (%)
$V_{jet}$	Jet velocity
D	Dimension of square hole
R	Blowing ratio of jet to crossflow
X	Streamwise direction
Y	Normal (to wall) direction
Z	Spanwise direction
U	X-component of averaged velocity
V	Y-component of averaged velocity
W	Z-component of averaged velocity
$u'v', v'w', u'w'$	components of Reynolds stress tensor.

#### INTRODUCTION

The ever-increasing demand for higher specific thrust of a gas turbine engine has resulted in turbine inlet temperatures exceeding the turbine blade material limits. To increase the life of the turbine blades, one has to keep the temperature of the blades below their melting point using some sort of cooling strategy. Film cooling is a technique in which rows of coolant jets are injected into the hot crossflow gas stream. These jets are deflected and strained by the crossflow and provide coverage of the blade surface from the hot gases. The interaction of the coolant jets with the crossflow involves complex and unsteady structures like the horseshoe vortex, the counter rotating vortex pair (CVP) and wake vortices. These structures control the jet penetration and its spreading rate. The effectiveness of film cooling is governed by the rate at which the coolant jets mix with the hotter surrounding flow. Important factors that influence the effectiveness are free-stream turbulence intensity levels, jet to mainstream momentum ratio and hole aspect ratio. The objective of this work is to study the effect of free-stream turbulence intensity on the various flow structures. The free-stream turbulence is characterized, in this

chapter, as an isotropic homogeneous grid generated turbulence. Hence, a Gaussian distribution can be used to approximate the fluctuation (Batchelor, 1953). The role of the various components of the Reynolds stress tensor in controlling the spreading and mixing of the jet with the mainstream and their dependence on free-stream turbulence intensity levels is studied in this chapter. Two freestream levels are studied: a low freestream turbulence level of 2% and a relatively high freestream level of 15%.

In order to reliably predict the jet-in-crossflow situation, the large scales have to be predicted accurately and the dynamics and interactions of small scales must be modeled realistically. This requirement calls for large eddy simulations (LES) of the jet-in-crossflow configuration.

## COMPUTATIONAL METHOD

The unsteady three dimensional Navier Stokes equations are solved using the projection method (Chorin, 1967). This is a fractional step approach in which an intermediate velocity field is calculated by neglecting the pressure gradients, and the pressure field is obtained as a solution to a Poisson equation derived using the continuity equation. This pressure field is used to update the velocity in the projection step. The temporal discretization is done using a second-order accurate Adams-Bashforth scheme. The calculation of the convective terms is done by a conservative formulation. A fourth order accurate finite difference scheme is used for these terms. The viscous dissipation terms are discretized using a fourth order accurate central difference scheme.

In LES, the governing equations are obtained by applying a filtering operation on the Navier-Stokes equations and the continuity equation. The filter function is represented as the convolution operator (Ghosal and Moin, 1995). The unfiltered fields give rise to subgrid scale stresses that require modeling. Following the dynamic mixed method of Zang et al (1993), these stresses are decomposed into a resolvable part and an unresolvable part. The resolved part is the Galilean invariant form of Bardina's (1983) scale similarity model (Speziale, 1985). The dynamic Smagorinsky model is used for the unresolved part of the stress and the dynamic coefficient is test filtered to avoid numerical instabilities.

The issue of filtering is very important for such numerically accurate simulations. On a non-uniform grid the filtering operator becomes a function of spatial location and hence gives rise to commutation error leading to low order of accuracy even with very high order accurate schemes (Ghosal and Moin, 1995). The issue of dependence of dynamic coefficient on aspect ratio of the grid cells when using grid based filters needs to be addressed on such non-uniform grids (Scotti et al, 1997). These issues are evaded here by using uniform grids with isotropic aspect ratio. In particular, the flow contains structures in almost all parts of the computational domain and hence, all parts of the domain need to be resolved with equal importance. For several reasons top hat filter is used (Zhou et al, 1989). It is easy to implement in a finite difference code. It has compact support, unlike Gaussian or exponential filters which violate this requirement for grid-based filtering. It is a positive or realizable filter i.e. if it filters a non-negative field, the filtered field is always non-negative.

## PROBLEM DESCRIPTION

A uniform Cartesian grid of  $122 \times 52 \times 32$  points is used for a domain of  $12D \times 5D \times 3D$  (Figure 1). At the inflow, a fully developed turbulent boundary layer profile is prescribed and a small scale turbulence field is superimposed on it. Box-Muller method is used to generate the

Gaussian distribution for the perturbation fields. The velocity field is specified at the jet inlet from the experiments of Ajersch et al (1995). The Reynolds number based on the jet velocity and the hole dimension is 4700. In the spanwise direction, the periodic boundary condition is applied. The domain size is taken such that free-stream conditions at the inlet can be used as the top plane boundary conditions. At the outflow, a convective boundary condition is used where the wave speed is determined from a flux balance.

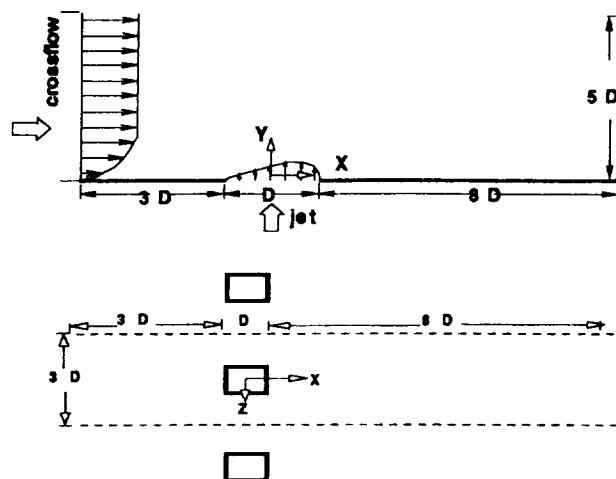


Figure 1 Schematic of the computational domain.

## RESULTS

Results are presented for two different turbulence intensity levels at various planes of the computational domain. The X- component of mean velocity and normal Reynolds stress are plotted in Figure 2 at streamwise locations  $X/D = 1.0, 3.0, 5.0$  in the jet center plane i.e.  $Z/D=0$ . For the mean velocity profiles, a good agreement is obtained between the experimental data of Ajersch et al (1995) and the computed results. The predicted magnitude of  $u'^2$  for the 2% and 15% Tu cases are different in the wake region and the freestream region, but do not show significant differences in the jet-region. This implies that in the jet-region turbulence levels are primarily controlled by the gradient-production of turbulence, and diffusion or convection of freestream turbulence is not significant. However, in the wake region, the higher turbulence levels for the 15%Tu case implies that associated with the crossflow entrainment into the wake region there is significant convection and diffusion transport of the freestream turbulence. Similar results were reported by Bons et al (1996) who reported penetration of high freestream turbulence into the near wall region. The present simulations imply that the primary mechanism of the penetration of high freestream turbulence is the crossflow entrainment into the wake region. Bons et al. (1996) reported that the net effect of the greater near-wall freestream turbulence levels is a reduction in the film-cooling effectiveness.

The distribution of normal stresses  $u'^2$ ,  $v'^2$ , and  $w'^2$  is shown in Figures 3, 4 and 5 respectively. It is observed that the high freestream turbulence primarily affects the streamwise ( $u'^2$ ) and spanwise ( $w'^2$ ) turbulence intensity, while the vertical intensity ( $v'^2$ ) is rapidly damped by the wall, and no significant influence of Tu can be seen on the  $v'^2$  contours. For the 15%Tu case, the streamwise intensity levels are higher in the near-wake region, as already noted in Figure 2, while the spanwise intensity levels are much higher downstream of an  $X/D$  of 1.5

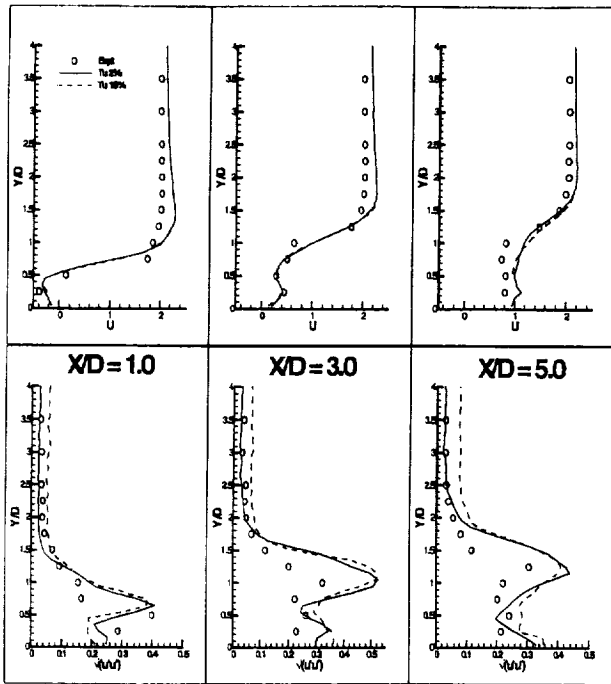


Figure 2: Mean velocity  $U$  and normal stress  $(u'^2)^{1/2}$  at the jet center plane ( $Z/D = 0$ )

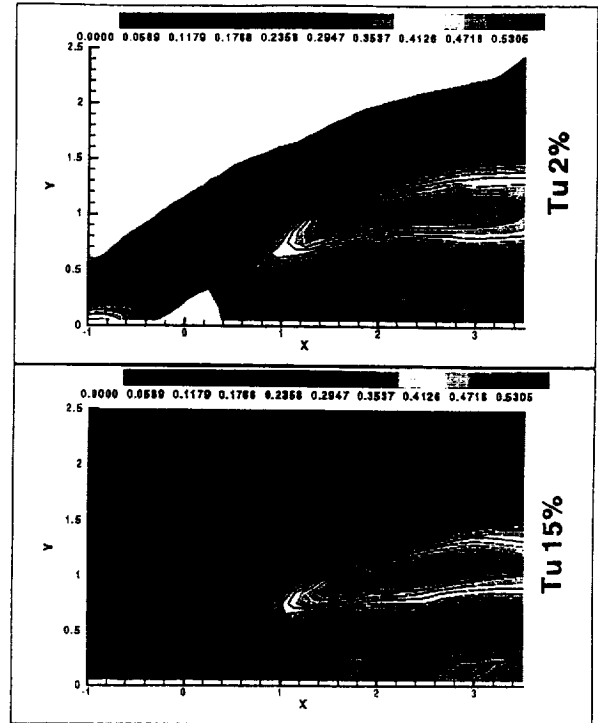


Figure 3: Streamwise normal intensity  $(u'^2)$  contours at the jet centerplane ( $Z/D=0$ )

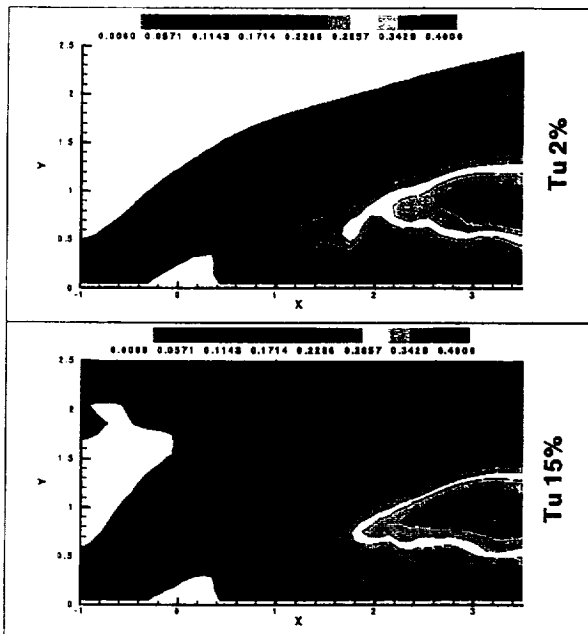


Figure 4: Vertical normal intensity contours  $(v'^2)$  along the jet centerplane ( $Z/D=0$ )

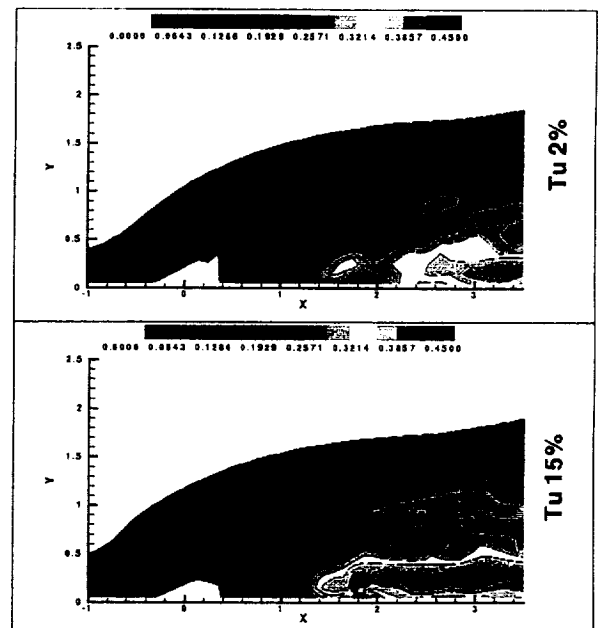


Figure 5: Spanwise normal intensity  $(w'^2)$  contours at the jet centerplane ( $Z/D=0$ )

Presence of high levels of normal stresses in a flow field having large mean velocity gradients will lead to increased production of the Reynolds shear stresses as shown in Figs. 7, 9, and 10 later. Further, the higher energy is re-distributed through non-linear mechanisms among the various components of stress tensor as well as scales of the flow field.

The time-averaged vorticity contours ( $\omega_x$ ) and velocity vectors are shown in Figure 6 at  $X/D = 3.0$ . The contours of the turbulent stress  $v'w'$  are presented at the same location in Figure 7. The CVP is an unsteady coherent structure and hence, time-averaged values, obtained after averaging over six flow-through periods, are shown to depict this organized coherent structure. The horseshoe vortex is also observed on the two sides of the CVP, and is associated with lower levels of  $\omega_x$  in the opposite sense of CVP. Figure 6 shows that the CVP is stronger and more organized in the lower turbulence intensity case where the highest vorticity contours occupy a larger fraction of the CVP core. The velocity vectors also indicate lower magnitudes of the secondary velocities ( $V$  and  $W$ ) along  $Z/D=0$  in the high turbulence intensity case.

In comparing the  $v'w'$  turbulent stress levels at 2% Tu and 15% Tu, it is observed that in the higher Tu case, the stress contours are more uniform and show greater lateral spread. This implies that the jet experiences greater lateral mixing with the crossflow in the presence of higher freestream turbulence intensity. The greater lateral mixing with the crossflow leads to a less coherent CVP as observed in Figure 6. The horseshoe vortex also weakens at higher Tu due to the greater lateral mixing in this case.

It can also be noted from Figure 7 that increasing the turbulence levels does not change the structure of the primary coherent structures (the CVP and the horseshoe), but it does affect the spread of the structures as well as the magnitudes of the stresses. The stresses attain their maximum value at the edges of CVP. The sign of these stresses are such that they oppose the CVP motion both along the upper and lower edges of the jet. Along the upper edges, a strong downward motion is induced by the CVP, and this is opposed by the positive stresses on the upper-right-half plane and negative stresses on the upper-left-half plane. Along the lower edges, a strong inward motion is induced by the CVP and is opposed by the negative stresses on the lower-right-half plane and positive stresses on the lower-left-half plane.

The vertical gradient of spanwise component of velocity is negative in near wall region below the CVP and is positive in the upper region of the CVP. In the gradient-approximation, the dominant production term for  $v'w'$  is proportional to the negative of this gradient, and therefore the observed distribution and signs of  $v'w'$  provides some support to the use of the gradient approximation for modeling  $v'w'$ .

The vorticity contour component normal to the surface  $\omega_y$  is shown in Figure 8 at a location  $Y/D = 0.1$  from the wall. Significant entrainment of the crossflow into the wake region is evident, and the footprints of the coherent wake vortices (Fric and Roshko, 1994) can be clearly seen in the figure. The larger excursion of the wake vortices in the lateral direction at the higher turbulence level (Figure 8) is representative of the greater lateral spreading of the jet.

The contours of turbulent stress  $u'w'$  are presented at the same location in Figure 9. The  $u'w'$  stress levels are higher for the 15%Tu case, particularly downstream of 2 hole diameters from the jet exit. These higher near-wall stresses at the higher Tu levels are clearly linked to the higher  $w'^2$  fluctuations observed in Figure 5, and are associated with the higher freestream turbulence entrained into the wake from the crossflow. Andreopolous and Rodi (1984) have identified the importance of  $u'w'$  in determining the lateral spread, and the higher  $u'w'$  stress levels predicted for the higher Tu case are partly responsible for the greater lateral spreading of the jet at the higher turbulence intensity.

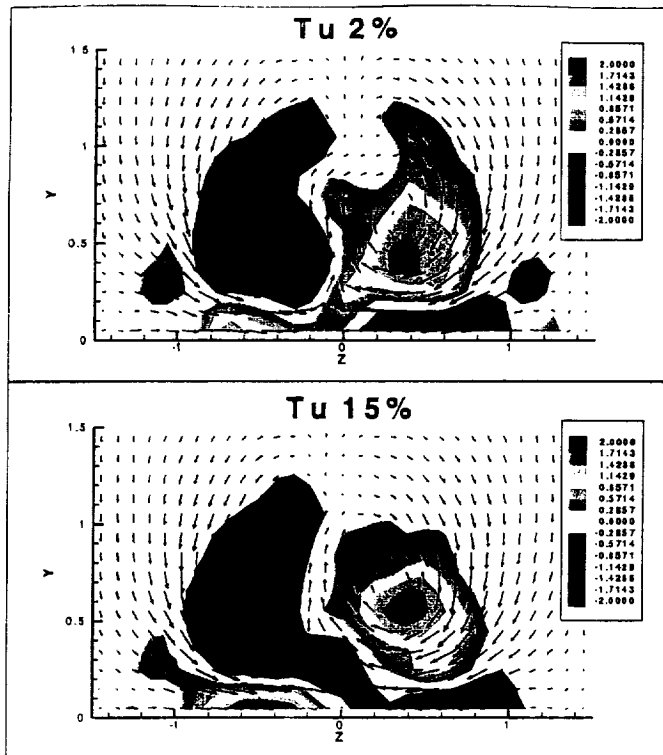


Figure 6 Contours of  $\omega_x$  and time averaged velocity vectors at  $X/D = 3.0$  for freestream turbulence intensity levels of 2% and 15%.

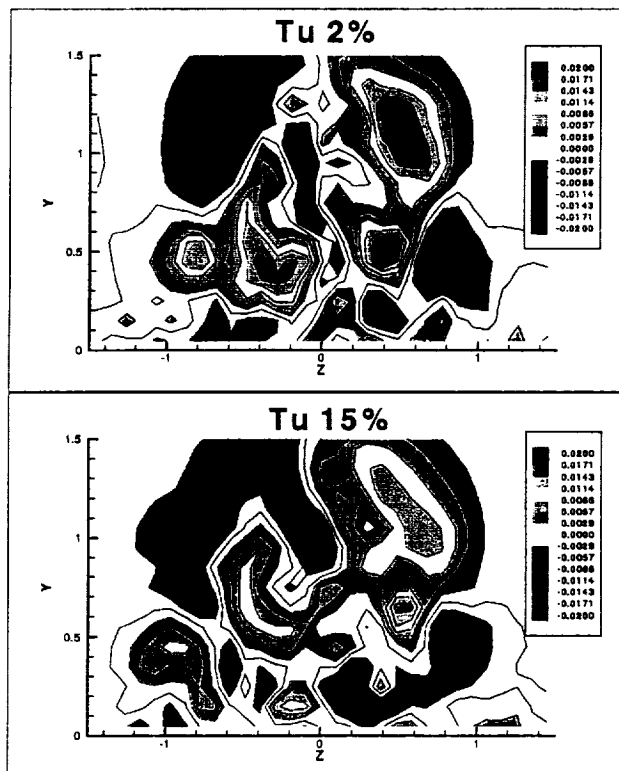


Figure 7 Contours of turbulent stress  $v'w'$  at  $X/D = 3.0$  for freestream turbulence intensity levels of 2% and 15%.

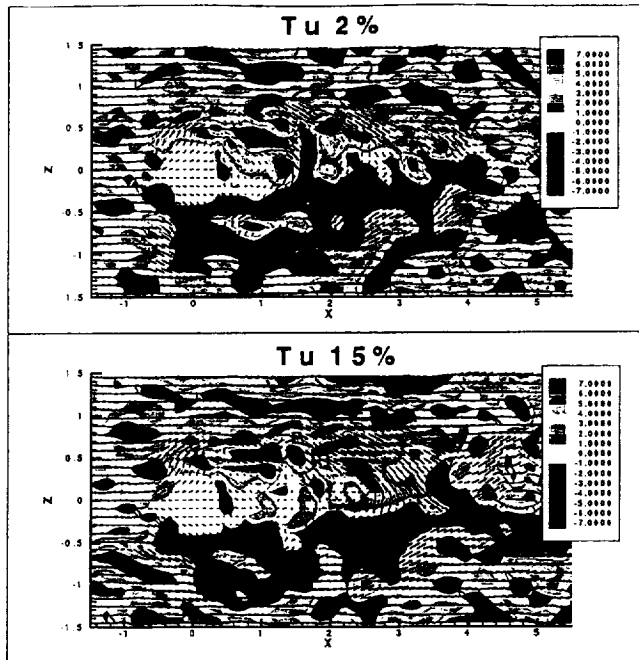


Figure 8 Contours of  $\omega_y$  and instantaneous velocity vectors at  $Y/D = 0.1$  for turbulence intensity levels of 2% and 15%.

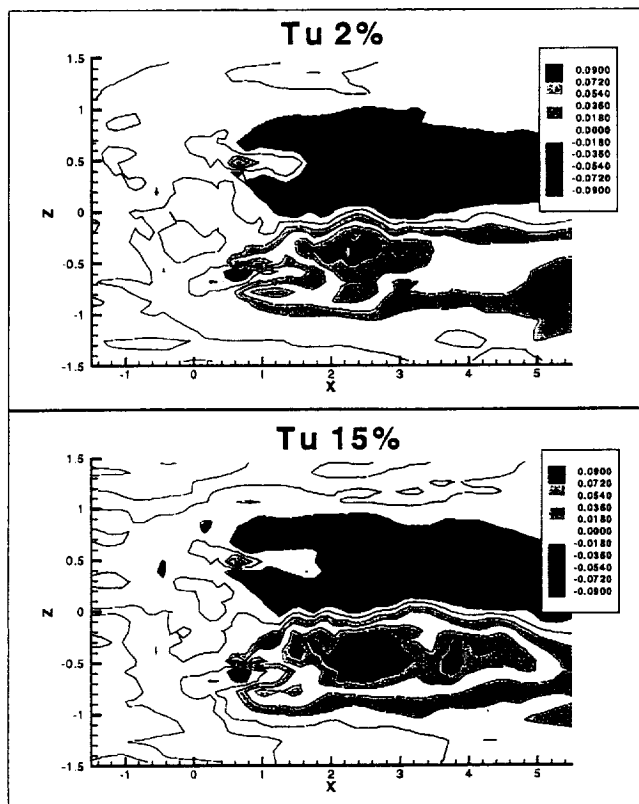


Figure 9 Contours of Reynolds stress  $u'w'$  at  $Y/D = 0.1$  for turbulence levels of 2% and 15%.

The production of  $u'w'$  stress appears to be primarily due to  $u'v'(\partial W/dY) + v'w'(\partial U/\partial Z)$ . Immediately after the jet exit, the presence of strong  $\partial U/\partial Z$  determines the local spreading of the jet around the hole. Along the edges of the jet on the leeward side of hole, we observe small regions of opposite signs for  $u'w'$  and these appear to

correlate with  $\partial U / \partial Z$ . Further downstream,  $u'w'$  appears to correlate best with  $\partial W / \partial Y$ , and does not show a strong correlation with  $\partial W / \partial X$ , which is not consistent with the gradient approximation. Thus the use of the gradient approximation to model  $u'w'$  may not be very appropriate.

The vorticity contours in the spanwise direction,  $\omega_z$  are shown in Figure 10 along the jet centerplane. Greater vortical activity and enhanced jet penetration is observed for the higher freestream turbulence intensity case. The presence of stronger freestream structures at higher turbulence intensity levels enhances the mixing at the jet-mainstream interface and hence increases the penetration of the jet much further into mainstream at downstream locations from the hole. A similar observation was made based on the PIV measurement of a jet (Gogineni et al, 1996). The vorticity generated at the jet interface on the leeward side and in the entrained crossflow boundary layer rolls up into spanwise structures. These structures are seen to have greater vorticity and are therefore more energetic for the higher Tu case. The extent to which these vortical structures penetrate into the mainstream can be used as the measure of mixing of jet with mainstream (Bons et al, 1996).

The contours of turbulent stress  $u'v'$  along the jet centerplane are presented in Figure 11. The contours of  $u'v'$  are mostly negative in the jet region and hence, the production of  $u'w'$  becomes positive in the regions where the vertical gradient of spanwise velocity is positive. This happens predominantly at downstream location of hole around the CVP. The greater production of  $u'w'$  at higher turbulence intensity levels was observed earlier in Figure 9. The negative levels of  $u'v'$  correspond to the mixing layer at the leeward side of jet. As the free-stream turbulence intensity is increased, the positive levels of  $u'v'$  are observed below the negative levels at downstream locations closer to the wall. The positive  $u'v'$  values observed in the wake of the jet correspond to the entrained crossflow boundary layer. Expectedly, these values are considerably higher for the higher Tu case. These higher  $u'v'$  values lead to greater mixing of the jet with the crossflow and can lead to lower effectiveness of the film cooling jet.

## CONCLUSION

Large eddy simulations of the jet-in-crossflow for two different free-stream turbulence intensity levels were performed. Only small-scale freestream turbulence with a Gaussian pdf is investigated. The results obtained are consistent with the experimental observations of various researchers (Andreopolous and Rodi, 1984, Ajersch et al, 1995, Gogineni et al, 1996). The role of turbulent stresses on jet penetration and lateral mixing is observed to be significant. Higher free-stream intensity is shown to lead to greater mixing between the jet and the mainstream both in the vertical and lateral directions.

Bons et al (1996) have reported that the integral length scales may play a significant role in effectiveness reduction. Hence, grid generated turbulence alone, would be inadequate to predict the effect of high Tu levels accurately. The effect of length scales and different Tu levels will be presented in the next chapter.

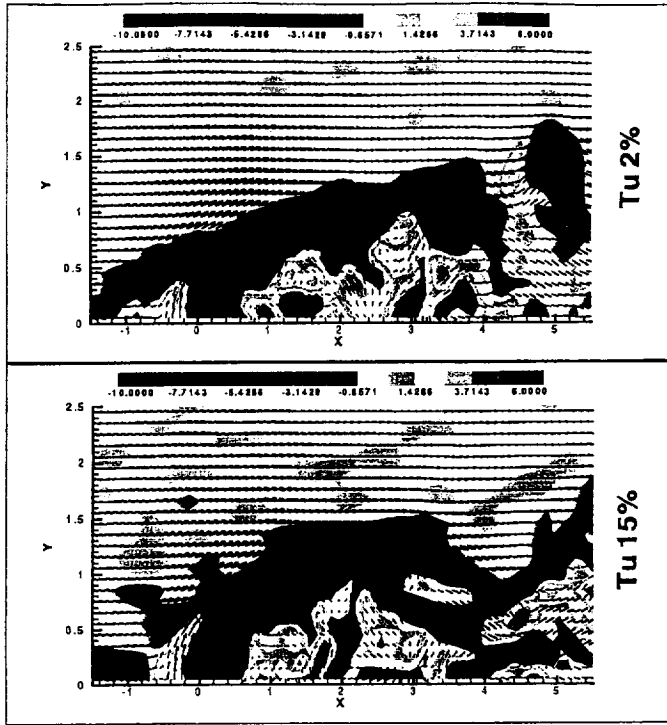


Figure 10 Contours of  $\omega_z$  and instantaneous velocity vectors at  $Z/D = 0.0$  for turbulence intensity levels of 2% and 15%

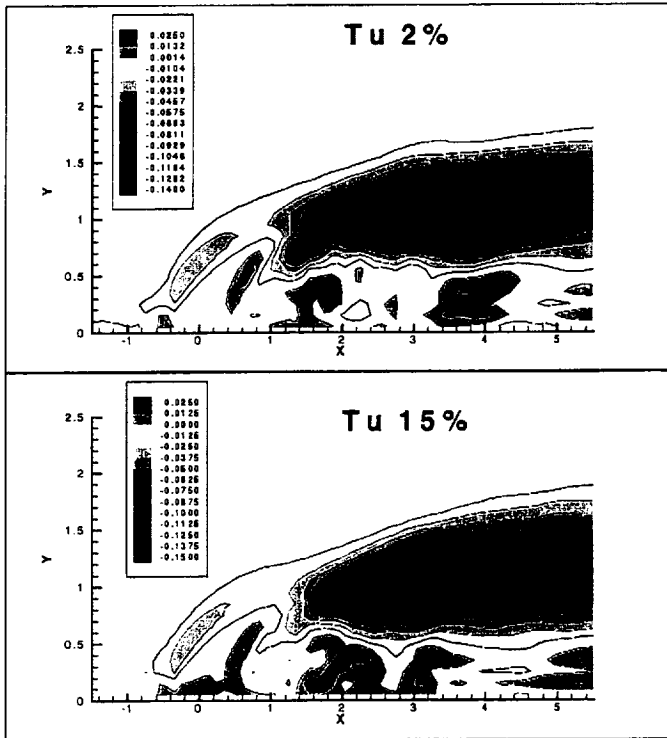


Figure 11 Contours of Reynolds stress  $u'v'$  at  $Z/D = 0.0$  for turbulence intensity levels of 2% and 15%.

## REFERENCES

- Ajersch, P., Zhou, J.M., Ketler, S., Salcudean, M. and Gartshore, I. A. (1995), *Multiple jets in a crossflow: detailed measurements and numerical simulations*, ASME 95-GT-9.
- Andreopoulos, J. and Rodi, W. (1984), *Experimental investigation of jets in a crossflow*. J. Fluid Mech., Vol. 138, pp. 93-127.
- Bardina, J, Ferziger, J.H. and Reynolds, W.C. (1983), *Improved turbulence models based on large eddy simulations of homogeneous, incompressible turbulent flows*, Report TF-19, Thermosciences Div., Dept. Mech. Eng., Stanford Univ.
- Batchelor, G.K. (1953), *Theory of homogeneous turbulence*, Cambridge University Press.
- Bons, J.P., MacArthur, C.D. and Rivir, R.B. (1996), *The effect of high free-stream turbulence on film cooling effectiveness*, Journal of turbomachinery, Vol. 118, pp. 814-825.
- Bons, J.P., Rivir, R.B., MacArthur, C.D. and Pestian, D.J. (1995), *The effect of unsteadiness on film cooling effectiveness*, AIAA 95-0306, 33<sup>rd</sup> Aerospace sciences meeting and exhibit
- Chorin, A.J. (1967), *A numerical method for solving incompressible viscous flow problems*, J. Comp. Phys., Vol. 2 pp. 12-26.
- Dubois, T., Jauberteau, F. and Temam, R. (1999), *Dynamic multilevel methods and the numerical simulation of turbulence*, Cambridge University Press.
- Fric, T.F. and Roshko, A. (1994), *Vortical structure in the wake of a transverse jet*. J. Fluid Mech., Vol. 279, pp.1-47.
- Ghosal, S. and Moin, P. (1995), *The basic equations for the large eddy simulations of the turbulent flows in complex geometry*, J. Comp. Phys., Vol. 118, pp.24-37.
- Gogineni, S.P., Rivir, R.B., Pestian, D.J. and Goss, L.P. (1996), *PIV Measurements of flat plate film cooling flows with high free stream turbulence*, AIAA 96-0617, 34<sup>th</sup> Aerospace sciences meeting and exhibit.
- Jordan, S.A. (1994), *Use of the large eddy simulation dynamic model for turbulent shear driven cavity flows*, ASME FED-Vol. 184 pp. 141-150.
- Kohli, A. and Bogard, D.G. (1997), *Effects of very high free-stream turbulence on the jet-mainstream interaction in a film cooling flow*, ASME 97-GT-121.
- Scotti, A., Meneveau, C. and Fatica, M. (1997), *Dynamic Smagorinsky model for anisotropic grids*. Phys. Fluids. Vol. 9 pp. 1856-1858.
- Speziale, C.G. (1985), *Galilean Invariance of subgrid scale stress models in large eddy simulation of turbulence*, J. Fluid Mech. Vol. 156, pp. 55-62.
- Zang, Y., Street, R.L. and Koseff, J.R. (1993), *A dynamic mixed subgrid scale model and its application to turbulent recirculating flows*, Phys. Fluids A Vol. 5 no. 12 pp. 3186-3196.
- Zhou, Y., Vahala, G. and Hossain, M. (1989), *A critical look at the use of filters in large eddy simulations*, Phys. Lett. A Vol. 139 no. 7 pp. 330-332.

## CHAPTER VI

# LARGE EDDY SIMULATIONS OF JETS IN CROSSFLOW: LARGE SCALE TURBULENCE EFFECTS

### ABSTRACT

Large eddy simulations of jets in crossflow are performed to study the effect of energy containing scales present in the freestream on the penetration and spread of the coolant jet. Two specific freestream turbulence conditions are examined, one corresponding to 15% small scale Gaussian turbulence, and the other corresponding to a 15% freestream turbulence that satisfies the Von-Karman spectrum and has its peak energy specified in the small wave number range (large scales). The small-scale freestream turbulence can be viewed to be similar to grid generated turbulence. The large scale freestream turbulence spectrum has energy peak at a small wave number (corresponding to a specified length scale taken to be 4 hole diameters in this study) and has energy in the inertial subrange for large wave numbers. In the present study, the jets are issued through a series of square holes into the main crossflow. The jet to crossflow blowing ratio is 0.5 and the jet Reynolds number is approximately 4,700.

Greater jet penetration and jet-mainstream mixing, in both the vertical and lateral directions, are observed for large-scale turbulence. The energy contained in large scales is mostly preserved although the energy carrying scales themselves undergo subsequent breakdown process due to the effect of the jet. In the nearfield of the jet, the large scales play a major role in enhancing the turbulent stresses, and the near wall transport. In the presence of the large scales, the horseshoe vortex is energized, and there is greater crossflow entrainment into the wake region. These large scale effects lead to significantly greater wall friction.

### NOMENCLATURE

$V_{jet}$	Jet velocity
D	Dimension of square hole
E	Energy spectrum (3-dimensional)
k	Wave number
R	Blowing ratio of jet velocity to crossflow velocity
Re	Reynolds number based on the jet velocity and hole diameter
X	Streamwise direction
Y	Normal (to wall) direction
Z	Spanwise direction
U	X-component of averaged velocity
V	Y-component of averaged velocity
W	Z-component of averaged velocity
$u_{rms}, v_{rms}, w_{rms}$	time-averaged velocity fluctuations for u, v, w
$u'v', v'w', u'w'$	components of shear stress tensor
$\Lambda$	Integral length scale

### INTRODUCTION

Film cooling of turbine blades, where rows of coolant jets are injected at an angle into the hot crossflow, is a commonly used technique to maintain the blade temperatures below a threshold value. The coolant jets are deflected and strained by the crossflow and provide coverage

of the blade surface from the hot gases. The interaction of the coolant jets with the crossflow involves complex and unsteady structures like the horseshoe vortex, the counter rotating vortex pair (CVP) and wake vortices. These structures control the jet penetration and its spreading rate.

The length scale of freestream turbulence is an important parameter that controls the development of the flow structures and the penetration and spreading of the jet. Typical turbulence intensities over a turbine blade can be quite high (15-20%); however, the majority of studies on film cooling have used low freestream turbulence levels (2-5%). Another important parameter of interest is the length scale of the freestream turbulence which has typically been represented in reported studies by grid generated turbulence. However, under realistic operating conditions, the blade experiences the flowfield emerging from the gas turbine combustor, and this flowfield is characterized by large coherent eddies and integral length scales that are 3-4 times the cooling hole diameter. Therefore, to accurately assess the behavior of the film cooling jet, the influence of freestream turbulence levels and length scales must be appropriately studied.

A number of studies have looked at the effect of freestream turbulence intensity and length scales on the vane heat transfer with and without film cooling (Kadotani and Goldstein, 1979a, 1979b; Ou et al., 1990; Bons et al., 1996; Kohli and Bogard, 1998a, 1998b; Ames, 1997a, 1997b; Radomsky and Thole, 1998). The general conclusion is that high freestream turbulence increases the mixing and surface heat transfer, and reduces the film cooling effectiveness. However, Bons et al. (1996) observed that an increase in film cooling effectiveness could be obtained with increasing turbulence levels in the region mid-way between the holes. A clear understanding of the various mechanisms involved is clearly not available due to the limited data, and additional measurements and computations are necessary. One drawback in the experiments reported has been the difficulty associated with the ability to simultaneously control the intensity levels and the length scales. Such control of intensity level and length scales can be more effectively provided in a time-and space accurate simulation, and forms the basis of the present study.

The objective of this study is to numerically study the effect of energy containing scales in the freestream on the various flow structures. Two different characterization of freestream scales are studied: (1) grid generated turbulence representing small-scale turbulence, and (2) turbulence that has Von Karman spectrum with a peak at low wave number representing large-scale turbulence. Small scale grid generated turbulence represents the majority of the film cooling studies conducted in wind tunnels, while the typical flowfield at the exit of the combustor is characterized by the Von Karman spectrum with inertial subrange isotropy (Ames, 1997a). In the present study, both these freestream length scales are simulated, and the effect of the differing length scales on the cooling jet dispersion is examined. In order to focus attention primarily on the length scale issue, the turbulence levels are maintained constant at 15% for the two cases.

The numerical study will be done through time and space accurate simulations of the filtered Navier Stokes equations (Large Eddy Simulations). The majority of the reported computational studies on the jet-in-crossflow configuration have primarily solved the Reynolds-Averaged-Navier-Stokes (RANS) equations, and due to the intrinsic time-averaging that is associated with these equations, the dynamical nature of the vortical structures can not be predicted. Further, turbulence models have to be introduced, and the accuracy of the time-averaged calculations is itself compromised by the validity of the model. Examples of RANS calculations are those of Patankar et al. (1977), Sykes et al. (1986), Kim and Benson (1992), and Garg and Gaugler, (1994, 1995). Since the dynamics of the large scale features are important, the large scales have to be predicted correctly and the interactions of small scales must be modeled

accurately. This requirement calls for large eddy simulations (LES), where all structures beyond a certain filter size are resolved, and the unresolved scales are modeled. To minimize numerical dissipation, an accurate numerical scheme has to be employed. More recently, Muldoon and Acharya (1999) have presented time-and space-accurate Direct Numerical Simulations (DNS) for a normally injected jet. Jones and Wille (1996) and Yuan and Street (1996) have presented Large Eddy Simulations (LES) that resolve the dynamics of the large scales and model the small scales, for a normally injected jet, and observed some of the reported phenomena in the experiments. As noted earlier, the main aim of this paper is to perform LES to understand the role of the large scales in free-stream on the penetration and mixing of the jet with the crossflow.

## COMPUTATIONAL METHOD

The unsteady three-dimensional Navier Stokes equations are solved using the projection method (Chorin, 1967). This is a fractional step approach in which an intermediate velocity field is calculated by neglecting the pressure gradients, and the pressure field is obtained as a solution to a Poisson equation derived using the continuity equation. This pressure field is used to update the velocity in the projection step. The temporal discretization is done using a second-order accurate Adams-Bashforth scheme. The calculation of the convective terms is done by a conservative formulation. A fourth order accurate finite difference scheme is used for these terms. The viscous dissipation terms are discretized using a fourth order accurate central difference scheme.

In LES, the governing equations are obtained by applying a filtering operation on the Navier-Stokes equations and the continuity equation. The filter function is represented as the convolution operator (Ghosal and Moin, 1995). The unfiltered fields give rise to subgrid scale stresses that require modeling. Following the dynamic mixed method of Zang et al (1993), these stresses are decomposed into a resolved part and an unresolved part. The resolved part is the Galilean invariant form of Bardina's (1983) scale similarity model (Speziale, 1985). The dynamic Smagorinsky model is used for the unresolved part of the stress and the dynamic coefficient is test filtered to avoid numerical instabilities.

The issue of filtering is very important for such numerically accurate simulations. On a non-uniform grid the filtering operator becomes a function of spatial location and hence gives rise to commutation error leading to low order of accuracy even with very high order accurate schemes (Ghosal and Moin, 1995). The issue of dependence of dynamic coefficient on aspect ratio of the grid cells when using grid based filters needs to be addressed on such non-uniform grids (Scotti et al, 1997). These issues are evaded here by using uniform grids with isotropic aspect ratio. In particular, the flow contains structures in almost all parts of the computational domain and hence, all parts of the domain need to be resolved with equal importance. For several reasons top hat filter is used (Zhou et al, 1989 and Ghosal, 1999). It is easy to implement in a finite difference code. It has compact support, unlike Gaussian or exponential filters which violate this requirement for grid-based filtering. It is a positive or realizable filter i.e. if it filters a non-negative field, the filtered field is always non-negative.

## PROBLEM DESCRIPTION

A schematic of the physical problem studied is shown in Fig. 1 where a single row of square coolant holes is injecting vertically upwards into the crossflow. This specific configuration has been selected to correspond to the geometry and measurements conditions (with grid

generated low freestream turbulence) reported by Ajersch et al (1995). Due to spanwise periodicity in the flow, the computational domain consists of a single coolant hole, and periodic boundary conditions are applied in the spanwise direction. A uniform Cartesian grid of  $122 \times 52 \times 32$  points is used for a domain of  $12D \times 5D \times 3D$  (Figure 1). At the inflow, a fully developed turbulent boundary layer profile is specified for the mean velocity profile, consistent with that reported by Ajersch et al. (1995). Both the inflow profile and the freestream conditions are perturbed, as described later, to generate the desired length scales and intensity levels. The velocity field at the jet-hole exit is specified from the experiments of Ajersch et al (1995). The Reynolds number based on the jet velocity and the hole dimension is 4700. The top boundary of the computational domain is chosen such that freestream conditions at the inlet can be used as the boundary conditions along the top plane. At the outflow, a convective boundary condition is used where the wave speed is determined from a flux balance.

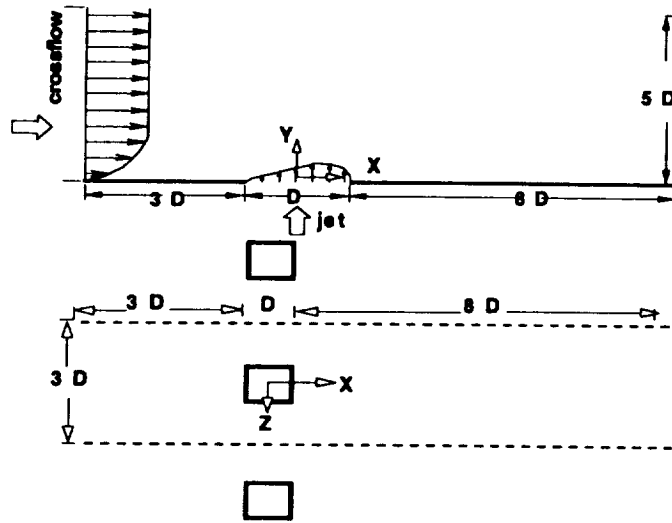


Figure 1: Schematic of the computational domain.

To specify grid generated turbulence at the inlet and the freestream, the velocity fluctuations at these locations are randomly specified from a Gaussian probability distribution function that is characteristic of grid generated turbulence. The random sampling is done using the Box-Muller method. This ensures that the random field has Gaussian probability density for a given variance level. The fluctuation levels are normalized in order to give 15 % turbulence intensity at the inlet and in the freestream in all three coordinate directions.

For the large scale turbulence case, the energy spectrum is prescribed by the following relation

$$E(k) = \frac{Ak^4}{(B+k^2)^{7/6}}$$

This spectrum behaves as  $k^4$  in the limit as  $k \rightarrow 0$  and as  $k^{-5/3}$  in the limit  $k \rightarrow \infty$ . The energy spectrum has a peak at the wave number  $k_m$  that is given by

$$k_m = \frac{2\pi}{\Lambda}$$

where  $\Lambda$  is the integral length scale of the energy containing eddies in free-stream. This location of peak determines the constant  $B$ . Spectrum signal is multiplied by random phase. Scrambling of phase information does not affect the energy distribution amongst scales as it contains the information about the orientation of eddies only. The negative wave numbers contain the conjugates of complex entries corresponding to positive wave numbers. Taking the inverse Fourier transform of this randomized spectrum will give the desired real signal. This signal is scaled with its rms value and multiplied by the given intensity. The turbulence intensity is chosen to be 15% to correspond to the small scale turbulence case, while the peak energy is specified at a  $\Lambda=4D$ . The choice of 4 hole diameters is based on typical values reported by Bons et al. (1996) and Kohli and Bogard (1998).

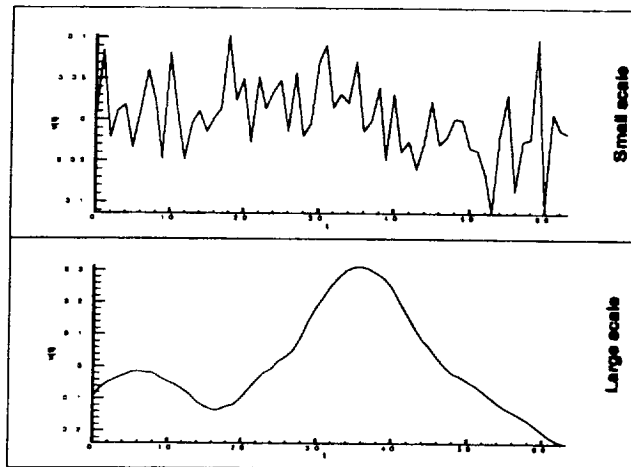


Figure 2: Representative random signals in freestream at  $X/D = -1.5, Y/D = 4.0$  and  $Z/D = 0.0$ .

At  $X/D=-1.5$ , Figure 2 shows the temporal-signature of the normal velocity component for both the small-scale freestream turbulence and the large-scale freestream turbulence. The figure illustrates the differences between the small scale turbulence with high frequency (small length scales) oscillations compared to the low frequency (large length scales) signature from a signal satisfying the Von Karman spectrum at the inlet ( $X/D = -3.5$ ) with peak energy at a wave number  $\Lambda=4D$ .

## RESULTS

In presenting the results, the focus is on examining the time-averaged results from the two simulations (small-scale freestream turbulence and large-scale freestream turbulence), and in highlighting the differences in the observed result. Comparisons with the published data of Ajersch et al. (1995) have been reported in Tyagi and Acharya (1999, 2000) and show good agreement. For comparison with experiments, the simulations were done with low freestream turbulence (2% turbulence intensity) to be consistent with the experimental configuration of Ajersch et al. (1995). Since the focus of the present paper is on high freestream turbulence, and specifically on length scale effects, comparison with measurements shown in Tyagi and Acharya (1999, 2000) are not reproduced here.

Figure 3 presents the spectrum of the X-component of velocity at  $X/D=-1.5$  (upstream of the jet), and at  $X/D=1.5$  and  $4.5$  (downstream of the jet). The spectra for both the large-scale and small-scale freestream turbulence is normalized by the maximum energy corresponding to the large-scale case. Upstream of the jet ( $X/D=-1.5$ ), the peak in the u-spectrum at the small wave

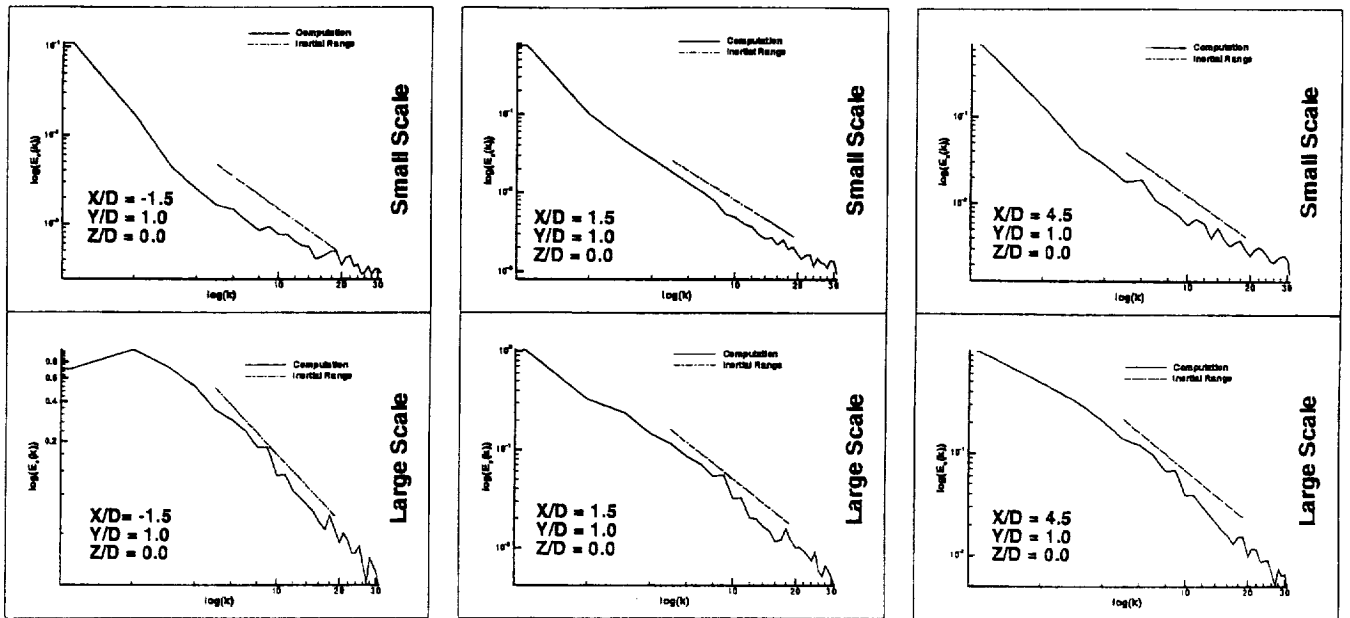


Figure 3: Spectrum of X-component of velocity field at three stations ( $X/D = -1.5, 1.5$  and  $4.5$ ) at jet centerplane and  $Y/D = 1.0$ .

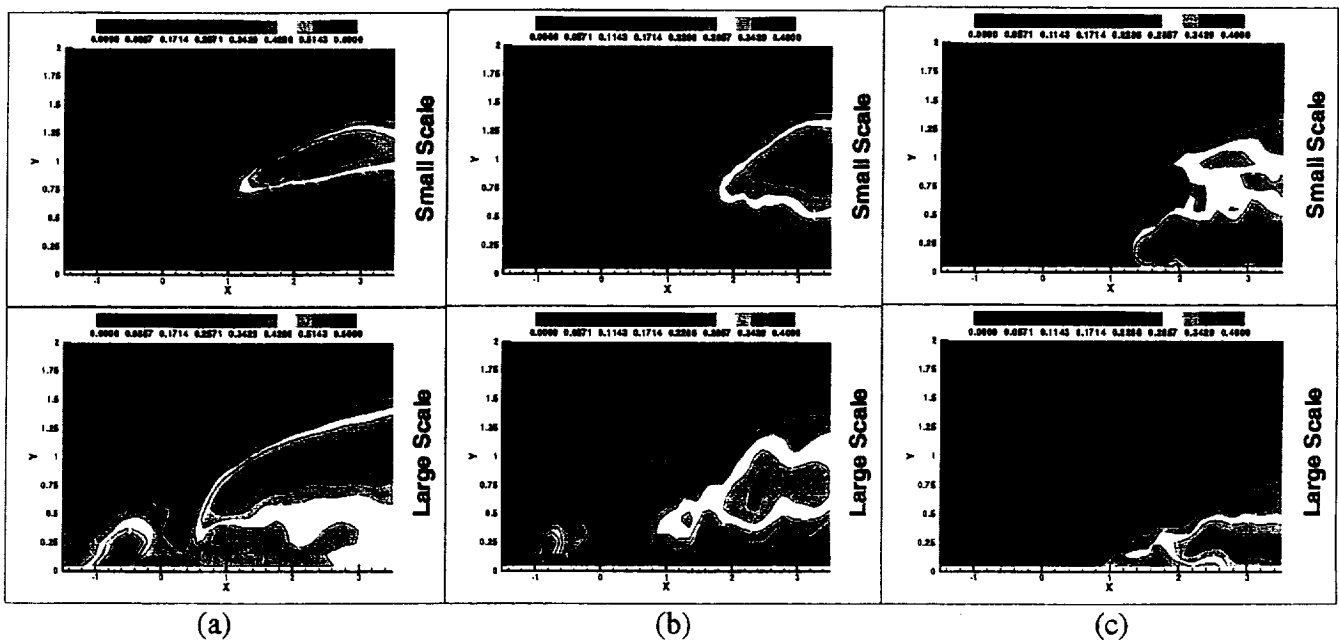


Figure 4: Contours of (a)  $u_{rms}$ , (b)  $v_{rms}$  and (c)  $w_{rms}$  along the jet centerplane

number corresponding to  $\Lambda=4D$  can be clearly observed for the large-scale freestream turbulence case, while the inertial subrange (with  $-5/3$  slope) is captured at the higher wave numbers. This peak at  $\Lambda=4D$  is significantly larger than the peak in the small-scale freestream turbulence case. The spectrum for the small-scale freestream turbulence case represents isotropic turbulence corresponding to the inertial subrange. Downstream of the jet ( $X/D=1.5$ ), in the jet region

( $Y/D=1$ ), the peak at the small wave number disappears, energy is transferred from this peak to the smaller scales, and the spectra for the two cases look similar, indicating the dominance of the jet-crossflow interaction in generating the scales of turbulence. However, the energy levels at all wave numbers are still somewhat higher for the large-scale freestream turbulence case reflecting the weaker role of dissipation in the presence of the larger scales.

Figure 4 show the contours of the time-averaged normal stresses ( $u_{rms}$ ,  $v_{rms}$  and  $w_{rms}$ ) along the jet center plane ( $Z/D=0$ ). Consistent with the observations in Figure 3, the  $u_{rms}$  values are seen to be much higher in the presence of large scale freestream turbulence. As noted earlier, this is due to the reduced role of dissipation at the larger length scales. In particular, the magnitude of the streamwise turbulence intensity associated with the horseshoe vortex system (upstream of the jet where the large scales still show peak energy as seen in Fig. 3) is nearly doubled for the large-scale turbulence intensity case. The greater energy in the horseshoe vortex system has ramifications on the downstream development of the horseshoe (as will be seen later in Fig. 5). For the large scale case, significantly greater streamwise turbulence intensity can also be seen in the wake of the jet, which in turn, may lead to greater heat transfer at the surface. The higher  $u_{rms}$  in the wake may be associated with entrainment into the wake of the crossflow that is associated with higher energies.

The  $v_{rms}$  contours shown in Figure 4b, again indicate that the large scales in the freestream energize the normal fluctuations, particularly in the early regions of the jet-crossflow interaction ( $-1 < X/D < 2$ ). The higher  $v_{rms}$  in the nearfield of the jet leads to enhanced jet-crossflow mixing, while the higher  $v_{rms}$  near the wall leads to increased skin friction (Fig.10) and is likely to lead to increased wall heat transfer. Several investigators have shown a strong correlation between the surface shear and heat transfer with normal velocity fluctuations, and this expectation is confirmed in the present study.

The  $w_{rms}$  velocity field shows higher values in the freestream and along the upper edges of the jet for the large scale case, but does not show larger values in the jet region or the in the wake regions. This is in contrast to the observations for the  $u_{rms}$  and  $v_{rms}$ .

The time-averaged streamwise vorticity contours and the velocity vectors at three transverse planes corresponding to  $X/D = 1.0, 3.0$  and  $5.0$  are shown in Figure 5. Asymmetry across the mid-plane can be observed, and is related to the asymmetry in the jet exit boundary conditions specified from the experimental data of Ajersch et al. (1995). The horseshoe vortex system can be seen to be considerably stronger and larger in the presence of large freestream turbulence scales. Evidence of this was seen earlier in Figure 4a, where upstream of the jet, the streamwise and wall-normal velocity fluctuations in the horseshoe vortex were considerably greater for the large-scale case. At  $X/D=1.0$  and  $3.0$ , the CVP is also seen to be stronger and exhibits greater penetration for the large scale case; this behavior is again linked to the higher energies ( $u_{rms}$  and  $v_{rms}$ ) in the jet and wake associated with the large scale freestream turbulence. At  $X/D = 8.0$ , the large scales and their effects seemed to have been considerably diminished, and little difference is observed in the time-averaged vorticity and vector plots. For both cases, the entrainment of the crossflow into the wake region below the CVP can be seen; this leads to wall vortices containing vorticity with the opposite sign to the CVP. As discussed by several investigators (Muldoon and Acharya, 1999; Kelso et al., 1996; Fric and Roshko, 1994) the crossflow entrainment and the development of wall vortices lead to the development of the wake vortex structure (see Fig. 7).

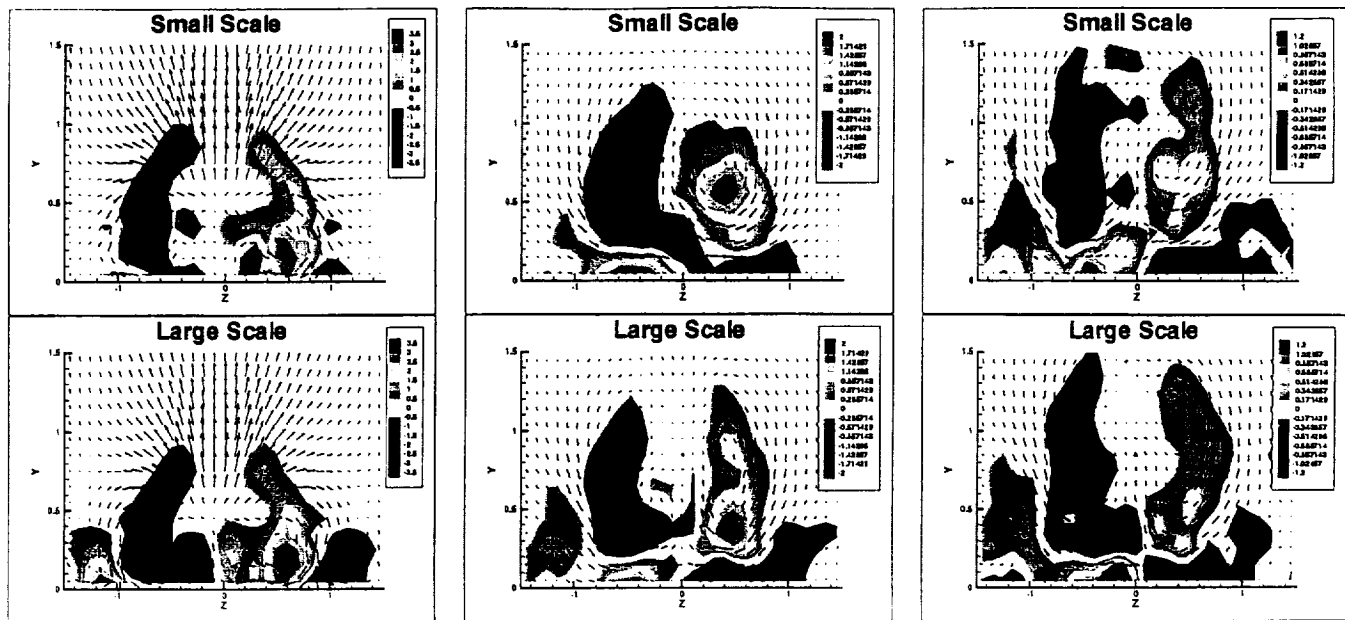


Figure 5: Contours of  $\omega_x$  and time averaged velocity vectors at planes  $X/D = 1.0, 3.0$  and  $5.0$

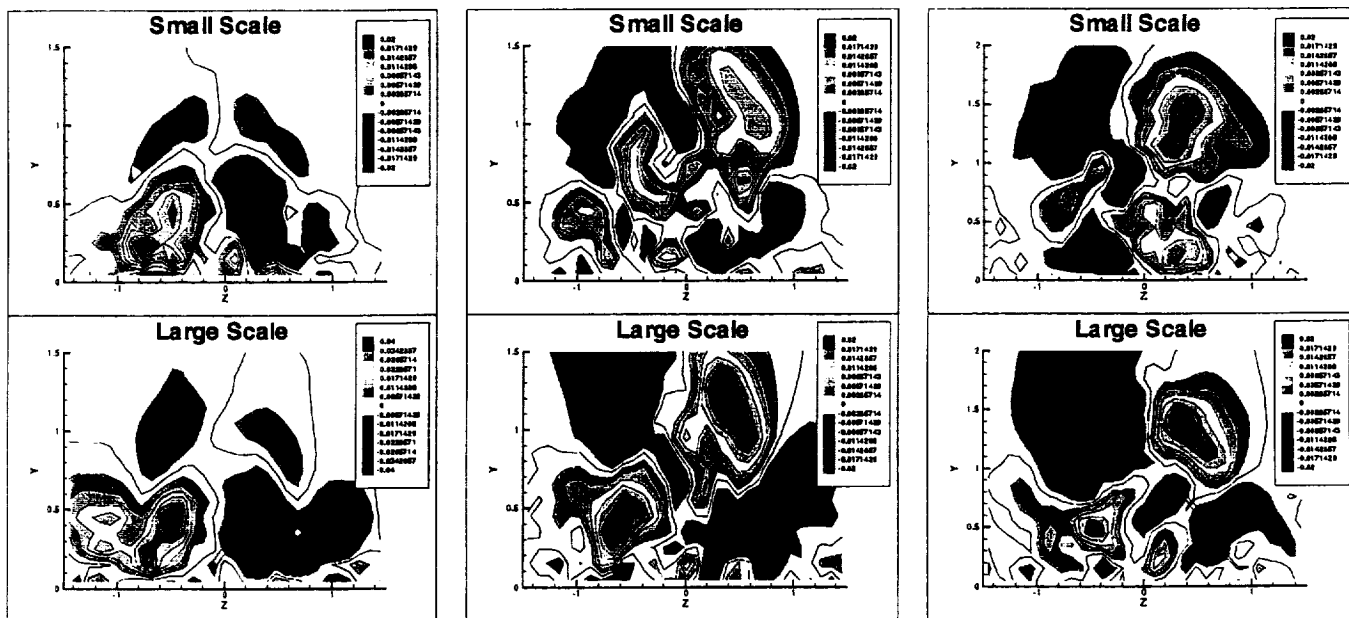


Figure 6: Contours of Reynolds stress  $v'w'$  at planes  $X/D = 1.0, 3.0$  and  $5.0$ .

The Reynolds stress contours  $v'w'$  in the transverse planes  $X/D = 1.0, 3.0$  and  $5.0$  are shown in Fig. 6, and, for the large-scale freestream turbulence case, considerably higher stress levels in the near field ( $X/D = 1.0$  and  $3.0$ ) are associated with both the CVP and the horseshoe vortex. The highest stresses are associated with the edges of the CVP and correspond to the positions of the maximum velocity gradients. The stress profiles at  $X/D=5$  for the two cases look similar, and reflect a decrease in the effect of the large scales as already observed.

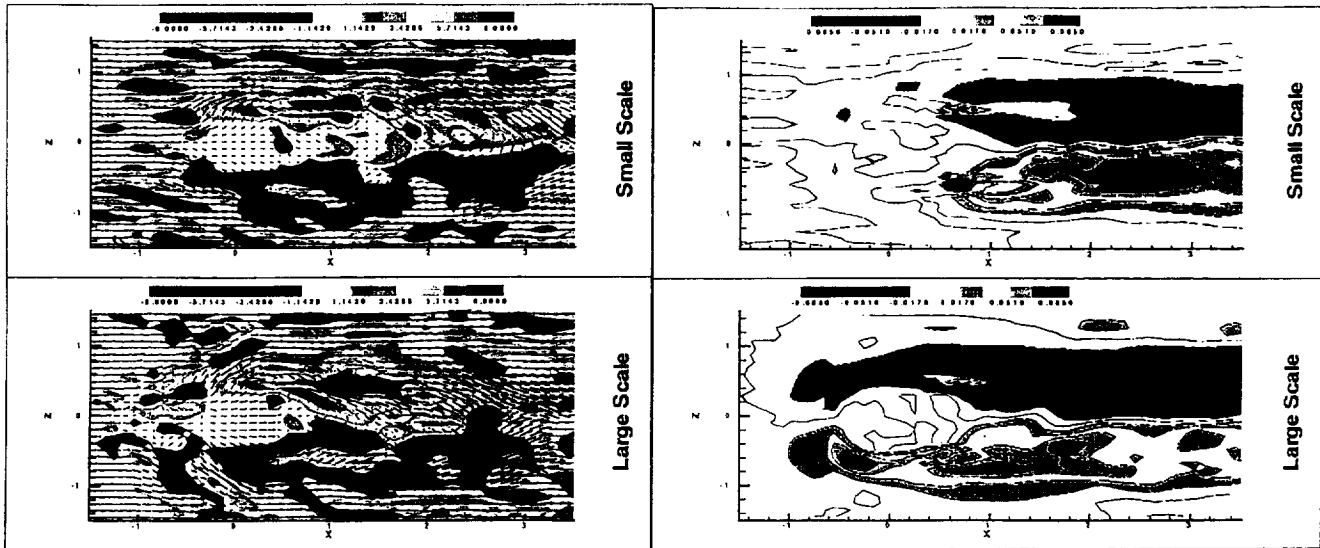


Figure 7: (a) Contours of  $\omega_y$  and instantaneous velocity vectors at  $Y/D = 0.1$  and (b) Contours of Reynolds stress  $u'w'$  at  $Y/D = 0.1$

Figure 7a shows the contours of the vertical vorticity component and velocity vectors along a horizontal plane ( $Y/D=0.1$ ) above the jet-exit. Figure 7b shows the corresponding Reynolds stress contours  $u'w'$  along this plane. The large-scale case clearly shows evidence of the horseshoe upstream of the jet (with reversed velocity vectors), while the small scale case does not clearly exhibit this flow separation. For the large scale case significant levels of the shear stress  $u'w'$  are generated along the edges of the horseshoe and the spanwise edges of the jet. These large values are again a consequence of high levels of streamwise velocity fluctuations noted earlier for the case of large-scale freestream turbulence. Clear evidence of wake vortices is seen in both cases, and as noted earlier, is a consequence of the crossflow entrainment into the wake, and the upward reorientation of the entrained flow. The primary difference between the large scale and the small-scale case is that in the large scale case, there is evidence of stronger crossflow entrainment (larger magnitudes of the entrained crossflow velocities) that manifests itself earlier in the near wake region. This is best illustrated by particle traces shown in Fig. 8, where the path of a particle injected on either edge of the jet-exit is displayed. Two views are presented one looking down, and the other looking from the transverse edge along a streamwise plane. It can clearly be seen that the particle entrained into the wake is reoriented in the vertical direction, confirming the earlier observations that the crossflow entrainment into the wake is the source of the wake vortex system. For the large-scale case, the entrainment into the wake and the upward reorientation begins immediately downstream of the jet exit ( $X/D = 0.5$ ), and for the two trajectories shown is completed by  $X/D = 3.0$ . For the small-scale case, the upward reorientation is delayed to  $X/D = 2.5$  and is completed downstream of  $X/D=3$ . The earlier entrainment of the crossflow for the large scale case is also associated with the location of peak stress being closer to the jet exit relative to the location of the peak stress for the small scale case.

The spanwise vorticity contours and velocity vectors along the jet centerplane are shown in Fig. 9a, while the corresponding shear stress  $u'v'$  in the vertical plane is shown in Fig. 9b. For the large scale case, the spatial perturbations in the freestream velocity is evident in the vorticity contour and the velocity vectors in Fig. 9a. As already noted, Fig. 9 also shows the substantially stronger horseshoe system obtained for large-scale freestream turbulence. The recirculation

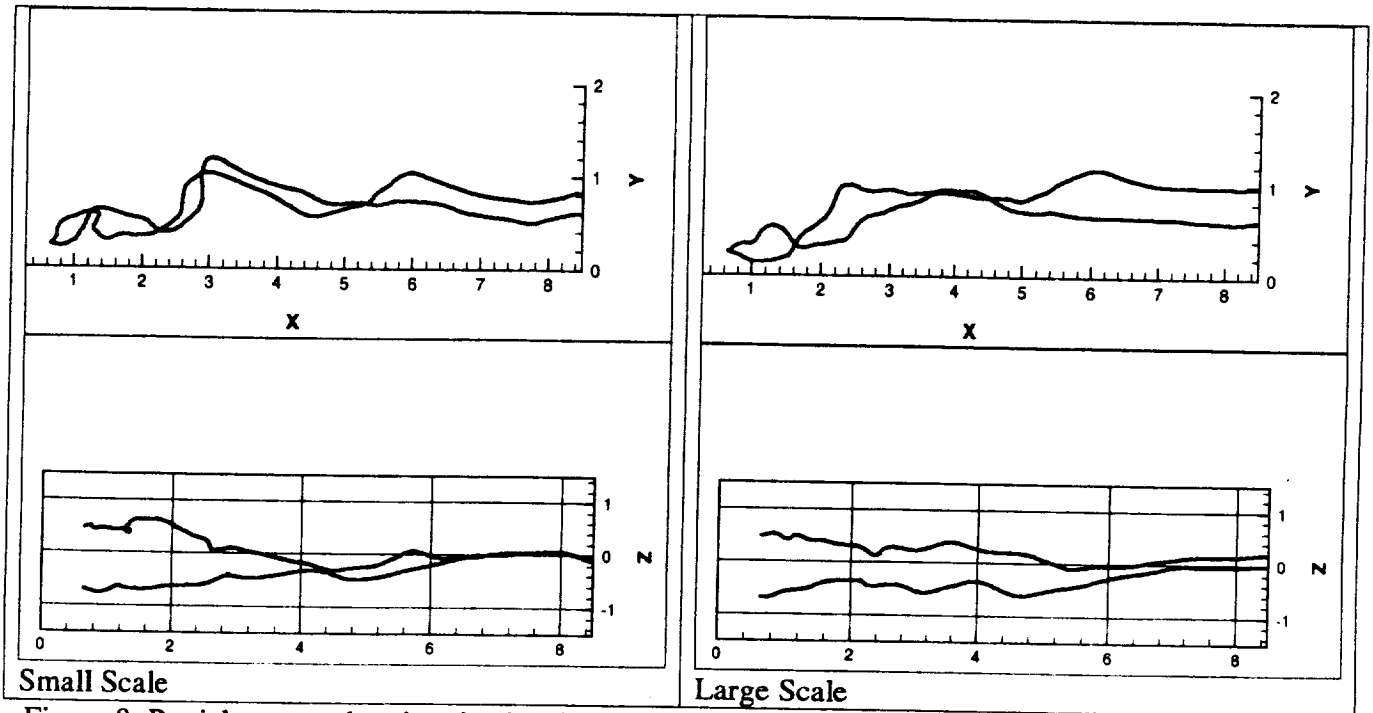


Figure 8: Particle traces showing the development of wake vortices (trace release stations at  $X/D = 0.7$ ,  $Y/D = 0.2$  and  $Z/D = \pm 0.6$ )

region is substantially smaller for the large-scale case due to the stronger crossflow entrainment. In both cases, spanwise vortices on the leeward edge of the jet are observed, and the highest velocity gradients ( $\partial U/\partial Y$  and  $\partial V/\partial X$ ) and shear stresses  $u'v'$  are associated with these vortical structures. For the large-scale case, the region of negative shear stresses, associated with the jet region, is much closer to the wall than for the small-scale case, reflecting the much greater mixing between the jet and the wake for the large-scale case. For this lifted jet configuration, the greater mixing of the lifted jet (cold) with the entrained crossflow (hot) may lead to improvements in film cooling. This should, of course be balanced by earlier observations, where for the large scale case, greater crossflow entrainment into the wake region can lead to greater heat transfer and reduced cooling.

Figure 10 presents the surface skin friction as well as the streamwise and spanwise vorticity components just above the surface. The skin friction is observed to correlate well with the streamwise vorticity. Recall that streamwise vorticity is associated primarily with the CVP, the wall vortex, and the horseshoe vortex. The peak skin friction below the CVP/wall vortex system is an order of magnitude higher (in the range of 2-3 in non-dimensional units) than at other locations corresponding to the horseshoe or the wake (in the range of 0.15-0.7). The skin friction for the large scale case is substantially higher in the near field ( $X/D < 3$ ) jet, and is consistent with the higher  $u_{rms}$  and  $v_{rms}$  observed near the wall for the large scale case. The higher wall friction is also likely to be associated with higher wall heat transfer. Note that in the region just downstream of the jet exit ( $0.5 < X/D < 2$ ), the flow separation in the small scale case leads to very small values of wall shear, while in the large scale case the absence of any significant recirculation in this region, as seen in Fig. 9, leads to high values of the wall shear.

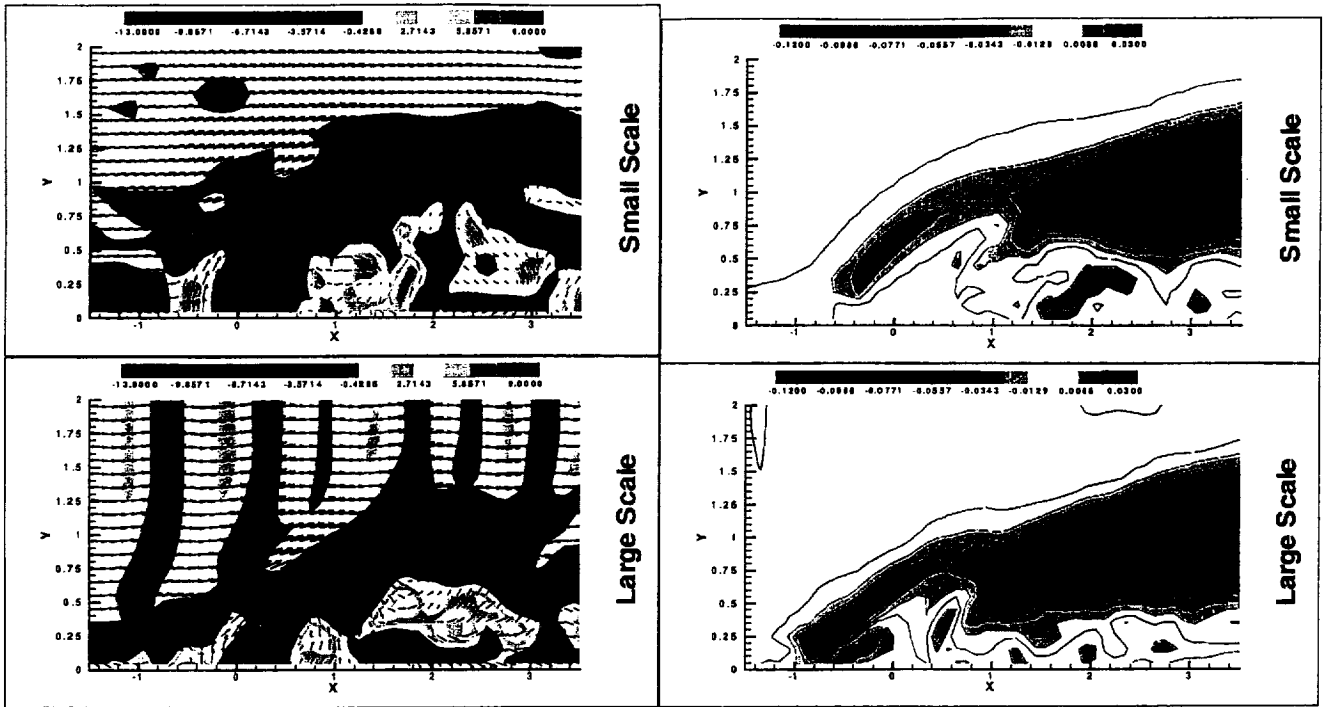


Figure 9: (a) Contours of  $\omega_z$ , and instantaneous velocity vectors at  $Z/D = 0.0$ , and (b) Contours of Reynolds stress  $u'v'$  at  $Z/D = 0.0$

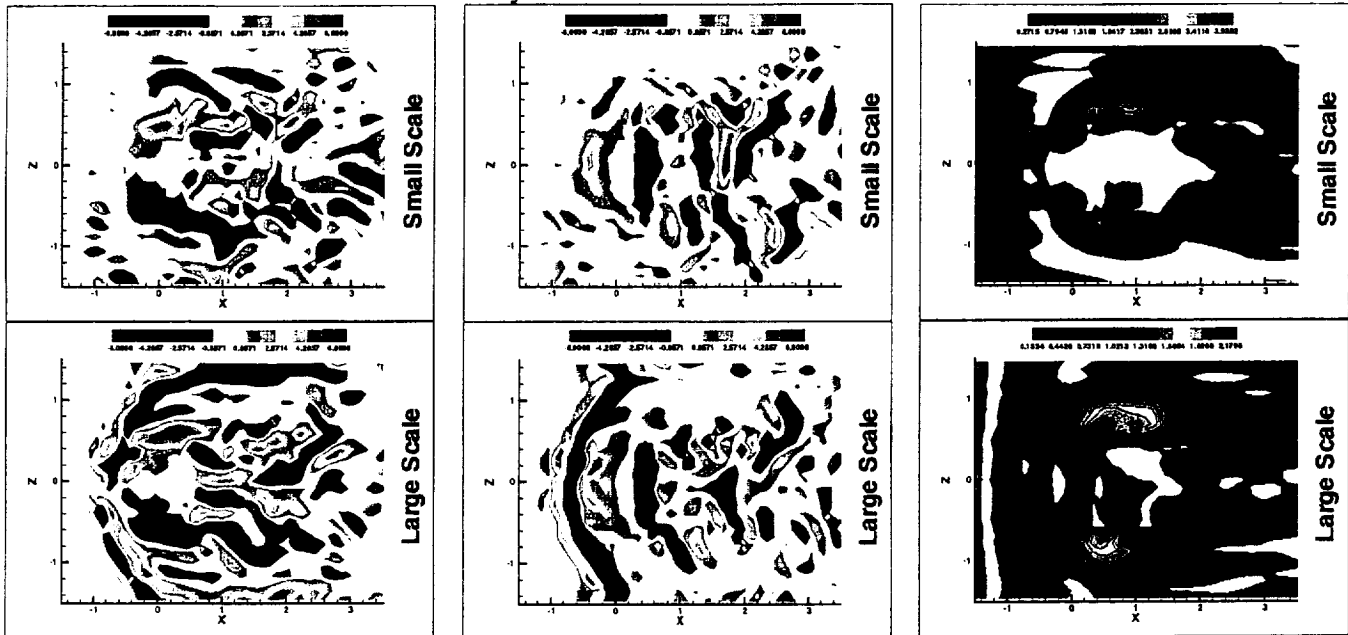


Figure 10: Contours of  $\omega_x$  and  $\omega_z$  at  $Y/D = 0.1$  and contours of wall shear stress.

## CONCLUDING REMARKS

Large eddy simulations of a vertically injected jet-in-crossflow were performed for two freestream turbulence length scales at 15% freestream turbulence intensity. The following represent some of the major observations made in this study.

- The larger length scales have a substantial impact on the turbulent stresses in the near field of the jet. Significantly larger values of  $u_{rms}$ ,  $v_{rms}$ , and the shear stress components are observed with the large-scale freestream turbulence in the region  $-1 < X/D < 3$ .
- The wall friction correlates well with the streamwise vorticity, and is substantially higher for the case of large-scale freestream turbulence.
- The jet-crossflow interaction plays a major role in dictating the flow scales in the jet region and the effect of the larger freestream scales is considerably reduced in this jet region.
- The effect of the large scales is significant in energizing the horseshoe vortex system, and in enhancing the crossflow entrainment into the wake region. As a consequence, the horseshoe is considerably larger and stronger for the large-scale case. The entrainment of the crossflow boundary layer into the wake is initiated earlier, and is stronger, for the large-scale case. Therefore, the recirculation region behind the jet is considerably diminished in the large-scale case. These large-scale effects are primarily responsible for enhancing the turbulence.

## REFERENCES

- Ajersch, P., Zhou, J.M., Ketler, S., Salcudean, M. and Gartshore, I. A. (1995), *Multiple jets in a crossflow: detailed measurements and numerical simulations*, ASME 95-GT-9.
- Ames, F. E. (1997a), *Aspects of vane film cooling with high turbulence: Part I-Heat transfer*, ASME 97-GT-239, ASME-IGTI Meeting, Orlando
- Ames, F. E. (1997b), *Aspects of vane film cooling with high turbulence: Part II-Adiabatic effectiveness*, ASME 97-GT-240, ASME-IGTI Meeting, Orlando
- Andreopoulos, J. and Rodi, W. (1984), *Experimental investigation of jets in a crossflow*. J. Fluid Mech., Vol. 138, pp. 93-127.
- Andreopoulos, J. (1985), *On the structure of jets in a crossflow*. J. Fluid Mech., Vol. 157, pp. 163-197.
- Bardina, J, Ferziger, J.H. and Reynolds, W.C. (1983), *Improved turbulence models based on large eddy simulations of homogeneous, incompressible turbulent flows*, Report TF-19, Thermosciences Div., Eng., Dept. Mech. Stanford Univ.
- Batchelor, G.K. (1953), *Theory of homogeneous turbulence*, Cambridge University Press.
- Bons, J. P., MacArthur, C. D., and Rivir, R. B. (1996), *The effect of high free-stream turbulence on film cooling effectiveness*, ASME J. of Turbomachinery, Vol. 118, pp. 814-825
- Chorin, A.J. (1967), *A numerical method for solving incompressible viscous flow problems*, J. Comp. Phy., Vol. 2 pp. 12-26.
- Dubois, T., Jauberteau, F. and Temam, R. (1999), *Dynamic multilevel methods and the numerical simulation of turbulence*, Cambridge University Press.
- Fric, T.F. and Roshko, A. (1994), *Vortical structure in the wake of a transverse jet*. J. Fluid Mech., Vol. 279, pp.1-47.
- Garg, V. K., and Gaugler R. E., 1995 "Effect of velocity and temperature distribution at the hole exit on film cooling of turbine blades", ASME paper 95-GT-2

- Garg, V. K., and Gaugler R. E., 1994 "Prediction of film cooling on gas turbine airfoils", *ASME paper 94-GT-2*
- Ghosal, S. (1999), *Mathematical and physical constraints on large eddy simulation of turbulence*, AIAA Journal, Vol. 37, no. 4, pp.425-433.
- Ghosal, S. and Moin, P. (1995), *The basic equations for the large eddy simulations of the turbulent flows in complex geometry*, J. Comp. Phy., Vol. 118, pp.24-37.
- Jones, W. P. and Wille, M. 1996 "Large eddy simulation of a round jet in crossflow" *Engineering Turbulence Modeling and Experiments 3*. Ed. Rodi, W. and Bergeles, G. pp.199-209
- Jordan, S.A.(1994), *Use of the large eddy simulation dynamic model for turbulent shear driven cavity flows*, ASME FED-Vol. 184 pp. 141-150.
- Kadotani, K., and Goldstein, R. J. (1979a), *On the nature of jets entering a turbulent flow: Part A-Jet –mainstream interaction*, ASME J. Engng. For Power, Vol. 101, pp. 459-465.
- Kadotani, K., and Goldstein, R. J. (1979b), *On the nature of jets entering a turbulent flow: Part B-Film cooling performance*, ASME J. Engng. For Power, Vol. 101, pp. 466-460.
- Kelso, R.M., Delo, C. and Smits, A.J. (1993), *Unsteady wake structures in transverse jets*, Fluid Dynamics Panel Symposium, UK, AGARD-CP-534.
- Kelso, R.M., Lim, T.T. and Perry, A.E. (1996), *An experimental study of round jets in cross-flow*, J. Fluid Mech., Vol. 306, pp.111-144.
- Kim, S.W., and Benson, T. J. (1992), *Calculation of a circular jet in crossflow with a multiple-time-scale turbulence model*, Int. J. Comp. Phys. Vol 59. pp. 308-315
- Kohli, A., and Bogard, D. G., (1988a), *Fluctuating thermal field in the near region for film cooling flows*, ASME J. of Turbomachinery, Vol. 120, pp. 86-91.
- Kohli, A., and bogard, D., (1988b), *Effects of very high free-stream turbulence on the jet-mainstream interaction in a film cooling flow*, ASME J. of Turbomachinery, Vol. 120, pp. 785-790.
- Muldoon, F. and Acharya, S. (1999), *Numerical investigation of the dynamical behavior of a row of square jets in crossflow over a surface*, ASME-IGTI99
- Ou, S., Mehendale, A. B., and Han, J. C. (1990), *Influence of high mainstream turbulence on leading edge film cooling heat transfer: effect of film hole row location*, ASME90-WA/HT-5, ASME Winter Annual meeting, Dallas.
- Patankar, S. V. Basu, D. K. and Alpay, S. A., (1977), *Prediction of the three-dimensional velocity field of a deflected turbulent jet*, Trans. SME I: J. Fluids Engng 99, pp. 758-762
- Radomsky, R. W., and Thole, K. A., (1998), *Effects of high freestream turbulence levels and length scales on stator vane heat transfer*, ASME 98-GT-236, ASME-IGTI Meeting, Stockholm.
- Scotti, A., Meneveau, C. and Fatica, M. (1997), *Dynamic Smagorinsky model for anisotropic grids*. Phys. Fluids. Vol 9 pp. 1856-1858.
- Speziale, C.G. (1985), *Galilean Invariance of subgrid scale stress models in large eddy simulation of turbulence*, J. Fluid Mech. Vol. 156, pp. 55-62.
- Sykes, R. I., Lewellen, W. S. and Parker, S. F. (1986), *On the vorticity dynamics of a turbulent jet in a crossflow*, J. Fluid Mech. vol. 80, pp. 49-80.
- Tyagi, M. and Acharya, S. (1999), *Large eddy simulations of jets in crossflow: Freestream turbulence effects*, FEDSM 99-7799, 3<sup>rd</sup> ASME/JSME Joint fluids engineering conference.
- Tyagi, M. and Acharya, S. (2000), *Large eddy simulations of jets in crossflow: Effect of jet inclination angle*, 4<sup>th</sup> ISHMT/ASME heat and mass transfer conference.

- Yuan L.L., and Street, R. L. (1996), *Large Eddy Simulation of a Jet in Crossflow*, ASME Fluids Engineering Division Vol. 242, pp.253-260
- Zang, Y., Street, R.L. and Koseff, J.R. (1993), *A dynamic mixed subgrid scale model and its application to turbulent recirculating flows*, Phys. Fluids A Vol. 5 no. 12 pp. 3186-3196.
- Zhou, Y., Vahala, G. and Hossain, M. (1989), *A critical look at the use of filters in large eddy simulations*, Phys. Lett. A Vol. 139 no. 7 pp. 330-332.

## CHAPTER VII

# LARGE EDDY SIMULATION (LES) OF INCLINED FILM COOLING JETS IN CROSSFLOW

### ABSTRACT

Large eddy simulations of a normal and an inclined jet in crossflow are performed to study the effect of jet inclination on the penetration and spread of the coolant jet. In the present study, the jets are issued through a square duct into the mainflow at two different inclination angles of 30° and 90°. The jet to crossflow blowing ratio is 0.5 and the jet Reynolds number is approximately 5,000.

Greater jet penetration and jet-mainstream mixing, in both the vertical and lateral directions, are observed for the normally injected jet. A significantly larger recirculation is obtained in the wake of the normal jet and is likely to lead to low film-cooling effectiveness in the near wake region. For normal jet injection, large pressure gradients are present, and clear evidence of spanwise rollers on the leeward side of the jet are observed. These features are not observed for the inclined jet. The wall skin friction in the near field of the jet is lower for the normally injected jet, and appears to correlate best with the streamwise vorticity.

### NOMENCLATURE

$V_{jet}$	Jet velocity
$D$	Dimension of square hole
$R$	Blowing ratio of jet to crossflow
$X$	Streamwise direction
$Y$	Normal (to wall) direction
$Z$	Spanwise direction
$U$	X-component of averaged velocity
$V$	Y-component of averaged velocity
$W$	Z-component of averaged velocity
$u'v', v'w', u'w'$	components of Reynolds stress tensor.

### INTRODUCTION

Film cooling of turbine blades, where rows of coolant jets are injected at an angle into the hot crossflow, is a commonly used technique to maintain the blade temperatures below a threshold value. The coolant jets are deflected and strained by the crossflow and provide coverage of the blade surface from the hot gases. The interaction of the coolant jets with the crossflow involves complex and unsteady structures like the horseshoe vortex, the counter rotating vortex pair (CVP) and wake vortices. These structures control the jet penetration and its spreading rate.

The inclination angle of the jet is an important parameter that controls the development of the flow structures and the penetration and spreading of the jet. The effectiveness of film cooling is governed by the vertical and lateral spreading of the jet, and typically an inclination angle of around 30° has been found to be most desirable from the perspective of increasing film cooling effectiveness. The objective of this work is to numerically study the effect of the jet inclination

angle on the various flow structures. Two jet-inclination angles are studied:  $90^\circ$  representing normal injection, and  $30^\circ$  representing simple-angle injection. The numerical study will be done through time and space accurate simulations of the filtered Navier Stokes equations (Large Eddy Simulations). Although the focus of the work is on the flow field, a qualitative idea of the heat transfer can be obtained by examining the dispersion of the jet in the crossflow and by the shear stress distribution at the wall.

The majority of the reported computational studies on the jet-in-crossflow configuration have primarily solved the Reynolds-Averaged-Navier-Stokes (RANS) equations, and due to the intrinsic time-averaging that is associated with these equations, the dynamical nature of the vortical structures can not be predicted. Further, turbulence models have to be introduced, and the accuracy of the time-averaged calculations are themselves compromised by the validity of the model. Examples of RANS calculations are those of Patankar et al. (1977), Sykes et al. (1986), Kim and Benson (1992), and Garg and Gaugler, (1994, 1995).

Since the dynamics of the large scale features are important, the large scales have to be predicted correctly and the interactions of small scales must be modeled accurately. This requirement calls for large eddy simulations (LES), where all structures beyond a certain filter size are resolved, and the unresolved scales are modeled. To minimize numerical dissipation, an accurate numerical scheme has to be employed. More recently, Muldoon and Acharya (1999) have presented time-and space-accurate Direct Numerical Simulations (DNS) for a normally injected jet. Jones and Wille (1996) and Yuan and Street (1996) have presented Large Eddy Simulations (LES) that resolve the dynamics of the large scales and model the small scales, for a normally injected jet, and observed some of the reported phenomena in the experiments. However, no DNS/LES studies have been reported for the inclined jet in a crossflow configuration. As noted earlier, the main aim of this work is to perform LES for normal and inclined jets in crossflow, and to understand the role of the large scales in the penetration and mixing of the jet with the crossflow.

## COMPUTATIONAL METHOD

The unsteady three-dimensional Navier Stokes equations are solved using the projection method (Chorin, 1967). This is a fractional step approach in which an intermediate velocity field is calculated by neglecting the pressure gradients, and the pressure field is obtained as a solution to a Poisson equation derived using the continuity equation. This pressure field is used to update the velocity in the projection step. The temporal discretization is done using a second-order accurate Adams-Bashforth scheme. The calculation of the convective terms is done by a conservative formulation. A fourth order accurate finite difference scheme is used for these terms. The viscous dissipation terms are discretized using a fourth order accurate central difference scheme.

In LES, the governing equations are obtained by applying a filtering operation on the Navier-Stokes equations and the continuity equation. The filter function is represented as the convolution operator (Ghosal and Moin, 1995). The unfiltered fields give rise to subgrid scale stresses that require modeling. Following the dynamic mixed method of Zang et al (1993), these stresses are decomposed into a resolved part and an unresolved part. The resolved part is the Galilean invariant form of Bardina's (1983) scale similarity model (Speziale, 1985). The dynamic Smagorinsky model is used for the unresolved part of the stress and the dynamic coefficient is test filtered to avoid numerical instabilities.

The issue of filtering is very important for such numerically accurate simulations. On a non-uniform grid the filtering operator becomes a function of spatial location and hence gives rise to commutation error leading to low order of accuracy even with very high order accurate schemes (Ghosal and Moin, 1995). The issue of dependence of dynamic coefficient on aspect ratio of the grid cells when using grid based filters needs to be addressed on such non-uniform grids (Scotti et al, 1997). These issues are evaded here by using uniform grids with isotropic aspect ratio. In particular, the flow contains structures in almost all parts of the computational domain and hence, all parts of the domain need to be resolved with equal importance. For several reasons top hat filter is used (Zhou et al, 1989 and Ghosal, 1999). It is easy to implement in a finite difference code. It has compact support, unlike Gaussian or exponential filters which violate this requirement for grid-based filtering. It is a positive or realizable filter i.e. if it filters a non-negative field, the filtered field is always non-negative.

### PROBLEM DESCRIPTION

A schematic of the physical problem studied is shown in Fig. 1a (for normal injection) and in Fig. 1b (for inclined injection). A uniform Cartesian grid of  $122 \times 52 \times 32$  points is used for a domain of  $12D \times 5D \times 3D$  (Figure 1). At the inflow, a fully developed turbulent boundary layer profile is prescribed. In the normal jet case, the velocity field is specified at the jet inlet from the experiments of Ajersch et al (1995). The Reynolds number based on the jet velocity and the hole dimension is 4700 for this case. For the inclined jet case, the velocity at jet inlet is prescribed from the experiments of Findlay et al (1996). The Reynolds number based on the jet velocity and the hole spanwise dimension is 5000 for this case. For both configurations, a periodic boundary condition is applied in the spanwise direction. The domain size is chosen such that free-stream conditions at the inlet can be used as the boundary conditions along the top plane. At the outflow, a convective boundary condition is used where the wave speed is determined from a flux balance.

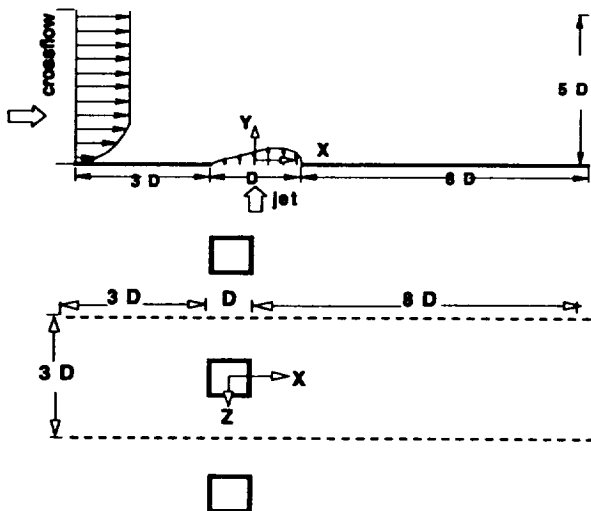


Figure 1a: Schematic of the computational domain for normal jets.

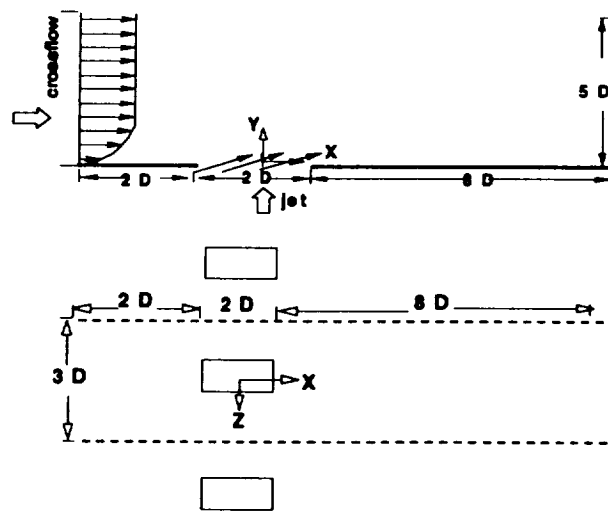


Figure 1b: Schematic of the computational domain for inclined jets.

## RESULTS

Results are presented for two different jet inclination angles at various planes of the computational domain. The X- component of mean velocity and rms fluctuations  $\sqrt{(u'u')}$  and  $\sqrt{(v'v')}$  are plotted at locations  $X/D = 3.0$  and  $5.0$  in the jet center plane,  $Z/D=0$  (Figure 2a and 2b). A good agreement is obtained between the present predictions and the experimental data of Ajersch et al (1995) for normal injection (Fig. 2b) and the data of Findlay et al (1996) for  $30^\circ$  simple injection (Fig. 2a). In the normal jets case (Fig. 2b), the mean profile at both  $X/D$  of 3 and 5 exhibits three distinct regions: the shear-layer or jet region at the top, the wake region in the middle, and a near-wall boundary layer region induced by the entrained crossflow. The  $u_{rms}$  appears to scale well with the  $\frac{\partial U}{\partial y}$ , with a maximum in the jet region and a minimum in the wake region. The  $v_{rms}$  is highest in the jet region and is damped rapidly as the wall is approached. At  $X/D=3.0$  and  $5.0$ , the peak  $u_{rms}$  and  $v_{rms}$  occur roughly around  $Y/D=1.2$ , while the vertical jet penetration distance is in the vicinity of  $Y/D=1.5$ . For the inclined jets (Fig. 2a), the jet penetration is considerably less (smaller than  $Y/D$  of 1), and wake effects are weaker. At  $X/D=3.0$ , the three regions noted in the normal injection case, although visible, are not as distinct. At  $X/D=5.0$ , the three regions are not visible, and wake recovery has progressed to a much greater degree than in the normal injection case. As for the normal injection case, the jet region appears to be associated with large rms values, but the magnitude of the rms values is nearly half of the values for the normal injection case. A notable exception is observed for the  $u_{rms}$  which shows a large peak (with values as high as 0.4) close to the wall. This large near-wall value of  $u_{rms}$  may be associated with the fact that the injected jet stays close to the wall, and its interaction with the entrained crossflow leads to significant production of turbulence near the wall.

The time-averaged vorticity contours ( $\omega_x$ ) and velocity vectors are shown in Figure 3 at a location  $X/D = 5.0$  from the center of the jet. The contours of the turbulent stress  $v'w'$  are presented at the same location in Figure 4. The CVP is an unsteady coherent structure and hence, time-averaged values, obtained after averaging over six flow-through periods, are shown to depict this organized coherent structure. The horseshoe vortex is also observed on the two sides of the CVP, and is associated with lower levels of  $\omega_x$  in the opposite sense of the CVP. In comparing the flow structures for the normal and angled-injection cases, Fig. 3 shows results consistent with the velocity profiles in Fig. 2, that is, for the normal injection case, the jet penetration in the vertical direction, and the associated CVP structure, is much larger. The lateral penetration of the CVP is also more for the normal-injection case. However, the horseshoe vortex along the periodic boundaries appears to be considerably smaller for normal injection, and may be associated with the fact that the larger lateral growth of the CVP with normal injection compresses the horseshoe toward the periodic boundaries and restricts its growth in the lateral direction. The crossflow entrainment into the wake leads to the formation of the wall vortex structures (Figure 3) as also noted by Fric and Roshko (1994). These structures are seen for both jet inclinations. However, for the inclined jet case, due to the proximity of the jet to the wall, the interaction of the entrained crossflow with the jet is stronger leading to more complex near wall structures.

The  $v'w'$  turbulent stress contours appear to correlate well with the CVP and the horseshoe vortex structures, implying that these large scale coherent structures in the flow are principally responsible for the Reynolds stresses. The locations of the peak stresses are shifted slightly

upwards relative to the eye of the large structures, and correspond with the locations where the velocity gradient and the production of the turbulent stress is the greatest. In comparing the turbulent stress levels for 30° and 90° injection, it is observed that the magnitude of the peak stress levels is larger in 90° case almost by a factor of 7. Note that these shear stresses can be viewed as turbulent forces that influence the flow motion, and that in the right-half plane ( $Z > 0$ ), a positive stress value impedes the flow motion while a negative value aids the flow. The CVP motion is observed to be primarily damped by the opposing action of the turbulent stress  $v'w'$ . For the inclined jet, the horseshoe vortex motion is seen to also weaken due to this stress. The distribution of stresses is in the opposite sense on the edges of the CVP below the jet. This opposes the near wall motion induced by the CVP.

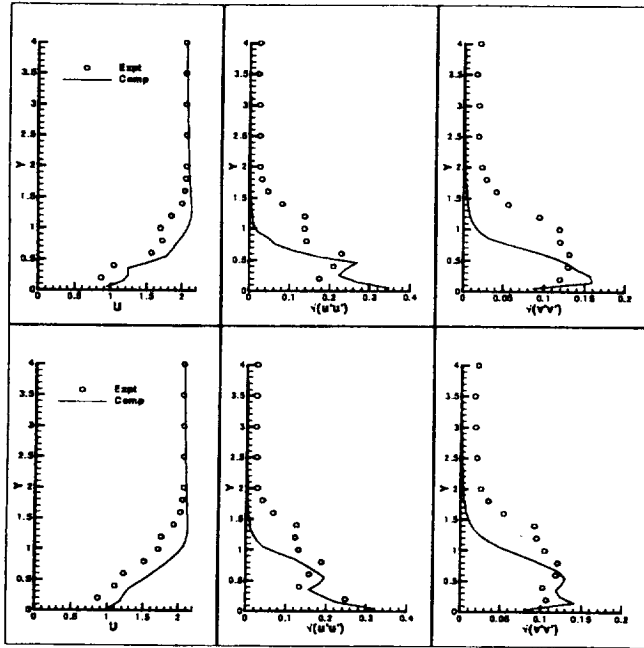


Figure 2a: Comparison of X component of mean velocity, rms components  $\sqrt{u'u'}$  and  $\sqrt{v'v'}$  at  $X/D = 3.0, 5.0$  respectively on the jet center plane ( $Z/D = 0.0$ ) for inclined jets (Experimental data is from Findlay et al 1996).

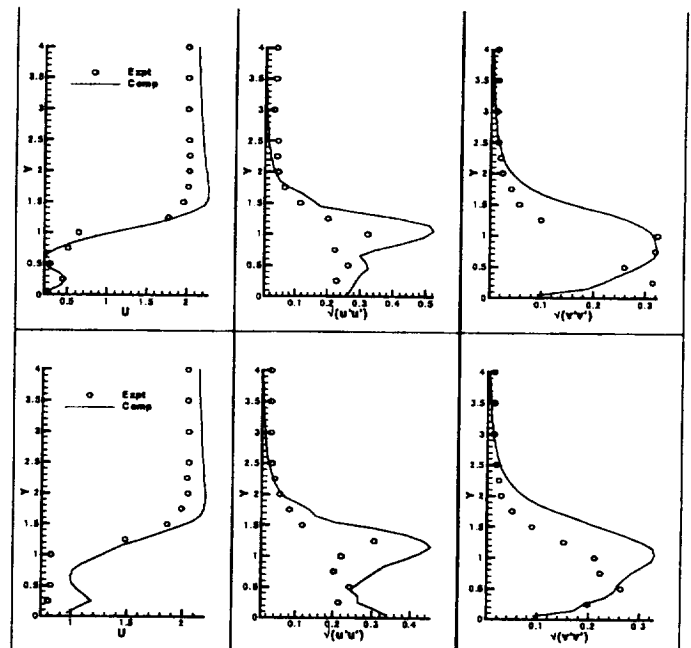


Figure 2b: Comparison of X component of mean velocity, rms components  $\sqrt{u'u'}$  and  $\sqrt{v'v'}$  at  $X/D = 3.0, 5.0$  respectively on the jet center plane ( $Z/D = 0.0$ ) for normal jets (Experimental data is from Ajersch et al 1995).

The vorticity contours of  $\omega_y$  are shown at location  $Y/D = 0.1$  from the wall (Figure 5). Significant entrainment of the crossflow into the wake region is evident, and the footprints of the coherent wake vortices (Fric and Roshko, 1994) can be clearly seen in the figure. For the 90° injection, the blockage effect is greater, and the velocity vectors in Fig. 5 indicate that the approaching crossflow is deflected laterally to a much greater degree by the 90° jet compared to the inclined jet. Behind the jet, there is stronger crossflow entrainment into the wake region for 90° injection, and clear evidence of wake vortices or vertically oriented eddies are observed. For 30° injection, since the jet is much closer to the wall, evidence of wake vortices (with complete

rollup) is not as strong in the instantaneous snapshot in Fig. 5. In both the 30° and 90° injection cases, it is observed that associated with the sweep of the crossflow boundary layer into the wake region, there is also an ejection of the wake fluid away from the jet centerplane. This behavior is more clearly observed in the 90° injection case. There is also greater excursion of the wake vortices in the lateral direction for the 90° injection and this is representative of the greater spreading of the jet. It is worth noting that in the instantaneous snapshots, no symmetry is preserved along the jet centerplane, and crossflow entrainment is seen to cross over the centerplane from one half of the jet to the other half (particularly for the 90° injection). It is also observed that the flow structures in the wake are stronger at 90° injection, with the maximum vorticity magnitude for the 90° injection nearly 75% greater compared to the 30° injection. This is due to the stronger crossflow entrainment for the 90° injection case. Kelso et al (1993, 1996) presented flow visualizations for these unsteady upright wake vortices. The vorticity at the jet-crossflow shear layer as well as the vorticity generated at the wall encounters the critical points in the flow field downstream to the hole. The vorticity generated at the wall and within the hole is stretched and re-oriented by mean velocity gradients to give rise to such flow structures (Figure 13 and 14).

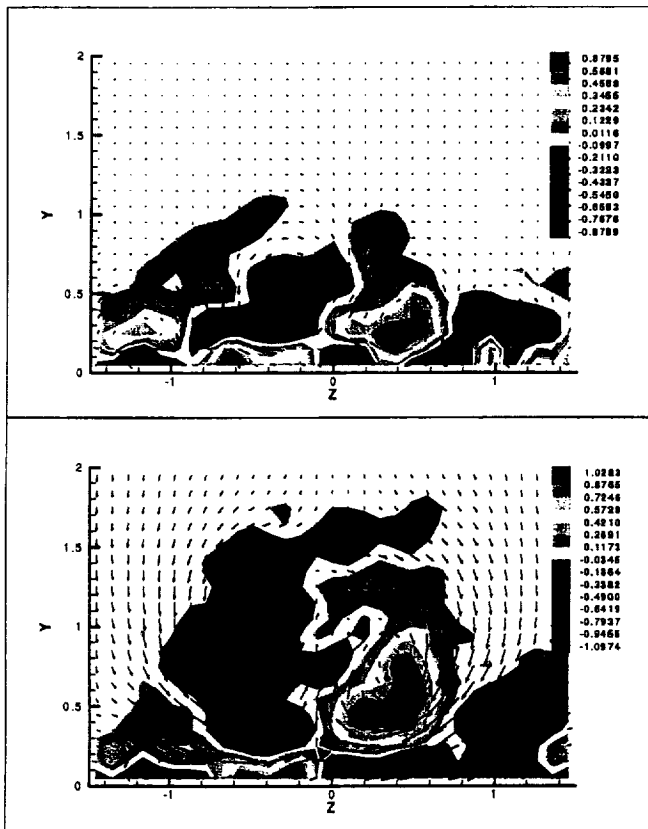


Figure 3: Contours of  $\omega_x$  and time averaged velocity vectors at  $X/D = 5.0$  for jet inclination angles 30° and 90°.

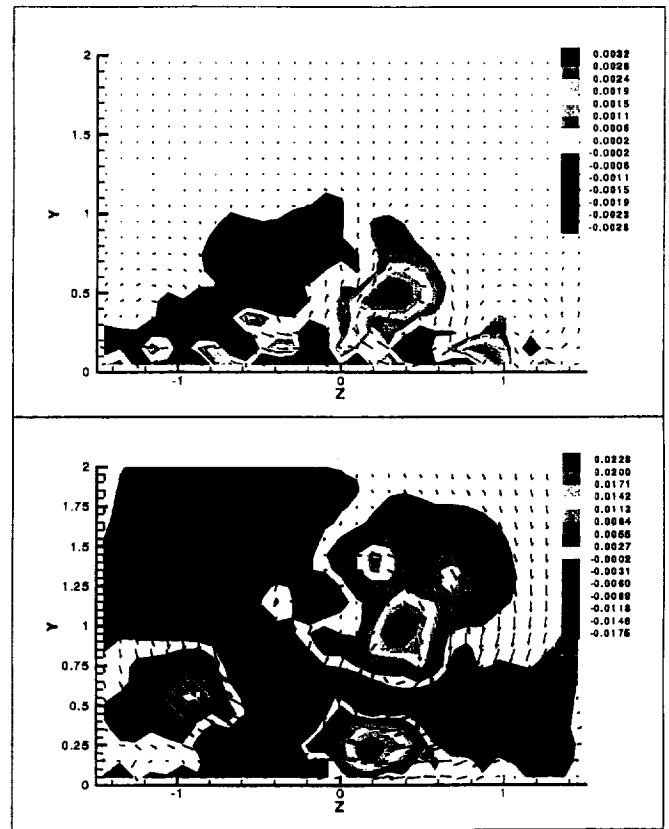


Figure 4: Contours of  $v'w'$  and time averaged velocity vectors at  $X/D = 5.0$  for jet inclination angles 30° and 90°.

The contours of turbulent stress  $u'w'$  that correspond to the vorticity contours in Fig. 5 are presented in Figure 6. As for the magnitude of  $\omega_y$ , the magnitude of  $u'w'$  is lower for inclined

jet, with peak values for the inclined jet lower by a factor of 2. Since  $u'w'$  represents the turbulent stress in the x-z plane, its magnitude is indicative of the extent of turbulent transport of momentum in the lateral direction (Andreopoulos and Rodi, 1984). The greater lateral transport in the 90° injection is evident from a comparison of the velocity vectors, where the influence of the jet clearly extends over a wider spanwise region for the 90° injection. The  $u'w'$  magnitude on this plane appears to be correlated with the magnitude of  $\frac{\partial W}{\partial x}$  and  $\frac{\partial U}{\partial z}$ , indicating the applicability of the gradient approximation for the turbulent stress. The production of this stress is primarily due to  $u'v'$  component working on  $\frac{\partial W}{\partial y}$  and  $v'w'$  component acting on  $\frac{\partial U}{\partial z}$ . Along the edges of the jet on the leeward side of hole, we observe the small regions of opposite signs for  $u'w'$ . After the jet exit, the presence of strong lateral gradient of streamwise velocity determines the local spreading of the jet around the hole. The magnitude of  $u'w'$  at this location decreases as the injection angle is increased. Further downstream, the vertical gradient of spanwise velocity component comes into play and attributes to the higher levels of  $u'w'$  and hence to the increase in the lateral spreading of jet.

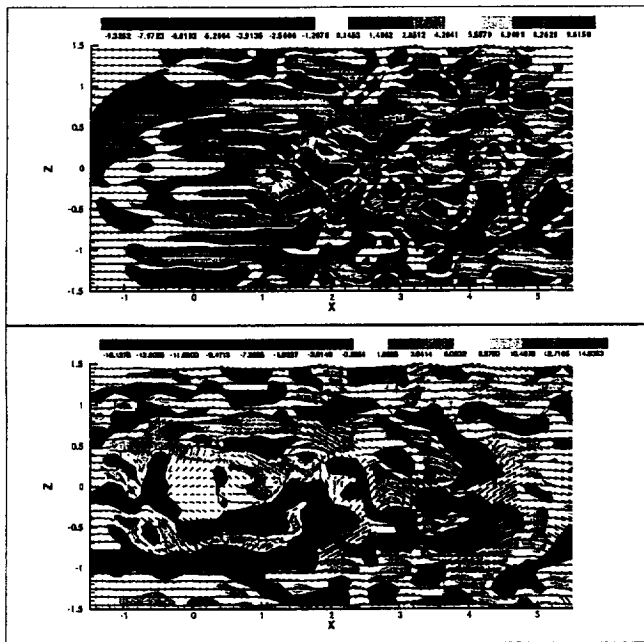


Figure 5: Contours of  $\omega_y$  and instantaneous velocity vectors at  $Y/D = 0.1$  for jet inclination angles 30° and 90°.

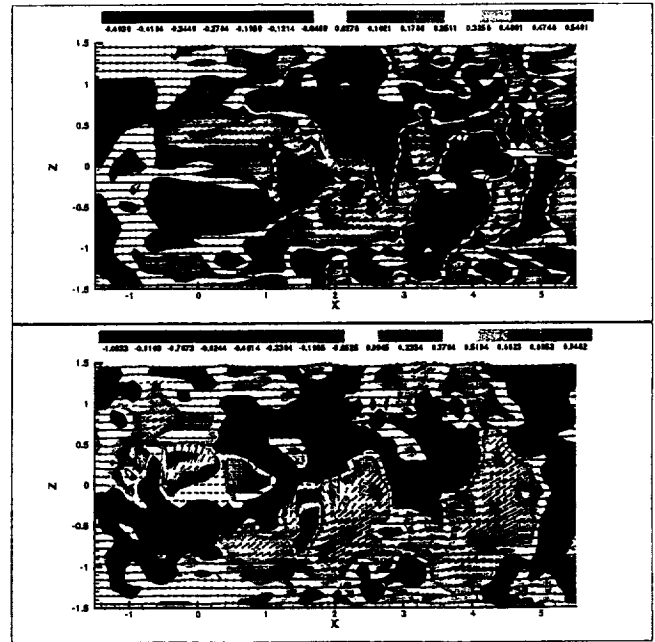


Figure 6: Contours of Reynolds stress  $u'w'$  at  $Y/D = 0.1$  for jet inclination angles 30° and 90°.

The contours of the spanwise vorticity  $\omega_z$  along the center plane of the jet ( $Z/D=0$ ) are shown in Figure 7. The substantially greater vertical penetration for the 90° jet-injection case is evident in Fig. 7, with the jet penetrating upwards up to nearly 1.75D for the 90° jet-injection compared to less than 0.75D for the 30° jet-injection. The spanwise rollers on the leeward side of the jet are clearly evident in the 90° jet-injection case, consistent with the experimental

observations of Fric and Roshko (1994) and Kelso et al. (1993, 1996). However, for the 30° jet-injection, the proximity of the jet to the wall damps the spanwise vorticity, and distinct spanwise rollers are not apparent in the instantaneous picture in Figure 7. The near-wall region clearly shows large scale sweep (instantaneous flow directed toward the surface) and ejection events (instantaneous flow directed away from the surface); this behavior is again more evident in the normal-injection case.

The development of the horseshoe vortex upstream of the jet can be clearly seen in the 90° jet-injection case in the  $\omega_z$  contours in Figure 7 and also in the  $\omega_z$  contours in Figure 12. For this case,  $\omega_z$  over the jet-hole region can be clearly observed in Figure 12, indicating the potential for crossflow ingestion into the hole region. For the 30° jet-injection case, the potential for such ingestion appears to be reduced.

The contours of the turbulent stress  $u'v'$  are presented in Figure 8. The contours of  $u'v'$  are mostly negative, and hence, the production of  $u'w'$  becomes positive in the regions where the vertical gradient of spanwise velocity is positive. This happens predominantly at downstream location of hole around the CVP. The greater production of  $u'w'$  at higher turbulence intensity levels enhances the lateral spread of the jet (Figure 5 and 6). The negative levels of  $u'v'$  correspond to the mixing layer at the leeward side of jet. For normal injection of coolant jets, the positive levels of  $u'v'$  are observed below the negative levels at downstream locations closer to the wall. These correspond to the wake region of the jet. Again, the magnitude of this stress is greater for 90° case.

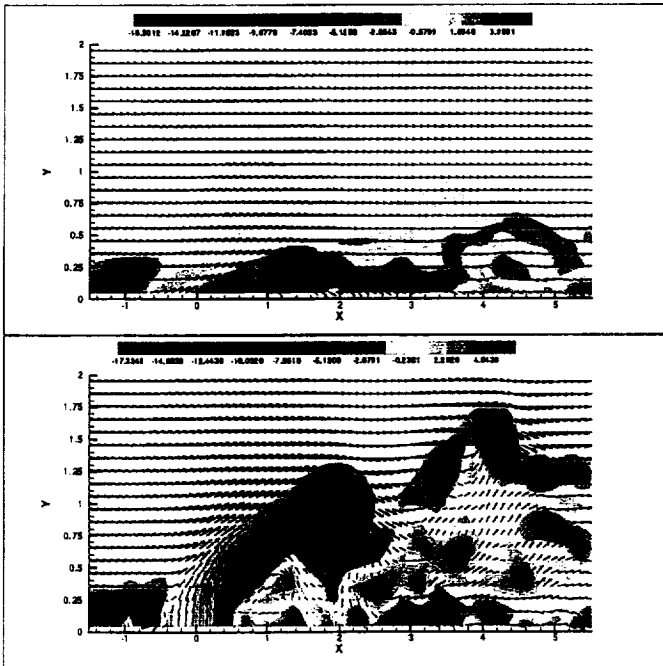


Figure 7: Contours of  $\omega_z$  and instantaneous velocity vectors at  $Z/D = 0.0$  for jet inclination angles 30° and 90°.

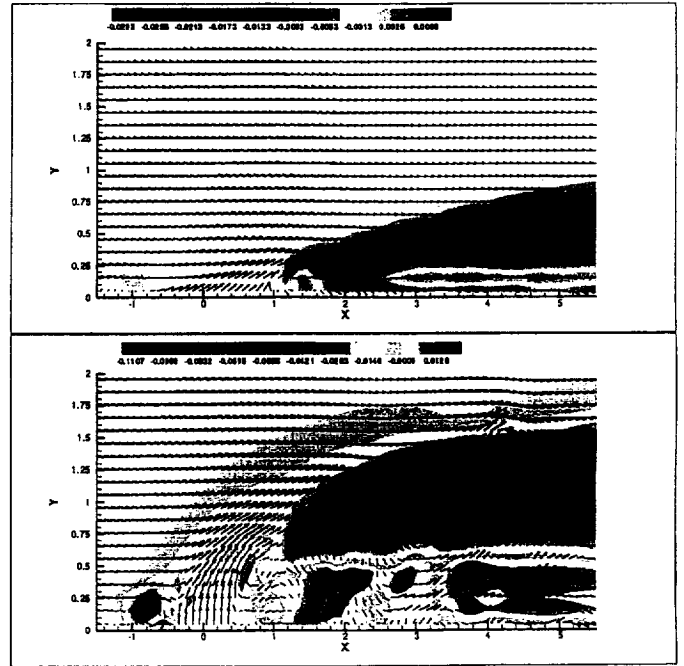


Figure 8: Contours of Reynolds stress  $u'v'$  at  $Z/D = 0.0$  for jet inclination angles 30° and 90°.

Figure 9 presents the pressure contours along the jet centerplane ( $Z/D=0$ ). The pressure gradients are expectedly larger for the  $90^\circ$  jet-injection case. The adverse pressure gradient upstream of the jet is clearly evident, and the signature of the horseshoe with a pressure-defect core can be seen. For  $90^\circ$  jet-injection, the spanwise rollers are clearly identified by the series of closed pressure contours. The pressure contours for the  $30^\circ$  jet-injection case are relatively more uniform downstream of the jet hole, and no evidence of spanwise rollers can be seen in the pressure contours.

The contours of skin friction coefficient on the wall are presented in Figure 10, and these are correlated with the magnitude of the  $\omega_x$ ,  $\omega_y$ ,  $\omega_z$  vorticity above the wall (Chong et al, 1998) shown in figures 11, 5 and 12 respectively. The low values of skin friction are representative of flow separation. In case of inclined jets, the flow separation region is small. For normal injection case, the horseshoe vortex in front of the jet is a very strong flow structure with a system of three eddies as shown in the  $\omega_z$  vorticity contours. The skin friction coefficient distribution upstream of the jet appears to reflect this behavior. The same correlation with  $\omega_z$  can be seen upstream of the inclined jet. However, the distribution of skin friction coefficients in the wake of jets is predominantly aligned in the streamwise direction and correlates best with  $\omega_x$  contours.

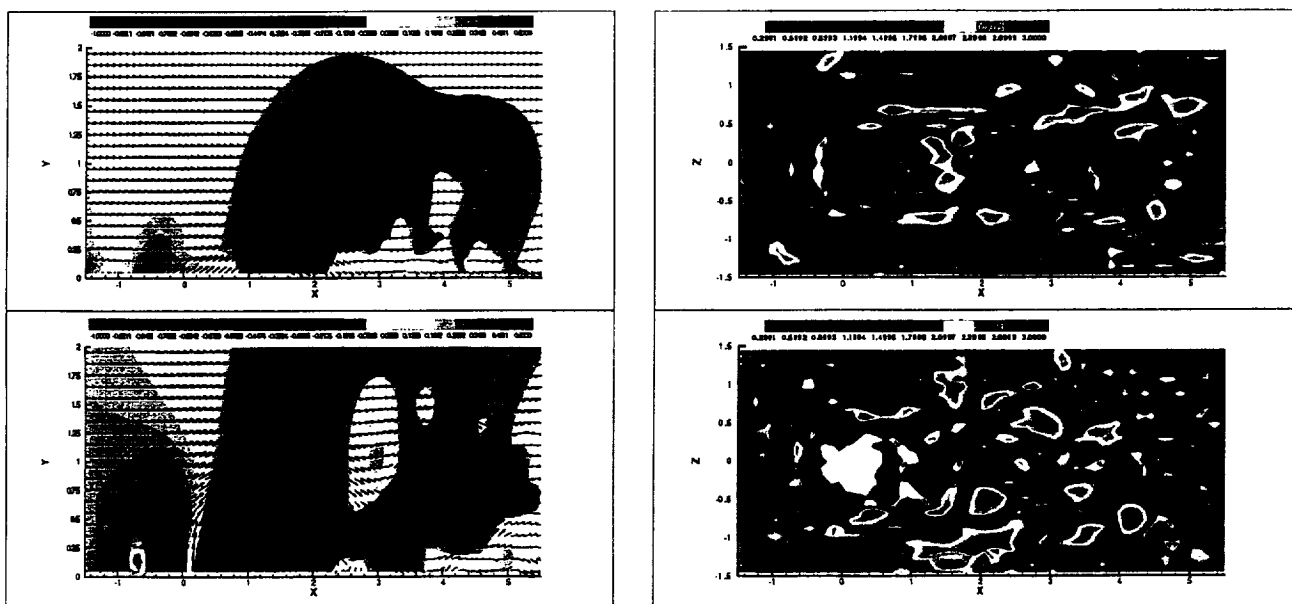


Figure 9: Contours of pressure and instantaneous velocity vectors at  $Z/D = 0.0$  for jet inclination angles  $30^\circ$  and  $90^\circ$ . Figure 10: Contours of skin friction coefficient at  $Z/D = 0.0$  for jet inclination angles  $30^\circ$  and  $90^\circ$ .

The particle traces are presented in Figures 13 (in the X-Z horizontal plane) and 14 (in the X-Y vertical plane) for the normal injection case to explain the development of the unsteady upright wake vortices. As stated earlier, the signatures of these wake vortices can be observed on a X-Z plane parallel to the wall (Figure 5). The particle traces are rendered with the magnitude of the

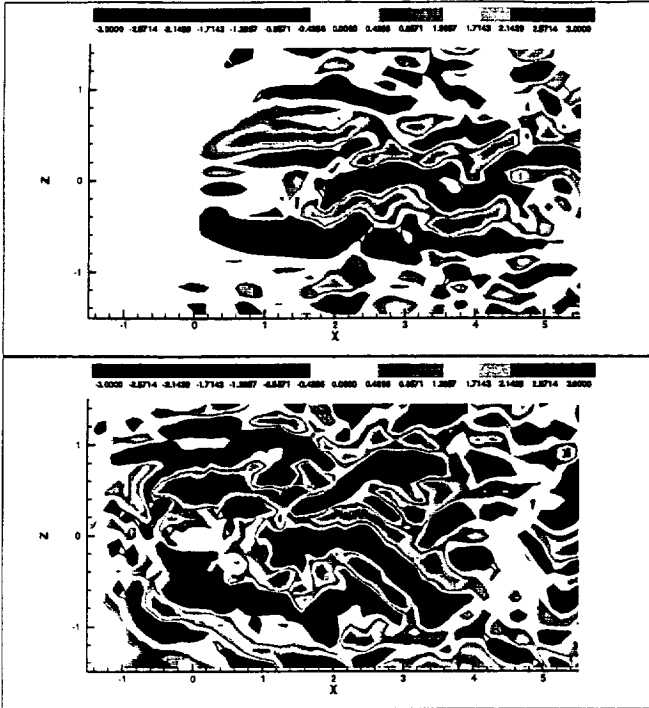


Figure 11: Contours of  $\omega_x$  at  $Y/D = 0.2$  for jet inclination angles  $30^\circ$  and  $90^\circ$ .

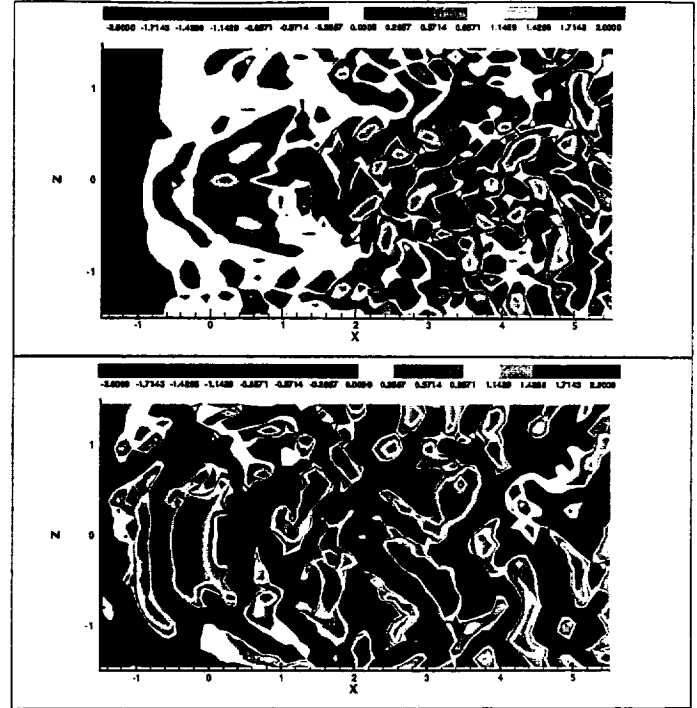


Figure 12: Contours of  $\omega_z$  at  $Y/D = 0.2$  for jet inclination angles  $30^\circ$  and  $90^\circ$ .

the Y component of vorticity. When the streamline is perpendicular to the wall and contains vorticity, we can deduce that the streamline and the vorticity are associated with the wake vortices. There appear to be three distinct mechanisms by which the wake vortices are generated. One mechanism for the generation of upright vortices comes from the crossflow entrainment into the wake region, and as shown in Figure 14, a streamline that originates in the crossflow boundary layer is entrained laterally into the wake region and is then deflected and entrained upwards leading to streamlines containing Y-vorticity that are perpendicular to the wall. The streamlines bend to the upright position close to the centerplane. This mechanism has been reported in the flow visualization pictures of Fric and Roshko (1994) and Kelso et al. (1993) where, close to the centerplane, the entrained crossflow forms a wall vortex which is reoriented into an upright wake vortex. A second mechanism, shown in Figure 13, stems from the deflection and entrainment of the horseshoe vortex originating upstream of the jet. For the particles just upstream of the jet exit (Figure 13), and originating from the horseshoe vortex, the streamlines are deflected in the wake to the upright position around  $1.5D$  from the jet center. There is significant vorticity present along these almost vertical lines indicating the core of wake vortices. Therefore, one can conclude that the major contribution to these upright wake vortices comes up from the re-orientation of streamlines in the vicinity of horseshoe vortex rather than the wall vortex which is generated by the crossflow entrainment. The third mechanism for the generation of Y-vorticity in the wake arises from the jet-crossflow interaction along the spanwise interfaces of the jet. Evidence of this can be seen in Figure 5.

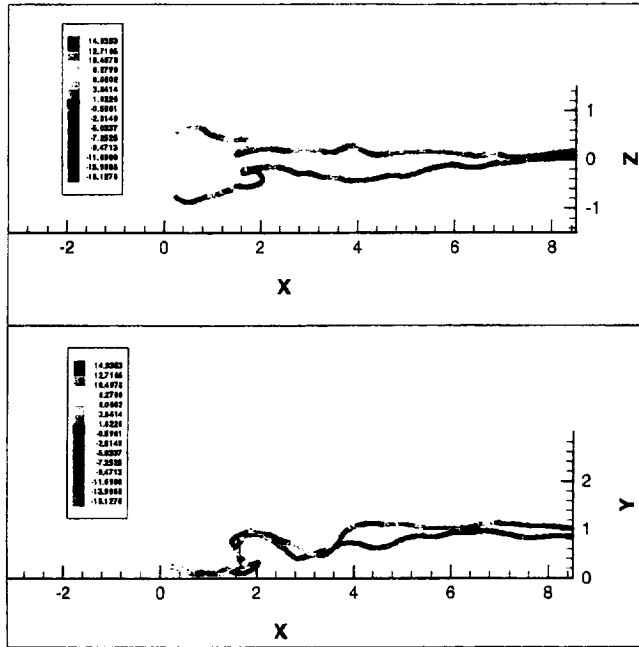


Figure 13: Particle traces originating from the location near the jet exit (near horseshoe vortex). ( $X=0.3D, Y=0.3D, Z=\pm 0.7D$ )

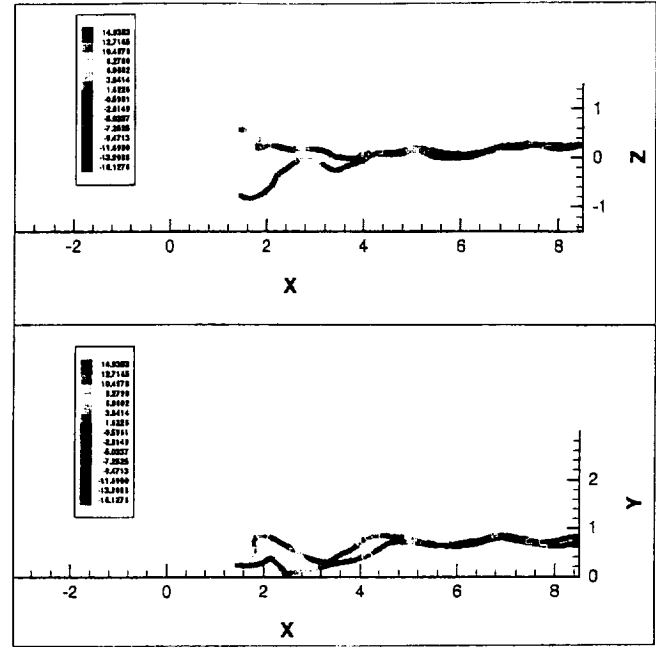


Figure 14: Particle traces originating from the location of crossflow entrainment (near wall vortex). ( $X=1.5D, Y=0.3D, Z=\pm 0.7D$ )

## CONCLUDING REMARKS

Large eddy simulations of the jet-in-crossflow for two jet injection angles were performed. The results obtained are consistent with the experimental observations of various researchers (Andreopolous and Rodi, 1984, Fric and Roshko, 1994, Ajersch et al, 1995, Findlay et al, 1996, Kelso et al, 1996). The following represent some of the major observations made in this study.

- The dispersion of jet in the mainstream is distinctly different for the two different injection angles of 90-degrees and 30-degrees (Ajersch et al (1995) and Findlay et al (1996)). Significantly greater penetration and mixing of the jet with the crossflow is observed for the normally-injected jet.
- Large pressure gradients in the normal injection case indicate larger separation regions and lead to reduction in the wall shear stress.
- The skin friction coefficient at the wall behind the jet correlates with the streamwise vorticity. For normal injection, the horseshoe vortex in front of the jet is responsible for low skin friction values upstream of the jet.
- The shear stress  $u'w'$  magnitude correlates well with the lateral spreading of the jet. The shear stress  $v'w'$  acts to damp the secondary vortex motions while  $u'v'$  controls the jet penetration and the mixing at the jet-mainstream interface. Normal injection of jets is associated with greater magnitudes of these turbulent shear stresses, and is responsible for the observed greater penetration of the jet and greater mixing between the jet and the mainstream.

## REFERENCES

- Ajersch, P., Zhou, J.M., Ketler, S., Salcudean, M. and Gartshore, I. A. (1995), *Multiple jets in a crossflow: detailed measurements and numerical simulations*, ASME 95-GT-9.
- Andreopoulos, J. and Rodi, W. (1984), *Experimental investigation of jets in a crossflow*. J. Fluid Mech., Vol. 138, pp. 93-127.
- Andreopoulos, J. (1985), *On the structure of jets in a crossflow*. J. Fluid Mech., Vol. 157, pp. 163-197.
- Bardina, J, Ferziger, J.H. and Reynolds, W.C. (1983), *Improved turbulence models based on large eddy simulations of homogeneous, incompressible turbulent flows*, Report TF-19, Thermosciences Div., Eng., Dept. Mech. Stanford Univ.
- Batchelor, G.K. (1953), *Theory of homogeneous turbulence*, Cambridge University Press.
- Chong, M.S., Soria, J., Perry, A.E., Chacin, J., Cantwell, B.J. and Na, Y. (1998), *Turbulence structures of wall-bounded shear flows found using DNS data*, J. Fluid Mech., Vol. 357, pp. 225-247.
- Chorin, A.J. (1967), *A numerical method for solving incompressible viscous flow problems*, J. Comp. Phy., Vol. 2 pp. 12-26.
- Coelho, S.L.V. and Hunt, J.C.R. (1989), *The dynamics of the near field of strong jets in crossflows*, J. Fluid Mech., Vol. 200 pp. 95-120.
- Dubois, T., Jauberteau, F. and Temam, R. (1999), *Dynamic multilevel methods and the numerical simulation of turbulence*, Cambridge University Press.
- Findlay, M.J., He, P., Salcudean, M. and Gartshore, I. A. (1995), *A row of streamwise-inclined jets in crossflow: measurements and calculations*, ASME 96-GT-167.
- Fric, T.F. and Roshko, A. (1994), *Vortical structure in the wake of a transverse jet*. J. Fluid Mech., Vol. 279, pp.1-47.
- Garg, V. K., and Gaugler R. E., 1995 "Effect of velocity and temperature distribution at the hole exit on film cooling of turbine blades", *ASME paper 95-GT-2*
- Garg, V. K., and Gaugler R. E., 1994 "Prediction of film cooling on gas turbine airfoils", *ASME paper 94-GT-2*
- Ghosal, S. (1999), *Mathematical and physical constraints on large eddy simulation of turbulence*, AIAA Journal, Vol. 37, no. 4, pp.425-433.
- Ghosal, S. and Moin, P. (1995), *The basic equations for the large eddy simulations of the turbulent flows in complex geometry*, J. Comp. Phy., Vol. 118, pp.24-37.
- Jones, W. P. and Wille, M. 1996 "Large eddy simulation of a round jet in crossflow" *Engineering Turbulence Modeling and Experiments* 3. Ed. Rodi, W. and Bergeles, G. pp.199-209
- Jordan, S.A.(1994), *Use of the large eddy simulation dynamic model for turbulent shear driven cavity flows*, ASME FED-Vol. 184 pp. 141-150.
- Kelso, R.M., Delo, C. and Smits, A.J. (1993), *Unsteady wake structures in transverse jets*, Fluid Dynamics Panel Symposium, UK, AGARD-CP-534.
- Kelso, R.M., Lim, T.T. and Perry, A.E. (1996), *An experimental study of round jets in crossflow*, J. Fluid Mech., Vol. 306, pp.111-144.
- Kim, S.W., and Benson, T. J. 1992 "Calculation of a circular jet in crossflow with a multiple-time-scale turbulence model" *Int. J. Comp. Phys.* Vol 59. pp. 308-315
- Patankar, S. V. Basu, D. K. and Alpay, S. A., 1977 "Prediction of the three-dimensional velocity field of a deflected turbulent jet" *Trans. SME I: J. Fluids Engng* 99, pp. 758-762

- Scotti, A., Meneveau, C. and Fatica, M. (1997), *Dynamic Smagorinsky model for anisotropic grids*, Phys. Fluids. Vol. 9 pp. 1856-1858.
- Speziale, C.G. (1985), *Galilean Invariance of subgrid scale stress models in large eddy simulation of turbulence*, J. Fluid Mech. Vol. 156, pp. 55-62.
- Sykes, R. I., Lewellen, W. S. and Parker, S. F. 1986 "On the vorticity dynamics of a turbulent jet in a crossflow" *J. Fluid Mech.* vol. 80, pp. 49-80
- Yuan L.L., and Street, R. L. 1996 "Large Eddy Simulation of a Jet in Crossflow" *ASME Fluids Engineering Division* Vol. 242, pp.253-260
- Zang, Y., Street, R.L. and Koseff, J.R. (1993), *A dynamic mixed subgrid scale model and its application to turbulent recirculating flows*, Phys. Fluids A Vol. 5 no. 12 pp. 3186-3196.
- Zhou, Y., Vahala, G. and Hossain, M. (1989), *A critical look at the use of filters in large eddy simulations*, Phys. Lett. A Vol. 139 no. 7 pp. 330-332.

## CHAPTER VIII

### REYNOLDS-AVERAGED-NAVIER STOKES (RANS) SIMULATIONS OF NORMAL FILM COOLING JETS IN CROSSFLOW

#### ABSTRACT

This study investigates the performance of several existing turbulence models for the prediction of film coolant jet in a crossflow. Two equation models employing  $k$ - $\epsilon$  and  $k$ - $\omega$  closures, broadly categorized as high Reynolds number formulations, low Reynolds number formulations, DNS based formulation and non-linear formulations have been used to simulate the flow. In all, seven different turbulence models have been tested. Predictions with different models have been compared with experimental results of Ajersch et al. (1995) and with each other to critically evaluate model performance. The assessment of models has been done keeping in mind that all models have been formulated for wall bounded flows and may not be well suited for the jet-in-a-crossflow situation. Close agreement with experimental results was obtained at the jet exit and far downstream of the jet injection region, but all models typically overpredicted the magnitude of the velocities in the wake region behind the jet. The present study clearly underscores the deficiencies of the current models, and demonstrates the need for improvements.

#### NOMENCLATURE

$C_\mu, C_{\epsilon 1}, C_{\epsilon 2}$	empirical constants appearing in $k$ - $\epsilon$ turbulence models
$D$	function used in the Low-Reynolds number $k$ - $\epsilon$ model; also jet diameter (=jet width)
$E$	function used in the Low-Reynolds number $k$ - $\epsilon$ model
$f_1, f_2, f_\mu$	empirical functions of turbulent Reynolds number in Low-Re $k$ - $\epsilon$ models
$f_3$	empirical function used in the Mansour-Rodi $k$ - $\epsilon$ model
$k$	turbulent kinetic energy
$P$	turbulence production term
$R$	jet-to-crossflow velocity ratio
$Re_t$	turbulent Reynolds number
$U, V, W$	mean velocity components in $x$ , $y$ , and $z$ directions respectively
$V_j$	mean jet velocity
$\overline{u'_i u'_j}$	Reynolds stresses
$\overline{u'^2}, \overline{v'^2}, \overline{w'^2}$	normal stresses w.r.t $x$ , $y$ , $z$ axes
$\overline{u'v'}, \overline{v'w'}, \overline{u'w'}$	shear stresses
$x$	coordinate in the cross-stream direction
$y$	coordinate normal to the wall
$z$	coordinate in the streamwise direction

#### Greek Letters

$\epsilon$	rate of dissipation of kinetic energy
$\tilde{\epsilon}$	modified dissipation rate
$\omega$	specific dissipation rate ( $=\epsilon/k$ )

$\mu, \mu_t$	dynamic and turbulent viscosity
$\nu, \nu_t$	kinematic and turbulent kinematic viscosity
$\rho$	density
$\sigma$	Prandtl number
$\alpha, \alpha', \beta'$	empirical functions in the k- $\omega$ model
$\beta$	empirical constant in the k- $\omega$ model

## INTRODUCTION

Film cooling of turbine blades is commonly employed to provide effective blade cooling that is needed to ensure long life of the turbine blades and to permit higher turbine inlet temperatures. The interaction of the coolant jet with the crossflow produces a highly complex, three-dimensional flow field in the vicinity of the jet injection. The flow is characterized by both large scale coherent structures and small scale turbulence, and the mixing process is controlled by the dynamics of these structures. The coherent structures of primary importance have been identified in the published literature to be jet shear-layer vortices which dominate the initial portion of the jet, the horseshoe vortices which wrap around the base of the jet, the counter rotating vortex pair (CRVP) which results from the impulse of the jet on the crossflow and the wake-vortices formed in the wake of the jet. Accurate prediction of such structures are necessary to correctly predict the jet penetration and reattachment length that are important for heat transfer calculations and the optimization of film cooling effectiveness.

Several experimental studies (see Fric and Roshko, 1994; Lee et al., 1994; Kelso et al., 1996, for example) and numerical investigations (see Garg and Gaugler, 1997; Kim and Benson, 1993; Walters and Leylek, 1997, for example) of a jet-in-crossflow have been reported. In the numerical studies, the primary approach adopted has been to use the Reynolds-Averaged Navier Stokes (RANS) solver which requires the prescription of a turbulence model. The two equation turbulence models (k- $\epsilon$  and k- $\omega$ ) have been used most extensively to simulate a jet-in-crossflow with varying degrees of success. A systematic study of film cooling by Demuren et al. (1986) revealed that the very complex flow field established behind the jet was not properly resolved and the turbulent mixing process was crudely simulated with the eddy viscosity model. Demuren (1993) also carried out computations using a multi-grid method and a second-moment closure model to approximate the Reynolds stresses. Although a fairly good prediction of mean flow trends was reported, there was considerable uncertainty regarding the accuracy of jet penetration height. Multigrid calculations by Claus and Vanka (1990) failed to predict the horseshoe vortex even with a highly refined grid. This was attributed partly to the inability of the k- $\epsilon$  model to resolve the complex turbulence field. Findlay et al. (1996) included the plenum in the computational domain for streamwise inclined jets. The computations underpredicted the streamwise injection of fluid from the jet and the flow field was not in good agreement with experimental results for most of the domain. Ajersch et al. (1995) conducted an extensive experimental investigation and a companion numerical simulation using a low-Re k- $\epsilon$  model along with a non-isotropic extension to the effective viscosity for near wall turbulence. The streamwise velocity in the jet wake was overpredicted and the recirculation region behind the jet was found to be smaller and closer to the surface than that observed in the measurements. Noticeable overprediction of shear stresses was observed and the simulation could not capture the local minimum in kinetic energy which was measured in the wake region of the jet.

The varied and often conflicting investigations carried out so far motivate the present study where several existing turbulence models and their performance in predicting the film cooling flow behavior is evaluated. The focus of this work is on the fluid dynamical behavior of the jet, and the ability of the turbulence models to correctly reproduce the expected physical behavior. Therefore heat transfer predictions are not included in the present work.

## PROBLEM DESCRIPTION

The film cooling configuration chosen corresponds to the experimental study of Ajersch et al. (1995) where measurements are presented for normal injection through square holes. The physical domain in Fig. 1 shows a single row of six square jets on a flat plate which represents the turbine blade surface. The computational domain is chosen to be a periodic module and is shown in Fig. 2 and by the dotted lines in Fig. 1. The experimental investigation for the above configuration was carried out for velocity ratios  $R=0.5, 1.0$  and  $1.5$ . However, the computations have only been carried out for the lowest velocity ratio of  $R=0.5$ , and the general flow characteristics for this case as predicted by the several models are evaluated by comparison with the measurements.

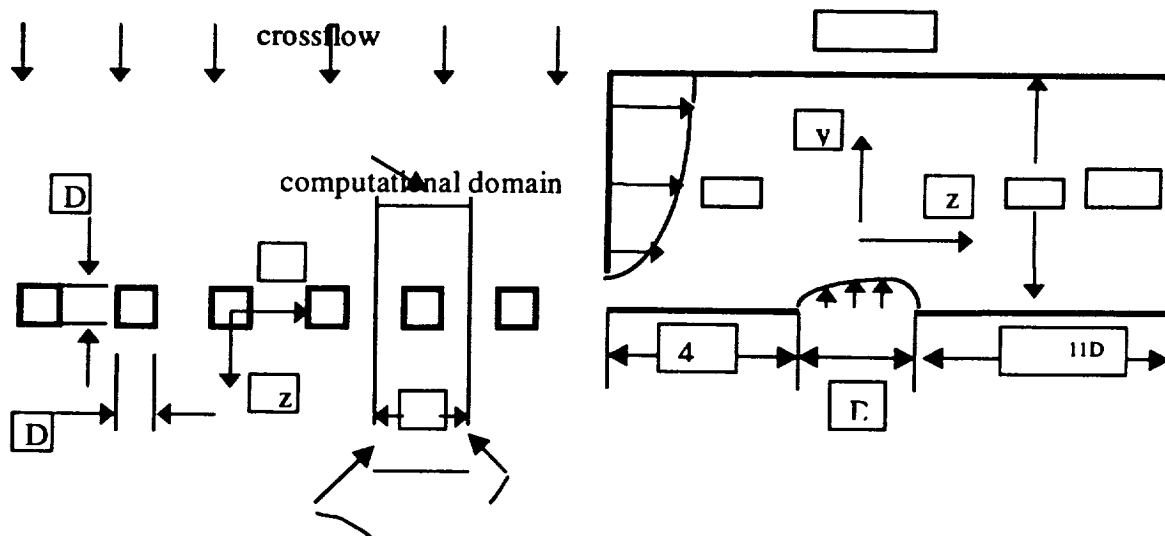


Fig. 1: Schematic of the physical problem Fig. 2: Side view of the computational domain

For the turbulence model to be viable, the main features of the flow are expected to be predicted correctly. In this work, we evaluate the performance of the models not only by the quantitative comparisons with the measurements reported by Ajersch et al. at a few selected locations (that do not provide a complete description of all the flow features), but also by examining if the models accurately predict the dominant features of the flow field.

## GOVERNING EQUATIONS

The steady state Reynolds averaged Navier Stokes equation contains the Reynolds stress tensor  $-\rho\overline{u_i u_j}$  which needs to be modeled by a closure approximation. The accuracy of the prediction is based on the adequacy of the closure expressions in capturing the flow physics. The different closure approximations described below include the high-Re models where the near-

wall sublayer effects are not resolved, various forms of the low Re models where the near wall damping effects are represented by different empirical expressions, and the non-linear models where turbulence anisotropy is incorporated through non-linear corrections to the linear stress-strain relations assumed in the linear turbulence models.

## TURBULENCE MODELS

A number of different models based on the k- $\epsilon$  and k- $\omega$  closures were used in this study. The various models, under appropriate categories, are listed below:

### 1 ) High-Re k - $\epsilon$ model

In the standard k- $\epsilon$  model (see Launder and Spalding, 1974) the Reynolds stress is modeled as

$$-\overline{\rho u_i' u_j'} = -\frac{2}{3} \rho k \delta_{ij} + 2\mu_t \overline{S}_{ij} \quad (1)$$

The eddy viscosity  $\mu_t$  is related to the turbulent kinetic energy k and to its dissipation rate  $\epsilon$  as

$$\mu_t = \rho C_\mu \frac{k^2}{\epsilon} \quad (2)$$

Note that eqn. (1) represents a linear relationship between the turbulent stress and the rate of strain, and forms the basis for all linear two-equation models.

The distributions of k and  $\epsilon$  in the flow field is determined from their modeled transport equations (Launder and Spalding, 1974). The source terms in the modeled equations are given by:

$$S_k = P - \epsilon; \quad S_\epsilon = C_{\epsilon 1} (\epsilon/k) P - C_{\epsilon 2} (\epsilon^2/k) \quad (3)$$

where P is the production of turbulence ( $= -\overline{\rho u_i' u_j'} (\partial \overline{u}_i / \partial x_j)$ ). The high-Re model avoids the need to integrate the modeled equations right down to the wall by making use of the universal behavior of near wall flows. The standard wall-function approach is thus used to specify the wall boundary conditions for velocity. This is done either in the form of a wall shear stress expression from Couette flow analysis or alternatively by determining the diffusion coefficient on the wall such that the computed shear stress on the wall matches that obtained from the Couette flow analysis.

For the turbulence kinetic energy a zero value is specified at the wall, while the value of dissipation at a near wall point is set, using a local equilibrium assumption, as  $\epsilon = C_\mu^{3/4} k^{3/2} / (0.4\delta y)$ .

### 2 ) Low Re models

The low-Re models resolve the viscous sublayer adjacent to the solid walls and use damping functions that ensure the transition from turbulent stresses to viscous stresses near the wall. The low-Re versions of both k- $\epsilon$  and k- $\omega$  closure models have been used in this study.

**a ) Low- Re k - ε models**

The source terms for k and ε in for the low-Re model take the form :

$$S_k = P - \epsilon; S_{\bar{\epsilon}} = C_{\epsilon 1} f_1 \frac{\bar{\epsilon}}{k} P - C_{\epsilon 2} f_2 \frac{\bar{\epsilon}^2}{k} + E \quad (4)$$

$$\text{where } \bar{\epsilon} = \epsilon - D \quad \text{and} \quad \mu_t = C_{\mu} f_{\mu} \frac{k^2}{\bar{\epsilon}} \quad (5)$$

A number of different low Re models (see Patel et al., 1985) have been proposed depending on their use of the functions  $f_1$ ,  $f_2$ , and  $f_{\mu}$  and the terms D and E. The models used in this study are the Launder-Sharma model (Launder and Sharma, 1974) and the Lam-Bremhorst model (Lam and Bremhorst, 1981). These two models have been selected due to the asymptotic consistency of their functions in the near wall region as well as in the fully turbulent regime. The Launder Sharma model uses  $\bar{\epsilon}$  as the dissipation variable and therefore the term D must asymptote to the nonzero value of  $\epsilon$  on the wall and should vanish in the fully turbulent regime where  $\bar{\epsilon}$  must tend to  $\epsilon$ . The term D for the Launder-Sharma model satisfies both the limits as has been shown by Patel et al. (1985). The asymptotic limits of the damping functions  $f_2$ ,  $f_{\mu}$  and the term E are also consistent with expectations.. The Lam-Bremhorst model on the other hand solves for  $\epsilon$  itself and therefore the term D is prescribed as zero. The  $f_{\mu}$  function for this model shows the correct variation in the near wall region but tends to unity somewhat slowly as compared to the Launder-Sharma model. This model also employs the function  $f_1$  to model the appropriate growth of  $\epsilon$  in the region very close to the wall. The  $f_2$  function in this model is modified in order to yield a zero value on the wall. Thus the sink term in the  $\epsilon$  equation is damped leading to the expected rapid increase of viscous dissipation as the wall is reached.

**b ) Low-Re k - ω model**

The low-Re k-ε models suffer from the lack of appropriate wall boundary condition for ε which is specified mostly by ad-hoc empirical functions for the near wall flow. The choice of the specific dissipation rate ω is therefore sometimes preferred since the near wall ω behavior is known and therefore the boundary condition at the wall can be specified more accurately. The transport equations for k and ω are given by Wilcox and Traci (1976), and have the following source terms:

$$S_k = P - \rho \beta^* \omega k; S_{\omega} = \alpha \frac{\omega}{k} P - \rho \beta \omega^2 \quad (6)$$

where  $\mu_t$  is given as  $\mu_t = \alpha^* \sqrt{\omega}$ . In implementing this model, all standard functions and constants for the low-Re version of the model, as given by Wilcox and Traci (1976), have been used. The functions in this model serve the same purpose as in the low-Re k-ε models and their asymptotic behavior has also been found to be consistent.

**3 ) DNS based low-Re k - ε model**

Rodi and Mansour (1993) proposed an improved model for the ε equation and a new  $f_{\mu}$  function using DNS data for a channel flow. The ε-budget computation for the different terms in

the  $\epsilon$  equation was used in conjunction with scaling arguments to obtain the following modeled form of the  $\epsilon$  equation source term.

$$S_{\epsilon} = C_{\epsilon 1} \frac{\bar{\epsilon}}{k} P - C_{\epsilon 2} f_3 f_2 \frac{\bar{\epsilon}^2}{k} + E \quad (7)$$

The constants and expressions as proposed by Rodi and Mansour (1993) have been used here with one exception. The expression for  $f_3$  was given as:

$$f_3 = \exp \left[ 2(P/\epsilon)/0.3Re_t^{1/2} \right] \quad (8)$$

The choice of 0.3 in the above equation is related to the 0.3 value that the structure function ( $= -\overline{u'v'}/k$ ) assumes in the center of a channel for fully developed turbulence. Since the flow considered here does not represent a fully developed turbulent channel flow, the factor of 0.3 was found to be inappropriate, and empirical adjustment of this constant led to a value of 2.1.

#### 4) Non-linear low-Re Models

Experimental studies carried out for the flow situation being considered here have shown that the flow is highly anisotropic due to strong curvature effects and therefore the non-linear models listed below have been tested to evaluate their performance in this highly complex flow situation.

##### a) Mayong - Kasagi Model

Mayong and Kasagi (1990) proposed an anisotropic extension to the eddy diffusivity model deduced from the interrelationship among the fundamental processes in the kinetic energy budget. Two additional terms containing quadratic velocity gradients and kinetic energy gradients have been added to the standard linear model. The first of these terms has been derived from the interrelationship between production and dissipation terms in the kinetic energy equation, and plays the role of exhibiting anisotropic characteristics for each Reynolds stress component over the whole flow field except for the immediate vicinity of the wall. The second term added has been derived from the balance between the diffusion and dissipation terms so that the wall-limiting condition for the normal Reynolds stresses is satisfied. The second term however does not satisfy the general frame invariance necessary for the broadest range of application, because the invariant condition is not generally satisfied in the immediate vicinity of a plane interface where turbulence is quasi-two-dimensional due to the blocking of a normal velocity component. More details of the model are found in Mayong (1988).

##### b) Speziale Model

Speziale (1987) derived a non-linear model by means of an asymptotic expansion which satisfies both realizability and invariance requirements. This model is expected to incorporate the streamline curvature effects by introducing quadratic velocity gradient terms and is expected to do better in flows where the differences in normal stresses are significant. Although the use of the original Speziale model has been reported primarily in conjunction with wall-functions, it has been implemented here in a low-Re model form with the damping functions in the near-wall region obtained from the Launder-Sharma model.

## COMPUTATIONAL DETAILS

The modeled transport equations were solved using a three dimensional CFD code developed by the authors based on the SIMPLER algorithm (Patankar, 1980). A control volume based finite difference formulation that uses a second order accurate central difference scheme for the viscous terms and a power law based scheme for the convective terms has been used. In calculating the source terms in the equations for momentum conservation and turbulence quantities, the first and second order derivatives were calculated using the Fornberg algorithm (Fornberg, 1988) employing fourth order accurate centered differencing scheme for interior points and second order accurate one-sided differencing for boundary points. A staggered grid arrangement with velocity components stored at the cell faces and all other scalar quantities located at the grid points is employed to avoid checkerboard fields. The system of equations was solved with the Tridiagonal Matrix algorithm employing an under-relaxation procedure to aid convergence .

A non-uniform grid (59x60x140) was set up in the computational domain (Fig. 2) with grid points clustered near the bottom wall and around the jet. The jet injection region was resolved with a 19x19 mesh. Inlet profiles for both the crossflow (at  $Z/D=-4.5$ ) and at the exit of the jet-hole were provided from the experimental data of Ajersch et al (1995). The measured data at the crossflow inlet corresponded closely with the 1/7-th turbulent boundary layer profile with a boundary layer thickness of  $2D$ . At the jet-hole exit, all three velocity components plus their rms values were available from the measurements, and these were interpolated to prescribe the numerical boundary conditions for both the mean velocity and the turbulence kinetic energy. A periodic boundary condition was implemented in the spanwise direction representing a transverse row of injection holes while at the outlet the normal gradient of all variables was prescribed as zero. At the top plane, free-stream conditions from the measurements were specified.

The equations were non-dimensionalized with the mean jet velocity,  $v_j$ , and jet width,  $D$ , and computations were carried out at a Reynolds number ( $v_j D / \nu$ ) of 4700 for a blowing ratio of 0.5. The mass residual in each cell was determined from the continuity equation and the maximum residual was established as the criterion for assessing the overall convergence of the field. At residual levels of  $10^{-6}$  -  $10^{-7}$  the solution was found not to change and the solution was considered converged in this range. Grid independence was checked by comparing the 59x60x140 grid (nearly 0.5 million nodes) solution (using the low Re  $k-\epsilon$  Launder Sharma model) with a more refined 71x90x200 grid (nearly 1.28 million nodes). The difference in the solution on the two grids was found to be minimal (maximum difference in the velocity values was less than 3%) as shown in Fig. 3.

## RESULTS AND DISCUSSION

A discussion of the model predictions and comparisons with the measurements of Ajersch et al. (1995) will be presented next. The following nomenclature will be followed hereafter while referring to the various models. The high-Re model will be referred to as HRE, the Launder-Sharma model as LS, the Lam-Bremhorst model as LB, the Mansour-Rodi model as MR, the non-linear Speziale model as SP, the non-linear Mayong-Kasagi model as MK and the  $k-\omega$  model as KW.

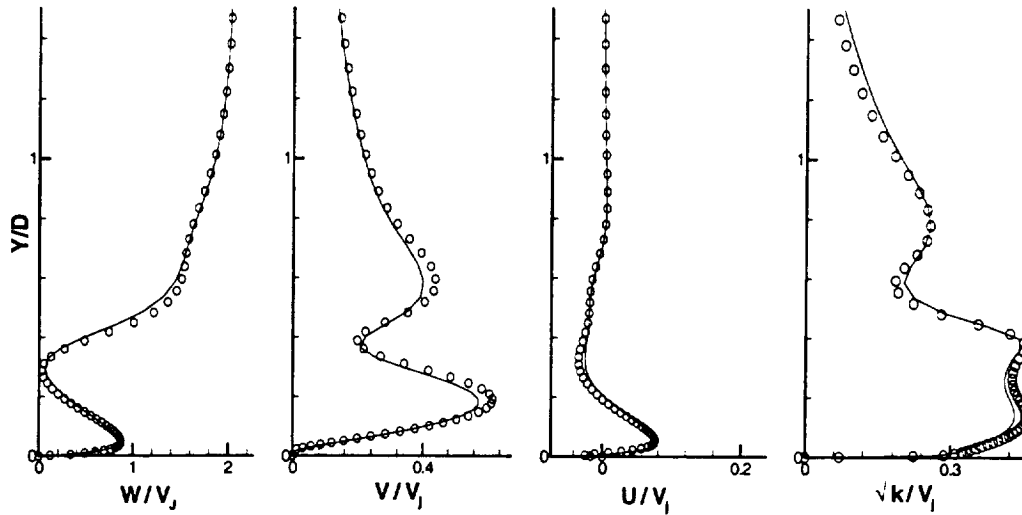


Fig. 3: Grid independence study with the LS model. Velocity and kinetic energy profiles at  $X/D=0$ ,  $Z/D=1$ :  $\circ$  71x90x200 grid; 59x60x140 grid.

### Mean Velocity and Turbulence Statistics

The mean velocity and turbulence kinetic energy profiles are compared with the experimental results of Ajersch et al. (1995) at two spanwise locations:  $X/D=0$  along the jet center plane in Fig. 4, and  $X/D=-0.5$  along the spanwise edge of the jet in Fig. 5. The figures show how the flow varies with distance  $Y/D$  from the wall at various downstream locations ( $Z/D=0, 1, 3, 5$  and  $8$ ). The main flow features namely the wake of the jet, the counter rotating vortex pair (CRVP) and the horse-shoe vortex are expected to be clearly evident along the  $X/D=0$  and  $0.5$  streamwise planes, and therefore comparison of model predictions with experimental data along these representative planes is likely to reveal how well the models capture the features of the flow. The flow features are also captured in the plots shown in Figs. 7 which present streamwise vorticity component superimposed by velocity vectors along a cross-stream plane.

Figure 4a shows the downstream development of the mean streamwise velocity ( $w/v_j$ ) along the jet center plane ( $X/D=0$ ). At the jet center ( $Z/D=0$ ), where the jet exit plane boundary condition are specified from experimental data, the model predictions compare well with measurements. One hole-diameter downstream of the jet ( $Z/D=1$ ), a reverse flow region close to the wall is observed in the measurements which is captured well by the HRE model, but all other models predict a much smaller reverse flow region. The differences in the length of the recirculation regions predicted by the various low-Re models and the HRE model is brought out very clearly by the vector plots presented later in Fig. 9. The HRE model behavior very close to the wall is strikingly different from the other models which typically show three distinct flow regions at this location - a wall-jet-like layer next to the wall with accelerating flow, a wake

region above it where low velocities are observed, and a shear layer with strong velocity gradients due to the velocity changing from low values at the top of the wake region to the free-stream value over a very short vertical distance. The wall-jet layer very close to the wall could not be validated as measurements very close to the wall was not available in the data set used in this study. However, several experimental investigations (Andreopoulos and Rodi, 1984) have revealed that a wall-jet structure does exist close to the wall even for low velocity ratio  $R$ , although this effect is stronger for the high  $R$  cases. At this location ( $Z/D=1$ ), immediately downstream of the jet, the low pressure in the wake of the jet induces laterally inward motion of the surrounding cross-flow fluid close to the wall towards the jet center-plane. The entrained fluid moves upwards, in the vicinity of the jet center-plane, towards the jet and it is then swept up by the bent-over jet (Fig. 9). The inward motion of the high momentum fluid towards the jet center plane close to the wall is partly re-oriented in the streamwise direction and leads to the formation of the wall-jet like structure (seen in Fig. 7).

Evidence of the wall-jet can also be seen from measurements at  $Z/D=3$  where there is a peak close to the wall and the velocities then drop to lower values in the wake region. The steep velocity gradient observed close to  $Y/D=1$  represents the shear-layer where the velocity changes from low values in the wake of the jet to the free-stream value. All models follow the experimental trends appropriately but typically over-predict the stream-wise velocity in the wake region. Also the shear-layer is closer to the wall which indicates that the wake-height is under-predicted at this center-plane location.

The large deviation of model predictions observed in the vicinity of the jet ( $Z/D$  between 1 and 3) indicate that the near field of the jet, influenced significantly by the dynamical behavior of the large-scale structures, is not properly modeled. The effect produced by the damping functions in the low- $Re$  models is therefore not accurate in the immediate vicinity of the jet.

At further downstream locations, measurements show that the velocity gradients in the wall-jet layer and the shear-layer are diminished, and flow recovery towards a boundary layer profile is observed. The velocity gradients are over-predicted in the wall-jet layer at  $Z/D=5$  while agreement with experimental results is better at  $Z/D=8$ . For  $Z/D$  greater than 3, the LB model shows the best agreement with experimental data. The LB model is known to give the correct asymptotic behavior  $-\overline{w'v'} \propto y^4$  in the near wall region due to the appropriate variation of the  $f_\mu$  functions in the immediate vicinity of the wall. The  $f_\mu$  function behavior of the LS model has been found to be more consistent in the fully turbulent regime and therefore it does not do as well as the LB model in the near wall region. The non-linear SP model does not show any significant improvements in the mean velocity field predictions and its trends are only slightly different from the LS model. This may in part be due to the fact that in the near wall region both these models employ the same damping functions and also that the non-linear quadratic terms introduced in the Reynolds stress terms in the SP model do not make any significant contribution. The MK model, at  $Z/D=5$  and  $Z/D=8$ , under-predicts the streamwise velocity gradients in the shear layer and consequently predicts a deeper penetration of the jet into the crossflow. The performance of the non-linear models cannot however be judged merely on the basis of mean velocity trends and a proper evaluation of the Reynolds stresses will be carried out in a later section in order to get the correct picture on these non-linear variants of the k- $\epsilon$  model.

The secondary motions in the cross-stream plane are evaluated by comparing the vertical velocity profiles in Fig. 4b and the cross-stream velocity in Fig. 4c. The vertical velocity distribution at the jet center ( $Z/D=0$ ) once again shows good agreement with experimental data

owing to the measured jet inlet conditions specified at the jet-exit plane. The large vertical velocity values ( $V/V_j$  greater than 1) are because the crossflow acts as a partial cover over the jet causing the jet to bend before leaving the jet exit and leads to the acceleration of the jet toward the downstream edge of the exit hole. In the reverse flow region, at  $Z/D=1$ , two peaks are recorded, the first peak off the wall is in the wake region where the reversing fluid is lifted up by the deflected jet, while the second peak corresponds to the deflection of the cross-stream over the jet. This trend is closely followed by the models although the peak values are predicted closer to the wall. This is primarily due to the predicted wake region being much closer to the wall and the jet penetration being under-predicted by the models in the jet center-plane. Additionally, the models differ in their prediction of the first peak value off the wall while the second peak is the same for all the low-Re models. The LB model predicts the lowest peak value while the MK model records the highest first peak value with the other models lying in between. These differences are related to the behavior of the damping functions for the various models with the LB model functions being asymptotically consistent while the  $f_\mu$  function of MK model tends to unity somewhat slowly. The dependence on these functions is further emphasized by the observation that the second peak is the same for all the low-Re models since the functions tend to unity at larger distances from the wall.

Further downstream, at  $Z/D=3$ , measurements suggest that, as for the streamwise velocity, the wake region is not properly predicted with the predictions showing a faster recovery. Measurements between  $Z/D=3$  and 8 show a negative velocity at the top of the bent-over jet which indicates that the cross-flow is coming down at this point. The downwash of the cross-flow as well as the low-velocity magnitudes in the wake region are not captured by the model predictions. This is probably due to the models predicting a smaller reverse flow region behind the jet which implies that the wake effect is not as strong as experimentally observed. The measurements continue to show a dual-peak structure at  $Z/D=3$ , while the predictions only show a single peak due to the faster flow recovery. The predicted magnitudes at  $Z/D=3$ , 5, and 8 show the same trends as at  $Z/D=1$ , with the KW model showing the largest peak values and the LB model showing the smallest magnitudes and the best agreement with the data. The behavior of the MK model at  $Z/D=5$  and  $Z/D=8$ , with the peak shifted upwards, is a consequence of the jet penetration being over-predicted at these locations.

The spanwise velocity ( $U/V_j$ ) presented in Fig. 4c should be zero along the jet center plane if the flow at all the inflow planes is symmetric. However, measurements indicate that the inflow at the jet exit plane ( $Y/D=0$ ) is not symmetric with the flow slightly skewed in the lateral direction. This asymmetry in the inlet profile is convected downstream, and is confirmed by the velocity measurements as well as the predictions at the jet exit ( $Z/D=0$ ) and immediately downstream of the jet ( $Z/D=1$ ). As the flow develops downstream, this asymmetry should reduce and the spanwise velocity across the jet-center-plane should become very small. The flow predictions show this trend. However, the measurements show high degree of scatter at downstream locations ( $Z/D=5, 8$ ) and therefore cannot be relied upon.

The kinetic energy (KE) profiles along the jet center-line are shown in Fig. 4d. The KE distribution is governed by a number of factors, the important ones being the interaction of the oncoming boundary layer and the jet, production due to the various velocity gradients  $\partial w/\partial y, \partial v/\partial z, \partial u/\partial x$  and strong streamline curvature effects especially in the vicinity of the jet. At the jet center-plane however, the production due to the gradient  $\partial w/\partial y$  seems to be the dominant process as a close correlation between the velocity gradient  $\partial w/\partial y$  (Fig. 4a) and the KE (Fig. 4d) can be seen. The peak KE values occur at approximately the same locations as the

peak velocity gradient positions. The HRE, LB and MK models over-predict the peak values at the jet center ( $Z/D=0$ ) while the other models show close agreement with measurements. The experimental profile at  $Z/D=1$  shows peak values in the wall-jet and lower-wake regions and in the shear-layer where strong gradients  $\partial w/\partial y$  occur. Model predictions show three peak values corresponding to the strong gradients in the wall-jet layer, the lower-wake region and the shear-layer. The HRE model over-predicts peak values in the wake region and in the shear layer. Further downstream at  $Z/D=3$  and  $Z/D=5$  two distinct peaks are observed in the measurements which once again correspond to the strong velocity gradient  $\partial w/\partial y$  at these positions. The non-linear and the low-Re k- $\epsilon$  model predictions in the shear layer are in good agreement with measurements at  $Z/D=3$ , but the HRE model over-predicts the peak level in this region while the KW model underpredicts the turbulence peak. The models do not behave appropriately in the wake region and are unable to accurately capture the peak value in the wake at  $Z/D=3, 5$  and  $Z/D=8$ . The LB model once again gives better predictions at these locations. However, the KW model significantly under-predicts the KE levels in the wake region. The behavior of the models in the near wall region is influenced by the dissipation rate  $\epsilon$  which forms the sink term in the KE equation. The  $\epsilon$  level in the near wall region is controlled by the functions  $f_1, f_2$  and the term  $E$ . Both  $f_1$  and  $E$  tend to increase the value of  $\epsilon$  near the wall and thereby reduce the KE levels. The influence of  $f_1$  is confined to a region very close to the wall in case of the LB model while it is unity for the other models. The term  $E$  is therefore dominant in the growth of  $\epsilon$  near the wall. The LB model has  $E$  equal to zero as the model solves for the dissipation rate itself and therefore the KE level in the near wall region is higher as compared to the other models. Clearly, it is more attractive to solve for  $\epsilon$  from a physical point of view. The KW model greatly under-predicts the KE levels in the wake region and as in the case of the low-Re k- $\epsilon$  models the function  $\alpha$  multiplying the production term in the  $\omega$  equation along with the constant  $\beta$  which tends to decrease the destruction term lead to very high values of  $\omega$  in the near wall region. The combined effect is to reduce the KE levels near the wall. The KE trends in the KW model case suggest that the model functions in the  $\omega$  equations are not appropriate as they lead to drastic reduction of the kinetic energy. The non-linear models do not show any significant improvements over their linear counterparts and are unable to predict the correct magnitudes in the wake.

The profiles along the edge of the jet ( $X/D=-0.5$ ) are shown in Fig. 5. The streamwise velocity at different downstream locations is expectedly higher than that along the jet center line (Fig. 4a), due to the weaker wake effect, which also results in reduced velocity gradients  $\partial w/\partial y$ . The wall-jet layer is also noticed here at  $Z/D=1$  with steep gradients in this region and in the shear layer region above the wake. The wake can be seen distinctly at this location, and all the models appear to capture the wake region well except the high-Re model. The wake gradually diminishes with increasing downstream distances, and beyond  $Z/D=3$  close agreement with experimental data is shown by all the models.

Vertical velocity comparisons have been shown in Fig. 5b. As at  $Z/D=0$  (Fig. 4a), velocities as high as 0.8 times the free stream velocity are predicted over the jet inlet hole due to the partial cover effect of the crossflow causing the flow to accelerate toward the downstream end. The measurements however do not show this peak at  $Z/D=1$ , and instead show two peak values, the one closer to the wall is due to the upward motion caused by the CRVP while the other peak at a larger distance from the wall is once again due to the crossflow deflected over the bent-over jet. The predictions show large near-wall deviations from the measured values with negative values close to the wall turning positive around  $Y/D=0.3$ . The negative values close to

the wall represent the outer downward moving parts of the CRVP, while the positive values represent the upper portions of the CRVP and the crossflow regions deflected upwards by the jet. Since the measurements do not show negative values close to the wall, it may be concluded that the CRVP in the experiments has a smaller lateral spread relative to the predictions. At  $Z/D$  locations further downstream, the measured and predicted velocities are primarily negative representing the downwash side of the CRVP. The measured behavior is captured well by the models at  $Z/D=3$  where the KW model over-predicts the peak downward velocity while the LB model underpredicts it. The experimental measurements shows some scatter in the data at  $Z/D=5$  and  $Z/D=8$  locations, although the general trend of the jet and the crossflow velocities are downwards toward the wall. The downward trend is maintained by the model predictions, but no meaningful comparison can be made with the experimental measurements due to the scatter in the data. In comparing the model predictions with each other, they follow the same trends as observed along the jet center line in Fig. 4 and therefore the arguments extended earlier to account for the model predictions are valid here as well.

Spanwise velocity comparisons in Fig. 5c indicate that the model predictions show good agreement with experimental profiles. The spanwise velocities are quite significant at the edge of the jet, and  $U/V_j$  reaches values as high as 1 close to the wall. At  $Z/D=0$  the spanwise velocity near the lower surface is negative which indicates that the flow is outwards and away from the jet center plane. Close agreement with measurements is observed at this location where the HRE model shows a relatively lower peak value. At  $Z/D=1$ , the velocities are all positive close to the wall indicating flow towards the jet center line. The CRVP entrains the surrounding crossflow fluid close to the wall resulting in positive cross-stream velocity near the wall. The velocity changes sign further away from the wall representing the upper half of the CRVP where the flow is moving away from the centerline. The peak negative value is obtained in the top regions of the CRVP structure and the models are in good agreement with measurements here. As the flow progresses downstream the CRVP structure diminishes in strength as seen from the experimental profile at  $Z/D=3$ . Models on the other hand predict a stronger structure at this location. At  $Z/D=5$ , both the measurements and predictions show a reduction in the strength of the CRVP. However, the measurements do not show any negative values along the top half indicating a pinched CRVP structure with a wider base and a narrower neck. Predictions, on the other hand, show negative velocities on the top half of the CRVP, both at  $Z/D=5$  and 8, indicating a CRVP that is more dispersed in the lateral direction than the experiments. The CRVP cannot be distinctly identified in the measurements at  $Z/D=8$  where the scatter in the data indicates that the structure has diminished in strength considerably. The models on the other hand show a distinct structure at this location. The LB model gives better predictions, as before, in the near wall region at  $Z/D=5$  and  $Z/D=8$ .

Kinetic energy profiles along the edge of the jet correspond to those in a developing boundary layer except in the immediate vicinity of the jet at  $Z/D=0$  and  $Z/D=1$ . At  $Z/D=0$  the models follow the experimental trends closely, but over-predict the peak level. Once again, a close correspondence between the velocity gradient  $\partial w/\partial y$  and KE trends is observed at  $Z/D=1$  where the peak values correspond to the maximum gradient locations. At this location however, the contribution of the gradient  $\partial U/\partial x$  has been found to be significant, largely due to the strong entrainment of the crossflow into the wake region. Model predictions typically show a number of local peak values corresponding to the large spanwise velocity gradients. At downstream locations the experimental profiles are like those

in a boundary layer and the models mimic this behavior appropriately, but they under-predict the peak KE levels. The LB and KW models show peak values very close to the wall at  $Z/D=5$  and  $Z/D=8$  and this is once again related to the steep stream-wise velocity gradients in the near wall region observed at these locations.

The normal stress profiles along the jet center plane ( $X/D=0$ ) are presented in Fig. 6. The experimental  $\overline{w'^2}$  profiles in Fig. 6a shows a correlation to the KE profile and the streamwise normal velocity gradient  $\partial w/\partial Y$  in Fig. 5d. This correlation is particularly strong in the far field ( $Z/D>5$ ) where peak values are obtained in the jet shear-layer region associated with high  $\partial w/\partial Y$  and turbulence production. In the near field, peak  $\overline{w'^2}$  values are observed in the shear layer and in the wall-jet region where large  $\partial w/\partial Y$  gradients are found. The correlation between  $\overline{w'^2}$  and  $\partial w/\partial Y$  is not taken into account by the linear eddy viscosity models where the stress  $\overline{w'^2}$  is assumed to be directly proportional to the gradient  $\partial w/\partial Z$  and therefore any simple eddy viscosity model is not expected to do well in this highly complex flow situation.

The measured trends of the stress  $\overline{u'^2}$  in Fig. 6b also show correlation with  $\partial w/\partial Y$ . In the near field ( $Z/D=1$ ), however, the near wall behavior also appears to correlate well with  $\partial U/\partial X$  which is high close to the surface due to the entrainment of the crossflow boundary layer into the wake region. The anisotropy in the near field of the jet injection close to the wall is clearly evident, and is associated with the dominance of the coherent structures in these regions. However, the low-Re and nonlinear models are found to reproduce this non-isotropic effect in a qualitatively satisfactory manner. At further downstream locations the dependence on the gradient  $\partial w/\partial Y$  becomes stronger especially in the wake of the jet where the normal stresses  $\overline{w'^2}$  and  $\overline{u'^2}$  show trends similar to the KE profiles. Models under-predict the stress levels in the wake region for  $Z/D \geq 3$  where the LB model gives better predictions in the near wall region.

The anisotropy of the flow in the vicinity of the jet is further demonstrated by the  $\overline{v'^2}$  profiles at  $Z/D=0$  and  $Z/D=1$  in Fig. 6c. In the near field the  $\overline{v'^2}$  profiles appear to scale with  $\partial V/\partial Y$ . At  $Z/D=3$  and  $Z/D=5$ , however, the effect of the gradient  $\partial w/\partial Y$  is apparent here with the peak  $\overline{v'^2}$  value occurring in the shear-layer region. The profile flattens out as the flow moves further downstream and at  $Z/D=8$  a closer correspondence can be seen with the velocity gradient  $\partial w/\partial Y$  rather than with  $\partial V/\partial Y$  (see Fig. 4b). The normal stresses are therefore not represented appropriately by the models. In the near field, the turbulence exhibits significant anisotropy. The flow field becomes more isotropic further downstream, but the gradient approximations relating  $\overline{u_i'^2}$  to  $\partial U_i/\partial X_i$  do not appear to be valid. Rather all stresses appear to correlate with  $\partial w/\partial Y$ .

The profiles for the shear stress  $\overline{w'v'}$  is presented in Fig. 6d. The peak value observed in the measurements and predictions are in the jet-shear-layer regions and is a consequence of the high  $\partial w/\partial Y$  in the shear layer region. This dependence is consistent with the fact that the product  $\overline{v'^2} \partial w/\partial Y$  is the dominant term in the production of  $\overline{w'v'}$ . Peak values are over-predicted by the models at  $Z/D=0$  location and only the KW model follows the experimental trends closely. The peak values decrease as the flow moves downstream where the stream-wise velocity gradients are reduced in the shear layer. At  $Z/D=3$  and beyond, the stress values are very small in the wake region where the velocities are low and fairly uniform. Model predictions in the recirculation region and further downstream follow the measured trends correctly largely due to the fact that

the eddy viscosity model also incorporates the dependence of  $\overline{w'v'}$  on  $\partial w/\partial y$ . The shear stress predicted by the models is found to change sign close to the wall at  $Z/D=1$  and is seen to follow the velocity trends reported in Fig. 4a where velocity gradients also change sign close to the wall.

In general, the model predictions for the turbulent shear stress  $\overline{w'v'}$  follow the measured trends fairly well in the shear layer and also reflect the appropriate dependence on velocity gradients. In comparing the model predictions, the HRE model shows the greatest level of over-prediction in the peak stress levels. This would lead to the greatest levels of turbulent transport, and is consistent with the observation that the HRE model is associated with the highest lateral jet penetration. The failure of the non-linear models to give better predictions over the linear ones was somewhat unexpected. The introduction of the non-linear quadratic terms in the stress-strain relationship in order to incorporate the effect of strong streamline curvatures are therefore insufficient and cubic terms must be included in order to obtain the desired stress-strain coupling. The introduction of merely quadratic terms in the SP and MK models do not produce the desired effect of streamline curvatures on the stress levels.

### Vector Plots and Vorticity Contours

Attention is now turned toward describing the overall features of the flow field by presenting vorticity contours and vector plots along a typical cross-stream plane. Figures 7 presents the velocity vectors superimposed on the streamwise vorticity contours at  $Z/D=3$  cross-stream plane. The predictions for all seven models evaluated are presented, and in each figure the same color scale is used in order to facilitate a comparison between the different model predictions.

At  $Z/D=3$ , the CRVP is clearly established and is the dominant feature in the flow field. The HRE model shows the greatest lateral spread which was also observed in the velocity comparisons shown in Fig. 5 where the spanwise velocities predicted by the HRE model are larger than those predicted by the other models. The MK model shows the greatest vertical spread of the jet, and this was also observed in Fig. 4, where in the MK model predictions, the shear layer region was displaced vertically upwards relative to other models and the measurements. The LB model predictions show the weakest CRVP, and the lowest levels of vertical and lateral spread. All the low-Re models show small negative velocities close to the wall between  $X/D$  of -1 and -1.5, and these reflect the manifestation of the horse-shoe vortex. It is the strongest, and can be clearly observed in the KW model predictions. Also of interest is the clear development of a wall-vortex structure in all the low-Re models. The wall-vortex is a manifestation of the crossflow entrainment into the wake region encountering an adverse pressure gradient in the spanwise direction near the jet centerplane. This adverse pressure gradient leads to flow reversal in the spanwise (XY) plane and the formation of the wall vortex structure close to the surface (as captured by the low-Re models). The vortex is confined between  $X/D$  of 0 and -0.5 at this  $Z/D$  location. As for the horse-shoe, the KW model predicts the strongest wall vortex structure. Note that the HRE model does not predict the wall vortex at all.

Details of the horse-shoe vortex predicted at  $Z/D=8$  location are shown in an enlarged view in Fig. 8. The horse-shoe can be clearly observed in all the model predictions, and show significant differences in size and strength, with the KW model showing the most significant horse-shoe structure.

The differences in the recirculation region behind the jet are presented in greater detail in Figure 9, which shows that the recirculation in all the low-Re models is qualitatively similar,

with the reversed flow being entrained upwards into the jet and then carried forward along its trajectory. The HRE model shows a much larger region of negative streamwise velocity, with strong crossflow entrainment into the wake. The recirculation region in the HRE model extends all the way till  $Z/D=1.5$ , while in the other models the recirculation region is less than  $1-D$  from the center of the jet-exit.

The region upstream of the jet marks the inception of the horse-shoe vortex. An exploded view of this region is shown in Fig. 10, where the KW model, the SP model and the MR model all show the inception of the horse-shoe at this  $X/D=0$  centerplane. Since all models show the horse-shoe vortex at constant- $Z/D$  planes further downstream (see Fig. 7, 8), this implies that for the models where the horse-shoe is not observed at  $X/D=0$  in Fig. 10, the inception may occur at other  $X/D$  planes. Evidence of this is seen in streamwise and spanwise vorticity contours (not shown here) at a constant  $Y/D$  plane ( $=0.05$ ) very close to the wall.

## CONCLUDING REMARKS

Numerical predictions for film cooling jet in a cross-flow have been carried out in this study using seven different turbulence models: a high-Re model (HRE), low-Re models (LS, LB, KW), non-linear models (SP, MK), and a DNS based low-Re model (MR). The mean flow velocity and turbulent statistic profiles in general agree fairly well with experimental trends. The CRVP is distinctly predicted by all the models, but only a few models manage to capture the horse-shoe structure correctly for the low blowing ratio case considered in this work. The HRE model is not very well suited for the specific flow situation as it does not resolve the near wall region properly. Although the mean flow profiles are predicted well, the turbulence levels are over-predicted and the HRE model is also unable to capture the recirculation in front of the jet. The HRE model predicts the largest levels of spanwise-jet-penetration, and substantially overpredicts the measured values of the spanwise and vertical velocities. The use of this model in such a complex flow situation is therefore not recommended. The LS model which resolves the near wall region follows the experimental trends correctly, but fails to predict the correct trends in the wake of the jet and does not represent the turbulent mixing taking place in this region appropriately. The near wall region behavior of the LB model is consistently good, and this model, in general, seems to provide the best agreement with measurements. Compared to the other models, the LB model shows the smallest levels of vertical and spanwise spread. However, predictions in the jet region do not follow the experimental trends correctly and the model is also unable to capture the recirculation in front of the jet. This structure is distinctly captured by the MR model. In this region the gradients in the vertical direction are of primary importance and the scaling arguments used for deriving the correlation terms in the  $\epsilon$ -budget (see Rodi and Mansour, 1993) hold good. In the jet and its vicinity, however, the gradients in the other directions cannot be neglected and therefore the simplified  $\epsilon$  budget is inadequate in the jet and its wake region. Clearly, the  $\epsilon$  budget needs to be optimized for the present flow situation using DNS data on lines similar to the MR model. The SP model predicts the turbulent characteristics trends correctly, but like the other models it is unable to resolve the variations observed in the wake of the jet. The MK non-linear model significantly over-predicts the vertical jet penetration. The inability of the SP and MK nonlinear models to give better predictions compared to the linear models is thought to be a consequence of the fact that the non-linear model coefficients were obtained through curve fitting of experimental data for simple wall bounded flows (see Mayong and Kasagi, 1990 and Speziale, 1987) and may not be well suited for the jet in a cross-flow situation. The improved predictions of the near wall structures obtained with the

KW model can be attributed in part to the fact that the boundary conditions specified for  $\omega$  are more accurate than those for  $\epsilon$ . This problem related to the  $\epsilon$  behavior near the wall has been pointed out by a number of researchers.

It is therefore clear from the present study that the models in there present form give overly simplistic predictions for the highly complex flow field being considered here. A comparison of the model predictions clearly reveals the need for better resolution of the the near wall region, asymptotic consistency of model coefficients and damping functions in the jet and wall bounded regions respectively, and an appropriate representation of the  $\epsilon$  budget. Also required is a suitable non-linear formulation to accurately predict the non-isotropic nature of the flow. An effort along these directions using DNS predictions for jet in a crossflow (Muldoon and Acharya, 1998; Sharma and Acharya, 1998) to guide the model development is being made by the authors and is to be reported shortly.

## REFERENCES

- Ajersch et al, P., Zhou, J.-M., Ketler, S., Salcudean, M., Gartshore, I. S., 1995, "Multiple Jets in a Crossflow: Detailed Measurements and Numerical Simulations," *ASME Paper 95-GT-9*, Int. Gas Turbine and Aerospace Congress & Exposition, Houston, Texas.
- Andreopoulos, J., and Rodi, W., 1984, "Experimental Investigation of Jets in a Crossflow," *J. Fluid Mech.*, Vol. 138. pp. 93-127.
- Clauss, R.W., and Vanka, S. P., 1990, "Multigrid Calculations of Jet in Crossflow," *AIAA Paper 90-0444*, AIAA 28<sup>th</sup> Aerospace Science Meeting, Reno, NV.
- Demuren, D.K., Rodi, W., and Schonung, B., 1986, "Systematic Study of Film Cooling with a Three-Dimensional Calculation Procedure," *J. of Turbomachinery*, Vol. 108, pp. 124-130.
- Demuren, A. O., 1993, "Characteristics of Three-Dimensional Turbulent Jets in Crossflow," *Int. J. Engng Sci.*, Vol. 31, No. 6, pp. 899-913.
- Durbin, P., 1991, "Near-wall Turbulence Closure without Damping Functions" *Theor. and Comp. Fluid Dynamics*, Vol. 3, No. 1, pp. 1-13
- Findlay, M., J., He, P., Salcudean, M., and Gartshore, I.,S., 1996, "A Row of Streamwise-Inclined Jets in Crossflow: Measurements and Calculations," *ASME paper 96-GT-167*, International Gas Turbine and Aeroengine Congress & Exhibition, Birmingham, UK.
- Fornberg, B. G., 1988, "Generation of Finite Difference Formulas on Arbitrarily Spaced Grids," *Mathematics of Computations*, Vol. 31, No. 184, pp. 699-706
- Foss, J., 1980, "Interaction Region Phenomena for the Jet in a Crossflow Problem," *Rep. SFB 80/E/161*, Univ. Karlsruhe.
- Fric, T. F., and Roshko, A., 1994, "Vortical Structures in The Wake of a Transverse Jet," *J. Fluid Mech.*, Vol. 279, pp. 1-47.
- Garg, V.K., and Gauler, R. E., 1997, "Effect of Coolant Temperature and Mass Flow on Film Cooling of Turbine Blade," *Int. J. Heat and Mass Transfer.*, Vol. 40, No. 2, pp. 435-445.
- Kelso, R. M., Lim, T. T., and Perry, A. E., 1996, "An Experimental Study of Round Jets in Crossflow," *J. Fluid Mech.*, Vol. 306, pp. 111-144.
- Kim, S. W., and Benson, T. J., 1993, "Fluid Flow of a Row of Jets in Crossflow- A Numerical Study," *AIAA Journal*, Vol. 31, No. 5, pp. 806-811.
- Lam, C. K. G., and Bremhorst, K. A., 1981, "Modified form of the k- $\epsilon$  Model for Predicting Wall Turbulence," *J. of Fluid Engineering*, Vol. 103, pp. 456-460.
- Launder, B. E., and Spalding, D. B., 1974, "The Numerical Computation of Turbulent Flows," *Computer Methods in Applied Mechanics and Engineering*, Vol. 3, No. 2, pp. 269-289.

- Launder, B. E., and Sharma, B.I., 1974, "Application of the Energy Dissipation Model of Turbulence to the Calculation of Flow Near a Spinning Disc," *Letters in Heat and Mass Transfer*, Vol. 1, pp. 131-138.
- Lee, S. W., Lee, J.S., and Ro, S.T., 1994, "Experimental Study on The Flow Characteristics of Streamwise Inclined Jets in Crossflow on Flat Plate," *J. of Turbomachinery*, Vol. 116, pp. 97-105
- Mayong, H. K., and Kasagi, N., 1990, "Prediction of Anisotropy of the Near-Wall Turbulence with an Anisotropic Low-Reynolds-Number  $k-\epsilon$  Turbulence Model," *J. of Fluids Engineering*, Vol. 112, pp. 521-524.
- Mayong, H. K., 1988, "Fundamental Studies on Two-Equation Turbulence Models for Numerical Prediction of Wall-Bounded Shear Flows and Heat Transfer," *Dr. Eng. Thesis, The University of Tokyo*.
- Muldoon, F., and Acharya, S., 1998, "Dynamics of Large Scale Structures for Jets in CrossFlow", accepted *ASME-International Gas Turbine Conference*, 1998, Stockholm, Paper ASME 98-GT-019
- Patankar, S. V., 1980, "Generation of Finite Difference Formulas on Arbitrarily Spaced Grids," *Mathematics of Computations*, Vol. 31, No. 184, pp. 699-706.
- Patel, V. C., Rodi, W., and Scheuerer, G., 1985, "Turbulence Models for Near-Wall and Low-Reynolds Number Flows : A Review," *AIAA Journal*, Vol. 33, pp. 1308-1318.
- Rodi, W., and Mansour, N. N., 1993, "Low Reynolds Number  $k-\epsilon$  Modelling with the Aid of Direct Simulation Data," *J. Fluid Mech.*, Vol. 250, pp. 509-529.
- Sharma, C., and Acharya, S., 1998, "Direct Numerical Simulation of Flow and Heat Transfer in a Periodic Channel Flow with Coolant Injection" *ASME- (IMECE)*, Anaheim, November 1998
- Speziale, C. G., 1987, "On Nonlinear  $k-l$  and  $k-\epsilon$  Models of Turbulence," *J. Fluid Mech.*, Vol. 178, pp. 459-475.
- Speziale, C. G., Abid, R., and Anderson, E. C., 1992, "Critical Evaluation of Two-Equation Models for Near-Wall Turbulence," *AIAA Journal*, Vol. 30, No. 2, pp. 324-331.
- Walters, D. K., and Laylek, J. H., 1997, "A Detailed Analysis of Film Cooling Physics Part I : Streamwise Injection with Cylindrical Holes," *ASME paper 97-GT-269*.
- Wilcox, D. C., and Traci, R. M., 1976, "A Complete Model of Turbulence," *AIAA Paper 76-351*.

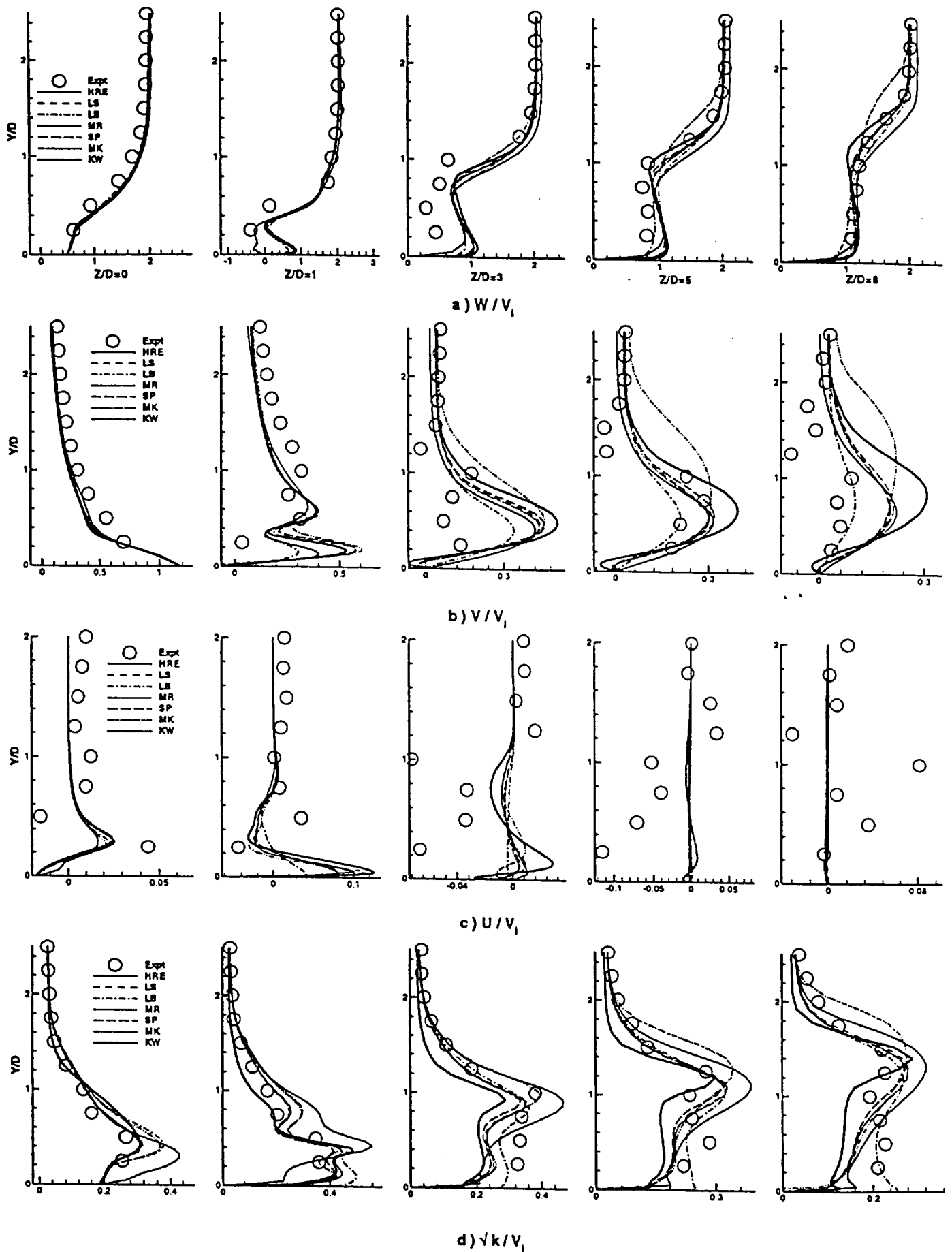


Figure 4 Velocity and kinetic energy profiles at  $X/D=0$  at different  $Z/D$  from center of the jet



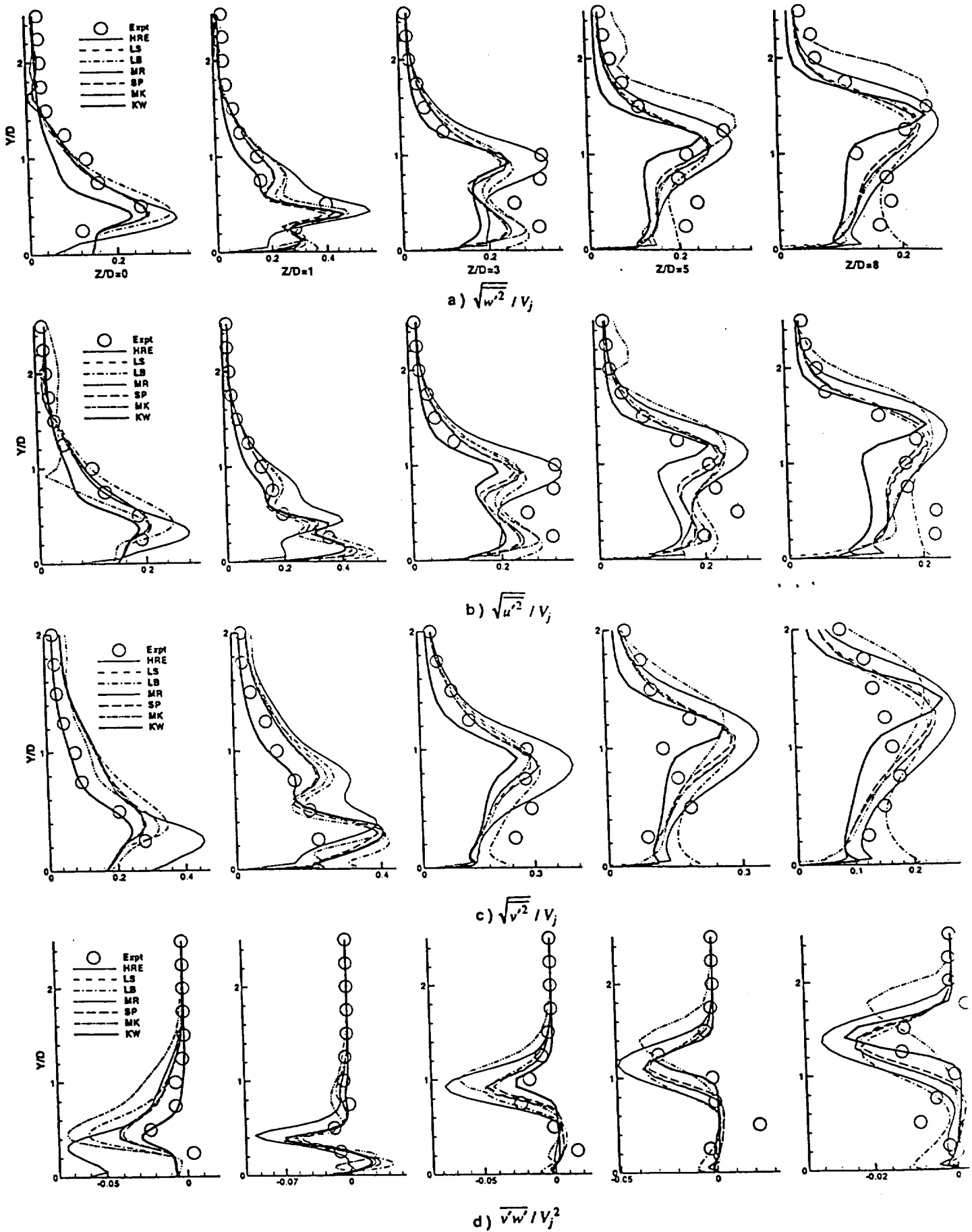


Figure 6 Stress profiles at  $X/D=0$  at different  $Z/D$  from center of the jet

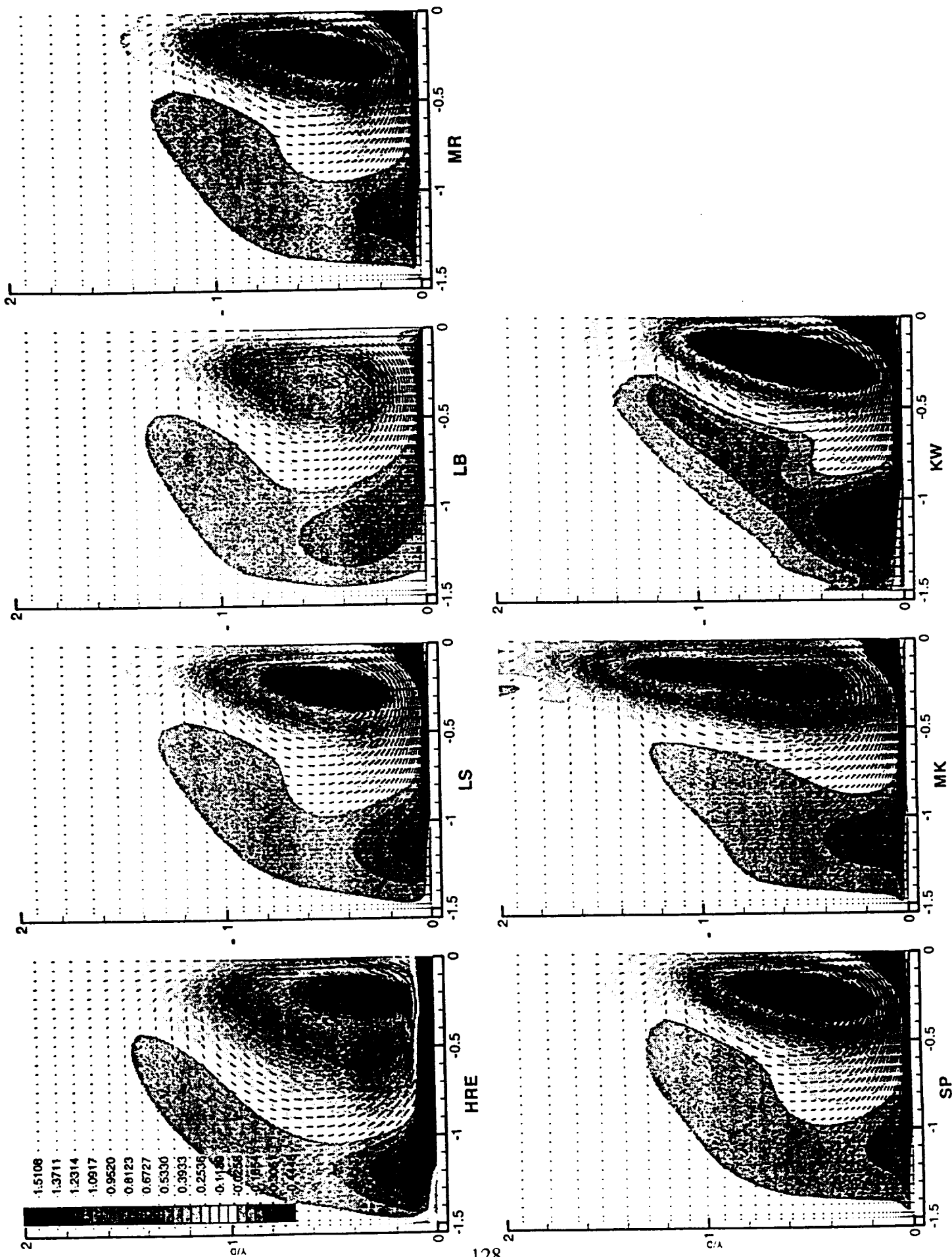


Figure 7 7-component of vorticity and velocity vectors in XY plane at  $Z/D=3.0$  for different models

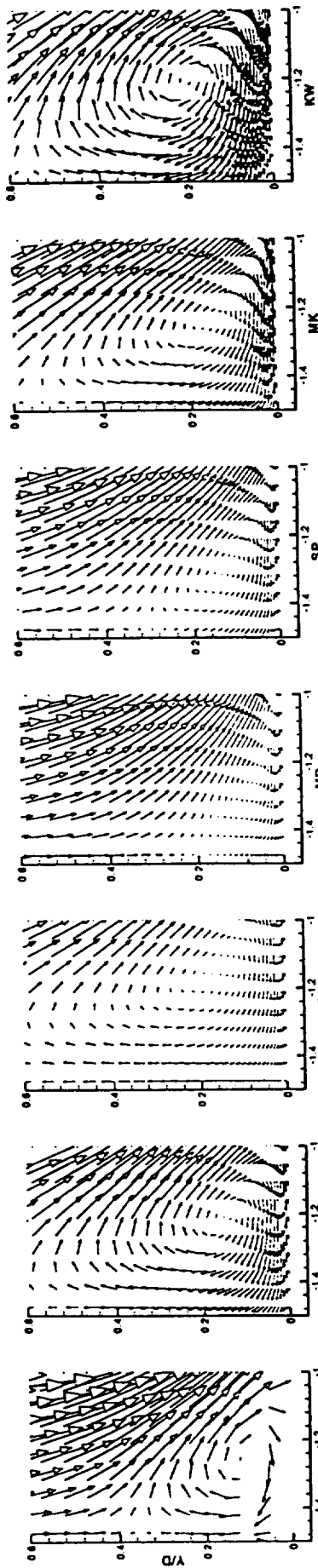


Figure 8 Velocity vectors in XY plane at  $Z/D=8$

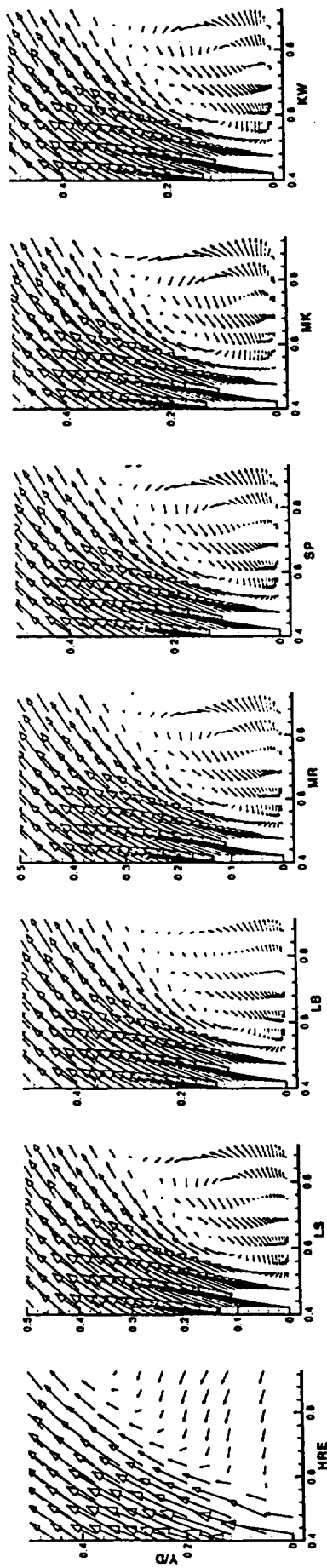


Figure 9 Velocity vectors in YZ plane at  $X/D=0$

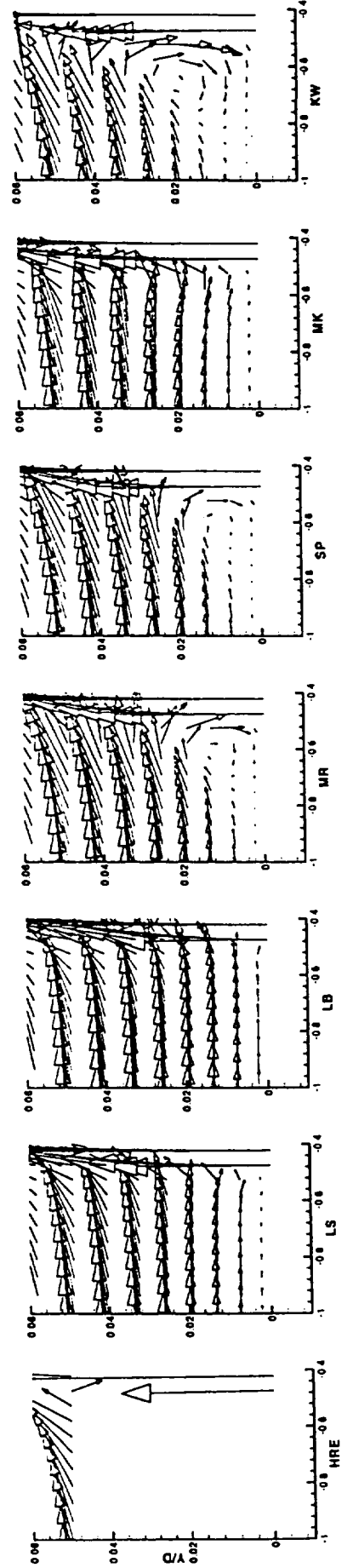


Figure 10 Velocity vectors in YZ plane at  $X/D=0$

## CHAPTER IX

### CONCLUDING REMARKS AND FUTURE WORK

In this report we have presented an outline of the numerical methodology used for DNS/LES/RANS and representative results for the flow field associated with the jet-in-a-crossflow configuration. In presenting the results, the focus has been on the flow dynamics rather than on the heat transfer, since the flow field has to be correctly predicted before there is any hope of correctly computing the surface heat transfer. Our efforts have been primarily concentrated in obtaining a better understanding of the flow physics associated with the interaction of the jet with the crossflow, and in evaluating the ability of turbulence models in capturing this flow physics. In a very broad sense, we have reached the following major conclusions.

- *The jet-in-crossflow configuration that is representative of film cooling flows is characterized by highly dynamical large scale structures. These large-eddy structures include the CVP, the horseshoe vortex, wall vortices, wake vortices, and jet shear layer vortices.*
- *DNS is able to correctly capture the flow physics and accurately predict the evolution and interaction of these structures.*
- *RANS simulations, with two-equation turbulence models, are unable to capture many of the large scale dynamical structures. Although different turbulence models produce qualitatively the same behavior, there are significant quantitative differences in the predictions depending on the model used. In general, RANS predictions over-predicted the jet penetration in the lateral direction, and significantly over-predicted the wake recovery. Best agreement was obtained with the Lam-Bremhorst model. The non-linear models were found to be inadequate in correctly describing the flow anisotropy.*
- *LES predictions were found to correctly describe the behavior of the large scale structures, and were found to be an accurate cost-effective alternative to the computationally expensive DNS calculations. The use of LES holds great promise for film cooling predictions since these computations can be done on workstations, and can accurately describe the flow physics.*

More specific conclusions regarding the flow physics and the inadequacy of the various models is presented at the end of each chapter.

Future work is now being carried out by us in three major directions as described below.

- *The DNS/LES codes are being used to understand the flow physics associated with film cooling flows. Issues being studied include: effect of high free-stream turbulence, effect of free-stream length scales, effect of rotation, effect of wake crossings, compound angle injection, multiple row injection, effect of hole aspect ratio, and plenum effects.*
- *DNS/LES simulations are being used to compute the statistics (higher order correlations) that appear in a modeled form in the RSTM and the two-equation turbulence models. We intend to evaluate the validity of the modeled expressions by comparing them with the*

*DNS/LES computed statistics. This comparison will allow us to better parametrize the constants or functions that appear in the closure expressions or to better capture the flow physics through a different form of closure expression. These improved turbulence models will be fed back into the RANS code.*

- *The DNS/LES codes are being improved to handle more complex geometries, and to be more computationally efficient. These activities include: incorporation of multi-block, multi-grid procedures, curvilinear/unstructured grids, improved differencing schemes (finite difference or spectral), improved solvers for the system of equations, code structuring and parallelization, and finally post-processing visualization tools. The ultimate goal is to be able to run LES codes for a complete airfoil incorporating multiple film cooling rows and plenum effects, and to do this in a cost-effective manner. Our initial successes with the LES code are extremely promising since, on a Digital Alpha 500 workstation, we are able to obtain in 1-2 days, complete runs (7-8 jet flow-through times over the blade surface) on a mesh that resolves the dynamics of all the important structures. If several workstations are hooked to run simultaneously, LES simulations can be obtained in less than a day.*

In closing, we would again like to express our gratitude to NASA Glenn Research Center and the Turbomachinery Flow physics group that supported our efforts and made this work possible.





# REPORT DOCUMENTATION PAGE

*Form Approved*  
OMB No. 0704-0188

Public reporting burden for this collection of information is estimated to average 1 hour per response, including the time for reviewing instructions, searching existing data sources, gathering and maintaining the data needed, and completing and reviewing the collection of information. Send comments regarding this burden estimate or any other aspect of this collection of information, including suggestions for reducing this burden, to Washington Headquarters Services, Directorate for Information Operations and Reports, 1215 Jefferson Davis Highway, Suite 1204, Arlington, VA 22202-4302, and to the Office of Management and Budget, Paperwork Reduction Project (0704-0188), Washington, DC 20503.

<b>1. AGENCY USE ONLY</b> ( <i>Leave blank</i> )		<b>2. REPORT DATE</b> September 1999	<b>3. REPORT TYPE AND DATES COVERED</b> Final Contractor Report	
<b>4. TITLE AND SUBTITLE</b>  Large Eddy Simulations and Turbulence Modeling for Film Cooling			<b>5. FUNDING NUMBERS</b>  WU-538-12-10-00 NAG3-1641	
<b>6. AUTHOR(S)</b>  Sumanta Acharya				
<b>7. PERFORMING ORGANIZATION NAME(S) AND ADDRESS(ES)</b>  Louisiana State University Mechanical Engineering Department Baton Rouge, Louisiana 70803			<b>8. PERFORMING ORGANIZATION REPORT NUMBER</b>  E-11859	
<b>9. SPONSORING/MONITORING AGENCY NAME(S) AND ADDRESS(ES)</b>  National Aeronautics and Space Administration John H. Glenn Research Center at Lewis Field Cleveland, Ohio 44135-3191			<b>10. SPONSORING/MONITORING AGENCY REPORT NUMBER</b>  NASA CR—1999-209310	
<b>11. SUPPLEMENTARY NOTES</b>  Project Managers, Chi R. Wang, (216) 433-5865, and Raymond E. Gaugler, (216) 433-5882, Turbomachinery and Propulsion Systems Division, NASA Glenn Research Center, organization code 5820.				
<b>12a. DISTRIBUTION/AVAILABILITY STATEMENT</b>  Unclassified - Unlimited Subject Categories: 02 and 34  This publication is available from the NASA Center for AeroSpace Information, (301) 621-0390.			<b>12b. DISTRIBUTION CODE</b>  Distribution: Nonstandard	
<b>13. ABSTRACT</b> ( <i>Maximum 200 words</i> )  The objective of the research is to perform Direct Numerical Simulations (DNS) and Large Eddy Simulations (LES) for film cooling process, and to evaluate and improve advanced forms of the two equation turbulence models for turbine blade surface flow analysis. The DNS/LES were used to resolve the large eddies within the flow field near the coolant jet location. The work involved code development and applications of the codes developed to the film cooling problems. Five different codes were developed and utilized to perform this research. This report presented a summary of the development of the codes and their applications to analyze the turbulence properties at locations near coolant injection holes.				
<b>14. SUBJECT TERMS</b>  Gas turbine; Turbulence; Computational fluid dynamics			<b>15. NUMBER OF PAGES</b> 140	
			<b>16. PRICE CODE</b> A07	
<b>17. SECURITY CLASSIFICATION OF REPORT</b> Unclassified	<b>18. SECURITY CLASSIFICATION OF THIS PAGE</b> Unclassified	<b>19. SECURITY CLASSIFICATION OF ABSTRACT</b> Unclassified	<b>20. LIMITATION OF ABSTRACT</b>	